TESIS DOCTORAL

Universidad de Granada

Programa de Doctorado en Ciencias de La Tierra

Novel technique to detect seismic signals and its application to map upper-mantle discontinuities beneath Iberia

Anahí Luciana Bonatto

Granada 2013

Editor: Editorial de la Universidad de Granada
Autor: Anahí Luciana Bonatto
D.L.: GR 726-2014
ISBN: 978-84-9028-894-8

TESIS DOCTORAL

Novel technique to detect seismic signals and its application to map upper-mantle discontinuities beneath Iberia

REALIZADA POR:

Anahí Luciana Bonatto

DIRECTORES DE LA TESIS:

Dr. Martin Schimmel

Dr. José Morales

Instituto de Ciencias de La Tierra "Jaume Almera"-CSIC

Instituto Andaluz de Geofísica -UGR

Compromiso de respeto derechos de autor

La doctorando Anahí Luciana Bonatto y los directores de la tesis "*Novel techniques to detect seismic signals and its application to map the transition zone discontinuities beneath Iberia*", garantizamos, al firmar esta tesis doctoral, que el trabajo ha sido realizado por el doctorando bajo la dirección de los directores de la tesis y hasta donde nuestro conocimiento alcanza, en la realización del trabajo, se han respetado los derechos de otros autores a ser citados, cuando se han utilizado sus resultados o publicaciones.

Granada 15 de Septeimbre de 2013

Directores de la Tesis	Doctorando
Fdo.: Dr. Martin Schimmel	Fdo.: Anahí Luciana Bonatto
Dr. José Morales	

Esta tesis está dedicada a
Ricardo
por su apoyo incondicional

Agradecimientos

El Instituto de Ciencias de la Tierra "Jaume Almera" -IJA- (CSIC) me ha concedido una beca Jae-Predoc del CSIC para realizar el doctorado en España. A quienes corresponda quisiera agradecer la oportunidad que se me ha brindado.

La realización de esta tesis no habría sido posible sin los datos proporcionados por los siguientes proyectos: TopoIberia, TopoMed, Rifsis, CGL2012-31472, P09RNM5100. Detrás de estos proyectos están los grupos y personas que se encargan de la instalación de las estaciones y de la adquisición de los datos. A todos ellos quiero agradecerles especialmente ya que realizan una ardua tarea para poner los datos a disposición de los investigadores. También quiero agradecer al proyecto WILLAS por compartir su base de datos, de los cuales algunos han sido utilizados en este estudio.

A mis directores de tesis, Martin y Pepe, quiero agradecer su apoyo y el haber confiado en mi para realizar este trabajo de investigación. A Pepe, quiero agradecerle especialmente por haberme acogido en el Instituto Andaluz de Geofísica -IAG- y por poner todos sus recursos a mi disposición. A Martin por guiarme, por proporcionarme ánimo y confianza cuando el trabajo se tornaba más complejo y por aconsejarme tantas veces sobre cómo lidiar con la política científica.

Quisiera agradecer también a la Dra. Eleonore Stutzmann por haberme dado la oportunidad de hacer una estancia de investigación en el *Institut de Physique du Globe de Paris* y por enseñarme a trabajar con las "funciones receptoras". A Antonio Villaseñor por haberme proporcionado su modelo de tomografía de onda P, que ha sido un aporte imortante para la interpretación de los resultados de esta tesis. A la Prof. Adriana Caldiz le agradezco especialmente por haber corregido la escritura de la tesis.

A mis compañeros del IJA y del IAG quiero agradecerles la predisposición para darme una mano siempre que fué necesario. A Janire por responder todas mis preguntas, incluso hasta unos días antes de su defensa. A Luisa por hacerme un lugar en su casa cuando lo necesité.

A Pocho y Adriana quisiera agradecerles y dedicarles parte de todo este esfuerzo porque los he visto sufrir y reir conmigo desde que tengo uso de razón y porque fueron los primeros en creer en mi. A Santi porque me alegra el día con sus ocurrencias y a veces me desestructura y otras me hace enojar. A Ricardo por ser mi compañero de aventuras y por ser un amigo incondicional.

TESIS DOCTORAL

Novel technique to detect seismic signals and its application to map upper-mantle discontinuities beneath Iberia

PALABRAS CLAVES: Estructura interior de la Tierra, discontinuidades del manto superior, zona de transición, detección de señales sísmicas, región Ibero-Maghrebí, IberArray, TopoIberia.

Resumen

En este estudio analizamos las discontinuidades de la zona de transición del manto superior a 410 km y 660 km de profundidad a partir de la detección de ondas sísmicas convertidas de P-a-s debajo de la región Ibero-Magrebí. Para este propósito, usamos eventos telesismicos registrados en 259 estaciones de banda ancha desplegadas mayormente por el proyecto TopoIberia. El análisis detallado de las discontinuidades de la zona de transición proporciona información acerca de la temperatura y composción del manto superior a las profundidades estudiadas. Este estudio añade nuevas restricciones para la mejor comprensión de la compleja y controversial región Ibero-Maghrebí.

Las ondas convertidas en las discontinuidades del manto superior llegan en la coda de la onda P junto con otras señales y usualmente son identificadas en los *stacks* de funciones receptoras. Aquí, construimos una técnica nueva de procesamiento, que se apoya en las funciones receptoras y que se basa en técnicas de correlación cruzada y de *stacking* para detectar y extraer señales de manera eficiente a partir de su coherencia, lentitud, tiempo de viaje y polaridad. A fin de añadir consistencia y robustez a las detecciones, nuestros resultados finales se basan en el análisis conjunto de las funciones receptoras y dos funcionales diferentes de correlación cruzada. Esto permite evaluar errores y rellenar gaps en las observaciones cuando alguna de las técnicas falla inherente a las características de la señal y el ruido. Finalmente, la profundidad de las discontinuidades se determina utilizando correcciones de tiempo obtenidas a partir de un modelo de velocidades 3D. Así, presentamos mapas topográficos de las discontinuidades 410-km y 660-km, que muestran variaciones en el espesor de la zona de transición debajo del área de estudio.

El espesor de la zona de transición debajo de Iberia central (240-250 km) está dentro del promedio global; la zona de transición es más ancha debajo del oeste de Marruecos (250-275 km), el Mar de Alborán (280-300 km) y el este de España (260-280); y es predominantemente fina debajo del sur de Portugal (220-240 km), el Golfo de Cádiz (220-250 km) y el área del Estrecho de Gibraltar (214 km). La zona de transición más ancha debajo del oeste de Marruecos y el este de España es mayormente debido a que la discontinuidad 660-km se encuentra a una profundidad mayor que el promedio global, mientras que la topografía de la discontinuidad 410-km es más suave. Aunque, debajo del este de España, se aprecia una leve depresión de la 410. Por otro lado, la profundidad de las discontinuidades está anti-correlacionada debajo del Mar de Alborán. Además, encontramos una correlación espacial entre el vulcanismo anorogénico Neógeno y la topografía de la 410. Todos estos resultados se discuten con el fin de añadir nuevas restricciones a la temperatura y composición de las anomalías de velocidad sísmica observadas en la zona de transición debajo de la controversial región Ibero-Magrebí. El ensanchamiento de la zona de transición del orden de 50 km -respecto al valor de referencia- debajo del Mar de Alborán sugiere que la loza de Alborán aún está lo suficientemente fría como para elevar la transformación de fase $\alpha - \beta$ y para deprimir la post-spinel. De forma similar, creemos que la loza del Tethys debajo de España -estancada en la base de la zona de transición- aún estaría fría y sería responsable de la depresión de la 660, mientras que un proceso de convección de pequeña escala encima de la 660 -activada por deshidratación de la loza- explicaría la depresión de la 410. Por otro lado, la zona de transición más ancha debajo de Marruecos es probablemente de origen composicional. La explicación preferida es que la depresión de la 660 se debe a la transición granate-a-perovskita sumado a un alto contenido de aluminio en el granate. La zona de transición más angosta debajo del Golfo de Cádiz, el Estrecho de Gibraltar y el sur de Portugal es mayormente debido a una 410 más profunda y pensamos que podría estar causada por un manto superior de elevada temperatura, que también ha sido inferido en imágenes tomográficas recientemente publicadas.

Adicionalmente, determinamos el espesor de las discontinuidades 410-km y 660-km e investigamos su variación espacial. Este análisis, muestra que ambas discontinuidades presentan variaciones espaciales en su espesor. En particular, la 660 es más ancha debajo del Mar de Alborán y el sur de España. Interpretamos la variación espacial en el espesor de la 410 como causada por variaciones en la concentración de agua dentro de la zona de transición debajo del área de estudio. Creemos que la 660 más ancha, de aproximadamente 30 km, debajo del Mar de Alborán y del sur de España es causada por la combinación de gradientes de velocidades debido a las transformaciones de fase post-spinel e ilmenita-a-perovskita.

Abstract

In this study, we analyze the upper-mantle transition zone discontinuities at a depth of 410 km and 660 km as seen from seismic P-to-s wave conversions beneath the Ibero-Maghrebian region. For this purpose, we use teleseismic events recorded at 259 broadband seismic stations deployed mainly by the TopoIberia project. The detailed analysis of the transition-zone discontinuities provides information on the temperature and composition of the upper mantle at the investigated depths. This study adds new constraints, which would help to improve the understanding of the complex and controversial Ibero-Maghrebian region.

The converted waves from the upper-mantle discontinuities arrive in the P-wave coda together with other signals and are usually identified on stacked receiver functions. Here, a new processing approach is built, which is leaned on receiver functions and which is based on cross-correlation and stacking techniques, to efficiently detect and extract signals by means of their coherence, slowness, travel time and polarity. In order to add consistency and robustness to the detections, our final results are based on a joint analysis of the receiver functions and two different cross-correlation functionals. This permits to assess errors and to bridge observation gaps due to detection failure of any of the techniques inherent to signal and noise characteristics. Finally, discontinuity depths are determined using time corrections obtained from a 3D velocity model. We present topography maps for the 410-km and 660-km discontinuities, which show variations in the transition zone thickness beneath the study area.

The transition zone thickness is about global average beneath central Iberia (240-250 km); it is thicker beneath west Morocco (250-275 km), the Alboran Sea (280-300 km) and east Spain (260-280); and it is predominantly thinner beneath south Portugal (220-240 km), the Strait of

Gibraltar area (214 km) and the Gulf of Cadiz (220-250 km). The thicker transition zone beneath west Morocco and east Spain is mainly due to a deeper 660-km discontinuity, while the topography of the 410-km discontinuity is smaller. Although, beneath east Spain, the 410 is slightly depressed. On the other hand, the discontinuities' depths are anti-correlated beneath the Alboran Sea. Additionally, we find a spatial correlation between the Neogene anorogenic volcanism and the topography of the 410-km discontinuity. These results are discussed to add new constraints on temperature and composition to seismic velocity anomalies observed in the transition zone beneath the controversial Ibero-Magrhrebian region. The transition zone thickening of about 50 km -from the reference value- beneath the Alboran Sea suggests that the Betic-Alboran slab is still sufficiently cold to elevate the $\alpha - \beta$ mineral phase transition and to depress the post-spinel one. Similarly, the cold Tethys slab -stagnant at the base of the transition zone- beneath east Spain is thought to be responsible for the 660 depression, while small-scale convection above the 660 -triggered by slab dehydration- may explain the 410 depression. On the other hand, the thicker transition zone beneath Morocco is probably of compositional origin. Our preferred explanation is that the 660 depression is due to the garnet-to-perovskite transition and a high aluminum content within garnet. The thinner transition zone beneath the Gulf of Cadiz, the Strait of Gibraltar and the south of Portugal is mainly due to a depressed 410 and is thought to be caused by high upper-mantle temperature, which is also inferred by recently published tomographic images.

Furthermore, we determine the widths of the 410-km and 660-km discontinuities and we investigate their spatial variations. This analysis has revealed that both discontinuities present spatial thickness variations. In particular, the 660 is thicker beneath the Alboran Sea and south Spain. We interpret the spatial variation of the 410 width as caused by variations in the water concentration in the transition zone beneath the study area. The thicker 660, of about 30 km, beneath the Alboran Sea and south Spain is thought to be caused by combined velocity gradients due to post-spinel and ilmenite-to-perovskite phase transitions.

Contents

1

General introduction

1.1 Motivation and organization of the thesis

The Ibero-Maghrebian region, comprising Spain, Portugal and the northern parts of Morocco and Algeria, has a complex tectonic history including a retreating subduction and extensional processes in the Alboran Sea basin (Royden, 1993; Faccenna et al., 2004; Spakman and Wortel, 2004), subduction-related magmatism from Late Cretaceous (100-66 My) to Pliocene (5.3-2.6 My), and Neogene subduction-unrelated magmatism of sub-lithospheric origin since Pliocene, which is mostly located in the south and east coast of Iberia and north Morocco (e.g. Lustrino and Wilson, 2007; Carminati et al., 2012). The origin of the sub-lithospheric magma source is a controversial topic (e.g. Lustrino and Wilson, 2007) as well as the origin of the Neogene extensional Alboran Basin (e.g. Platt and Vissers, 1989; Royden, 1993; Bokelmann et al., 2011). A location map and names of the main tectonic units are given in Fig. 1.1.

Tomography studies reveal a positive P-velocity anomaly beneath the Alboran Sea extending form the base of the crust across the entire upper mantle (Spakman, 1990; Blanco and Spakman, 1993; Wortel and Spakman, 2000; Calvert et al., 2000; Villaseñor et al., 2003; Piromallo and Morelli, 2003; Spakman and Wortel, 2004; Faccenna et al., 2004; Garcia-Castellanos and Villaseñor, 2011; Bezada and Humphreys, 2012; Monna et al., 2013). This anomaly, follows the arcuate shape of the Gibraltar Arc (composed of the Betic and Rif mountain ranges) but lose its geometry or resolution as the transition zone (TZ) is approached, at an approximate depth of 400 km. This heterogeneity has been explained through two different geodynamic models which also account for the formation of the Alboran Sea extensional basin embedded in a compressional regime. Different types of continental delamination or convective removal have been proposed (Platt and Vissers, 1989; Seber et al., 1996; Calvert et al., 2000) and, as opposite models, subduction of oceanic lithosphere with slab-tearing or partial slab-detachment (Faccenna et al., 2004; Gutscher et al., 2002; Wortel and Spakman, 2000; Garcia-Castellanos and Villaseñor, 2011; Bezada and Humphreys, 2012). Independently from the tomography studies, SKS splitting (Buontempo et al., 2008; Díaz et al., 2010) and P-wave dispersion analyses (Bokelmann and Maufroy, 2007) are consistent with the presence of a subducted oceanic

Figure 1.1: Map of the westernmost Mediterranean region showing the location of the western mountain ranges developed during the Alpine Orogeny (the Rif, the Tell Atlas, the Betic Cordillera, the Cantabrian Mountains, the Pyrenees, and the Alps), the Atlas Mountains and the location of a nest of deep earthquakes beneath Granada. The inset shows the shallow and intermediate depth earthquakes (depth $\leq$ 200 km and mb $\geq$ 3) inside the study area taken from the NEIC catalogue (`http://earthquake.usgs.gov/earthquakes/eqarchives/epic`). The white line shows the Nubia-Eurasia plate boundary, which is more diffuse in the Alboran Sea region (red dotted line).

lithosphere (Bokelmann et al., 2011). Nevertheless, there is still room for the different interpretations. Additionally, recent tomographic images have revealed a negative P-velocity anomaly beneath the Gulf of Cadiz and south Portugal (Monna et al., 2013). This anomaly extends to the base of the model reaching the upper-mantle transition zone. The authors suggest that this negative anomaly might be related to hot mantle temperatures and to the origin of the sub-lithospheric magma source responsible for the anorogenic magmatism in the Mediterranean.

Indirect evidences on upper-mantle temperature, composition, position and vertical extension of the heterogeneities revealed in tomographic images are needed. These additional constrains would help the interpretation of the velocity anomalies and can be achieved using seismic analysis. The study of the 410-km and 660-km discontinuities (or TZ discontinuities) is probably one of the best approaches, since these discontinuities are globally observed mineral phase transitions which, as function of composition, respond with depth and thickness variations to temperature anomalies (e.g., Helffrich, 2000). The discontinuities are not resolved with seismic tomography and their study requires the detection and identification of seismic body waves which directly interact with the discontinuity through a reflection and/or wave type conversion (from P to S, or S to P). Reflection/conversion coefficients are typically smaller than 5 % and the corresponding small-amplitude signals are concealed in a multitude of other scattered waves. This makes it difficult to identify the signals on individual records.

Upper mantle discontinuities are most commonly studied using the receiver function technique (RF) (Phinney, 1964; Vinnik, 1977; Langston, 1979; Ammon, 1991) which enhances the P-to-s conversions and P-wave reflections from discontinuities below the recording stations. In **Chapter 2** we build a new processing approach which is leaned on RFs and which is based on cross-correlation and stacking techniques; part of this chapter has been published as a research article in the *Geophysical Journal International* (Bonatto et al., 2013). The instantaneous phase coherence obtained from analytic signals forms the backbone of one of the cross-correlation approaches and stacking used. We focus on P-to-s conversions whose detection and extraction are based on their coherence, slowness, travel time and polarity; such conversions are used to map the 410-km and 660-km discontinuities. In order to add consistency and robustness to the detections, our final results are based on a joint analysis of two different cross-correlation functionals and RFs. In addition, this approach permits to

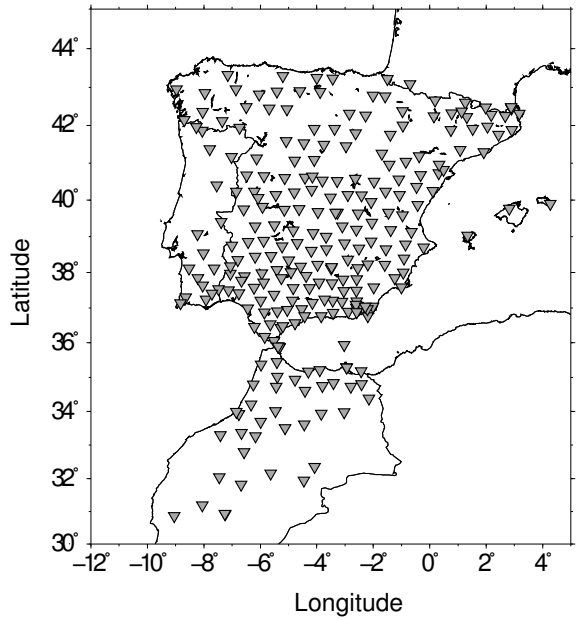

Figure 1.2: Location of seismic stations from the TopoIberia seismic network and from other collaborating institutions (see Section 1.5) used in this thesis.

assess errors and to bridge observation gaps due to detection failure of any of the approaches. Our study of the TZ discontinuities is based on the extraordinary dataset obtained from the TopoIberia seismic network (Díaz et al., 2009), which we describe in **Chapter 3**. For our analysis, we use teleseismic events recorded from 259 three-component broadband stations (Fig. 1.2). In **Chapter 4**, we present maps of the upper mantle TZ discontinuities beneath the Ibero-Maghrebian region and we discuss the results in relation with the tomographic images from Villaseñor et al. (2003). A correlation between the anorogenic magmatism and the 410 and 660 topography is also investigated. Additionally, we study the presence of low seismic-velocity zones atop the 410-km discontinuity, which are probably related to the presence of a melt layer caused by an increased water concentration in the TZ (Revenaugh and Sipkin, 1994; Schmerr and Garnero, 2007). Our analysis extends previous RF studies of the TZ discontinuities beneath the study area (van der Meijde et al., 2005; Dündar et al., 2011; Bonatto et al., 2013) and the new data volume permits to resolve new TZ

topography. It is worth mentioning that the results for the Alboran Sea region and north Morocco have been published in the *Geophysical Journal International* (Bonatto et al., 2013). The analysis for the entire Ibero-Maghrebian region is at present part of a paper in preparation. Finally, in **Chapter 5**, we determine the thickness of the 410-km and 660-km discontinuities, which provide additional information to constraint the mantle temperature and composition. In particular, the 410 thickness is a very sensitive probe of mantle conditions (Katsura and Ito, 1989; Wood, 1995; Smyth and Frost, 2002). Our results provide additional and independent constraints to aid and strengthen the interpretation of the seismic velocity anomalies, which has direct implications for the understanding of the geodynamic state of the western Mediterranean. In what follows, we introduce different key concepts which are significant for a better understanding of this thesis.

1.2 Upper mantle

The Earth's upper mantle extends from the base of the crust (or Moho discontinuity) to a depth of about 700 km (Fig. 1.3). Based upon results from seismological research, the Earth's upper-mantle is divided into different sections. These sections are separated by seismic discontinuities that correspond to abrupt changes in the seismic velocity and/or velocity gradient and/or material density (see Fig. 1.3). The upper-mantle sections are:

- The lithosphere (or LID): the outer solid part of the Earth, including the crust and uppermost mantle. It is a region of high seismic velocity and its thickness varies from 50-100 km beneath oceans to 150-250 km beneath the older continental shields. The discontinuity which defines the lower limit of this layer is known as the LAB (lithosphere-asthenosphere boundary), which corresponds to a seismic velocity decrease with increasing depth.

- The asthenosphere (or LVZ): a weak region underlying the relatively strong lithosphere. It is a region of diminished velocity or negative velocity gradient proposed by Beno Gutenberg in 1959. This layer is bounded by the LAB and by a seismic discontinuity at a depth of about 220 km -the Lehmann discontinuity (Lehmann, 1959, 1961a)- which corresponds to a velocity increase with increasing depth. The LID and the LVZ are essential to plate tectonic theory.

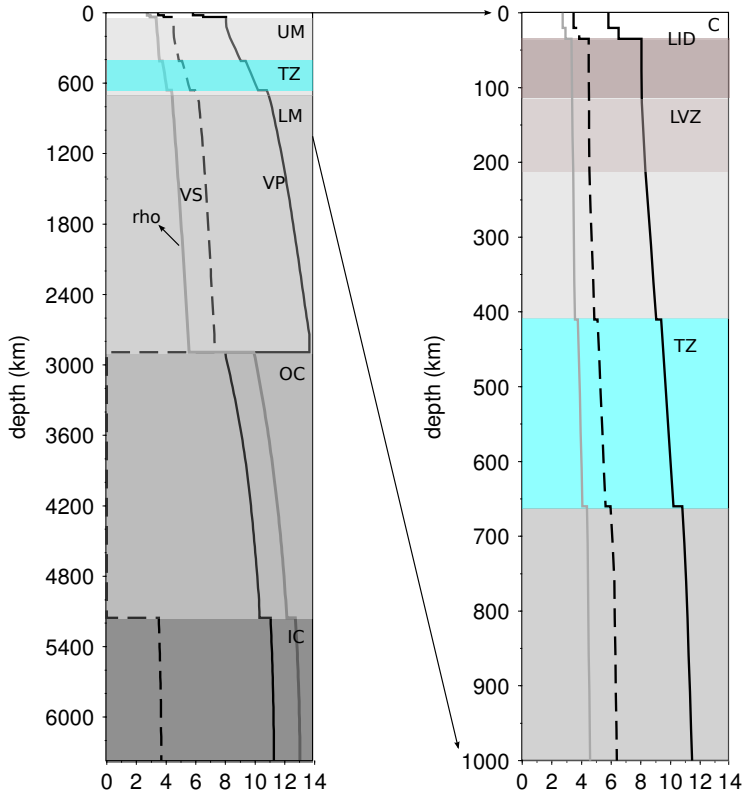

Figure 1.3: Left: Earth's gross structure from seismology. Different lines correspond to P- (black) and S-wave velocity (dashed) in km/s (and mass density (gray) in g/cm^3) as function of depth according to reference Earth model AK135 (Kennett et al., 1995), which, for the upper mantle, only accounts for the 410-km and 660-km discontinuities. C: crust; UM: upper mantle; LID: lithosphere; LVZ: low-velocity zone or asthenosphere; TZ: upper-mantle transition zone; LM: lower mantle; OC: outer core; IC: inner core. Right: P- and S-wave velocity (and mass density) as function of depth in the Earth's mantle between surface and a depth of 1000 km.

- The region between 220 km and 410 km: limited by the Lehmann discontinuity and the seismic discontinuity at a depth of 410 km. It is a region where the seismic velocity gradually increases as the 410-km discontinuity is approached.

- The transition zone: a region of high seismic wave-speed gradient. It is bounded by two seismic discontinuities at a depth of 410 km and 660 km, which correspond to increases in seismic wave speed with increasing depth. This region play an important role in the convection models of the mantle (e.g., Bercovici and Karato, 2003). Inside this region, at an approximate depth of 510 km, there is another seismic discontinuity, which corresponds to a velocity increase with depth and is thought to be a regional feature.

For further details on the upper-mantle structure see Anderson (2007) [pp. 91-108] and references therein.

The seismic discontinuities in the Earth reflect mineralogical phase transformations, changes in the chemical composition of the material, or changes in other elastic properties of waves. Although these changes are generally referred to as discontinuities, they represent regions where the physical and/or chemical properties change very rapidly over a finite depth interval.

This thesis focuses on the discontinuities of the upper-mantle TZ. Throughout this thesis, and whenever not specified we will use TZ to refer to the upper-mantle transition zone which is bounded by the 410-km and 660-km discontinuities.

1.2.1 Upper mantle composition

The most abundant minerals in the upper mantle are olivine, pyroxenes (orthopyroxene, clinopyroxene), and garnet (e.g., Frost, 2008). Their relative proportions along an oceanic geotherm are shown in Fig. 1.4, which correspond to the pyrolitic model of the mantle where the mineral olivine is the most abundant (60 % of the total volume). Inside the TZ olivine is not stable and is replaced by high pressure polymorphs with approximately the same composition. One polymorph is wadsleyite (also called β-spinel type), and the other is ringwoodite (a mineral with the γ-spinel structure) (Fig. 1.4) (Frost, 2008). These olivine phase transitions occur over narrow pressure (depth) intervals. Other phase changes in non-olivine phases, such as those of garnet or pyroxene (Fig. 1.4), are gradual and occur over broad depth intervals. Below about 700 km, all the minerals of the upper mantle begin to become unstable

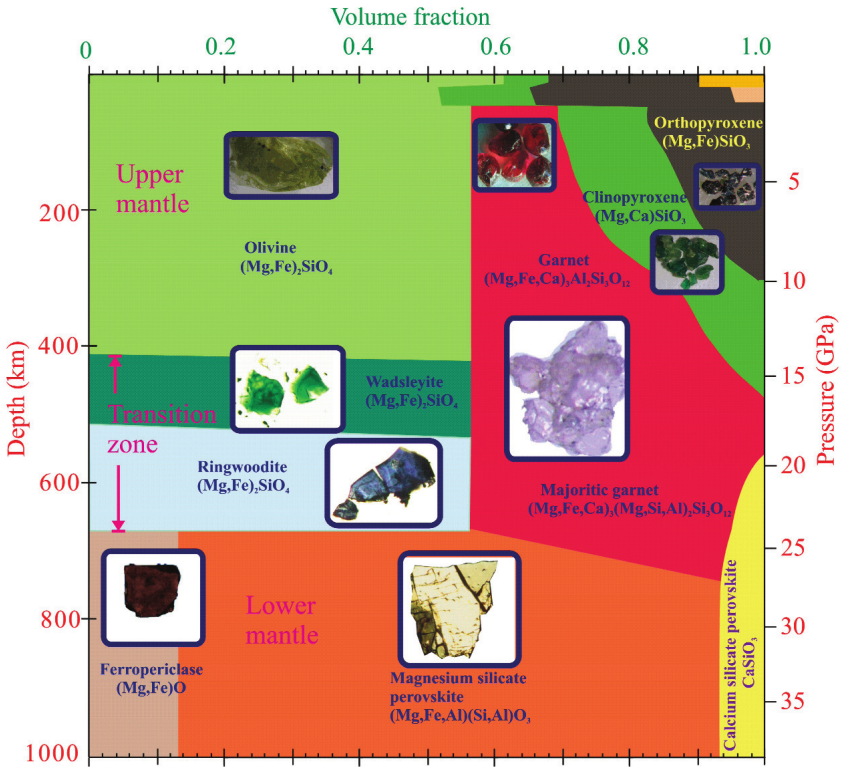

Figure 1.4: Mineral volume fractions for the top 1000 km of a pyrolitic mantle composition and mineral phase changes of the different mantle components (from Frost (2008)).

and the most abundant mineral is the silicate-perovskite that constitutes 93% of the lower mantle (Murakami et al., 2004, 2007).

The changes in mineralogy inside the TZ yield different seismic discontinuities that print distinctive signatures in seismic records and are detected using seismic wave processing tools. The study of these discontinuities, their global or regional distribution, their topography and sharpness sets boundary conditions for mantle dynamics and petrology. Therefore, the existence of dense seismic networks such as the TopoIberia seismic network is essential to produce more realistic and more detailed images of the Earth's interior.

1.2.2 Olivine-related TZ discontinuities

The seismic discontinuities in the TZ at a depth of 410 km, 510 km and 660 km are related to mineral phase changes in the olivine($(Mg, Fe)_2SiO_4$)-system (Fig. 1.4) (see reviews in Shearer, 2000; Helffrich, 2000).

The 410-km and 660-km discontinuities (hereafter referred to as 410 and 660, respectively) limit the TZ. Their names came from the depths at which they are found globally in seismology studies (e.g., Shearer, 1991, 1993; Gu and Dziewonski, 1998; Lawrence and Shearer, 2006). In an upper mantle of pyrolitic composition, the 410 is the result of the olivine-to-wadsleyite (or $\alpha \rightarrow \beta$) transition (at about 13-14 GPa in Fig. 1.4) (e.g., Ringwood, 1975), while the 660 is the dissociation of ringwoodite into perovskite+magnesiowustite ($rw \rightarrow pv + mw$ or post-spinel transition) (at about 23-24 GPa in Fig. 1.4) (e.g., Ringwood, 1975; Ito and Takahashi, 1998). The left panel of Fig. 1.5 illustrates these phase relations in the $(Mg, Fe)_2SiO_4$ (olivine) system at a constant temperature of 1600°C. The green line marks the typical $Mg - Fe$ proportion. Note that the phase transitions show a region of a certain width where product and reactant coexist (e.g., dotted region in the α-β phase). Inside this interval the mineral phase transformations progress through a zone of transitional seismic properties interpolating those above and below the phase change (Bina and Wood, 1987). Several seismological studies have shown that the 410 and the 660 are sharp, with a prevailing velocity increase occurring over a depth range of 10 km or less (e.g., Paulssen, 1988; Benz and Vidale, 1993; Vidale et al., 1995; Collier and Helffrich, 1997; Landes et al., 2006).

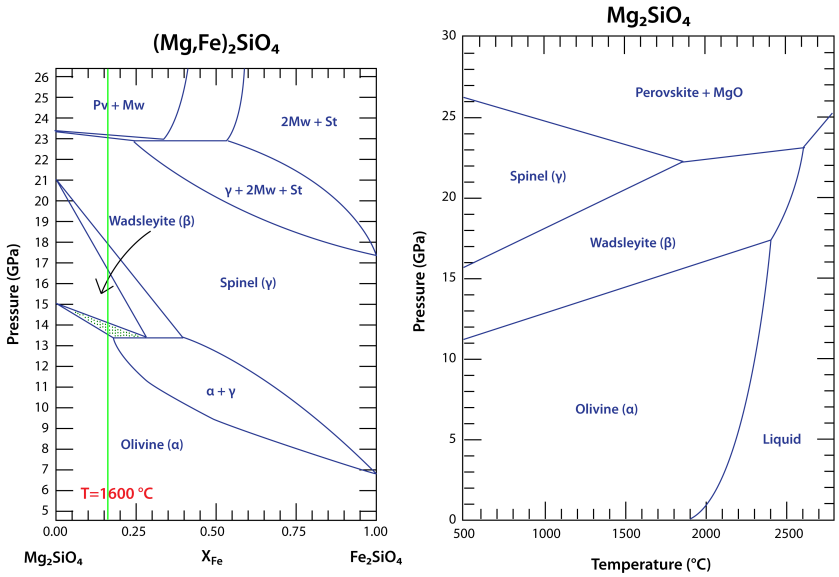

Figure 1.5: Phase relations in the $(Mg, Fe)_2SiO_4$-system (left) and the corresponding pressure-temperature relations in the pure Mg_2SiO_4-system, modified from Fei and Bertka (1999) (in `http://serc.carleton.edu/NAGTWorkshops/mineralogy/mineral_physics/phase_equilibria.html`).

At around a depth of 510 km the olivine goes through another phase transition, the wadsleyite transforms to ringwoodite ($\beta \rightarrow \gamma$-spinel transition) with a positive Clapeyron slope of 6.9 MPa/K (Helffrich, 2000; Suzuki et al., 2000).

1.2.3 Using the 410 and 660 depths to infer changes in TZ temperatures

Temperature anomalies in the mantle move the phase changes to different pressures (depth) according to the Clapeyron slopes (dP/dT) (slope of the blue boundaries in the pressure-temperature diagram of Fig 1.5) (Bina and Helffrich, 1994). The Clapeyron slope associated to the 410 and 660 are 4 $MPaK^{-1}$ and -1.3 $MPaK^{-1}$, respectively (Katsura et al., 2003, 2004; Litasov et al., 2005). Due to the opposite sign in the Clapeyron slopes of the phase change responsible for each discontinuity, the 410 and 660 depths changes are anti-correlated as a response to a thermal anomaly

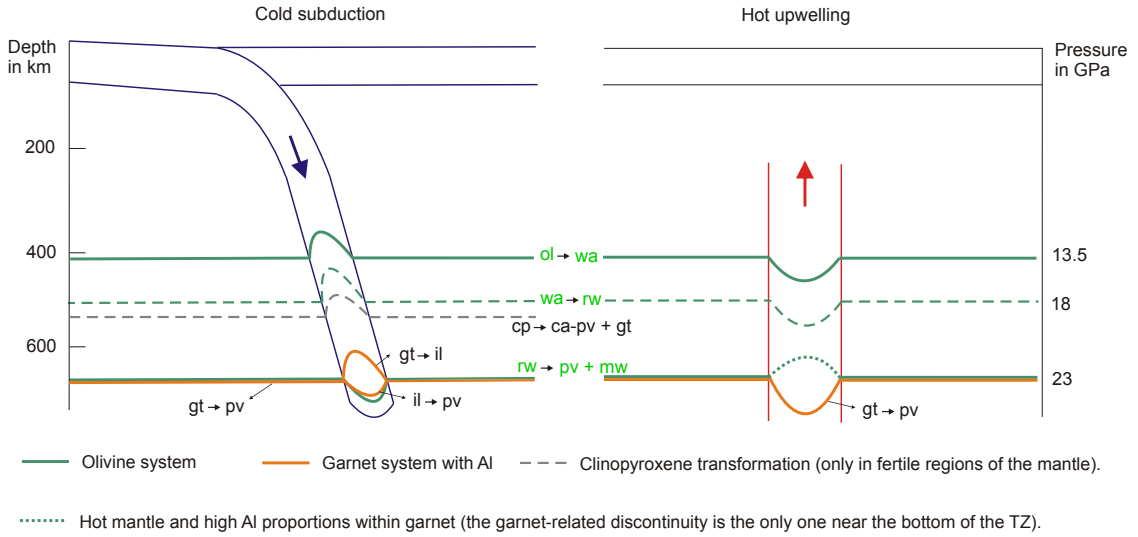

Figure 1.6: A schematic figure to show the approximate depth (pressure) of the different TZ phase transformations and their thermal response: olivine-system (green); garnet-system (orange) under the assumption of at least 4 % of Al in garnet (B.1 in Appendix B). The grey line shows the phase transition clinopyroxene to calcium-perovskite plus garnet in a fertile region of the mantle (B.4 in Appendix B).

(see the green lines in Fig. 1.6 which show the response of the phase transitions in the olivine system to a cold (left) and a hot (right) thermal anomaly). While the 410 becomes shallower in colder regions and deeper in hotter ones, the 660 behavior is opposite. As a consequence, in a mantle dominated by the olivine phase transitions, the TZ becomes thicker near subducted slabs and thinner beneath plumes or high temperature regions related to small scale mantle convection (Vidale and Benz, 1992; Helffrich, 2000; Collier et al., 2001; Lawrence and Shearer, 2006). For an overview of past studies on the 410 and 660 depths in different tectonic settings see Kind and Li (2007).

The presence of other transforming and non-transforming phases may complicate the analysis (see Appendix B) and their influence should be considered in the final interpretation.

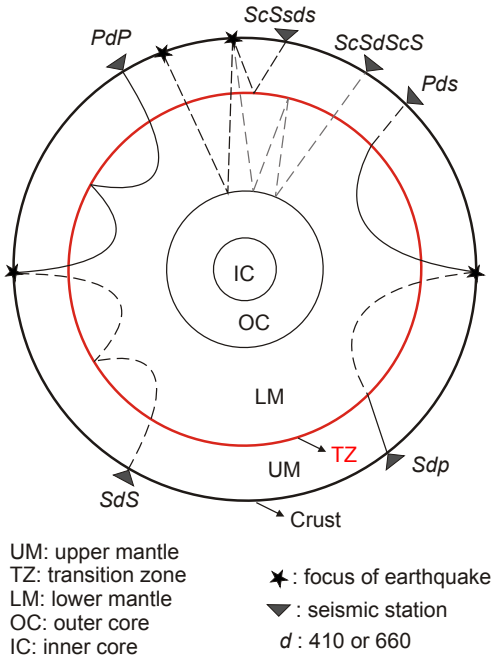

Figure 1.7: A cartoon showing example ray-paths for different phases used to study the 410 and 660 discontinuities: underside reflections (SdS, PdP); P-to-s (Pds) and S-to-p conversions; ScS reverberations including top-side reflections (e.g., $ScSsds$) and bottom-side reflections (e.g., $ScSdScS$). P waves are shown as continuous lines, S waves as discontinuous lines. The red circle indicates either the 410 or the 660 discontinuity.

1.3 Research methods

The 410 and 660 are among of the best documented discontinuities in the upper mantle. The TZ discontinuities are generally studied through the detection and identification of different body wave phases which interact with the discontinuities (Fig. 1.7 or see Shearer (1991) for other phases which are less commonly used). These seismic phases are present in the seismic records and the choice of the method for the study of the 410 and 660 discontinuities is determined by the location of the study region and by the coverage of seismic stations in the area of interest.

1.3.1 Seismic phases

Long-period precursors to SS or PP (SdS or PdP where d is the discontinuity depth) resulting from underside reflections at the upper-mantle discontinuities are mostly used to map the global depth of these reflectors (because of the wide distribution of bounce points) or to study them beneath oceanic areas (e.g., Shearer, 1993; Flanagan and Shearer, 1998, 1999; Deuss and Woodhouse, 2002; Deuss et al., 2006). Nevertheless, SS precursors are preferred to PP because they have a better ray coverage and less interference with other seismic phases (e.g., Shearer, 1991). Differential times between the precursors and SS (i.e. t_{SS}-t_{SdS} where d is the discontinuity depth) provide a measure of the two-way S travel time between the surface and the discontinuity. Structure near the sources and the receivers is relatively unimportant since the SS and SdS ray paths are nearly identical except near the bounce points.

Short period P-to-s conversions have also been used in global studies (Chevrot et al., 1999; Lawrence and Shearer, 2006; Tauzin et al., 2007). Nevertheless, owing to the limited geographic distribution of seismometers, the P-to-s and S-to-p conversions are mostly used to study the discontinuities beneath continents since the conversions occur beneath the stations (e.g., Vinnik, 1977; Paulssen, 1985; Dueker and Sheehan, 1997; Li and Yuan, 2003; Shen et al., 2008; Eagar et al., 2010). The 410 and 660 are commonly studied through detection of P-to-s conversions. Differential travel times between P-to-s conversions and P provide a measure of the one-way S travel time between the surface and the discontinuity. Using an adequate velocity model, this one-way travel time can be translated to discontinuity depth.

To a lesser extent, short period ScS reverberations have also been used to study the 410 and 660 beneath continents (e.g., Revenaugh and Jordan, 1991; Suetsugu et al., 2004). For an overview of past studies on 410 and 660 discontinuities in different tectonic settings and with different seismic phases see Kind and Li (2007).

1.3.2 Spatial resolution

One problem in using the SS precursors to study in detail the topography of the TZ discontinuities is their relatively low resolution due to the long periods of these phases. The achieved spatial resolution with the different seismic phases is controlled by the size of the first Fresnel zone, which is frequency dependent. This zone is the area where the elementary waves (following Huygens-Fresnel principle) that belong to the

same wave-front interfere with each other constructively, which in practice is defined as the area where the travel paths differ by less than a half period (Sheriff, 1996). SS precursors have a complex Fresnel zone with a minimax characteristic saddle shape and with an extension larger than 1000 km (Neele et al., 1997). Therefore, these phases are not suited to study variations in the 410 and 660 topography over small distances. On the other hand, short period P-to-s conversions are more adequate to exploit the high spatial resolution provided by dense seismic arrays such as the TopoIberia seismic network (see Section 1.5 and Chapter 3). The Pds signal is formed within the first Fresnel zone, which depends on the frequency of the signal and the depth of the discontinuity, d. The first Fresnel zone for the $P410s$ and $P660s$ phases at a depth of 410 km and 660 km, respectively, is a circular area with a radius of less than 100 km, for frequencies larger than 0.1 Hz.

1.3.3 Detection of P-to-s converted phases in the seismic records

P-to-s conversions from mantle discontinuities arrive in the P-wave coda and are difficult to observe directly on seismograms mainly because of their low amplitude. These coda phases are commonly studied through the receiver functions (RFs) technique (Phinney, 1964; Vinnik, 1977; Langston, 1979; Ammon, 1991) which enhances the P-wave conversions and reflections from discontinuities below the recording stations using teleseismic earthquakes. For a better understanding of RFs see Appendix A.

Under the assumption of lateral homogeneity and considering teleseismic earthquakes, most of the P-wave energy arrives on the vertical (Z) component and the SV-wave energy, such as P-to-s conversions, on the radial (R) component. To enhance the P-wave conversions and reflections, the RFs use the deconvolution of the Z component from the R which is equivalent to spectral division in the frequency domain. The division of small amplitudes (spectral holes), however, makes the spectral division unstable and regularization of the deconvolution is required. A common regularization approach is the water level technique (Clayton and Wiggins, 1976), (see Appendix A), which nevertheless may cause artifacts. Also the presence of high frequency noise is known to impair the deconvolution (Clayton and Wiggins, 1976) and often handled through the multiplication of a Gaussian window during spectral deconvolution or through the application of a low-pass filter.

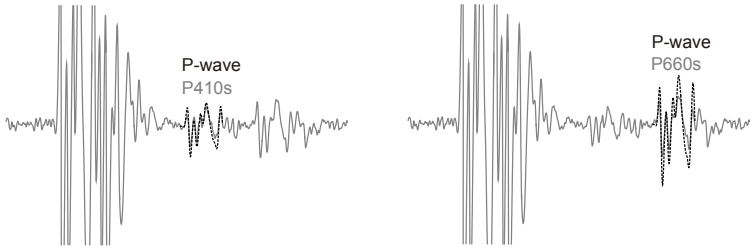

Figure 1.8: Synthetic data example to show the waveform similarity between the P phase from the vertical component (black) and the corresponding P-to-s conversions at the 410 and 660. Shown are the R component (grey) and the P phase from the Z component (black) of an event at 80° epicentral distance and a depth of 35 km. The P phase was shifted by 42.8 s and 65.8 s, respectively.

Here, we build a new processing approach to detect the $P410s$ and $P660s$ phases. This approach is leaned on RFs and is based on cross-correlation and stacking techniques; the method will be discussed in detail in Chapter 2. With individual stations, the coda phases can be detected whenever they are coherent with a template or a pilot, like the direct P waveform. Fig. 1.8 illustrates the waveform coherence between the direct P-wave (as recorded in the Z component) and the P-to-s converted waves at the 410 and 660 discontinuities (as recorded in the R component) using a synthetic data example. To make the waveform similarity more evident, both phases have been plotted in a superimposed way. At thicker discontinuities or equivalently for smaller wave length, the reflection/transmission coefficient becomes too frequency dependent to maintain a coherent waveform. However, the P-to-s conversions and P-wave reflections are expected to be coherent with the waveform of the first arrival for conversion/reflection at discontinuities which are thinner than one fourth of the wavelength (Richards, 1972; Paulssen, 1988; Bostock, 1999). Taking advantage of this property, coherence measurement tools are applied to detect P-to-s conversions by their waveform coherence, slowness, travel time and polarity. In order to add consistency and robustness to the detections, our final travel times are based on a joint analysis of two different cross-correlation functionals and RFs. Additionally, this approach permits to assess errors and to bridge observation gaps due to detection failure of any of the proposed approaches. The estimated travel times are then

used to map the discontinuities.

1.4 The western Mediterranean and the Ibero-Maghrebian region

The geodynamic evolution of the western Mediterranean during the Cenozoic is dominated by the subduction of the Tethys oceanic lithosphere beneath the Eurasian plate in a north dipping direction followed by slab retreating (or slab roll-back) and splitting in different directions (Royden, 1993; Lonergan and White, 1997; Faccenna et al., 2004; Spakman and Wortel, 2004; Rosenbaum et al., 2002). One of the fragments, the Alboran slab, retreats towards the west-southwest diverging from the Algerian slab and the Apennines slab which undergoes south and east retreat, respectively (see geodynamic reconstructions in: Faccenna et al., 2004; Spakman and Wortel, 2004; Verges and Fernandez, 2012). The subduction process initiates near the Gulf of Lyon in the Oligocene (30 My) as a consequence of the convergence of Africa with respect to Europe, which starts in the Cretaceous between 120-83 My (Rosenbaum et al., 2002). The current convergence rate is of 2-6 mm/y (Argus et al., 1989; Demets et al., 1990; Stich et al., 2006; Fadil et al., 2006; Vernant et al., 2010). In the western sector, roll-back occurs during subduction of the African paleomargin with possible continental subduction of the Iberian paleomargin (e.g. Morales et al., 1999). The convergence of Africa and Europe gives origin to the Alpine orogeny that forms the westernmost mountain ranges of the Alpide belt. From west to east, this mountain belt comprises the Rif, the Tell Atlas, the Betic Cordillera, the Cantabrian Mountains, the Pyrenees, the Alps and the Apennine Mountains (some of these ranges are depicted in Fig. 1.1 and in Fig. 1.9). The origin of the Neogene extensional Basins (see ligth-green areas in Fig. 1.9) is attributed to the back-arc extensional processes during the retreating of the subducted slabs (e.g. Faccenna et al., 2004; Spakman and Wortel, 2004). Nevertheless, the nature of the Alboran Basin is in debate because some scientists attribute its origin to a delamination process or convective removal of an overthickened continental crust (Platt and Vissers, 1989; Calvert et al., 2000).

The Ibero-Maghrebian region, our area of interest, is located in the westernmost end of the present location of the boundary between the Nubian and Eurasian plate (see inset in Fig. 1.1). In the Atlantic Ocean, the plate boundary separates oceanic lithosphere while in the Alboran Sea (western Mediterranean), the contact is not well

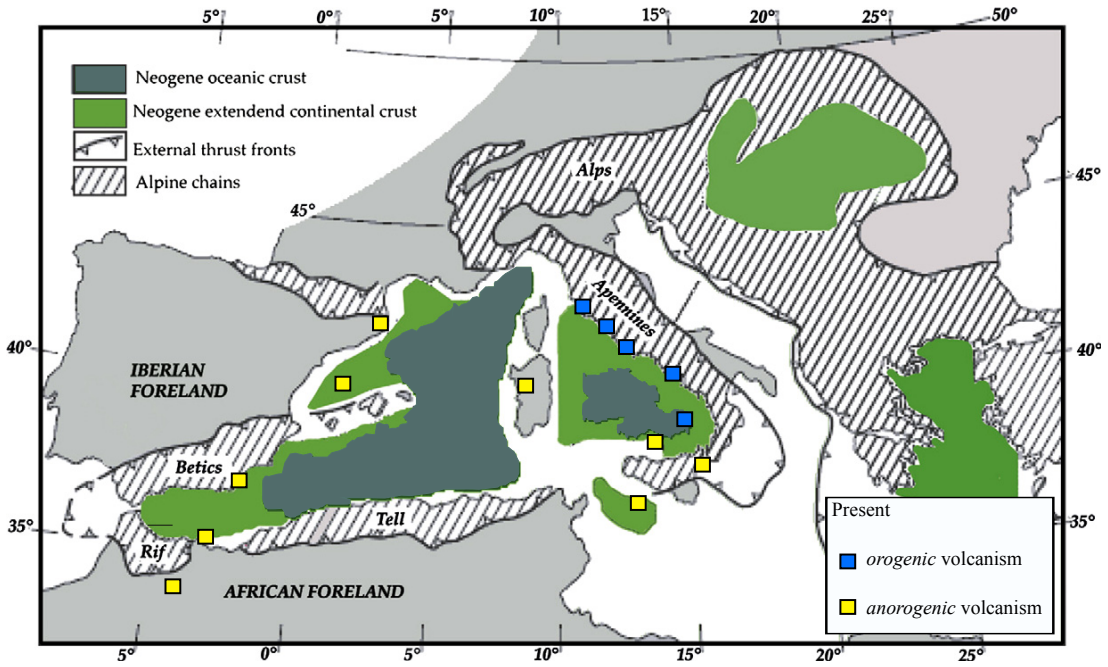

Figure 1.9: Illustrative tectonic map of the western Mediterranean (modified from Comas et al. (1999)) showing the Neogene basins (light-green areas), the location of the active *orogenic* and *anorogenic* volcanism (extracted from Faccenna et al. (2004)) and the mountain ranges of the Alpide belt.

defined (e.g., Mezcua and Martínez-Solares, 1983; Negredo et al., 2002; Vernant et al., 2010) and involves a continental collision. The seismic activity occurs from shallow to intermediate depth in a diffuse band which extends to both sides of the Strait of Gibraltar (see inset in Fig. 1.1), leading to a poorly-defined plate boundary (Mezcua and Martínez-Solares, 1983). Neotectonic modeling of the Ibero-Maghrebian region has also indicated a diffuse geometry of the plate boundary in this area (Negredo et al., 2002). Earthquake activity stops at a depth of 150 km and reappears in a small area south of Granada at a depth of about 630-660 km (red star in Fig. 1.1) (Buforn et al., 2011; Bezada and Humphreys, 2012).

1.4.1 Deep earthquakes beneath Granada

The origin of the deep isolated events beneath Granada is still an open question, mainly because the physical processes that permit the occurrence of deep earthquakes are not well understood. Shallow earthquakes ($\leq$ 60km) are explainable by the brittle failure of rocks. However, increasing pressure with depth tends to inhibit fracture and sliding, while increasing temperature promotes ductile flow. There are three primary mechanisms proposed for the generation of deep earthquakes. Here we explain the mechanisms of very deep earthquakes, depth $\geq$ 550 km; for a complete review and bibliographic citations see Green and Houston (1995); Houston (2007):

(1) Dehydration embrittlement: refers to brittle failure assisted by high fluid pore pressures that counteract the high normal stress due to large overburden pressures. The viability of this mechanism to generate very deep earthquakes depends on the availability of fluids at relevant depths. The α-to-β phase transition could carry water deeper into the mantle TZ. However, this phase transition is capable of storing increasing amounts of water. Thus, net water would not be released during the phase transition, and the availability of free fluid to promote brittle fracture is questionable.

(2) Transformational faulting in metastable olivine: shear instabilities are triggered by the heat release and sudden volume change of the olivine phase transition to denser forms (α-to-β and α-to-γ). The shear instability requires that the starting phase exists metastably in the stability field of the final phase, so that the shear zone could grow aseismically. The final phase acts as a lubricant permitting shear slip to occur. This model requires sufficiently low temperatures inside the slab to inhibit the transformation of the low-pressure phase as the slab gradually subducts to deeper higher pressure-temperature environs. However, it is unclear to which extent the phase transformation inhibition is sustained in long timescales relevant to subduction (e.g., several million years).

(3) Thermal shear instabilities: refers to shear localization produced by a positive feedback between temperature-dependent slab rheology and shear deformation that generates viscous heating. Under certain conditions, the feedback exponentially increases the localization of shear strain, leading to apparently abrupt failure on a shear zone. The rheological structure of a cold slab can be simply

explained as a weak cold core surrounded by stronger regions. The cooler slabs are weaker and rapid deformation will focus the stress onto the strong regions. In this model, shear instabilities can occur in the strong regions if strain rate is large; thus earthquakes could occur in the regions surrounding the weak core.

The three mechanisms mentioned are temperature dependent. Although the mechanism of deep earthquakes is still unclear, it seems that the thermal structure of the slab is central to deep earthquake problems. Thus, constraints on the slab temperature near the hypocenter (see Chapter 4) would help to characterize the scenarios of the different deep earthquakes.

1.4.2 Tomographic images of the upper mantle

Most tomography studies have revealed a positive P-wave velocity anomaly (or cold anomaly) beneath the Alboran Sea and southeast Spain (see B in Fig. 1.10) which follows the arcuate shape of the Gibraltar Arc but loses its geometry (or resolution) at the base of the upper-mantle TZ; this anomaly plunges into the mantle to the east (Spakman, 1990; Blanco and Spakman, 1993; Wortel and Spakman, 2000; Calvert et al., 2000; Piromallo and Morelli, 2003; Spakman and Wortel, 2004; Faccenna et al., 2004; Garcia-Castellanos and Villaseñor, 2011; Bezada et al., 2013; Monna et al., 2013). There is a long debate on the origin and shape of this anomaly (Platt and Vissers, 1989; Royden, 1993; Seber et al., 1996; Wortel and Spakman, 2000; Gutscher et al., 2002; Faccenna et al., 2004; Bokelmann et al., 2011; Verges and Fernandez, 2012) as it is an important clue to understand the regional geodynamic state of the Ibero-Maghrebian region. The lack of consensus is in part due to the fact that the exact location and shape of this anomaly differs among different author's publications. Furthermore, the continuity of the anomaly in depth as well as its steep dipping to the east has been questioned and attributed to the uneven distribution of teleseismic ray paths in the westernmost Mediterranean (Calvert et al., 2000). Recent high resolution images (Bezada et al., 2013) show that the positive anomaly has an arcuate shape, it is vertically continuous, it is located beneath the western Alboran Sea and is more than 600 km long. However, independent observations of any of these features are still needed. The tomographic images also show a broad positive anomaly in the TZ beneath the northern Apennines, the northwestern Mediterranean, southern

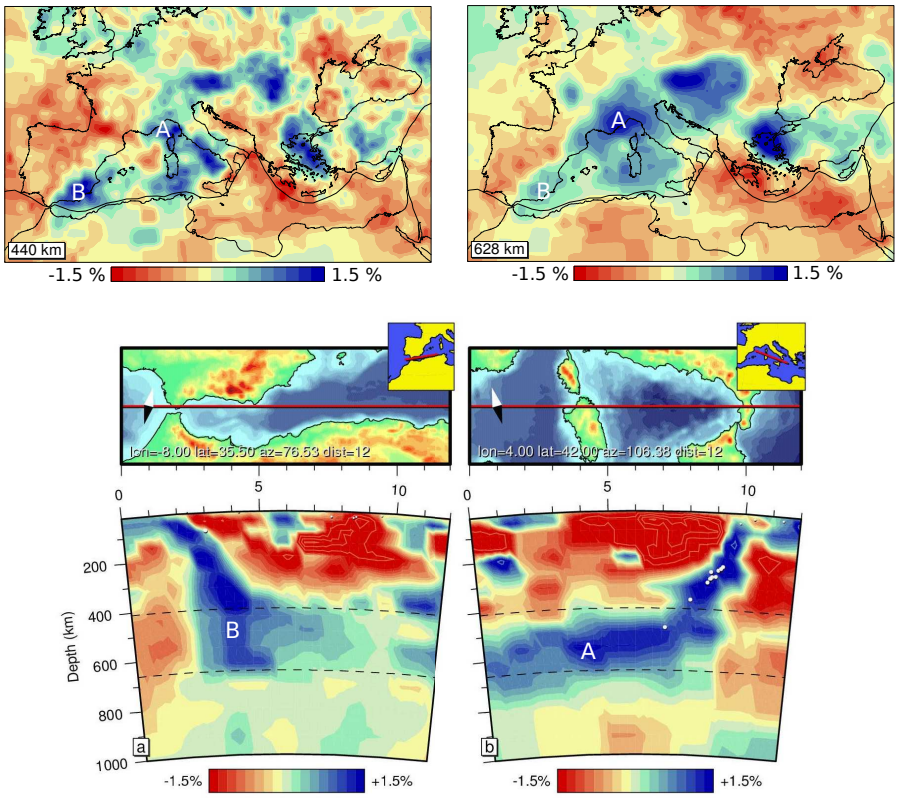

Figure 1.10: Top: Map view of P-wave tomographic images for two different depths at 440 km (left) and 628 km (right) (from Villaseñor et al. (2003)). Bottom: cross-sections along different transects shown at the top of each slice (from Spakman and Wortel (2004)).

France, and the Alps (see A in Fig. 1.10), which are interpreted as the remnant of the west Alpine-Tethys subducted slab (Spakman and Wortel, 2004). It can be seen that the western end of this anomaly reaches the Pyrenees and the north Balearic Sea (map view images in Fig. 1.10).

1.4.3 A controversial geodynamic scenario in the Alboran Sea area

Although the general geodynamic scenario of the Ibero-Maghrebian region is understood and is related to a subduction process which started in the Oligocene, this particular area comprises a complex tectonic setting still controversial. The origin of the controversy lies in the geodynamic model which best explains the existence of an extensional basin (Alboran Sea) developed in the early Miocene (23-5.3 My) which is embedded in a compressional regime and which is coeval with the uplift and shortening of the Betic and Rif mountains (e.g. Platt and Vissers, 1989; Royden, 1993; Bokelmann et al., 2011). In this context, the explanations of the heterogeneity in the Alboran Sea involve (1) different types of continental delamination or convective removal (Platt and Vissers, 1989; Seber et al., 1996; Calvert et al., 2000) or (2) retreating subduction of oceanic lithosphere with slab-tearing or partial slab-detachment (Faccenna et al., 2004; Gutscher et al., 2002; Wortel and Spakman, 2000; Garcia-Castellanos and Villaseñor, 2011; Bezada and Humphreys, 2012).

In model (1) an over-thickened continental lithosphere is detached by convective removal or delamination causing extension of the Alboran Basin and uplift around the margin. Convective removal was firstly proposed by Platt and Vissers (1989) and delamination by Seber et al. (1996). These models are also known as 'continental models' and are consistent with continental collision or subduction; for a schematic explanation see Fig. 1.11 (b). Model (2) was originally proposed by Royden (1993) arguing that the subduction of oceanic lithosphere followed by slab rollback causes the extension within the Alboran Basin. These models, also known as 'oceanic models', have gained more popularity; for a schematic explanation see Fig. 1.11 (a). Several authors reconcile both groups of models (e.g. Duggen et al., 2003; Garcia-Castellanos and Villaseñor, 2011; Bezada and Humphreys, 2012). For example, based upon results from tomography, Bezada and Humphreys (2012) proposed that the delamination event occurred as a result of subduction of the Alboran lithospheric mantle along with the larger slab that they find presently under the westernmost Mediterranean. Independently from the tomography studies, SKS splitting (Buontempo et al., 2008; Díaz et al., 2010) and P-wave dispersion analyses (Bokelmann and Maufroy, 2007) are consistent with the presence of a subducted oceanic lithosphere. Nevertheless,

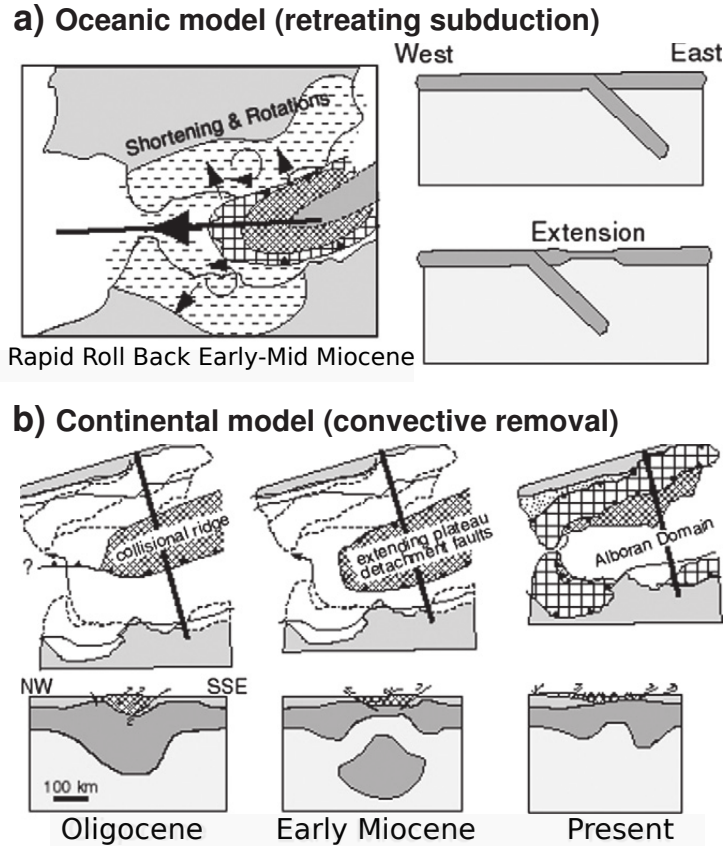

Figure 1.11: Two types of geodynamic models proposed for the Alboran Sea (from Calvert et al. (2000) and modified by Bokelmann et al. (2011)), a) the retreating subduction model of Lonergan and White (1997); Gutscher et al. (2002), and b) the convective removal model of Platt and Vissers (1989).

there is still room for different interpretations.

1.4.4 Anorogenic magmatism

The complexity of the region increases if the mafic Neogene subduction-unrelated (or *anorogenic*) volcanism is considered (Fig. 1.9). This volcanism extends from the eastern Atlantic Ocean to central Europe and the western Mediterranean and it is still active in some regions (e.g. Lustrino and Wilson, 2007; Lustrino et al., 2011; Carminati et al., 2012). Several petrological and geodynamical models have been proposed in the literature to explain the deep-origin magmas (sub-lithospheric), which are summarized in fig. 18 in Lustrino and Wilson (2007). The models require either (i) active asthenospheric (or deeper) mantle convection (i.e., mantle plumes) or (ii) lithospheric extension (or delamination and detachment) to induce passive, adiabatic, decompression melting of both asthenospheric and lithospheric upper mantle. The main difference between both models is that model (i) needs a hot buoyant, deep mantle source. The prevalence of plume models in recent decades has been sustained by many researchers largely on the basis of geochemical arguments (e.g., Hoernle et al., 1995; Oyarzun et al., 1997; Macera et al., 2003; Duggen et al., 2009). Recently, Duggen et al. (2009) reconcile both groups of models (see Fig. 1.12). In Duggen's model, the stem of the plume is in the Canary Islands and the mantle plume material travels laterally along a subcontinental lithospheric corridor (i.e., at depths that are usually occupied by continental lithospheric mantle) more than 1500 km to the western Mediterranean, marking its route over the last 15 My through a trail of intraplate volcanism. In this model, the anorogenic magmatism occurs in areas of thinned lithosphere (due to delamination or other extensional processes). When the extent of thinning lithosphere of a particular part of the corridor allowed sufficient upwelling, decompression melting occurs as in model (ii). Nevertheless, the existence of a physically continuous mantle source to explain the anorogenic magmatism is still questionable because it is mainly sustained on the compositional similarity (incompatible trace elements and Sr-Nd-Pb isotopic composition) between the igneous rocks of distant volcanoes (Lustrino, 2011). Recent tomography studies have revealed for the first time a clear low P-velocity anomaly beneath the Gulf of Cadiz that reaches the upper-mantle transition zone (TZ) in the Strait of Gibraltar (Monna et al., 2013).

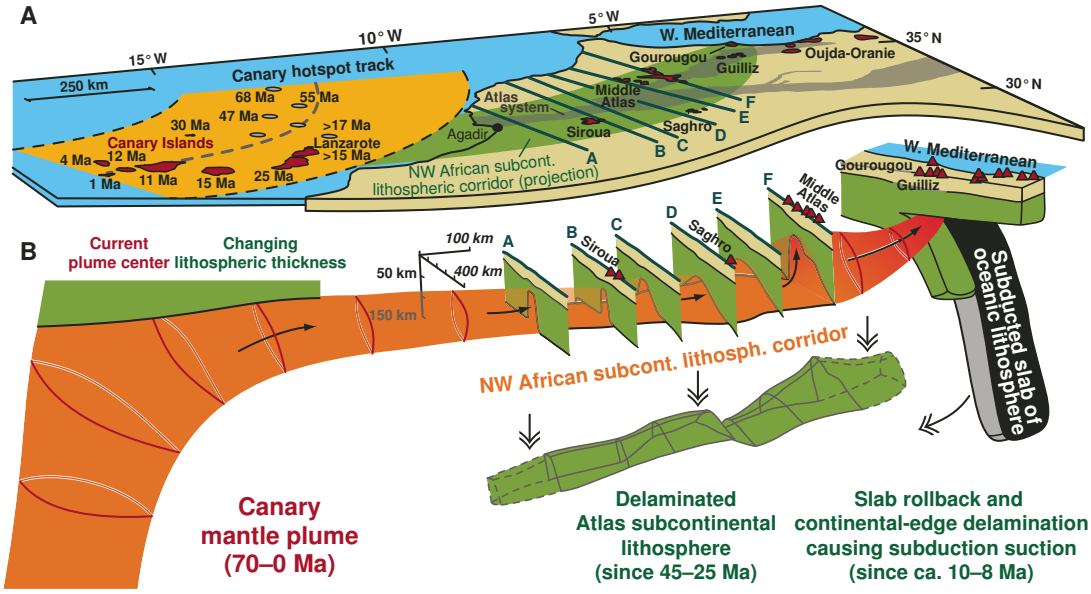

Figure 1.12: Map of the northwest African plate (A) and flow of Canary mantle plume material under northwest Africa through a subcontinental lithospheric corridor in a three-dimensional model (B) (from Duggen et al. (2009)). For a complete explanation of this figure see the caption of fig. 1 in Duggen et al. (2009).

This anomaly is interpreted as hot mantle material which is probably related to the alkaline magmatism of western Portugal.

1.4.5 Seismic discontinuity studies

The compositional discontinuity which separates the crust from the mantle (Moho) has been mapped in detail beneath Iberia and its surrounding waters through a compilation of seismic reflection data (Díaz et al., 2010). These data show the deepest Moho beneath the Pyrenees (50 km) and the shallowest Moho beneath the Alboran Sea (15-18 km), the Valencia Trough (13-15 km) and the Atlantic domain (10 km). These results are consistent with a crustal thinning beneath the Alboran Sea, the Valencia Trough and the Atlantic domain. Beneath Morocco the Moho depth has been investigated through P-wave RFs analysis (Mancilla et al., 2012). The Moho depths are consistent with a thickened crust (of about 35-44 km) beneath northwestern Morocco, and with a significantly thinned crust (of about 22-30 km) beneath northeastern Morocco. These results seem to support that the high topography in the Middle Atlas domain is not isostatically compensated at the crustal level.

The boundary between the high-viscosity lithosphere and the low-viscosity asthenosphere (or LAB) defines a low-velocity zone below the Moho. This discontinuity has been investigated in the Gibraltar Arc area using P-wave and S-wave RFs (Dündar et al., 2011). The results indicate a 90-100 km thick lithosphere from the northwest part of Africa to southern Portugal across the Atlantic, west of Gibraltar as well as in the Betics, while it is thinner beneath the Alboran Sea (of about 60 km). The authors attribute their results to a delamination process.

The TZ discontinuities in the Ibero-Maghrebian region have been studied through detection of P-to-s converted waves (Chevrot et al., 1999; Tauzin et al., 2007; van der Meijde et al., 2005; Dündar et al., 2011; Bonatto et al., 2013). Chevrot et al. (1999) and Tauzin et al. (2007) studied the global distribution of TZ thickness (TZT), including in their analysis a small number of Spanish stations. Van der Meijde et al. (2005) estimated the TZT beneath 22 stations located in the entire Mediterranean region, with 4 of them in Iberia and 2 in Africa (1 station in Melilla and the other in Morocco). Their results indicate a thicker TZ beneath the western coast of Spain and beneath the station in Melilla, with a maximum thickness of about 280 km. At the stations in central Spain and Morocco, their results show an averaged TZT of

about 257 km. With the installation of new permanent stations and the deployment of large seismic arrays, such as the IberArray, more data are available and it is now possible to study the TZ discontinuities as well as the TZT in a detailed way. Dündar et al. (2011) used 38 stations to evaluate whether the TZ presents thickness variations beneath the Alboran Sea and its surroundings. They found no hint of local changes in the TZT. Recently, using the data from the first deployment of IberArray (43 stations), we published the first detailed topography maps for the 410 and 660 discontinuities in the Alboran Sea area (Bonatto et al., 2013). The results are in good agreement with van der Meijde et al. (2005); the Alboran Sea area is discussed in Sections 4.4.2.3, 4.4.2.4 and 4.4.2.6 of Chapter 4.

1.5 TopoIberia data set

In this thesis we use the data set belonging to the TopoIberia project (`http://www.igme.es/internet/TopoIberia/default.html`) (Díaz et al., 2009). This multidisciplinary project involves more than 100 researchers from 10 different Spanish institutions:

- Instituto de Ciencias de la Tierra 'Jaume Almera'
- Instituto Geológico y Minero de España
- Real Instituto y Observatorio de la Armada
- Universidad Autónoma de Barcelona
- Universidad de Barcelona
- Universidad de Cádiz
- Universidad Complutense de Madrid
- Universidad de Granada
- Universidad de Jaén
- Universidad de Oviedo

One of TopoIberia major aims consists of the deployment of a high resolution multi-component seismic array called IberArray. This has been the first large-scale dense station deployment in Europe. The multidisciplinary dense system of station deployment (broadband seismic stations, GPS receivers and MT sensors) of TopoIberia has been pioneered in the US by EarthScope. The seismological component IberArray of the TopoIberia project permitted to gather continuous three-component broadband data during more than 6 years. This technological observatory platform provides us with a huge seismological database with more than 250 broadband seismic stations deployed along the Iberian Peninsula and north of Morocco. However, not all the stations were active at the same time. The installation process was performed in three phases moving the stations from south to the north and lasted 6 years, starting in January 2007. The stations are still recording in north Spain. Additionally, other institutions collaborate with TopoIberia by sharing their own data bases. In Spain these are the Instituto Geográfico Nacional (IGN), the Instituto Geologic de Catalunya (IGC), the Real Instituto y Observatorio de la Armada (ROA), the Universidad Complutense de Madrid (UCM) and the Instituto Andaluz de Geofísica (IAG). Furthermore, many different foreign research groups collaborate or share data through their projects such as WILAS, PYROPE, PICASSO (USA, Münster, Bristol), and the Institut Scientifique, Universitè Mohammed V Rabat (Morocco).

Certainly, this pretentious project significantly increases the high-quality information available for the study of geological and geophysical processes in the Iberian Peninsula and its surroundings. Besides, it puts Spain into the leading edge of international research on basic research into orogenic processes as well as the preparation, prevention, and mitigation of geological risk in tectonically active and highly populated areas.

2

Methodology: detection of P-coda phases

2.1 Introduction

The TZ discontinuities are generally studied through the detection and identification of different body wave phases present in the seismic records (Shearer, 1991, 2000). The P-to-s converted waves at the 410 and 660 arrive in the P-wave coda together with multiply reflected and scattered waves. Coda phases are characterized by low amplitudes and consequently are difficult to identify within the multitude of different other phases in individual records. However, the P-to-s conversions and P-wave reflections are expected to be coherent with the waveform of the first arrival for conversion (or reflection) at discontinuities which are thinner than one fourth of the wavelength (Richards, 1972; Paulssen, 1988; Bostock, 1999). At thicker discontinuities or equivalently for smaller wavelength, the reflection/transmission coefficient becomes too frequency dependent to maintain a coherent waveform. Therefore, with individual stations, these coda signals can be detected whenever they are coherent with the direct P waveform. Taking advantage of this property, we have applied coherence measurement tools to detect coda signals by their waveform similarity as function of lag time. We apply different cross-correlation techniques between components of teleseisms recorded at individual stations. Finally, the signals are identified by the measured travel time, slowness and polarity. In order to add consistency and robustness to the detections, our final approach is based on a joint analysis of two different cross-correlation functionals and RF. Furthermore, this approach permits to assess errors and to bridge observation gaps due to detection failure of any of the approaches.

2.2 Method

2.2.1 Theoretical background

In order to determine the waveform similarity between the coda phases and the P phase, we apply two cross-correlation techniques which are based on different strategies: the classical cross-correlation geometrically normalized (CCGN) and the phase cross-correlation (PCC) presented by Schimmel (1999). To enhance coherent

signals and to suppress incoherent noise, we use the phase-weighted stack (PWS) (Schimmel and Paulssen, 1997).

2.2.1.1 Cross-correlation tools

In analogy to the classical cross-correlation, the PCC measures the waveform similarity between two signals as function of lag time. The PCC is based on the instantaneous phase similarity of the corresponding analytic traces. Given a seismic trace $s_1(t)$, the PCC detects the signals included in $s_1(t)$ that are coherent with a reference or pilot wavelet, $s_2(t)$. For this purpose, wavelet $s_2(t)$ is shifted in time and compared with the corresponding portion of the seismic trace $s_1(t)$. The PCC expression is given by:

$$PCC_\nu(t) = \frac{1}{2T} \sum_{\tau=\tau_0}^{\tau_0+T} \{|e^{i\phi_1(t+\tau)} + e^{i\phi_2(\tau)}|^\nu - |e^{i\phi_1(t+\tau)} - e^{i\phi_2(\tau)}|^\nu\}, \tag{2.1}$$

where $e^{i\phi_1(t)}$ and $e^{i\phi_2(t)}$ are the amplitude-normalized analytic signals, while $\phi_1(t)$ and $\phi_2(t)$ are the instantaneous phases of the seismic trace $s_1(t)$ and the pilot $s_2(t)$, respectively. T is the pilot length in samples, t is the lag time and τ_0 is the start time of the correlation window. The normalization term $1/(2T)$ ensures that $|PCC_\nu(t)| \leq 1$, with $PCC_\nu = 1$ in case of perfect correlation and $PCC_\nu = -1$ for anti-correlation. The sharpness of the transition between similarity and dissimilarity is controlled by the power ν. We use PCC with $\nu = 1$ throughout this thesis.

In addition to the technique described above, we employ the CCGN, which is the classical cross-correlation normalized by the geometric energy of the traces. This measure varies between -1 and +1, where +1 corresponds to perfect sign coherence, and -1 corresponds to perfect coherence of signals of different polarity. The CCGN expression is given by:

$$CCGN(t) = \frac{\sum_{\tau=\tau_0}^{\tau_0+T} s_1(t+\tau)s_2(\tau)}{\sqrt{\sum_{\tau=\tau_0}^{\tau_0+T} s_1(t+\tau)^2 \sum_{\tau=\tau_0}^{\tau_0+T} s_2(\tau)^2}}. \tag{2.2}$$

CCGN and PCC are independent approaches, which are based on different strategies. PCC is amplitude unbiased and is more sensitive to waveform coherence than

CCGN and, therefore, well suited for the detection of coherent weak amplitude signals. CCGN is based on the sum of signal amplitude products and is therefore less sensitive to waveform coherence. The decreased sensitivity may favor signal detection when there is less waveform similarity due to waveform distortion.

2.2.1.2 Phase-weighted stack

The PWS suppresses signals that do not stack coherently. This technique uses the phase stack (PS) as a time-dependent weight of the linear stack (LS). PS measures the phase coherence based on the similarity of the instantaneous phases and is obtained by summing up the envelope normalized analytic signals. The PWS expression is given by:

$$PWS(t) = LS(t)PS(t) = \frac{1}{N}\sum_{j=1}^{N} s_j(t) \left| \frac{1}{N}\sum_{k=1}^{N} e^{i\phi_k(t)} \right|^{\nu}, \tag{2.3}$$

where $s_j(t)$ is the j-th seismic trace and $\phi_k(t)$ is the instantaneous phase of the corresponding analytic signal. Each sample in the LS is weighed by the coherence of the instantaneous phases obtained from all individual traces $s_j(t)$. Thus, small amplitude signals which are coherent are enhanced through the attenuation of incoherent noise. The PS acts as a phase similarity filter. The parameter ν controls the sharpness between phase similarity and dissimilarity. The LS is retrieved with $\nu = 0$. In what follows, we will use PWS with $\nu = 2$ for synthetic and real data.

2.2.2 Detection of P-coda phases using cross-correlation

In order to detect the weak amplitude converted and reflected phases at the upper mantle discontinuities, we combine cross-correlation (CCGN, PCC) and stacking (PWS) techniques. Under the assumption of lateral homogeneity and considering teleseismic earthquakes, most of the P-wave energy arrives on the vertical (Z) component and the SV-wave energy, such as P-to-s conversions, on the radial (R) component. Therefore, we will only consider the R and Z components of teleseismic recordings from individual stations. First, we extract a pilot wavelet (P_Z) from the Z component, which contains the P phase and part of its coda with the later arriving depth phases. Then, we perform PCC and CCGN between the pilot P_Z and the R and Z components. For each cross-correlation method, we obtain an R and Z correlogram (hereafter referred to as PCCR or CCGNR and PCCZ or CCGNZ). The maximum

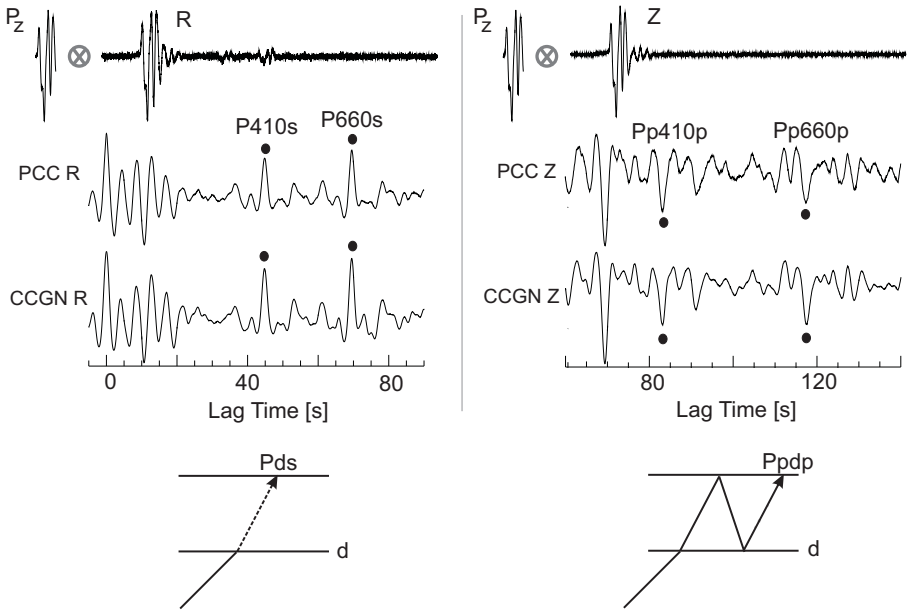

Figure 2.1: PCC and CCGN are performed between the pilot P_Z and the R and Z components. For each cross-correlation method an R and Z correlogram is obtained (PCCR or CCGNR and PCCZ or CCGNZ). PCC and CCGN provide relative travel times with respect to the P phase through their correlation maxima. At 0 s the correlograms (e.g. PCCR and CCGNR) show the P phase maximum and for any positive lag time the correlograms show the converted ($P410s$ and $P660s$) and the multiply reflected ($Pp410p$ and $Pp660p$) waves maxima/minima.

amplitudes are obtained for lag times where P_Z and a particular coda segment on the R or Z component show waveform similarity. Fig. 2.1 shows an example of signal detection using the correlation (PCC and CCGN) of a pilot P_Z with the R and Z components. The example uses a synthetical seismogram for an event at 55° distance (the synthetic data generation is explained in 2.3.1). P_Z, R and Z are shown at the top and the corresponding correlations at the bottom of Fig. 2.1. The correlation maxima of PCCR and CCGNR at about 45 s and 70 s are due to the waveform similarity of the P_Z with the $P410s$ and $P660s$ conversions. For these phases, the coherence value is larger than for other coda signals. The maximum at zero lag is due to the recorded P phase on R. In analogy to PCCR and CCGNR, correlation minima

on PCCZ and CCGNZ show the topside P-wave reflections $Pp410p$ and $Pp660p$ from the 410 and 660 upper-mantle discontinuities. The negative correlation is due to the polarity change of the reflections with respect to the pilot P_Z. The figure shows that PCC and CCGN provide relative travel times with respect to the P phase through their correlation maxima and minima.

Depth phases, such as pP, sP and their near source multiples (pmP, smP) are included into P_Z since they are similarly affected by receiver site discontinuities. The inclusion of the depth phases aids the detection of receiver structure since their respective lag time for the depth conversions and reflections is the same as for the direct P-wave. This is in analogy to the teleseismic source function in RF studies. Phases related with the source depth (such as pP, pmP, etc) may also correlate with the P phase. However, the use of a pilot with depth phases decreases the correlation of the depth phases with respect to a pilot which consists only of the direct P-wave. The final stacking over different events eliminates the source signature, enhances the signals which arrive consistently, such as near receiver conversions and reflections, and attenuates spurious arrivals. To illustrate the source equalization, the correlograms of four different events (same depth and different source function) have been stacked using LS and PWS. The correlograms using PCC and CCGN and their respective stacks are shown in Fig. 2.2. The first four lines in each panel show PCC (left) and CCGN (right) correlograms for the different events. The last two lines show the results when using LS and PWS to stack the correlograms. Notice that both stacking techniques attenuate phase side lobes due to the different source functions, although the PWS has a better signal-to-noise ratio (SNR) than the LS. This example uses events from the same depth, which means that near source site reverberations stack constructively due to the source equalization. However, these signals are still more attenuated in the real data stacks due to the different source depths and source site heterogeneities for each event.

Fig. 2.3 shows an example where the approach has been applied using teleseisms from epicentral distances of 65° to 95° registered at the Spanish station CART (Fig. 2.3 a). Blue crosses show the piercing points as obtained from a P-to-s conversion at a depth of 510 km to illustrate the sampled TZ by the $P410s$ and $P660s$ phases. Move-out corrected radial correlograms are shown in Fig. 2.3 (b). We obtained these correlograms using a P_Z of 100 s length, a fixed relative slowness parameter of - 0.1 $s/\circ$, and a reference distance of 80°. Working with relative times allows us to perform

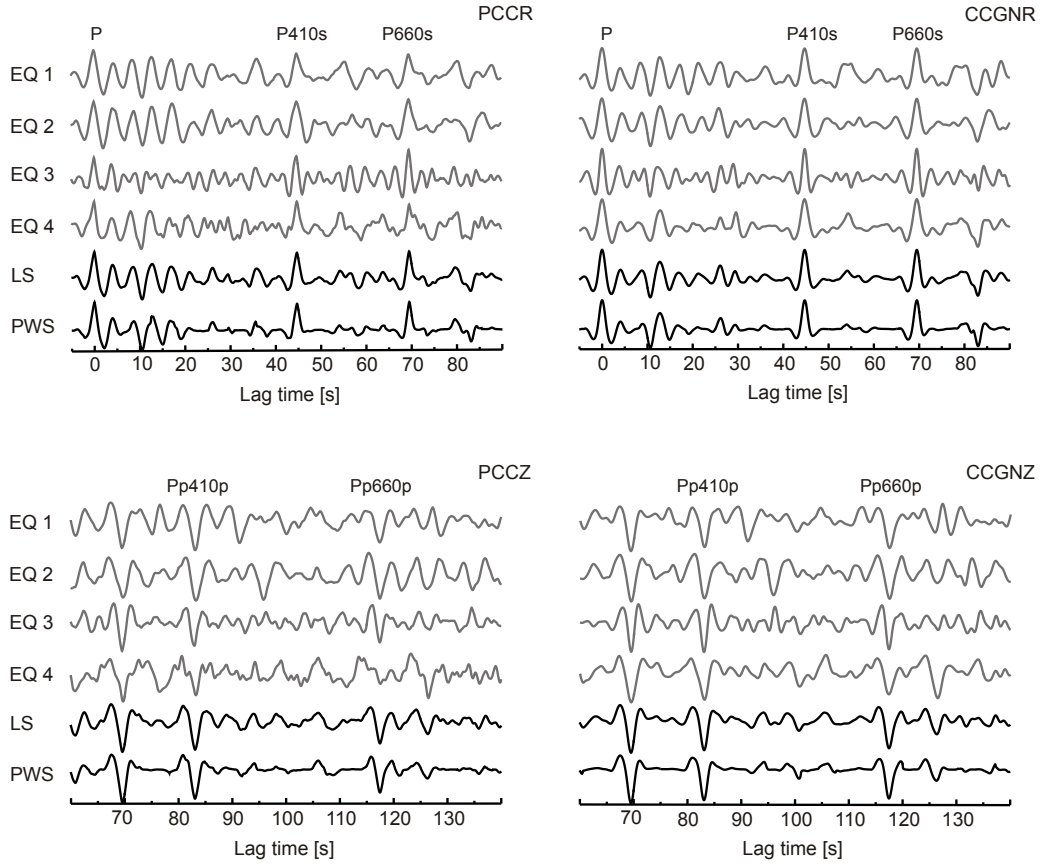

Figure 2.2: Synthetic examples of the LS and PWS are depicted in black at the bottom of each figure. P, $P410s$, $P660s$, $Pp410p$ and $Pp660p$ are indicated above their respective arrival time. Top: PCC and CCGN between the pilot P_Z and the R component are depicted in grey for each synthetical event. Bottom: PCC and CCGN between the pilot P_Z and the Z component are depicted in grey for each event.

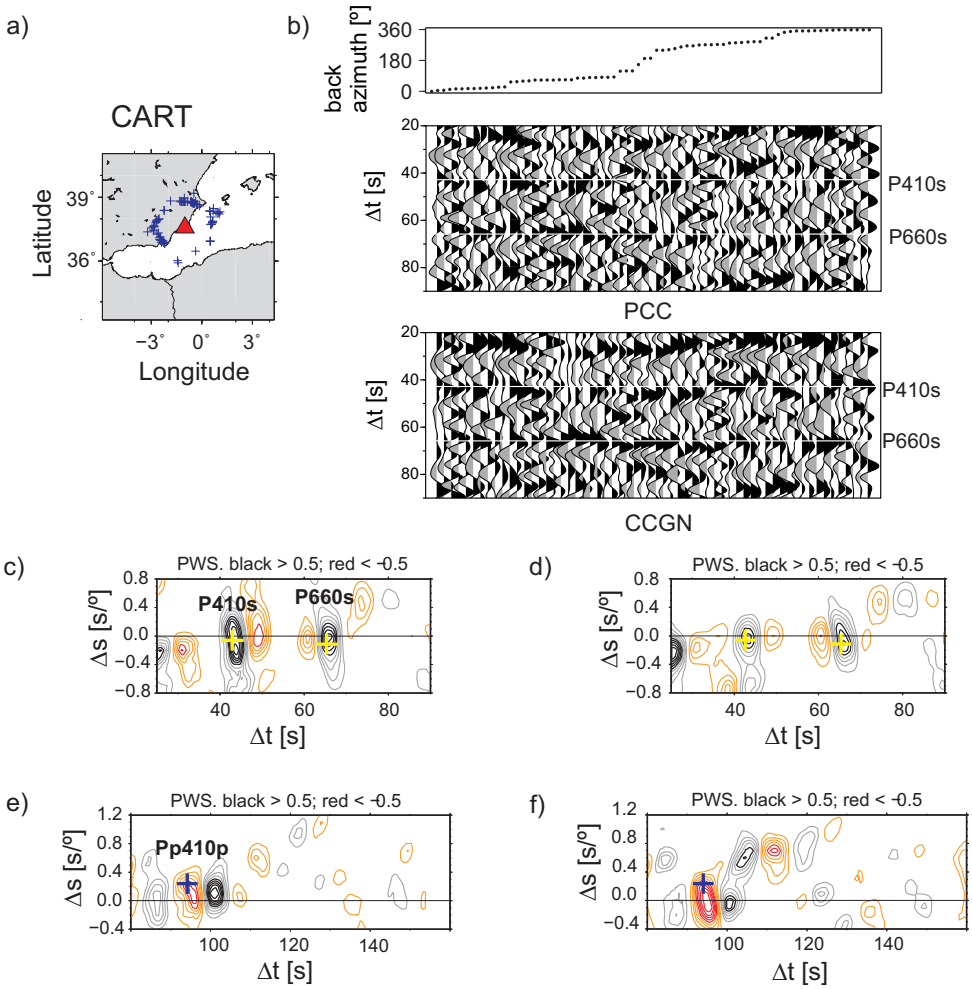

Figure 2.3: Real data example for the Spanish station CART. a) Station location and P510s piercing points (epicentral distances between 65° and 95°); we included the 510 in AK135 by introducing an imperceptible increase in the density at a depth of 510 km. b) Move-out corrected radial correlograms sorted by their back azimuths. White lines indicate P410s and P660s theoretical relative travel times. Note that P410s and P660s are consistently seen in contiguous tracks for certain back azimuths. c) PWS of PCCR correlograms with piercing points shown in (a). Yellow crosses mark the expected P410s and P660s signals using model AK135. Normalized amplitudes larger than 0.5 and smaller than -0.5 are contoured in black and red, respectively. Note the clear detection of P410s and P660s phases. d) Same as (c) but for CCGNR. e) PWS of PCCZ correlograms with epicentral distances between 70° and 120°. The blue cross marks the expected Pp410p signal using AK135. Note the clear detection of the Pp410p phase. f) Same as (e) but for CCGNZ.

linear move-out corrections. $P410s$ and $P660s$ phases are consistently seen in the CCGNR time-back azimuth section, while the PCCR correlograms show intermittently the same phases with a lower SNR. We attribute this difference to the loss of waveform coherence due to noise contamination. The unambiguous detection of $P410s$ and $P660s$ phases is obtained in the relative time-slowness domain, where the reference is the P phase and the stack is performed using a range of slowness values. This approach is also known as slant-stack and permits identification of phases in time and slowness. The signals are detected with respect to the P phase, which means that the obtained travel time and slowness values are relative values with respect to the values of the P phase. The PWS of PCCR and CCGNR correlograms from Fig. 2.3 (b) are displayed in Fig. 2.3 (c) and (d). These figures show a clear detection of $P410s$ and $P660s$ phases close to the reference values of relative time and slowness and with positive coherence value (black contours). For a reference distance of 80°, as the one used in the stacking of Fig. 2.3 (c), the $P410s$ arrives at relative time of 42.8 s and the $P660s$ at 65.8 s, both with positive coherence value and negative relative slowness. Fig. 2.3 (e) and (f) show the slant-stacks of PCCZ and CCGNZ for events registered at station CART with epicentral distances between 70° and 120°. These figures show a clear detection of $Pp410p$ at expected relative time and slowness and with negative amplitude (red contours). However, there is no evidence for a $Pp660p$ detection. Detection of topside reflections from the 410 and 660 is a more difficult task due to the great variability of these phases caused by the two extra trajectories through the upper mantle and crust. $Ppdp$ phases (where d is the discontinuity depth) are therefore more sensitive to lateral heterogeneities than the P phase, which can affect the waveform similarity and the travel times.

The **summary of the method** is as follows:

- Extract a pilot wavelet P_Z from the Z component of a teleseism which contains the P phase and part of its coda.
- Perform the cross-correlation (PCC, CCGN) between P_Z and R and Z components.
- Apply the PWS through a slant-stacking approach to detect the coda phases by their relative travel time, polarity and slowness.

Relation with Receiver Functions method

Discontinuities beneath seismic stations are commonly studied through the detection of P-to-s conversions in receiver functions (RFs). These are based on deconvolution of the Z component from the R, which is equivalent to spectral division in the frequency domain. This process removes the source wavelet and complexities, while it enhances P-to-s conversions from the receiver site discontinuities. The division of small amplitudes (spectral holes), however, makes the spectral division unstable and regularization of the deconvolution is required. A common regularization approach is the water-level technique (Clayton and Wiggins, 1976) (see Appendix A) which nevertheless may cause artifacts. Also, the presence of high frequency noise is known to impair the deconvolution (Clayton and Wiggins, 1976) and often handled through the multiplication of a Gaussian window during spectral deconvolution or through the application of a low-pass filter.

Our processing approach (presented above) is based on cross-correlation, which is equivalent to spectral multiplication in the frequency domain, and therefore, there is no need of regularization. However, as we suppress the amplitude information, we only retrieve the kinematic response of the Earth while RF retrieve the dynamic response. The RF can be expressed in terms of cross-correlation (Clayton and Wiggins, 1976; Ammon, 1991; Galetti and Curtis, 2012), its analytic expression in the spectral domain is:

$$RF(w) = \frac{Z^*(w)\ R(w)}{Z^*(w)\ Z(w)}, \tag{2.4}$$

where Z^* is the complex conjugate of Z. The numerator of equation 2.4 is the cross-correlation between Z and R in the spectral domain, while the denominator is a positive real number which functions as a frequency dependent normalization factor. In our approach, we avoid division and compute only the nominator of equation 2.4 if we use the classical cross-correlation instead of the CCGN. Using equation 2.4 the classical cross-correlation can be expressed as:

$$Z^*\ R = \{Z^*\ Z\}\ RF, \tag{2.5}$$

which shows that our approach (cross-correlation between Z and R) is equivalent to a RF which is multiplied by the auto-correlation of the source, i.e., a symmetric function in the time domain, peaked and centered at t=0s. Thus, the cross-correlation represents the receiver site response convolved with a function that is relatively compact.

This is in analogy to the spiking deconvolution technique (e.g. Shearer, 2009, pp. 190) from seismic exploration, where the recorded seismogram is cross-correlated with the vibroseis source function to obtain a time series that represents the Earth's response convolved with the auto-correlation of the source. For both, our cross-correlation approach and RF, the source function or pilot (P_Z) is the teleseismic source function (Langston, 2001), composed of the source function and near source reverberations.

2.3 Synthetic analysis

In what follows, we present synthetic data examples to show some important aspects of the techniques. We are going to focus our attention on the choice of the pilot length. Further on, we show the robustness of the cross-correlations and RF (water-level deconvolution) towards different levels of noise contamination.

Our synthetic data are simple and we do not try to mimic real seismograms, which are very complicated mainly due to source complexity and complex wave propagation in the heterogeneous real Earth. Converted and reflected phases arrive together with a multitude of other different phases. These are the reflections at crustal and at upper-mantle discontinuities and/or heterogeneities, core-mantle reflections (PcP) and depth phases, among many others. Some of the different phases arriving in the first 150 seconds after the P phase are depicted in Fig. 2.4, which shows their relative travel time curves as function of distance. The arrival time of each phase can be retrieved from the intersection of the vertical line (e.g., vertical green lines at fixed distance 42° and 90°) and the travel time curve of the corresponding phase. In addition, Fig. 2.5 (a) and (b) show two complete synthetic seismograms from 42° and 90° epicentral distance, respectively, obtained with the Direct Solution Method (Geller and Takeuchi, 1995; Kawai et al., 2006) and using the IASP91 Earth's model (Kennett, 1991). Vertical grey lines mark P-to-s conversions, P-wave reflections and some energetic phases which may interfere with them. As it can be deduced from the travel time curves (Fig. 2.4), more interference with other signals is expected for smaller epicentral distances. In what follows, we only consider P, pP and sP and their respective P-to-s conversions and P reflections at the Moho, 210, 410 and 660 discontinuities. The inclusion of other phases complicates the interpretation and does not add more information to our analysis.

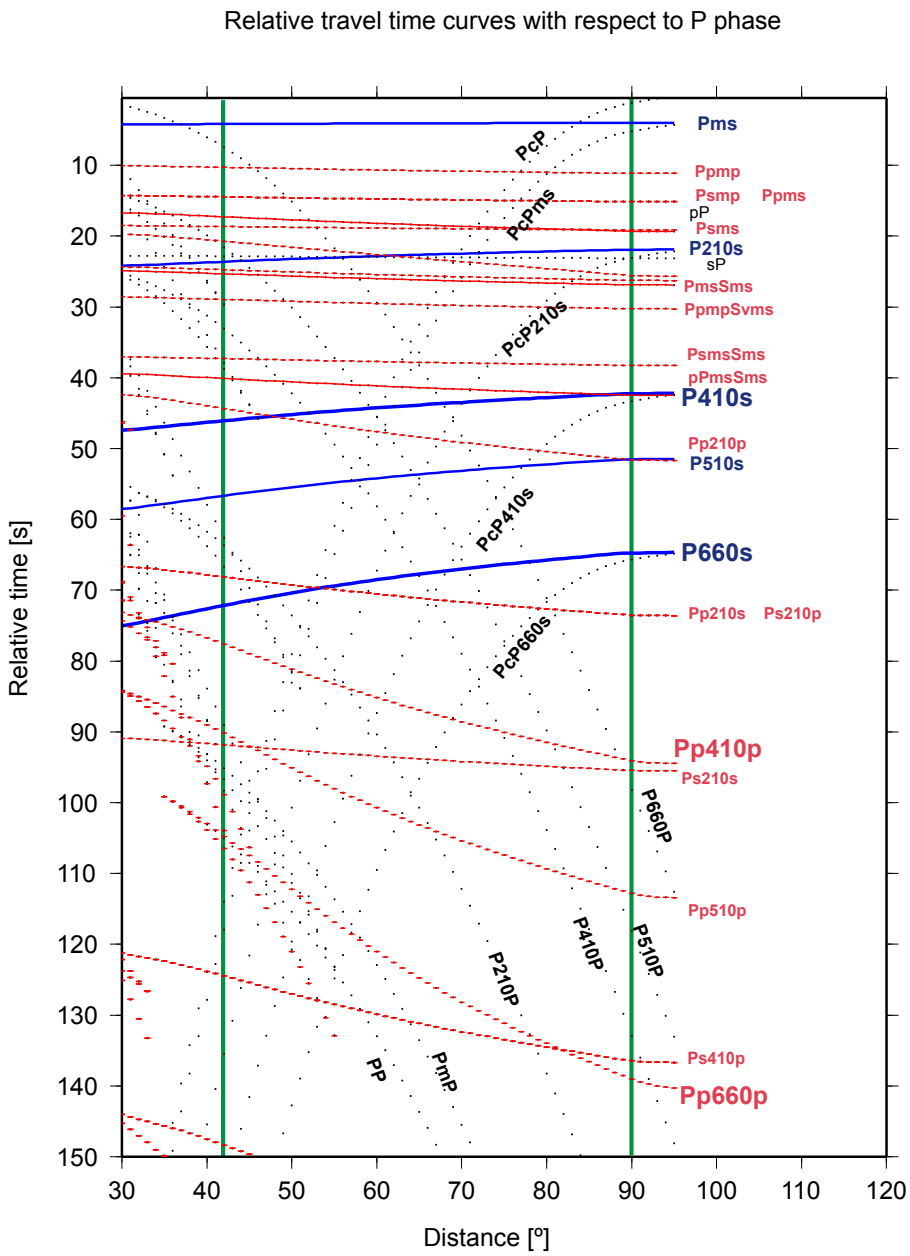

Figure 2.4: Travel time curves relative to the first arrival (P phase) as obtained using AK135 velocity model. Different colours represent P-to-s conversions (blue), P phase topside reflections (red dotted lines) and P-to-s conversions of core-mantle reflections (black dotted lines) at the Moho, 210, 410, 510 and 660 discontinuities. The intersection of these curves with the green vertical lines indicate the relative travel time of each phase for events occurring at the epicentral distances 42° and 90°.

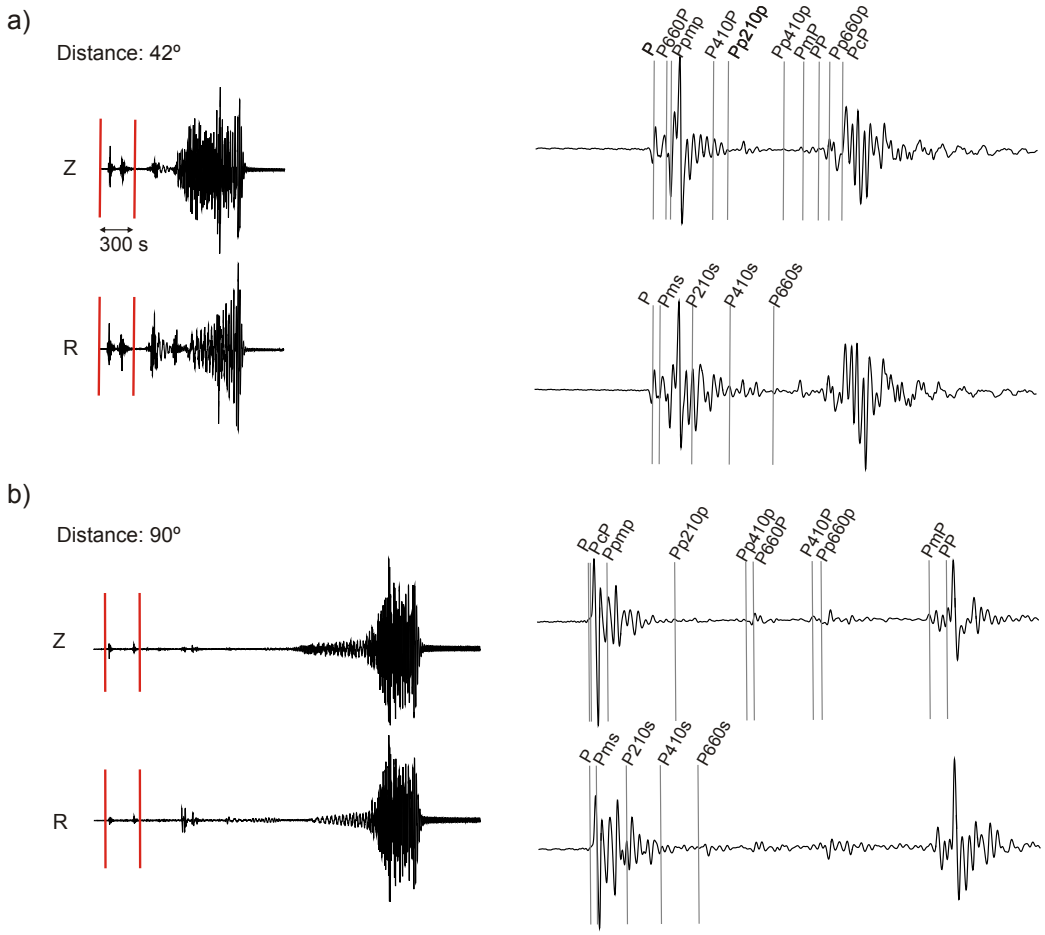

Figure 2.5: Synthetic seismograms obtained with the Direct Solution Method and the IASP91 Earth's model. a) Left: Z and R components of a teleseism at 42° epicentral distance. Right: 300 s window (vertical red lines in left panel) with vertical grey lines marking P-to-s conversions, P phase reflections and other energetic phases which may interfere with them. (b) Same as figure (a) for a teleseism at 90° epicentral distance.

2.3.1 Generating synthetic data

Synthetic seismograms were generated using the WKBJ (Chapman et al., 1988) algorithm and the convolutional model of the seismic trace. This algorithm provides synthetic seismograms for body waves in a 1-D (spherical or flat) Earth using the WKBJ approximation to solve the second order wave equation for high frequencies.

2.3.1.1 Convolutional model of the trace and Green functions

Seismic wave propagation in the Earth is approximated as linear, satisfying the principle of superposition. This means that based on linear system theory, the wavefield is fully characterized by the Earth's impulse response.

The output of a linear system to an input signal is the convolution of the input with the impulse response of the system. The impulse response of the Earth is known as the Green function. For a lateral homogeneous Earth, with velocity and density varying only with the Earth's radius and as a high frequency approximation, this Green function, $\mathbf{g(t)}$, is a series of impulses corresponding, in time and amplitude, to reflection and transmission coefficients at layer boundaries. In this context, the seismic trace, $\mathbf{x(t)}$, is the output of the Earth system when the input signal is the time function of the source, $\mathbf{s(t)}$. The noise component, $\mathbf{n(t)}$, is additive. Thus, using the convolutional model, the seismic trace can be expressed as:

$$x(t) = s(t) * g(t) + n(t) \tag{2.6}$$

2.3.1.2 WKBJ synthetic data and processing

The synthetic data was built by computing a simplified Green function of the R and Z components with the WKBJ algorithm and using the AK135 (Kennett et al., 1995) velocity model. To keep the seismic traces as simple as possible, our synthetic seismograms consisted of P, pP and sP and their respective P-to-s conversions and P reflections at the Moho, 210, 410 and 660 discontinuities. The Green functions were computed for different source depths (0 km, 20 km and 35 km) and epicentral distances every degree from 55° to 65°, and were convolved with different source functions for each event. The source functions were 10 to 12 seconds long and were generated from random number sequences filtered in different frequency bands with central frequency at 0.4 Hz (band width $\sim$ 0.6 Hz). Unless otherwise noted, the

records have been contaminated by adding random noise (bandpassed from 0.02 to 1.0 Hz) with a maximum amplitude of 2 % of the P phase maximum amplitude.

Finally, we extracted a pilot wavelet from the Z component starting at the onset of the P phase and ending 10 to 20 seconds later, depending on the event depth to include the depth phases. Then, the cross-correlations between the pilot and the R component of the corresponding event were performed using $\text{PCC}_{\nu=1}$ and CCGN. Finally, RFs were computed using a frequency domain deconvolution with the water-level regularization (see Appendix A).

2.3.2 Pilot length

The length of the pilot is an important parameter in our approach. As has been stated in Section 2.2.2, a longer pilot attenuates the correlation value due to other signals (different than Pds) which are also coherent with the first arrival waveform. Figs 2.6 (a) and (b) show two pilots of 10 and 20 s duration, respectively, for a synthetic teleseism at 55° epicentral distance and a hypocenter at a depth of 35 km. The pilot in Fig. 2.6 (a) is composed of the P phase while the pilot in Fig. 2.6 (b) also includes the pP and sP phases. Fig. 2.6 (c) shows the R component with the grey vertical lines pointing out the arrival of the $P410s$ and $P660s$ phases. Each of these phases is followed by the P-to-s conversion of pP and sP at the corresponding discontinuity ($pP410s$, $sP410s$, $pP660s$ and $sP660s$), which also correlate with the P phase.

The correlograms obtained using both pilots are shown in Figs 2.7 (a) for PCCR and (b) for CCGNR. The black correlograms correspond to the 10 s pilot, while the red ones to the 20 s pilot. After the correlation maxima of $P410s$ and $P660s$, both correlograms (black and red) show the negative correlation maxima of $pP410s$ and $pP660s$, respectively. Moreover, the positive correlation maximum after $pP410s$ is due to the $sP410s$ phase. The $sP660s$ maximum is not clear because it arrives together with other P-wave reflections ($Pp410p$). These undesired depth phases appear more attenuated when using the 20 s pilot (red correlograms).

The overall signal to noise amplitude ratio has been improved by using the 20 s pilot. This is expected since the pilot became more complicated and phases which are similar to the P phase but not similar to the combination of P, pP, and sP waveforms (and their respective near source reverberations) are attenuated through a decreased coherence.

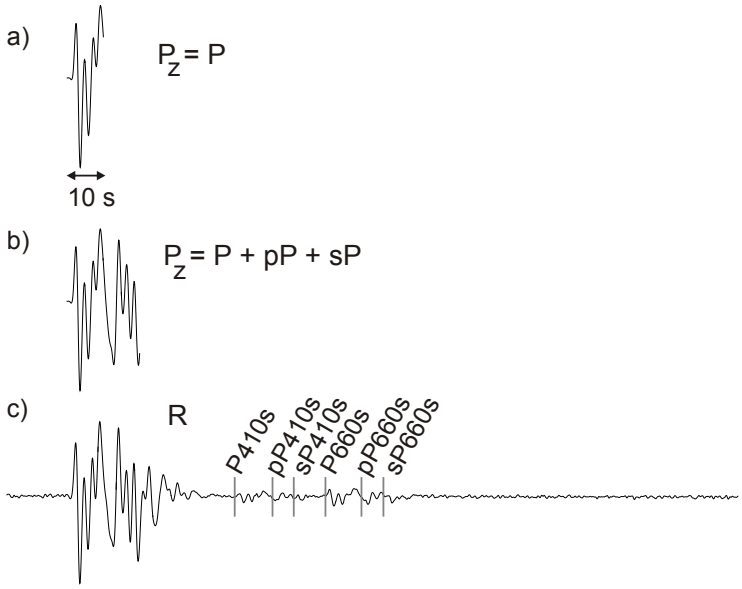

Figure 2.6: Different pilot (P_Z) lengths. a) 10 s pilot including only the P phase extracted from the Z component of a synthetic teleseism at 55° epicentral distance and a hypocenter at a depth of 35 km. b) 20 s pilot including the P, pP and sP phases. c) The corresponding R component.

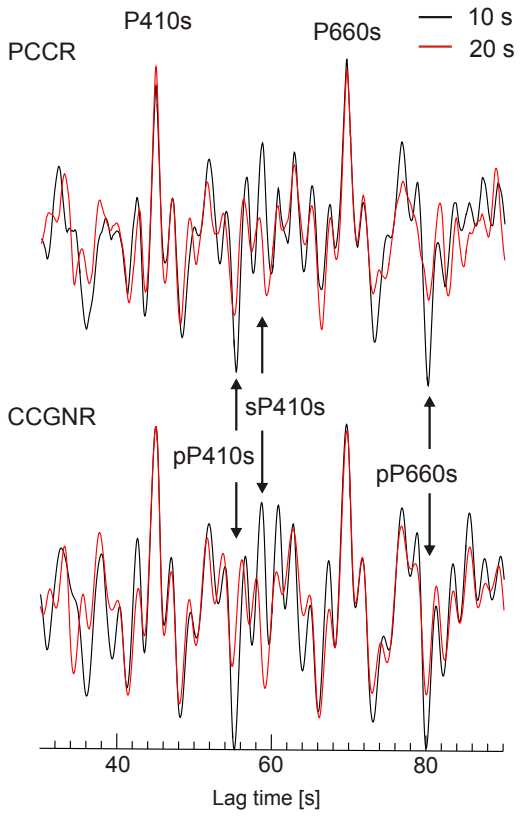

Figure 2.7: Correlograms using different pilot (P_Z) lengths. Top: PCCR correlograms when using the 10 s pilot with the P phase only (black) or the 20 s pilot which contains the P, pP and sP phases (red). Bottom: same as top panel but for CCGNR.

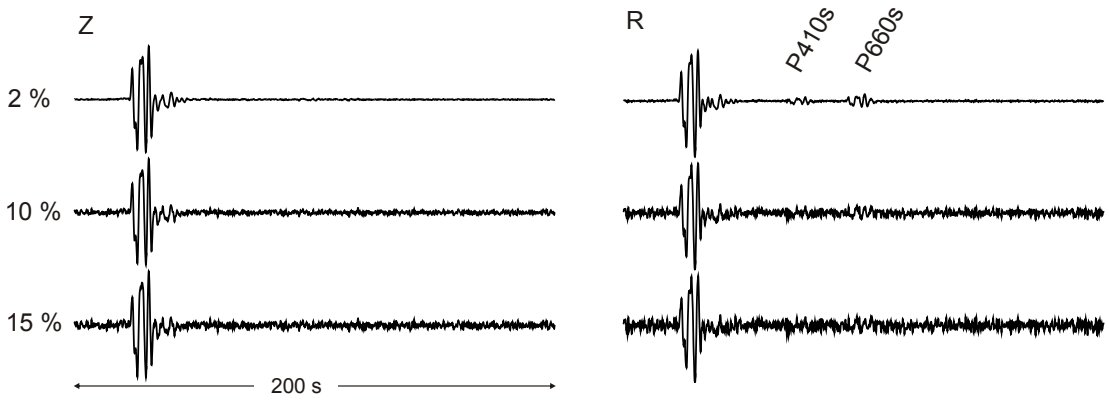

Figure 2.8: Synthetic seismogram contaminated with different noise levels, which were defined as a percentage (2 %, 10 % and 15 %) of the P phase maximum amplitude in the Z component. Left: Z component. Right: R component. $P410s$ and $P660s$ are marked for a reference.

2.3.3 Noise influence

Ambient noise is perhaps the most disturbing component in seismograms because it is always present and cannot be easily eliminated. Fortunately, the random waveform nature of this noise and its relative low amplitude for strong events permit a good performance of cross-correlations. On the other hand, noise may be amplified in deconvolution (see equation A.5 in Appendix A). However, RFs with a good SNR and with clear detections can be obtained by using an adequate water-level parameter in the deconvolution. Normally, the optimum water-level parameter is achieved by visual inspection of the resultant RF, which makes it a subjective election. In what comes next, we are going to present synthetic seismograms contaminated with noise of different amplitude to illustrate the PCC's, CCGN's and RF's performance in the presence of noise.

The synthetic seismograms in Fig. 2.8 have been contaminated with different noise levels which were defined as a percentage (2 %, 10 % and 15 %) of the P phase maximum amplitude in the Z component. From the R component (right panel), it can be seen that $P410s$ and $P660s$ are obscured by the noise amplitude for increasing noise levels (indicated at the right end of each trace). On the other hand, in the

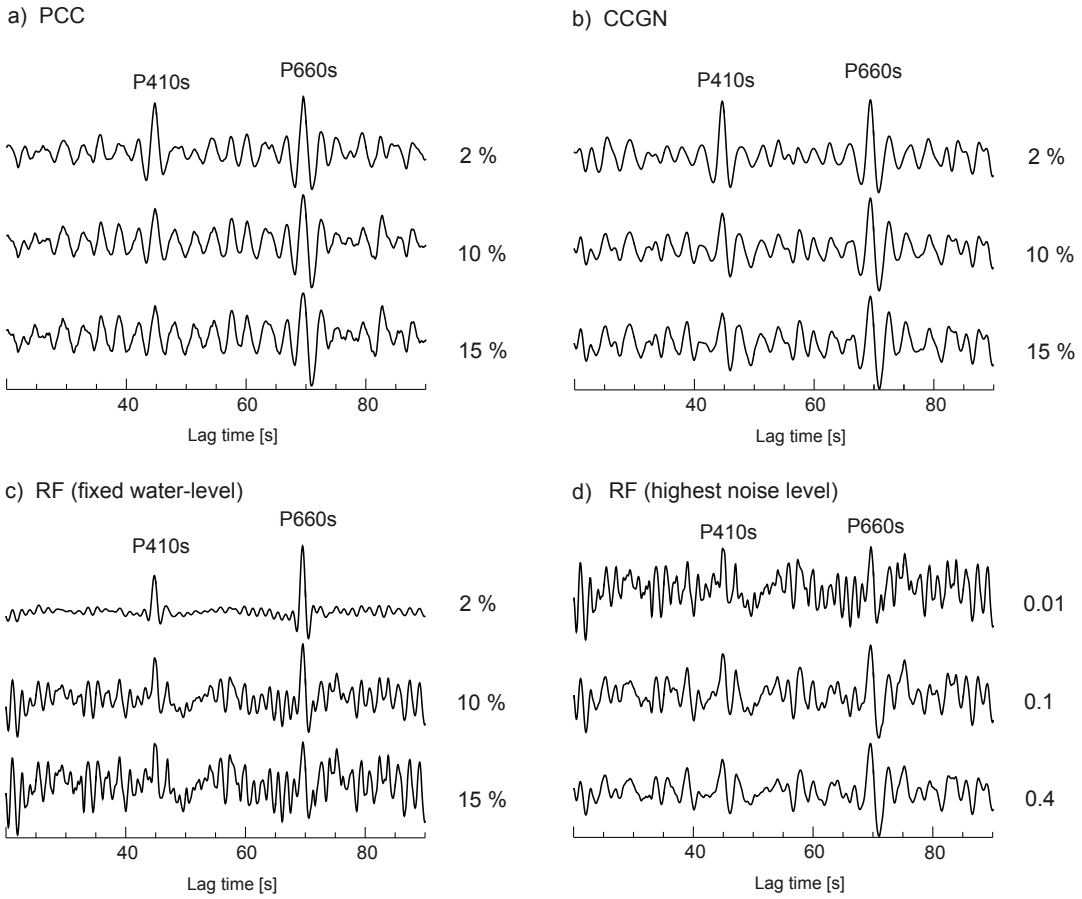

Figure 2.9: a) PCCR correlograms obtained from the R components in Fig. 2.8 and using a 13 s pilot. b) CCGNR correlograms obtained from the R components in Fig. 2.8 and using a 13 s pilot. c) RFs (water-level parameter of 0.01) obtained from the R components in Fig. 2.8 and using a 13 s pilot. $P410s$ and $P660s$ are detected with smaller amplitude for higher noise levels. d) Radial RFs obtained for the 15 % noise level data and varying water-level parameters (0.01, 0.1, 0.4).

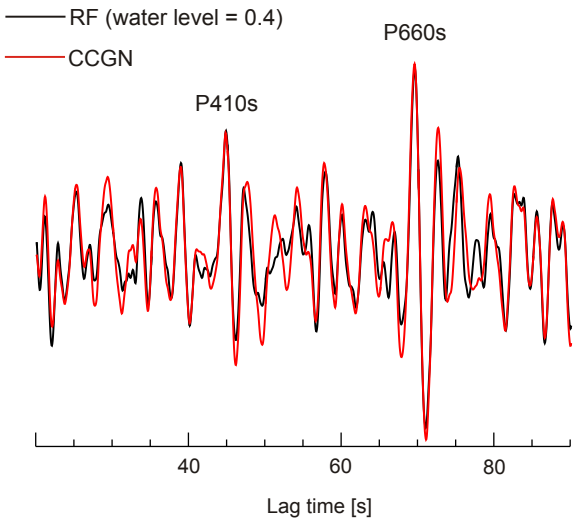

Figure 2.10: $CCGNR$ (red) and radial RF (black) using a water-level parameter of 0.4

radial correlograms (Fig. 2.9 a for PCCR and b for CCGNR) and in the radial RFs (Fig. 2.9 c) it is still possible to distinguish both P-to-s conversions for every noise level, however, they present a lower amplitude (lower SNR) for increasing noise levels. Noise contamination in RFs can be reduced by choosing higher values of the water-level parameter. Fig. 2.9 (d) shows the RFs when using different water-level parameters (0.01, 0.1 and 0.4) and the seismogram with the highest noise level (15 %). Higher water-level values reduce the amplitudes of the high frequency noise.

The water-level deconvolution and the classical cross-correlation are closely related operations. This relation can be deduced from the analytical expression of the water-level deconvolution ($k = 1$ in Eq. A.6 of Appendix A). As the water-level becomes larger and near to 1, the denominator of this equation is approximately a constant value, turning the deconvolution into a scaled version of the classical cross-correlation. Fig. 2.10 illustrates the similarity between the CCGN and the RF from the water-level deconvolution when using a high water-level parameter of 0.4. Both time series were plotted together before normalization of amplitudes.

2.3.4 Robustness analysis

To perform the robustness analysis, we constructed a special data set from the one described in Section 2.3.1. We used 33 superficial events, one for each epicentral distance (between 55° to 65°) and source depth (0 km, 20 km and 35 km). The corresponding records were contaminated by adding random noise (filtered in 0.02-1 Hz) of different noise level. For each seismogram and noise level, we used 21 different random noise realizations to permit a statistical analysis of the robustness of the detections as a function of the noise level. The noise level was defined as a percentage of the P phase maximum amplitude in the Z component, ranging from 2 % to 30 %. This way, theoretical test data was generated for 9 different noise levels. This analysis is meant to be a proof of concept test and it is not our intention to compare the synthetic data results with the real data.

For each of the 9 noise levels (2 % to 30 %), we computed radial correlograms (PCCR and CCGNR) as explained in Section 2.2. The pilot wavelets were 12 s long and started with the P phase. Additionally, RFs were computed using a frequency domain deconvolution with a water-level parameter of 0.1 to avoid the division with numbers smaller than 10 % of the maximum power $|Z|^2$ (no Gaussian filter during deconvolution). The radial correlograms or RFs for each of the 21 noise realizations and each noise level were stacked using PWS with the reference slowness for the $P660s$ phase at 60° distance and corresponding linear time corrections. At the end, we obtained 21 stacks for each technique (PCC, CCGN, RF) and noise level from which we determined the travel time of the $P660s$ phase. The respective mean and standard deviations are shown in Fig. 2.11 (a) relative to the noise free arrival times. The increasing error bars (standard deviations) manifest a higher detection variability due to the increasing noise contamination. For small noise, PCC often shows the smallest time variations which we attribute to the high waveform sensitivity inherent to its phase coherence approach. However, for a large noise contamination the waveforms are more corrupted and PCC travel times have a larger variation around the mean than CCGN and RF. Nevertheless, the most stable mean travel times are obtained with PCC, which are centred at the expected time for all noise levels. It seems that CCGN and RF are differently affected by the large amplitude noise since these approaches are less waveform sensitive than PCC. This is why the CCGN and RF mean travel time at large noise level diverges from the mean value for

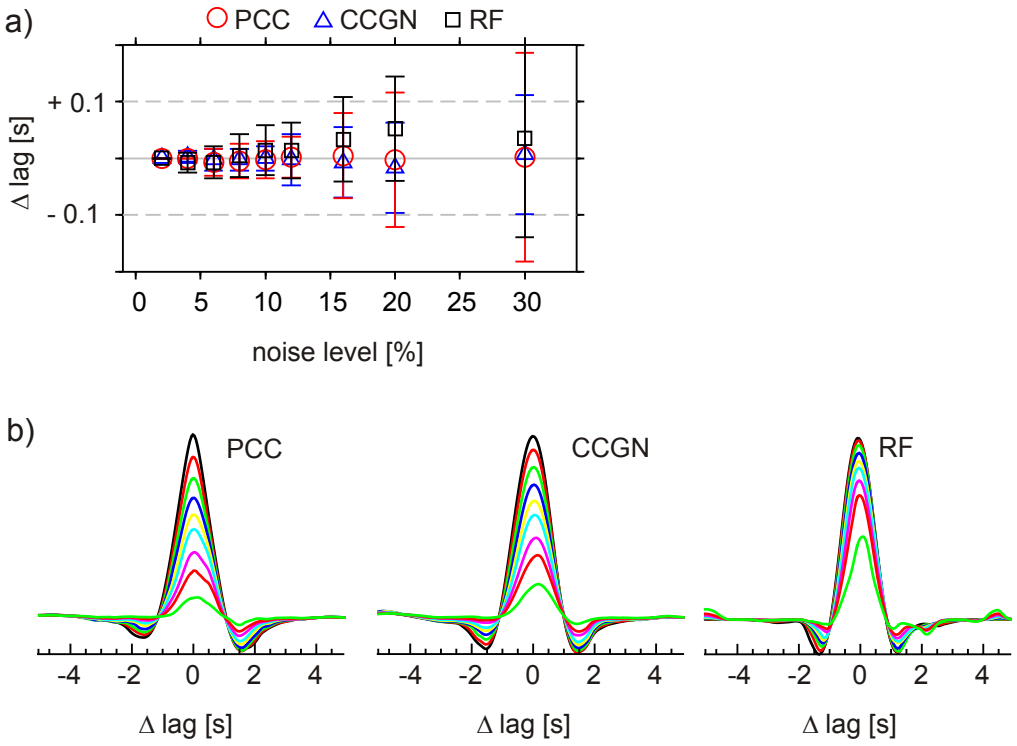

Figure 2.11: Synthetic data robustness analysis. For each noise level (2 to 30 %) we computed the R correlograms (PCC and CCGN) and RFs (water-level deconvolution with water-level parameter of 0.1). The PWS was performed using the reference slowness for the $P660s$ phase and linear move-out corrections. a) Mean and standard deviations of $P660s$ travel times based on 21 different noise realizations per noise level. The mean time has been plotted with respect to the theoretical $P660s$ travel time. b) PWS waveforms for PCC, CCGN and RF for each noise level and random noise realization. Decreasing amplitudes are due to decreasing coherence for increasing noise level.

noise free data. In the RF, the presence of noise in the components may breakdown the deconvolution due to amplification of the high frequency components of noise which is usually controlled by the application of a frequency low-pass filter before deconvolution. Anyhow, noise may destroy signal waveforms at any frequency which destabilizes the deconvolution through loss of signal coherence. This is independent of the water-level which avoids instabilities due to the division of small numbers. Using lower values for the water-level parameter (e.g. 0.02) causes mean lag time variations already at lower noise levels.

Fig. 2.11 (b) shows the PWS of PCCRs, CCGNRs and RFs for each noise level and only one of the 21 data sets. This figure shows the decreasing amplitudes (coherence values) obtained for the increasing noise levels. What is more, it can be seen that the maxima are slightly shifted in time, which is manifested in the lag time variability shown in Fig. 2.11 (a). It is visible that the PCC's maxima are smaller than the CCGN's and RF's maxima. This is due to the fact that PCC measures a lower coherence due to its higher sensitivity to waveform perturbations. This is not a problem to our approach since we do not use the absolute values of the coherence.

This robustness analysis demonstrates that with reasonable noise level the performance of PCC, CCGN and RF is similar. Thus, the three independent approaches can be used together to add consistency to the results and to bridge observation gaps due to breakdown of any of the methods inherent to data characteristics. This study has been performed with the $P660s$ phase and random noise without loss of generality. For conversions at other depths, the results are expected to be similar for similar signal amplitudes. Besides random noise, signal destruction may also happen due to the interference with other signals. This has not been investigated here.

2.4 Real data examples

We now employ a subsidiary data set from the TopoIberia data base to investigate the $P410s$ and $P660s$ detection in individual stations. The map of Fig. 2.12 shows the location of the 9 broad band stations used in this analysis. The objective is to quantify the differences in the estimated travel times for the three approaches.

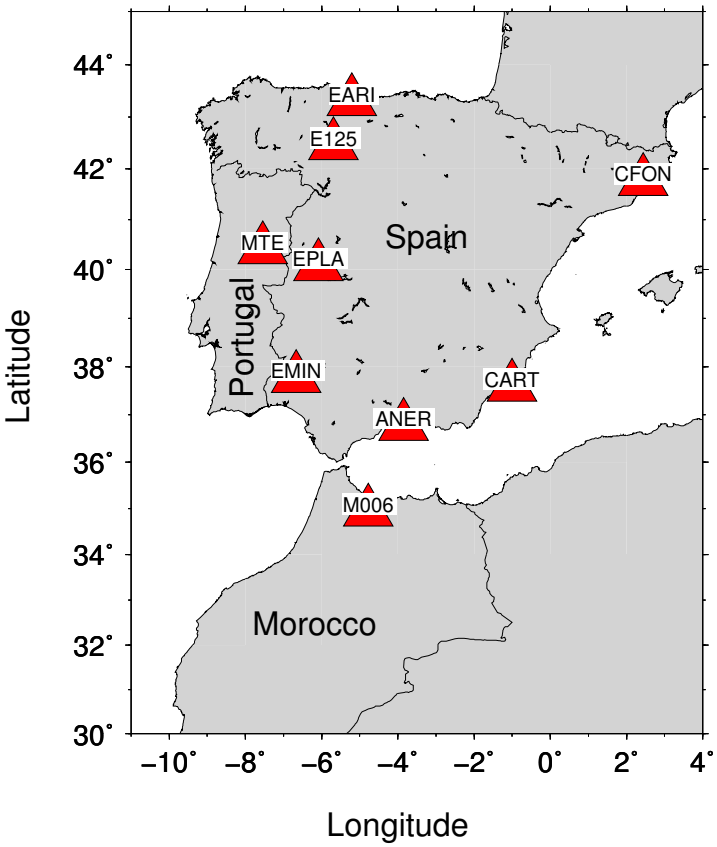

Figure 2.12: Distribution of 9 seismic stations (red triangles) where we investigate the detection of $P410s$ and $P660s$.

2.4.1 Processing

Based on the quality of the records, we selected for each station between 27 and 103 earthquakes for the available data from January 2007 to December 2011. The epicentral distances are between 65° and 95° and the magnitude, mb, range is 5.1 to 7.2.

The Z and R components were bandpass filtered between 0.02 and 0.12 or 0.03 and 0.2 Hz. The choice of the frequency band for each station is based on the clarity of the figures. From the Z components of each recorded event, we extracted a 100 s pilot, which contains the P phase and part of its coda. Then, the cross-correlations (PCC and CCGN) were performed between the pilot and the corresponding R component. Additionally, RFs were computed using the water-level deconvolution with a water-level parameter of 0.1. Two quality controls were applied over these RFs. The RFs were discarded when the amplitudes prior to the P phase were larger than the amplitudes after the P phase. The second condition was that the RFs must have an amplitude maximum in the vicinity of zero seconds. After the quality control, between 16 to 91 RFs were left for each station. For a direct comparison of the three techniques, only data that pass the RFs quality controls were used.

Finally, the cross-correlation functions and RFs were stacked in the relative time and slowness domain using the PWS. Further details on the processing are given in Chapter 3, where the entire data set is being used to analyse the TZ beneath Iberia and Morocco.

2.4.2 Detection of P-to-s conversions at individual stations

Fig. 2.13 shows the individual correlograms and RFs, which were move-out corrected using a fixed relative slowness parameter of -0.1 $s/\circ$ and a reference distance of 80°, for the stations in Fig. 2.12. Note that Fig. 2.13 continues in Appendix C. In general, Fig. 2.13 shows that the individual RFs and CCGNRs have a better SNR than the PCCRs. In this figure, the correlograms and RFs are arranged by increasing back azimuth. The black amplitudes are positive and the grey ones are negative. On some time-back azimuth sections, it is easy to distinguish the $P410s$ and $P660s$ phases (e.g., ANER, CART, EMIN), which are the positive-amplitude signals close to the theoretical travel times marked with the white lines at 42.8 s ($P410s$) and 65.8 s ($P660s$). In other sections, it is more difficult to discriminate the $P410s$ and $P660s$

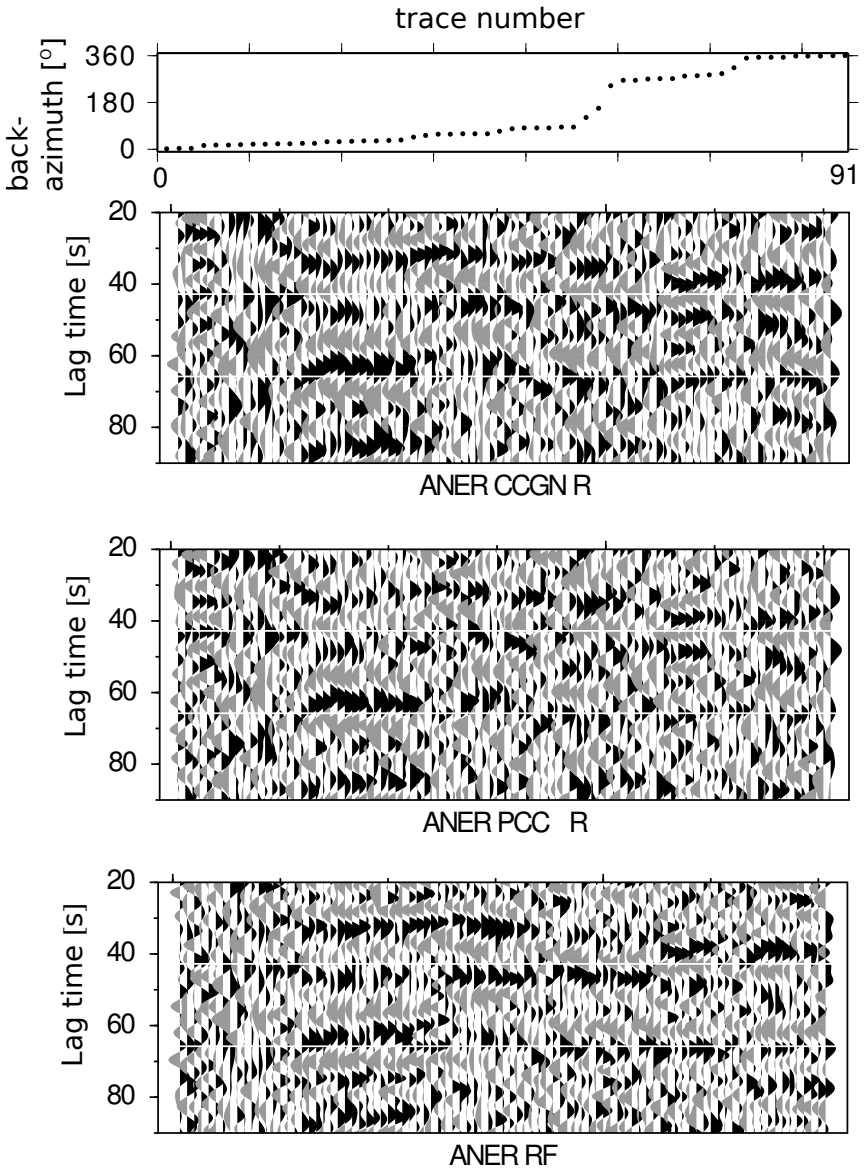

Figure 2.13: Move-out corrected CCGNRs, PCCRs and RFs sorted by their back-azimuth for the stations shown in Fig. 2.12 (see Appendix C for the remaining stations). Original seismograms were filtered in the 0.02-0.12 Hz frequency band. Correlograms and RFs are move-out corrected for a reference epicentral distance of 80°. Horizontal white lines mark the $P410s$ and $P660s$ relative arrival times in AK135.

phases from other signals due to the lower SNR (e.g., CFON, MTE, EARI) or due to the low number of traces (e.g., EPLA, E125, M006). The sine-like travel time modulation which can be observed in some of the time-back azimuth sections (e.g., see the $P660s$ arrivals for ANER and EARI) may indicate the presence of topography or a dipping discontinuity (Nagaya et al., 2008).

Other phases can be distinguished in some time-back azimuth sections. Positive-amplitude signals appear intermittently between 20-25 s and/or 30-35 s (e.g., ANER, CART, EMIN, EARI). These signals may correspond to P-to-s conversions from discontinuities at a depth of about 200-250 km (probably the Lehmann discontinuity) and 300-350 km, respectively. Additionally, a positive-amplitude signal appears, also intermittently, between 45-55 s (e.g., CART, MTE, EARI, EMIN). This signal seems to be consistent with a $P510s$ phase.

We performed the stacks in the relative time-slowness domain to obtain estimates of the converted phase ($P410s$, $P660s$) travel times. For the reference distance (80°) that we used to compute the stacks, the $P410s$ arrives at the relative time of 42.8 s and the $P660s$ at 65.8 s, both with a positive coherence value and a negative relative slowness. Fig. 2.14 shows the PWS of the correlograms and RFs shown in Fig. 2.13. Note that Fig. 2.14 continues in Appendix C. To facilitate the signal identification, we added the theoretical travel times and slowness values for the converted phases: Pms, $P210s$, $P410s$ and $P660s$ (white crosses) and for the multiply reflected phases: $Ppmp$, $Ppms$, $Pp210p$, $Pp210s$ (black crosses). The amplitudes were normalized to unity in two time intervals which are separated with the vertical black line at 30 s. The time axis starts at 4 s to exclude the large amplitudes of the P phase in the R component. Therefore, the conversion from the Moho is not seen in any of the stacks due to the begin time of 4 s. Besides, the frequency range is too low to resolve signals from shallow discontinuities as those which appear in the time interval from 0 to 20 s. Nevertheless, the extraction of these signals is not the objective of our study. The grey contours indicate normalized-positive amplitudes larger than 0.3. Some of the stacks show clear detections of both phases, $P410s$ and $P660s$, with the three techniques (e.g., ANER, CART, MTE, EARI, E125 and M006). Other stacks show a clear detection of both phases with one or two techniques. For the station CFON, the $P410s$ phase is only detected in the stacks of the CCGNRs and PCCRs, while for the station EPLA this phase is detected only with the RFs. For the station EMIN, the $P660s$ phase is detected in the stacks of the CCGNRs and RFs. In some

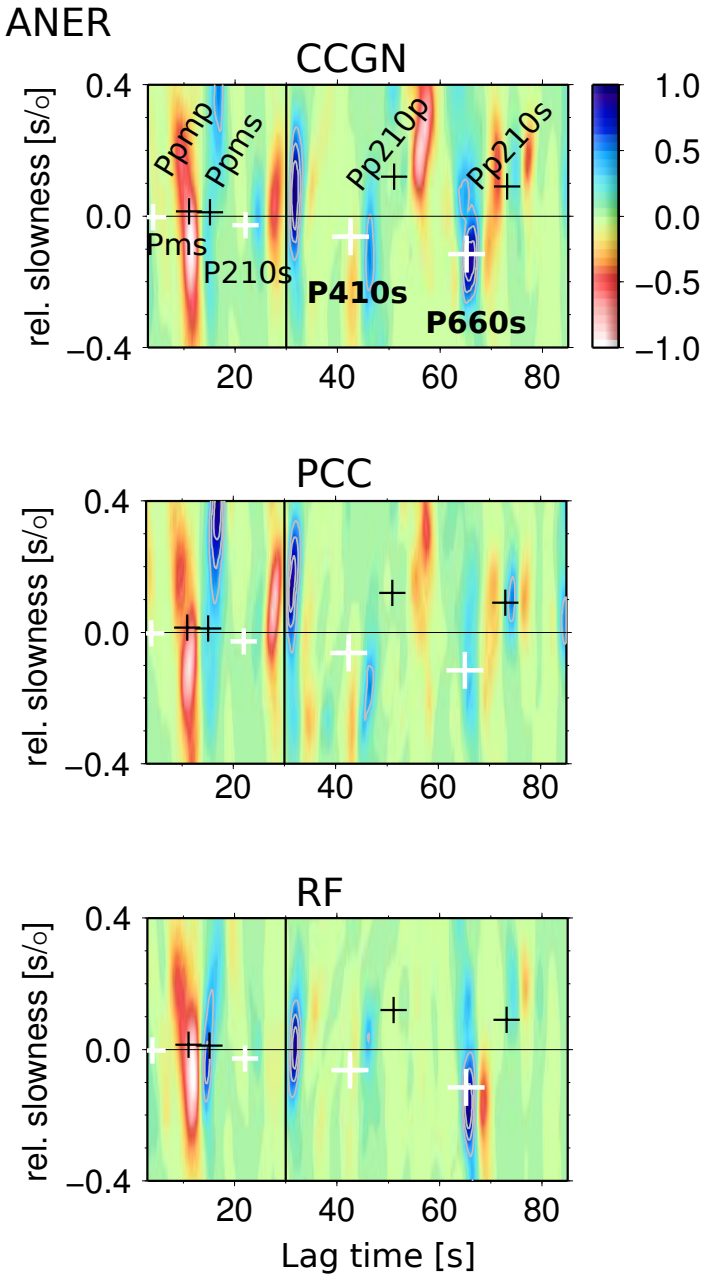

Figure 2.14: Slant-stack examples for the 9 stations shown in Fig. 2.12 (see Appendix C for the remaining stations). The corresponding seismic sections are shown in Fig.2.13. Each panel shows the PWS of CCGNs, PCCs and RFs, respectively. For a reference, theoretical relative time (x-axis) and slowness (y-axis) values are marked with white crosses for Pms, $P210$, $P410s$ and $P660s$. Black crosses mark P-wave reflections. The vertical black line at 30 s separates the time intervals where the amplitudes were normalized to 1. Contours are drawn for positive amplitudes (blue to light blue) larger than 0.3.

stacks, the $P410s$ and/or $P660s$ appear with positive relative slowness. The positive slowness may indicate a discontinuity with topography or the presence of small lateral anomalies, which deflect the waves so that the incidence angle becomes larger than for a spherical symmetric Earth model in concordance to the observed slowness.

Clear detection of a P-to-s conversion at 300-350 km is only observed in the stacks of station EARI. This is probably due to the intermittency with which the Pds (where d is between 300 and 350) phase appears for other stations. This phase stacks coherently only when it is present in the majority of the correlograms or RFs. Similarly, the only reliable detection of $P510s$ is observed in the stack for CART (marked with the black arrow). There are also stacks which show a clear positive-amplitude signal near 20 s (EARI). This is probably the conversion at the Lehmann discontinuity, $P210s$ phase, however, the multiply reflected phases from the Moho are expected in the same time interval.

To estimate mean values of the travel times, we performed a bootstrap resampling of 21 repetitions for each stack and each technique. This way, we obtained time standard deviation values to measure variations in the observed relative travel times. We also assess the robustness of the $P410s$ and $P660s$ phases. The results are summarized in Table 2.1. The standard error (σ) on our travel-time measurements range from 0.1 to 1.1 s. The largest standard deviation values were found for CFON (with CCGN) and M006 (with PCC). These large errors could be due to the low number of stacked data and/or due to the strong 3D heterogeneities including topographic variations beneath these stations. The measured travel times for $P410s$ and $P660s$ are also depicted in Fig. 2.15 using different symbols to discriminate the results from the different techniques. Vertical bars indicate the 95 % bootstrap confidence interval. In general, we see that for each station the 95 % confidence intervals of the three techniques are overlapped and that the measured travel times follow the same trend (larger/smaller than the reference value). Moreover, no systematic time variations are visible for none of the methods. All this means that the measured time values with CCGN, PCC and RF are consistent and that we can trust the estimated time values from a single technique. The parameter δt_{max} in Table 2.1 measures the maximum difference among the mean travel time values estimated with each technique. Considering only the stations with a significant data number (ANER, CART, CFON, MTE, EARI and EMIN), these δt_{max} values range from 0.3 to 1 s . These travel time differences are expected for real data where the small amplitude coda phases are often

Table 2.1: $P410s$ and $P660s$ detections

Station	Δt_{P410s} CCGN [s]	Δt_{P410s} PCC [s]	Δt_{P410s} RF [s]	δt_{max} [s]	Δt_{P660s} CCGN [s]	Δt_{P660s} PCC [s]	Δt_{P660s} RF [s]	δt_{max} [s]	Events
ANER	46.8 ± 0.4	47.6 ± 0.2	46.6 ± 0.5	1	66.3 ± 0.3	66.8 ± 0.3	66.6 ± 0.3	0.5	91
CART	42.6 ± 0.7	42.2 ± 0.3	42.2 ± 0.2	0.4	67.3 ± 0.2	67.8 ± 0.6	67.6 ± 0.2	0.5	78
CFON	44.4 ± 0.3	44.9 ± 0.5	-	0.5	68.9 ± 0.4	68.8 ± 1.1	68.5 ± 0.4	0.3	56
MTE	42.5 ± 0.3	41.9 ± 0.3	42.2 ± 0.1	0.6	64.1 ± 0.3	64.2 ± 0.6	64.2 ± 0.3	0.1	76
EPLA	-	-	44.1 ± 0.1		66.7 ± 0.4	66.4 ± 0.6	66.8 ± 0.4	0.4	22
EARI	41.8 ± 0.2	41.6 ± 0.3	41.5 ± 0.5	0.3	64.4 ± 0.2	64.2 ± 0.2	64.6 ± 0.2	0.4	82
E125	44.2 ± 0.1	44.3 ± 0.2	43.5 ± 0.3	0.8	66.4 ± 0.2	66.0 ± 0.3	67.0 ± 0.2	1	16
M006	40.6 ± 1	41.7 ± 0.6	42.5 ± 0.2	1.9	66.8 ± 0.3	66.1 ± 0.6	67.9 ± 0.2	1.8	23
EMIN	43.3 ± 0.2	43.1 ± 0.3	43.0 ± 0.3	0.3	65.1 ± 0.4	-	64.6 ± 0.7	0.5	82

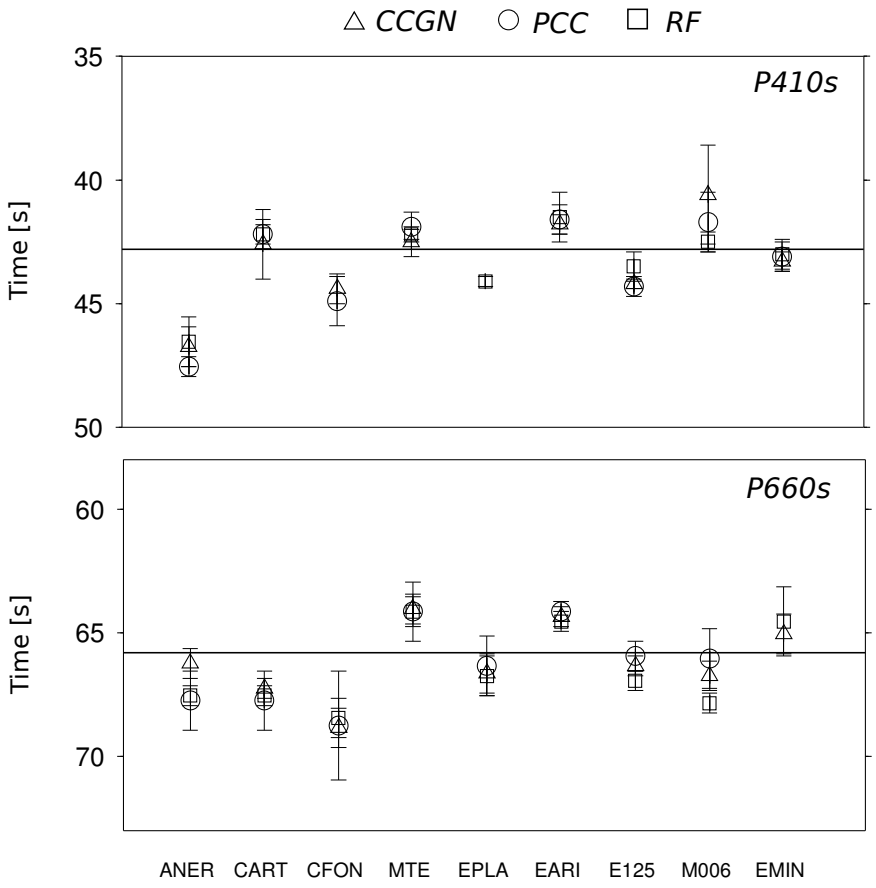

Figure 2.15: Measured travel times for $P410s$ (top) and $P660s$ (bottom) phases at stations ANER, CART, CFON, MTE, EPLA, EARI, E125, M006 and EMIN. Different symbols represent the travel time values for the different techniques CCGN (triangles), PCC (circles) and RF (squares) and vertical bars represent the 95 % bootstrap confidence interval ($2 * \sigma$).

obscured by other signals and noise, and where signals are less coherent due to the presence of structural heterogeneities. As a consequence, the observed differences can be attributed to the different strategies of the employed methods, which differently handle the detection of less coherent signals. Differences in the travel time measurements of the coda phases indicate data complexities and also indicate that at least one of the approaches is less suited to accurately detect the signals due to the present signal and noise characteristics for this detection. It is often not possible to determine which of the approaches provide the better time measurement and we therefore understand the variations in the time measurements as an indicator of inconsistencies due to data complexity. That is, the smaller the travel time variations among the three methods, the more certain we are about having obtained a correct coda phase detection. What is more, the mean travel time obtained from the detections with the three techniques can stabilize against systematic and non-systematic errors. Note that a small standard deviation of travel time measurements obtained for one single approach cannot reveal systematic time errors due to some strange noise (e.g., see Fig. 2.11 at high noise level). Therefore, we propose to merge the independent Pds (d=410 or 660) detections from each bootstrap repetition for each of the three techniques. This way, robust mean and standard deviation values can be obtained for the $P410s$ and $P660s$ travel times at each station.

2.5 Discussion and conclusions

We have presented a new processing approach based on cross-correlation and stacking techniques to detect weak amplitude phases that arrive in the P phase coda. As cross-correlation functional, we have used the CCGN, which is the classical approach to measure waveform similarity and the PCC, which is based on instantaneous phase coherence and which has not been widely explored before (Schimmel et al., 2011). We have proposed to use these cross-correlations (PCC and CCGN) together with RFs to stabilize the detections against errors and to bridge observation gaps. Without noise or with low to reasonable noise level, the results of the three techniques are similar but inherent to their different strategies the signals are detected differently. Similar results obtained through different methods (Fig. 2.15) add robustness and confidence to the detections and interpretations. Varying results or non-detections are expected for more difficult data, depending on the signal and noise characteristics.

Therefore, the variations of the final results and the amount of approaches which lead to an independent detection can be used as a quality indicator. Our procedure is a step forward to stabilize against detection problems and to identify more ambiguous detections. Another advantage is that one automatically bridges observation gaps by one or the other method. Each difficult detection is a special case due to the non-stationarity of signals and noise and none of the methods will lead to satisfying detections for all cases.

PCC is amplitude unbiased and more sensitive to waveform coherence than CCGN and RF. Coherent signals are therefore accurately detected even in the vicinity of other larger amplitude signals which may bias the detections with CCGN (figs 3 and 4 in Schimmel (1999), fig. 1 in Schimmel et al. (2011)). Our synthetic data tests (Fig. 2.11) show that PCC may even provide more stable results than CCGN and RF at high noise levels. Of course, PCC fails when signals cannot be detected by their coherence. In these cases, CCGN is usually the better approach. The water-level deconvolution used to compute the RFs has the inconvenience that the choice of the water-level parameter is a subjective task. However, we have used a fixed water-level parameter of 0.1 and a quality control over the RFs amplitude, which simplify the automatic computation of RFs. In practice, we see that the detection of $P410s$ and $P660s$ in individual records is a more difficult task, which can be deduced from the individual traces in the time-back azimuth sections (Fig. 2.13). We attribute this complexity to the loss of waveform coherence with the reference phase, which is particularly disadvantageous to the PCC. Nevertheless, the $P410s$ and $P660s$ phases are well detected with the three techniques in the time-slowness domain. We observed that the 95 % confidence interval of the estimated time values with each technique are overlapped and that they follow the same trend, regardless of the technique. All this suggests that the measured time values with CCGN, PCC and RF are consistent and that we can rely on the estimated time values from a single technique.

Cross-correlations have been used before to detect P-to-s conversions from the upper-mantle discontinuities (Paulssen, 1985, 1988; van der Lee et al., 1994; Schimmel, 1999). However, while we use a 100 s pilot wavelet, these studies used a shorter one that comprises only the P phase or part of it, e.g. in Paulssen (1985, 1988) and van der Lee et al. (1994) the pilots were about 5-6 s long. Besides, they normalized the correlograms with respect to the auto-correlation maximum of the P phase, and linear stacks were employed to identify the signals. Shearer (1991) resorted to the

cross-correlation between components to detect P-to-s conversions and other phases using a global data set. For the Pds phases a 41 s reference wavelet was preferred and correlation peaks were plotted without previous stacking. Similar to this study, our approach can be used to detect other phases such as SdS, PdP, Sdp, etc with an adequate definition of the pilot.

3

Data set

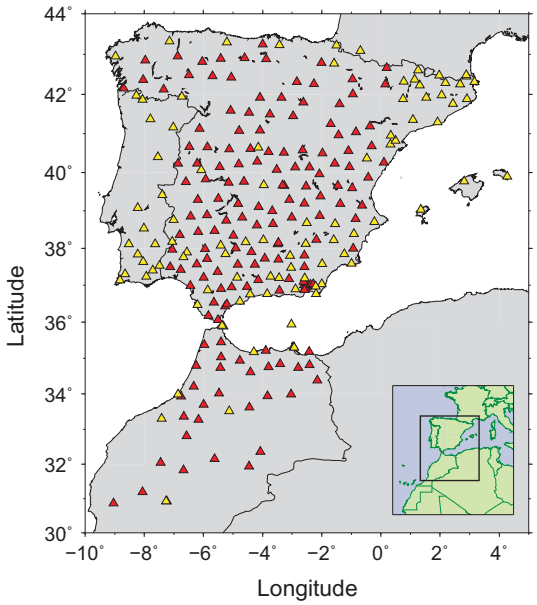

Figure 3.1: Locations of the stations used in this study. Red triangles correspond to the IberArray stations from the TopoIberia project. Yellow stations are from other collaborating institutions (see Section 1.5). The station names, position and corresponding network codes are listed in Appendix D.

3.1 Introduction

The data used are from stations shown in Fig. 3.1. The corresponding station names, their positions and network codes are listed in Appendix D. Most of our data are from IberArray and we may refer with the TopoIberia seismic network to the entire data base used in this work. The TopoIberia seismic network (IberArray in Fig. 3.1) is a large data base, which comprises worldwide earthquake records. In this chapter, we describe our data base and the processing used for the computing of the correlograms and the receiver functions that are used in the detection of the $P410s$ and $P660s$ converted phases (Chapter 4).

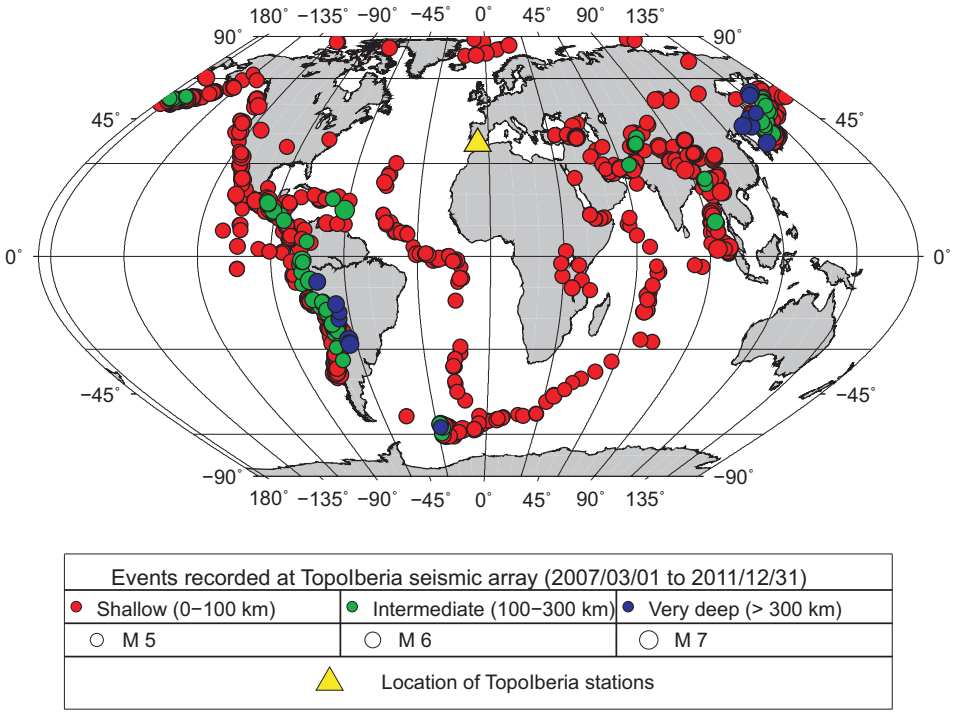

Figure 3.2: Worldwide map showing the selected earthquakes from a distance range between 35° and 95° and registered at the TopoIberia stations (before any quality control). The yellow triangle denotes the location of the TopoIberia seismic network.

3.2 Data selection

We selected events from the TopoIberia data base, with epicentral distances between 30° and 90°, and a magnitude mb between 5.5 and 7.5 for a time period of 5 yr (from January 2007 to December 2011). The epicentral distance range excludes the 410 and the 660 triplication and the P-wave path through the core-mantle boundary and D" region. The magnitude range includes events with sufficient energy to detect the converted phases but avoids complicated and long source-time functions from very large earthquakes. This data set consists of 1044 teleseismic earthquakes registered in 259 broad band stations from the IberArray network. As the stations were not simultaneously active, not all the events were recorded in all the stations. Fig. 3.2 shows the worldwide distribution of the selected earthquakes and the grey bars in

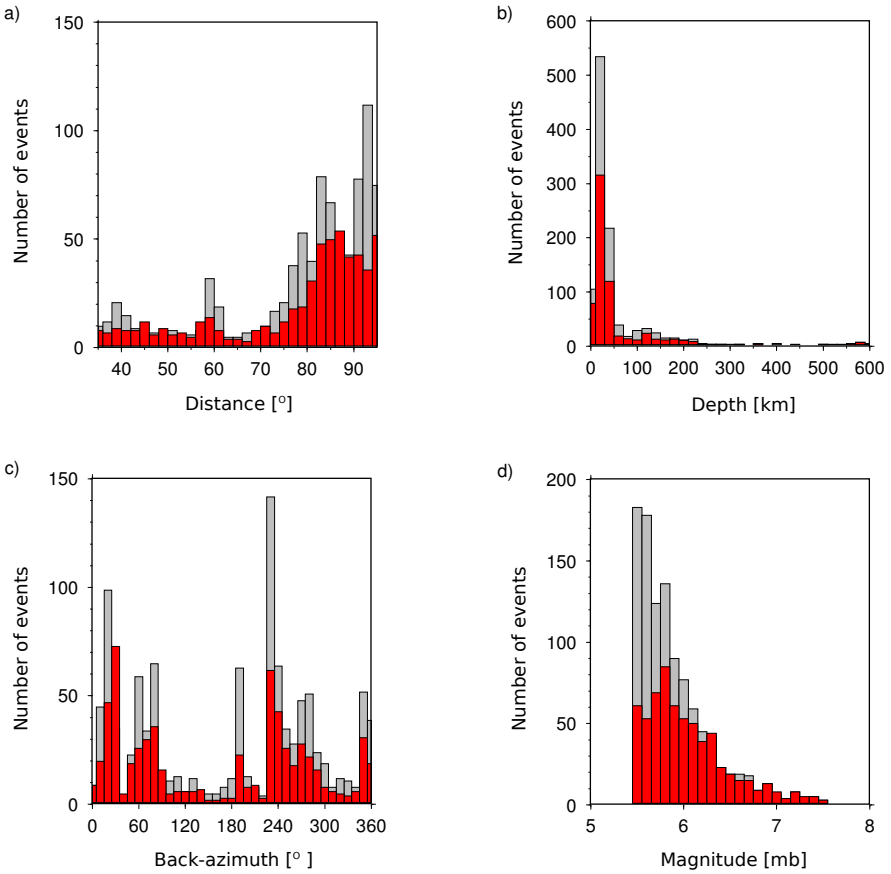

Figure 3.3: Histograms of earthquake (a) distance, (b) depth, (d) back-azimuth and (c) magnitude. The grey bars correspond to the initial data set and the red bars to the final data set after quality controls over Z and R components.

Fig. 3.3 show the corresponding histograms of distance, depth, back-azimuth and magnitude. The majority of events came from epicentral distances larger than 65° and from back-azimuths mainly in the southwest-northeast direction.

3.3 Processing and final data set

The three components of each seismogram were rotated into the ZRT coordinate system and decimated to lower the sample frequency to 10 sps. The rotated components were band-passed filtered in the frequency range 0.03-0.2 Hz. The choice of

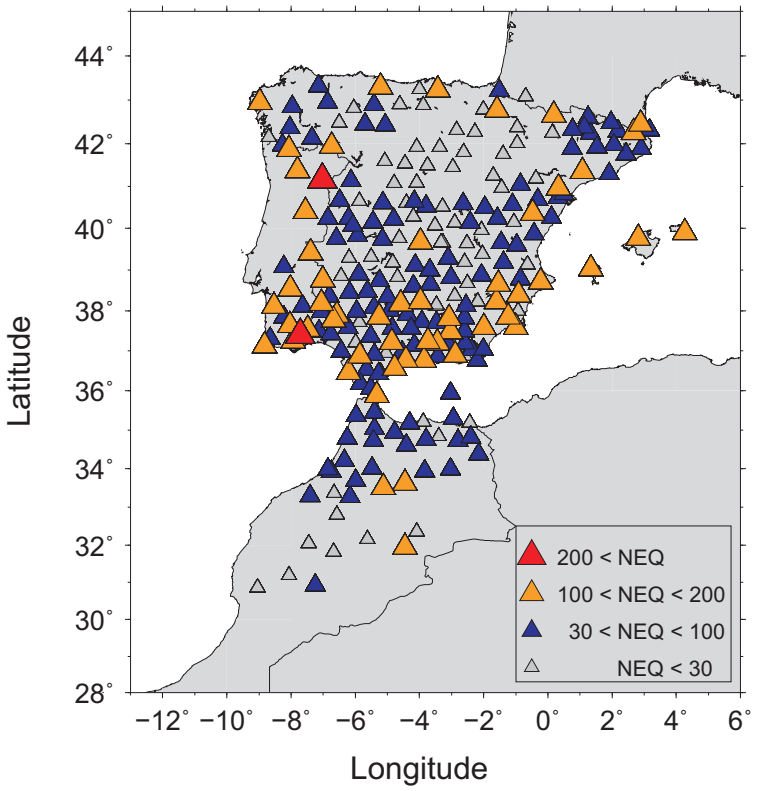

Figure 3.4: Stations with number of events (distance range: 65° to 95°) which passed the quality control over Z and R components. Different colours and triangle sizes are used to discriminate between stations with different number of events. These, are specified in the box at the bottom right.

the frequency band was based on the reported sharpness of the 410 and 660 (4-10 km thick) (Collier et al., 2001; Vidale et al., 1995; Benz and Vidale, 1993; Paulssen, 1988). If we use the rule of thumb, which posits that only significant energy is converted from discontinuities thinner than one-half of the P-wavelength (Bostock, 1999), all the frequency components of the P-wave larger than 0.5-1 Hz which are converted at the 410 and 660 would not have sufficient energy to provide a detection.

An STA/LTA algorithm (Withers et al., 1998) was used to perform a quality control and for an approximate first arrival time picking on the Z components to define the start time of the pilots. We used a 10 s window to compute the STA and a 100 s window to compute LTA. Data with $\{STA/LTA\}_{max} \leq 4$ were rejected, where

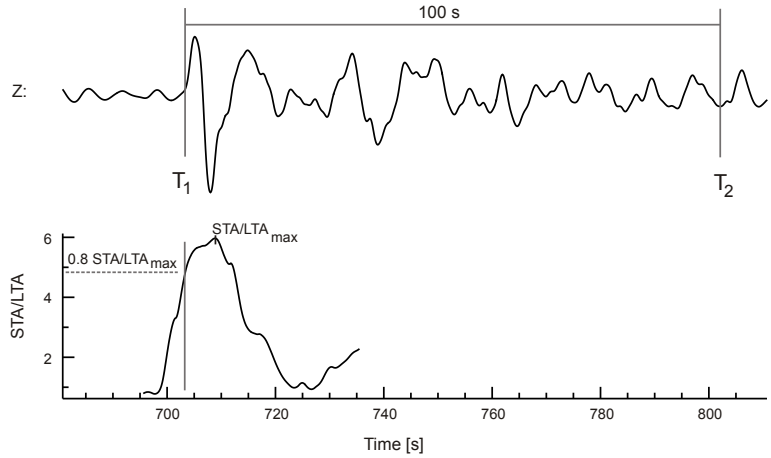

Figure 3.5: Example of a good quality Z component. Top: real data example of a filtered Z component in 0.03-0.2 Hz, which passed the quality control. T_1 and T_2 indicate the begin and end time of the pilot wavelet, P_Z. Bottom: the corresponding STA/LTA time series. STA/LTA_{max} is the maximum amplitude ratio, while "0.8 STA/LTA_{max}" denotes the STA/LTA amplitude used to define T_1. We used an STA window of 10 s and an LTA of 100 s.

$\{STA/LTA\}_{max}$ is the maximum amplitude ratio. Then, the events were visually inspected to check the quality of the R components. We discarded the events with low SNR in the R component and those with a P-wave amplitude in R larger than for the corresponding Z component. The red bars in Fig. 3.3 (a), (b) and (c) show the epicentral distance, depth, and back-azimuth distributions for the data set that passed all the quality controls. The majority of these events correspond to epicentral distances larger than 65° (509 earthquakes from a total of 621). As shown in Fig. 2.4 (in Chapter 2), the upper mantle conversions for earthquakes with distances smaller than 65° suffer from interference with other phases. Therefore, we finally used the teleseismic events in the distance range between 65° to 95°. The map on Fig 3.4 schematically shows the number of earthquakes recorded at each station, which are summarized in Table D.1 (in Appendix D). It can be appreciated that the number of events per station is very heterogeneous in the entire study area.

The begin time of the pilot in the Z component was defined as the time where the STA/LTA amplitude reaches 80 % of the $\{STA/LTA\}_{max}$; this is denoted as T_1 in Fig. 3.5. Then, a 100 s pilot was extracted automatically from the Z components.

As the approaches used to perform the converted phases detections are based on cross-correlation techniques, a very accurate start time of the pilot is not required since it does not affect the position in time of the correlation maxima.

3.4 Building of correlograms and receiver functions

We used the 509 good-quality teleseismic events located between 65° and 95° epicentral distances to compute the correlograms and RFs. This distance range practically ensures vertical incidence and reduces interference with other phases. A pilot wavelet was extracted from the filtered Z components, and the PCC and CCGN were performed between each pilot and the corresponding R component. Then, RFs were computed for the same data set using the water-level deconvolution with a water-level parameter of 0.1. A cosine taper filter was used to attenuate artifacts due to discontinuities at the ends of the pilot. Deconvolution was performed in the spectral domain (see Appendix A).

Although the three techniques are suited to detect P-to-s converted energy from the 410 and 660, individual RFs and CCGNRs in our data set have usually better SNR than PCCRs. Fig. 2.13 (in Chapter 2) show individual PCCRs, CCGNRs and RFs sorted by their back-azimuth for a subset of stations from the TopoIberia data base. These are representative results which show that the signal identification in the time-back azimuth sections of PCCRs is more difficult than in the CCGNRs or RFs sections.

We applied independent quality controls over individual RFs and PCC- and CCGN-correlograms. These controls were based on SNR which was defined as the rms ratio of the absolute amplitudes in a 30 s window before and after the P phase arrival in the corresponding PCCR, CCGNR or RF. Columns 6, 7 and 8 in Table D.1 (in Appendix D) show the number of PCCRs, CCGNRs and RFs which have passed the quality control. In general, the number of RFs (8819) is larger than the number of CCGNRs (8085) and PCCRs (8027).

Fig. 3.6 shows the piercing points of P-to-s conversions at a discontinuity at 510 km depth obtained with the 8085 event-station pairs used to compute the CCGNRs. This figure illustrates the approximate region in the upper mantle sampled by $P410s$ and $P660s$ phases. Piercing point locations for PCCRs and RFs are very similar to

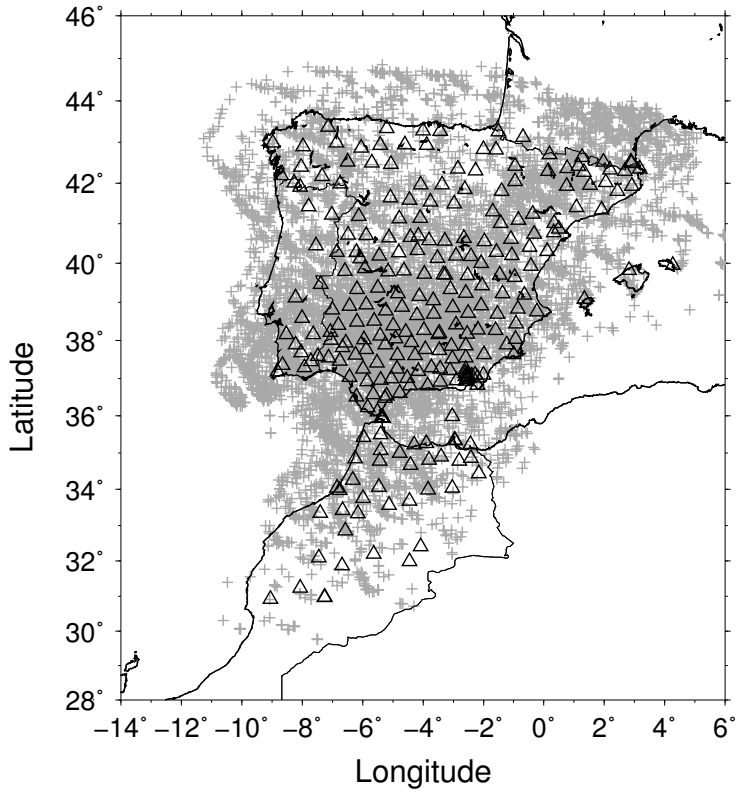

Figure 3.6: $P510s$ piercing points (gray crosses) in the Iberian Peninsula and north Morocco for the teleseismic events located between 65° and 95° of epicentral distance. Black triangles show the station locations.

Fig. 3.6. The number of piercing points is larger in south Spain and its surroundings, while the rest of the area presents a few less abundantly covered parts, such as the north of Spain or the central part of Morocco, which is mostly due to the different station deployment time during the selected time interval of the IberArray data base.

3.5 Data consistency

In this section, the whole data base is used to identify the upper-mantle conversions on the R component arriving in the relative travel time interval between 25 s and 85 s. Additionally, the data consistency is investigated when the frequency band of the

filters and the pilot length change.

3.5.1 Frequency

PCC- and CCGN-correlograms and RFs were computed after filtering the whole data set in three frequency bands with increasing frequency range (0.02-0.12 Hz, 0.03-0.2 Hz and 0.04-0.5 Hz) and using a 100 s long pilot. Linear time corrections were applied using the reference slowness for the $P510s$ phase at 80° distance and all the positive peaks of PCCRs, CCGNRs and RFs were saved. These peaks constitute potential detections of converted phases, since for the predicted upper-mantle conversion it is expected that P (in the Z component) and Pds (in the R component) have the same polarity. Fig. 3.7 shows the number of positive peaks per 1-s time interval as function of relative time for each of the three techniques. The abscissa has been normalized by the maximum number of peaks extracted from the highest frequency band in the time interval 25-85 s to allow the comparison of results among the different frequency bands. The mean value of peaks in the same interval has been subtracted to eliminate the offset (in the abscissa) due to the increasing density of maxima in individual PCCRs, CCGNRs and RFs for increasing frequency range. Note that all maxima were used regardless their coherence or amplitude value. We did not use the coherence or amplitude values because these are very similar for all the peaks in individual PCCRs, CCGNRs and RFs. It is the relative number of coherently stacked maxima which would provide the signal detection while the influence of the coherence or amplitude value is smaller. This is a conclusion that may be easily drawn from the observation of Figs 2.13 and 2.14 (in Chapter 2). In Fig. 3.7, different line styles are used to discriminate the results from the three frequency bands: continuous (0.02-0.12 Hz), dotted (0.03–0.2 Hz) and dotted-point (0.04–0.5 Hz). Besides, vertical lines mark the theoretical arrival time of $P410s$ (42.8 s) and $P660s$ (65.8 s) at 80° epicentral distance for the reference model AK135. The number of positive peaks for the three techniques shows two maxima which are consistently seen in the three frequency bands and which correspond to the $P410s$ and $P660s$ phases. For the three techniques, the number of peaks near the $P410s$ phase does not seem to depend much on the frequency band. Thus, the number of potential detections of $P410s$ in individual records does not increase or decrease with the frequency band. On the other hand, the number of peaks for the $P660s$

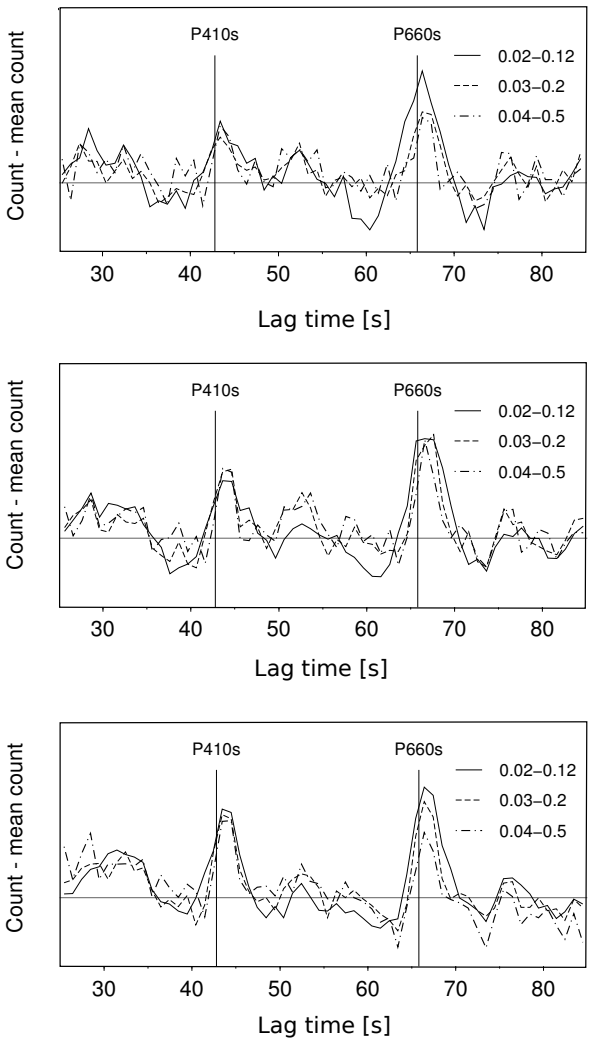

Figure 3.7: From top to bottom: number of positive peaks per 1-s time interval in PCCRs, CCGNRs and RFs as function of relative time and using different frequency bands. The values were normalized with the maximum number of peaks in the time interval 25-85 s and the mean value of peaks in the same interval was subtracted. Vertical lines mark the theoretical arrival time of $P410s$ (42.8 s) and $P660s$ (65.8 s) at 80° distance for the reference model AK135. The horizontal line corresponds to the mean value of peaks per 1-s time interval. Different line styles are used to discriminate between results from different frequency bands: continuous (0.02-0.12 Hz), dotted (0.03-0.2 Hz) and dotted-point (0.04-0.5 Hz).

phase presents differences among the three techniques and frequency bands. While the number of peaks for the PCC and RFs seems to have a frequency dependence (for lower frequencies we counted more peaks near $P660s$), the CCGN shows similar number of peaks for the three frequency bands. Other maxima in these figures, such as those before $P410s$, after $P660s$ and between both phases could correspond to other known converted phases, such as $P300s$, $P510s$ and other less known phases such as the conversions beneath the 660 discontinuity.

3.5.2 Pilot length

We have investigated the number of potential detections which result from using different pilot lengths. In this way, we have plotted analogous results for the intermediate frequency band, 0.03-0.2 Hz, and three different pilots of 25 s, 50 s and 100 s duration. The results are depicted in Fig. 3.8. Here, the subtraction of the mean is not needed because the number of peaks does not change much with the pilot length. The number of positive peaks exhibits two maxima, consistently seen for the three pilot lengths and near the relative times of the corresponding theoretical phases. In general, the number of positive peaks near $P410s$ and $P660s$ for the PCC and CCGN does not depend much on the pilot length. However, the RFs show that the largest pilot presents the smallest difference between the number of peaks near $P410s$ and $P660s$.

3.6 Discussion and conclusions

The number of records that remain after the quality controls is significantly smaller than the number of events in the original data set. This is not unexpected because the useful data always corresponds to a small percentage of the available data (e.g. Shearer, 1991; Mancilla et al., 2012). The increasing number of stations in local and regional networks turns to be a great advantage because it permits to exploit the great potential of the useful records. The 259 stations that we use provide a vast volume of data which leads to an unprecedented data coverage for the study of the 410 and 660 discontinuities and the TZT beneath the Iberian Peninsula and Morocco.

The analysis with the three different frequency bands (Fig. 3.7) suggests that the lowest frequency band (0.02-0.12 Hz) is the more adequate to perform the processing of the entire data set since two of the three techniques show a higher number of

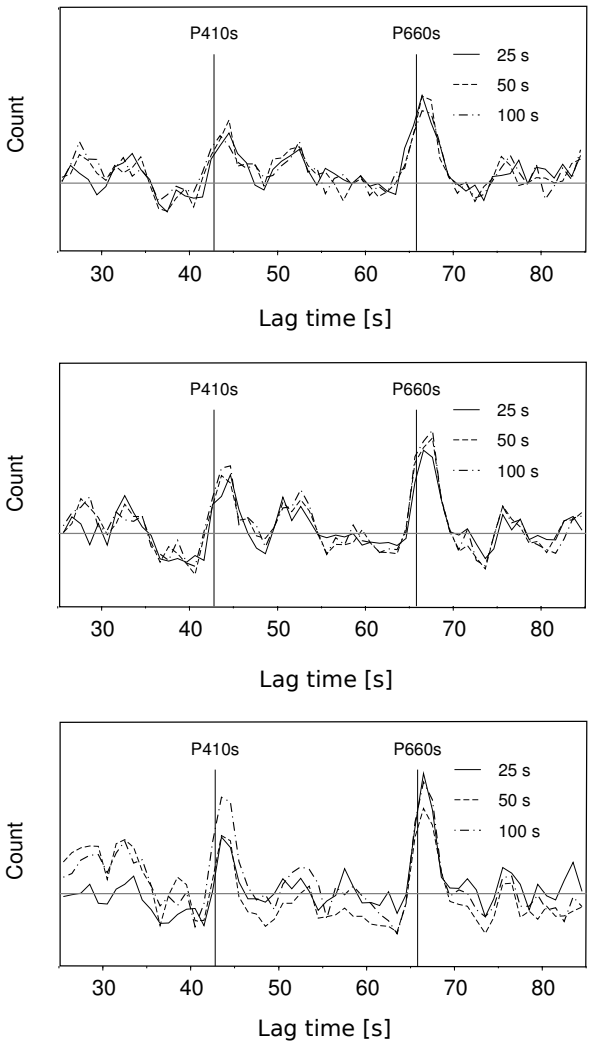

Figure 3.8: From top to bottom: number of positive peaks per 1-s time interval in PCCRs, CCGNRs and RFs as function of relative time as obtained when different pilot lengths are used. The values were normalized with the maximum number of peaks in the time interval 25-85 s. The horizontal line corresponds to the mean value of peaks per 1-s time interval. Different symbols are used to discriminate between results from different pilot lengths: continuous (25 s), dotted (50 s) and dotted-point (100 s).

signals in the lower frequency band. However, the number of detections near $P410s$ and $P660s$ for the three frequency bands and techniques is considerably larger than for other time intervals. This enables us to conclude that any of the three frequency bands proves to be a good choice. This result permits us to base our choice of frequency band on other important aspects, such as time-slowness resolution and spatial resolution. The higher frequency bands are more adequate to better constraint the $P410s$ and $P660s$ detections in time and slowness. On the other hand, the spatial resolution is also related to the frequency band. The spatial resolution is controlled by the size of the first Fresnel zone. This zone comprises the area where the elementary waves that belong to the same wave-front interfere with each other constructively, which in practice is defined as the area where the travel paths differ by less than a half period (Sheriff, 1996). The Pds signal is formed within the first Fresnel zone, which depends on the frequency of the signal and the depth of the discontinuity, d. The first Fresnel zone for the $P660s$ phase at a depth of 660 km is a circular area with a radius of about 100 km for the frequency band 0.03-0.2 Hz and of about 60 km for 0.04-0.5 Hz. This is so, if we consider that constructive interference occurs over travel paths that differ by $T/6$ (T is the period which corresponds to the central frequency of the frequency band). The corresponding radius of the first Fresnel zone for the $P410s$ phase at a depth of 410 km is about 70 km for 0.03-0.2 Hz and 50 km for 0.04-0.5 Hz. Thus, in the frequency band 0.03-0.2 Hz, the 410 (and 660) depth obtained with a P-to-s conversion corresponds to a circular area of about 70 km (100 km) which is also the approximate spatial resolution.

Additionally, the number of peaks near $P410s$ and $P660s$ for PCC and CCGN does not show strong dependence on the pilot length choice. However, we have seen that for the RFs the smallest differences between the number of detections near $P410s$ and $P660s$ is obtained with the largest pilot. In line with this observation, in Chapter 2 we have shown that clear signal detection is obtained with a pilot sufficiently large to contain the depth phases. Thus, we consider that the 100 s pilot is the more adequate pilot length to perform the data processing. In general, for both analyses (frequency and pilot length) we have seen that the number of signals near $P660s$ is always larger than near the $P410s$.

An interesting feature in Figs. 3.7 and 3.8 is the striking time shift of the number of peaks near the $P410s$ and $P660s$ phases with respect to the reference values. This is probably due to a not considered velocity structure beneath the study area.

Such effect can be minimized by applying time corrections based on realistic velocity models for the study area.

4

Transition zone discontinuities beneath Iberia and Morocco

4.1 Introduction

In the general introduction of this thesis, we explained the importance of studying the Earth's discontinuities. They relate seismological observations to the Earth's thermal and chemical state with a precision that cannot be achieved by tomography studies. In particular, the study of the TZT, and the 410 and 660 discontinuities provide additional constraints on the upper-mantle thermal structure and composition.

Here, we map the 410 and 660 discontinuities through detection of P-to-s converted phases and we estimate the TZT beneath the Ibero-Maghrebian region. Our analysis is based on the extraordinary dataset obtained from 259 broad band stations mostly deployed by the TopoIberia project (Díaz et al., 2009). In this study we present the first detailed maps for the 410 and 660 discontinuities and the TZT in the Ibero-Maghrebian region. Our analysis permits us to provide constraints on the present-day upper-mantle thermal structure and composition beneath the study area. We relate our results with the tomographic images by Villaseñor et al. (2003) and with the most recent tomography results by Monna et al. (2013) and Bezada et al. (2013). We further explore evidences (independent of tomography) of the location of the Alboran Sea slab at TZ depths and its possible relation with the occurrence of deep localized earthquakes in this area (Buforn et al., 1995, 2011; Bezada and Humphreys, 2012).

4.2 Data and method

Our data set has been extracted from the TopoIberia data already described in Chapter 3. It is composed of 1044 events from epicentral distances between 30° and 90°. Of these, 509 events of distances between 65° and 95° have been used to carry out the final processing. The selection of events is based on the SNR in the Z component and on the subsequent visual check of the R component.

In order to map the 410 and 660 discontinuities in the Iberian Peninsula and Morocco, $P410s$ and $P660s$ phases are detected in the seismic records using three independent techniques (PCC, CCGN and RF) (see Bonatto et al. (2013) and Chapter 2 for further details on these techniques and for further references). The joint usage

of the three approaches adds consistency and robustness to our results and helps to bridge observation gaps due to the breakdown of any of the approaches.

Correlograms and RFs are computed following the processing described in section 3.4 (Chapter 3). We analyse 8819 RFs, 8085 CCGNs and 8027 PCCs. To enhance the weak-amplitude P-to-s conversions, we use the PWS (Schimmel and Paulssen, 1997) of correlograms (and RFs) in bins of common piercing point (CPP) areas. The robustness of the detected signals is evaluated using a bootstrap resampling approach (Efron and Tibshitani, 1986). Finally, robust detections are visually inspected and converted to depth through an adequate velocity model.

4.2.1 Stacking of correlograms and receiver functions

In order to stack, the data need to be grouped into bins. The bin size is a trade off between the number of piercing points inside the bin (larger bins contain more piercing points increasing the SNR of the stacks) and the spatial resolution controlled by the Fresnel zone (larger bins average the discontinuity depth over areas which can be larger than the Fresnel zone). The piercing point density depends on the station and event distribution and is variable over the entire study region. The variable piercing point density implies a variable discontinuity visibility, which we account for using adaptive bins of variable size depending on the local number of piercing points. On the other hand, to exploit the high spatial resolution of the converted phases and to avoid signal destruction due to destructive interference, we use bin sizes smaller than the first Fresnel zone of the $P660s$ phase. For the used frequency band, this zone is a circular area with a diameter of about 2° (see Discussion in Chapter 3). The bin sizes vary between 0.8°, 1° and 1.6° width in latitude and longitude and were located every 0.25° in both directions (see schematic example of the bin size and overlap in Fig. 4.1 a). Although the grid step results in variable redundancy, we choose to use a homogeneous grid for a better numerical treatment of the results. Fig. 4.1 (b) shows the location of the centre of each bin. The grid is composed of 1391 bins for PCC, 1396 for CCGN and 1400 for RF. The bin size at each centre location for the CCGN-correlograms is depicted in Fig. 4.1 (c) using different colours to discriminate between bins of different size: blue (0.8° width), red (1° width) and yellow (1.6° width). The number of piercing points per bin which equals the number of CCGN-correlograms to be stacked for each bin is shown in Fig. 4.1 (d). This last

figure shows the available data density and areas where we expect a higher robustness of results due to the higher discretization into independent data bins. The best data coverage is in the southern Iberian region and in the Pyrenees. Analogous figures for the PCC-correlograms and RFs are shown in Fig. 4.2. Small differences in the data coverage are observed when comparing Fig. 4.1 (d), Fig. 4.2 (b) and Fig. 4.2 (d), which, however, do not have a meaningful influence on the results.

For an unambiguous detection of $P410s$ and $P660s$, the data are stacked per bin using the PWS in the time-slowness domain (as shown in Figs 2.3 c and d). The robustness of the measurements is assessed during the stacking as outlined in the following section 4.2.2.

4.2.2 Robustness analysis and quality criteria

A bootstrapping technique (Efron and Tibshitani, 1986) of 21 repetitions has been used to estimate the uncertainties in our relative travel time measurements, $t_{P410s}-t_P$ and $t_{P660s}-t_P$. For each bin we randomly pick the same number of radial correlograms (or RFs) and we perform the stack in the relative time and slowness domain. Finally, we use the 21 stacks to compute mean and standard deviation values of relative travel time and slowness for each detected signal. The signals are identified as positive or negative maxima with amplitude larger than twice the absolute mean amplitude of the stack in the time interval 30–80 s but we only consider the positive amplitude signals, which correspond to the expected polarity for the $P410s$ and $P660s$ phases. This has been done for each bin and processing technique (PCC, CCGN and RF) to assess the robustness of the individual detections per bin.

In order to discard bins with ambiguous $P410s$ and $P660s$ detections, an automatic quality control has been performed by analysing the positive amplitude maxima in the time-slowness stacks. We discard stacks (of PCCRs, CCGNRs or RFs) without signals inside the time intervals 36.8-48.8 s and 59.8-71.8 s, and the relative slowness interval of $\pm$ 0.4 $s/^\circ$. These time intervals are defined as $\pm$ 5 s from the $P410s$ and $P660s$ relative times in AK135 (Kennett et al., 1995) for a reference distance of 80°, which are 42.8 s for $t_{P410s} - t_P$ and 65.8 s for $t_{P660s} - t_P$. Additionally, we discard signals with bootstrap uncertainty larger than 1.5 s. This time uncertainty corresponds to a depth uncertainty value of about 15 km for the 410 and 660. Finally, the number of bins with stacks that satisfy the automatic quality criterion are

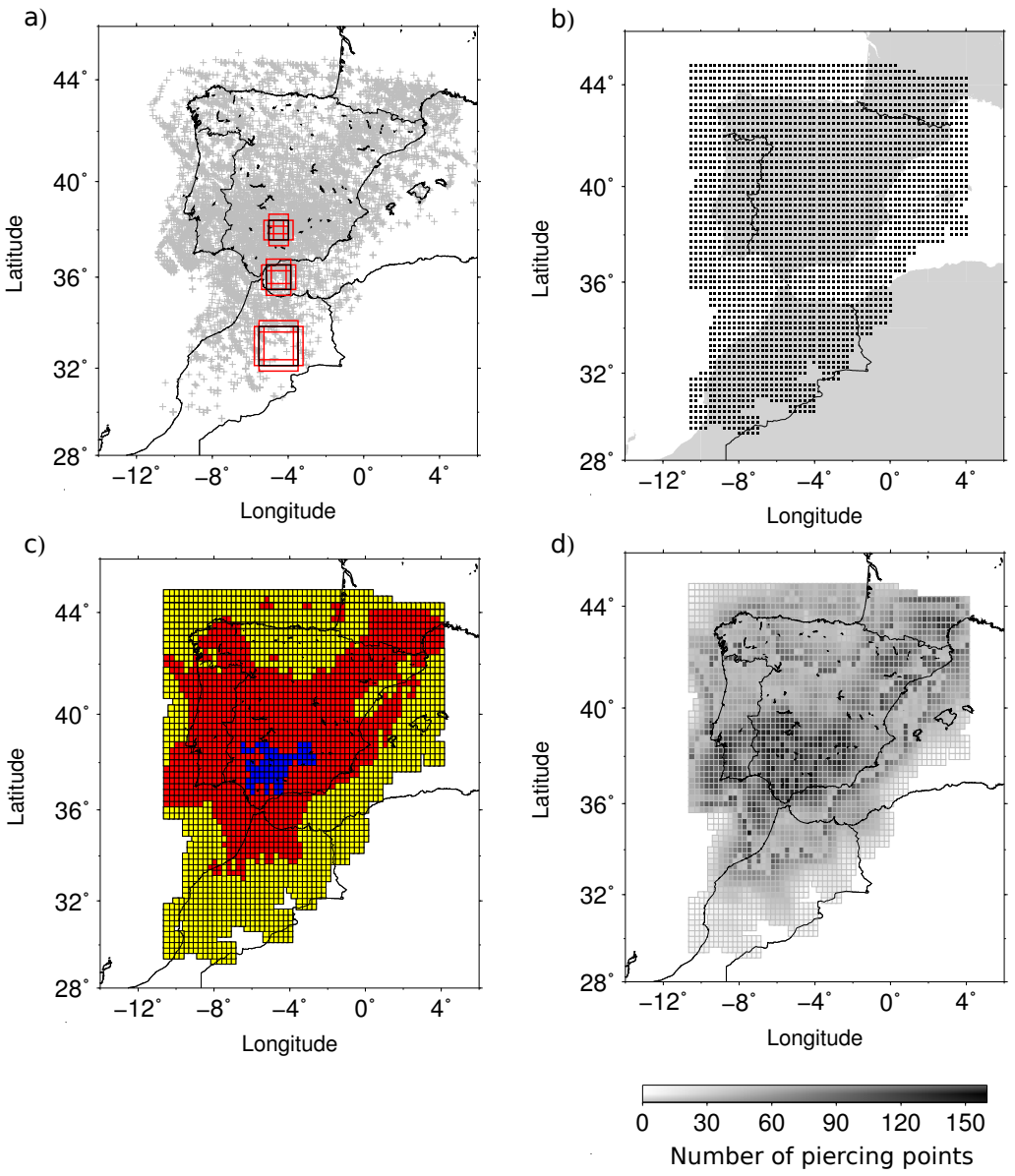

Figure 4.1: a) Schematic example of bin overlap and size. The bins are squares of 0.8°x0.8°, 1°x1° and 1.6°x1.6° width and are located every 0.25° in latitude and longitude. b) Location of the bin centres used to compute the PWS for CPP data. c) Bin size for CCGN-correlograms: *blue* = 0.8° width; *red* = 1° width; *yellow* = 1.6° width. d) Data density for the bins shown in (c). The best data coverage is obtained in south Iberia and in the Pyrenees.

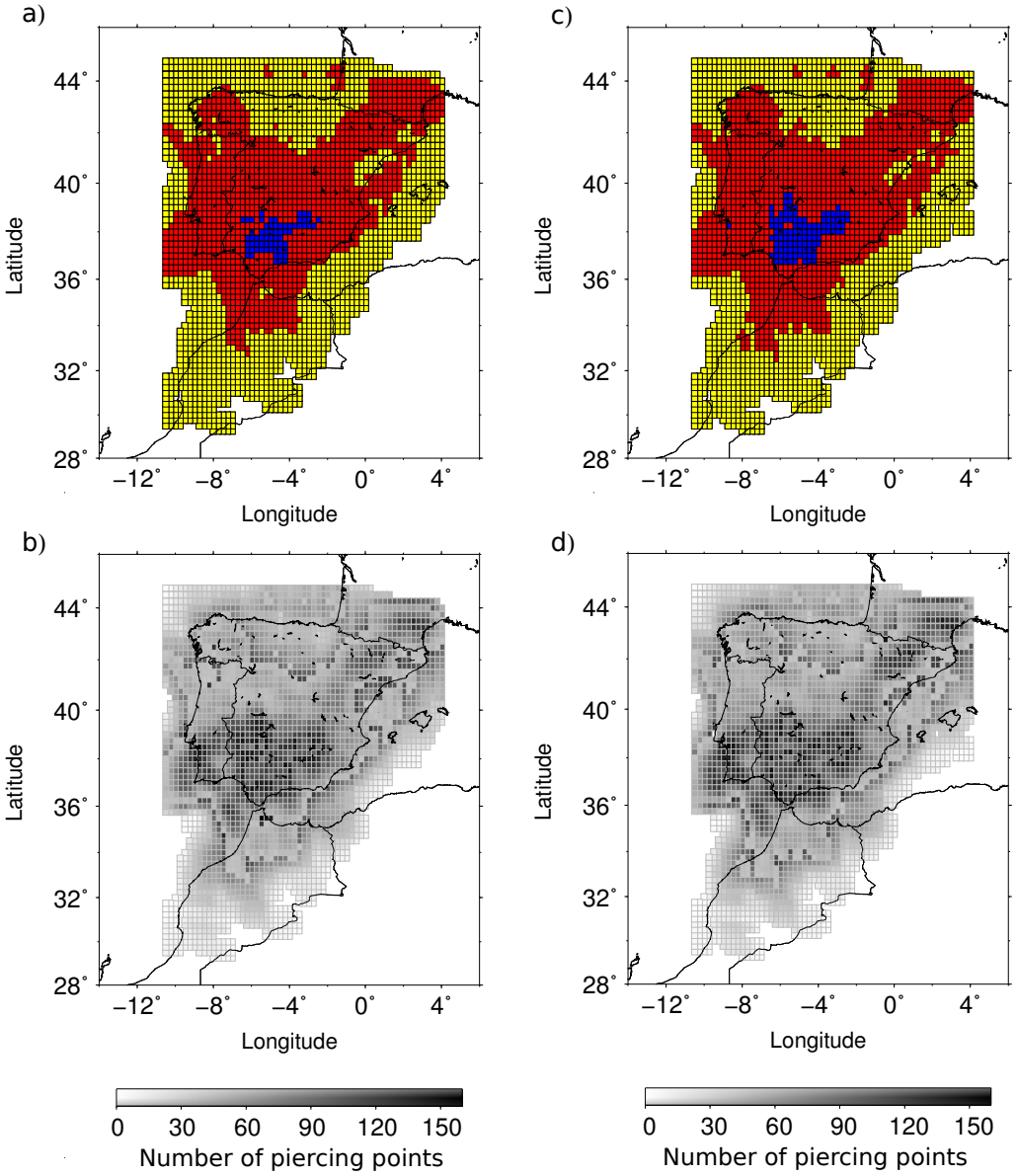

Figure 4.2: a) Bin size for PCC-correlograms: *blue* = 0.8° width; *red* = 1° width; *yellow* = 1.6° width. b) Data density for the bins shown in (a). c) Bin size for RFs. d) Data density for the bins shown in (c).

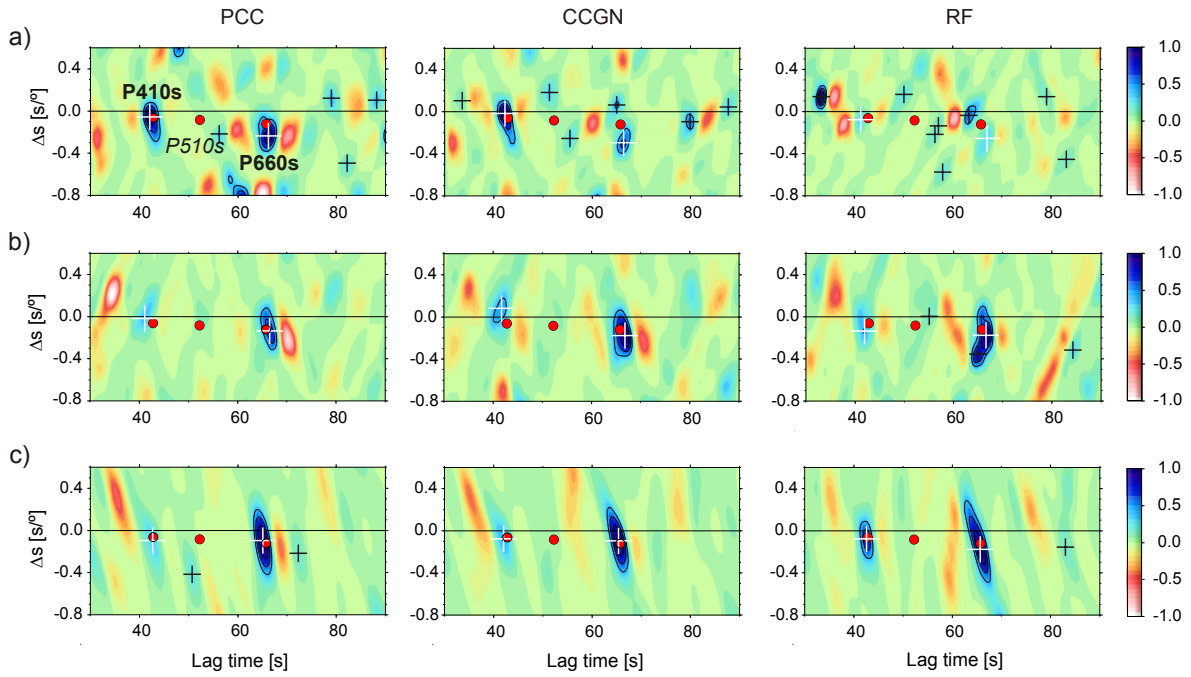

Figure 4.3: Representative examples of PCCR, CCGNR and RF stacks that have passed the quality controls. The central latitude and longitude of the bins are: (a) (37°,0°), (b) (37.75°,−1°) and (c) (42.75°,−1.5°). Red circles mark the theoretical relative travel time and slowness values for the $P410s$, $P510s$ and $P660s$ phases. White crosses show detections of $P410s$ and $P660s$, while black crosses show other positive-amplitude maxima that have passed our detection criteria.

598 for PCC, 809 for CCGN and 850 for RF. Time standard deviation values of the signals inside the time intervals 36.8-48.8 s and 59.8-71.8 s range between 0.09-1.5 s (mean value of 0.5 s) for PCCRs, between 0.07–1.5 s (mean value of 0.4 s) for CCGNRs and between 0.08–1.5 s (mean value of 0.4 s) for RFs. Most of the stacks that pass the quality controls show only one clear signal near $P410s$ (and/or $P660s$) as it is the case for the stacks of Fig. 4.3 (c). However, some stacks present more than one signal near the reference time of $P410s$ and $P660s$, as shown in Fig. 4.3 (a) for CCGNRs and RFs stack, and Fig. 4.3 (b) for the RFs stacks. Therefore, we perform a visual quality control by inspecting the time-slowness stacks of the three techniques simultaneously in order to decide which of the detected signals is actually the $P410s$ and/or $P660s$ phase. The visual inspection also permits to discard data when a clear identification of phases is not possible. In Fig. 4.4, we plot the mean

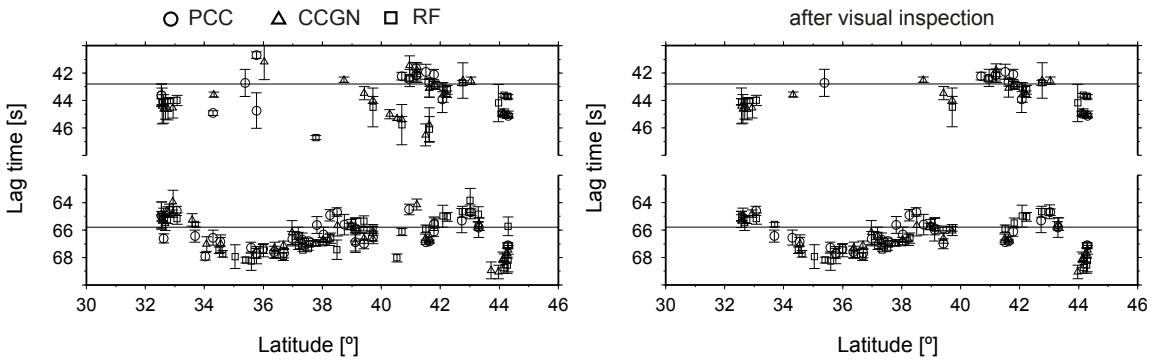

Figure 4.4: Mean and bootstrap uncertainty values of relative travel time measurements along a north-south profile at longitude $-2.5°$. Left panel: all the detected signals that satisfy the automatic quality controls. Circles, triangles and squares mark the mean relative time values for $P410s$ and $P660s$ phases identified in the PCCR, CCGNR and RF stacks, respectively. Thin lines indicate the relative times in model AK135. Right panel: same as left panel but after an additional visual inspection to exclude less reliable detections.

values of relative time measurements along a north-south profile at $-2.5°$ longitude, after the automatic quality control (left panel) and after the additional visual inspection (right panel). The figure illustrates the importance of the visual inspection to clean the profile from ambiguous detections.

Note that in Fig. 4.3 the red circles mark the theoretical relative travel time and slowness values for the $P410s$, $P510s$ and $P660s$ phases in AK135. As the 510 is not a first order discontinuity in AK135, we included this discontinuity in AK135 by introducing an imperceptible increase in the density at a depth of 510 km.

4.2.3 Integrated detections and depth conversions

The joint usage of the independent approaches permits us to stabilize the detections against measurement errors, to use the measurement variability as a robustness indicator and to bridge observation gaps (see Bonatto et al. (2013) and Chapter 2 for further details on these techniques and for further references). Thus, we merge the independent Pds (d=410 or 660) detections from each bootstrap repetition for each

of the three techniques. This way, we obtain new mean and standard deviation values for the relative travel times $t_{P410s} - t_P$ and $t_{P660s} - t_P$ at each latitude-longitude bin.

Absolute 410 and 660 depths are conditioned by the velocity model used to perform the depth conversion of the estimated mean relative travel time values. Thus, in order to convert travel times to discontinuity depths accurate v_p and v_s models are needed for the upper mantle beneath the study area (the lower mantle anomalies do not affect the depth estimates due to the reference phase with common wave path below the discontinuity). Seismic tomography models can be used to estimate time corrections, which, however, should be used with caution. Blurred not well localized anomalies and inversion artifacts will introduce errors to the travel time corrections. Furthermore, seismic velocity anomalies are often underestimated inherent to the regularization of tomographic inversions.

Here, we use the P-wave tomography model by Villaseñor et al. (2003) to account for volumetric seismic velocity anomalies beneath the study area and to correct the estimated relative travel times before depth conversion. For this purpose, we compute average 1-D P-wave velocity profiles for 2°x2° bins centred at the central latitude and longitude of each CPP bin. Corresponding S-wave velocity profiles are derived from the P-velocity anomalies, δv_p, by employing a constant factor $\delta v_s / \delta v_p$ =1.5. This factor typically ranges between 1.5 and 2 in the upper mantle (Ritsema and Van Heijst, 2002), depending on the type of anomaly (thermal and/or compositional). The scaling of localized P- or S-wave velocity models is often used to perform RF time corrections (Duecker, 1997; Li et al., 2002; van der Meijde et al., 2005). We compute time corrections (between the arrival times predicted by the local velocity model and AK135) to correct the relative travel time measurements of $P410s$ and $P660s$. Finally, the corrected time values are converted to depth using AK135. A more accurate depth correction is not performed due to the not yet totally resolved upper-mantle velocity structure beneath Iberia and Morocco. The time corrections are shown in Fig. 4.5 (a) for the $P410s$ phase and in Fig. 4.5 (b) for the $P660s$ phase. Note that these are positive in the Alboran Sea area to compensate the measured relative travel times, which are smaller due to the presence of positive P-velocity anomalies. The time corrections, which are added to the observations with the corresponding sign shown in Fig. 4.5, are between -1.2 to 0.3 s for the $P410s$ phases and between -1.2 to 0.6 s for the $P660s$ phases. These time corrections translate to depth corrections of about -12 km to 6 km. Changing the applied constant velocity perturbation ratio $\delta v_s / \delta v_p$

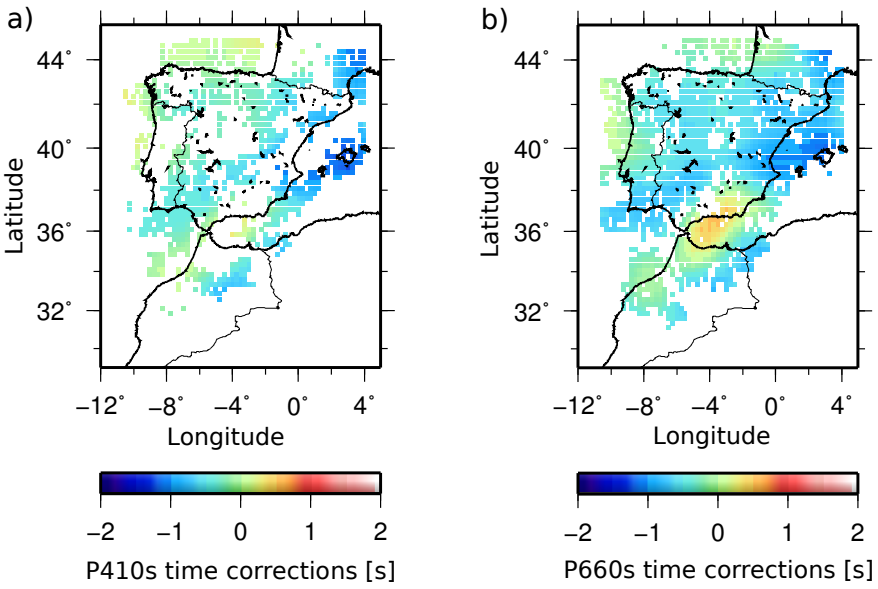

Figure 4.5: Travel time corrections computed using P- and S-wave velocity profiles derived from the P-wave tomography model by Villaseñor et al. (2003). a) $P410s$ corrections and b) $P660s$ corrections.

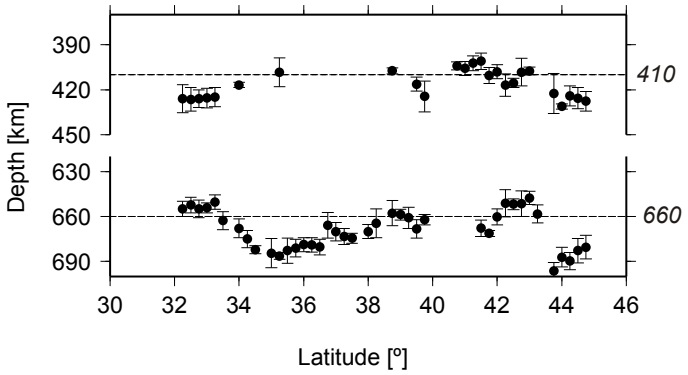

Figure 4.6: Mean and uncertainty values of 410 and 660 depths along the north-south profile at longitude −2.5° (same profile of Fig. 4.4), after time correction. Where possible we use three independent approaches (PCC, CCGN and RF) to estimate the plotted values. Circles mark the discontinuity depths obtained for each location along the profile, without distinguishing between techniques. Thin lines indicate the nominal depths of 410 km and 660 km for the corresponding discontinuities.

=1.5 to 2 leads to high end depth corrections for the P-to-s conversions which are in the order of -18 km to 9 km. Fig. 4.6 shows the final 410 and 660 depth values along the north-south profile presented in Fig 4.4 after averaging the results from the three independent approaches and after time corrections. In this figure, both discontinuities are deeper near 44°, which is probably due to underestimated time corrections.

The distribution of our estimated depth values for the 410 and 660 discontinuities before time corrections is shown in Figs 4.7 (a) and (b) with grey filled bars. Vertical black continuous lines are at 416 km and 669 km and show the average values of the apparent discontinuity depths. After time correction (red unfilled bars), the average depth values move to 412 km and 663 km, which are indicated with red lines and which are closer to the reference values (indicated with grey lines at 410 km and 660 km). Corresponding depth uncertainty values of the 410 and 660 apparent depths are depicted in Figs. 4.7 (c) and (d). These values remain unmodified after time correction. Most uncertainty values are smaller than 8 km for both discontinuities, which means that our depths' uncertainty quality criterion of 15 km (1.5 s) is sufficiently large not to interfere with the significant signal detection. The upper labels in Figs 4.7 (a) and (b) show the predicted temperature variation using Clapeyron slopes of 4 $MPaK^{-1}$ for the olivine-wadsleyite transition (410) (Katsura et al., 2004) and -1.3 $MPaK^{-1}$ for the post-spinel transition (660) (Katsura et al., 2003) (see Discussion for further details).

Note that the blue colour dominates in Fig. 4.5, which means that most time corrections are negative. This is expressed through a negative shift of the apparent depths in Figs 4.7 (a) and (b). This indicates that the tomography-derived velocities are on average lower than the AK135 seismic velocities.

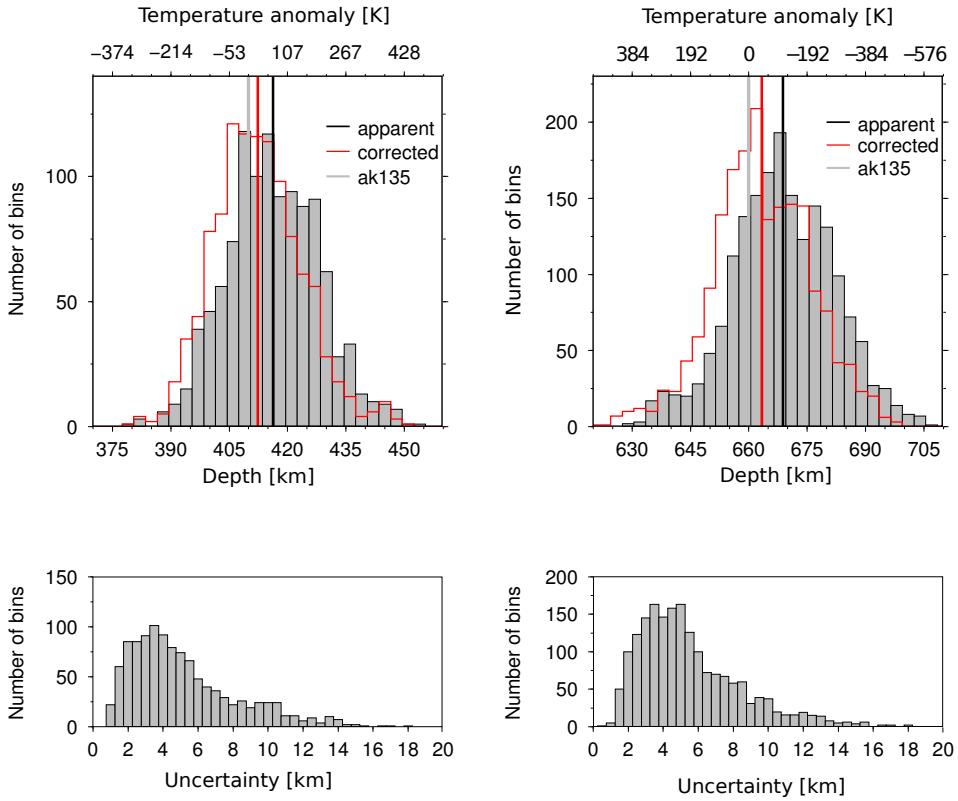

Figure 4.7: Distribution of our estimated (a) 410 and (b) 660 apparent depths (grey filled bars) and corrected depth values (red unfilled bars). Corresponding uncertainty values are depicted in (c) and (d). Discontinuity depths in AK135 are shown with the grey lines. The black continuous lines mark the average apparent depth values of 416 km and 669 km, while the black dashed lines show the average depths of 412 km and 663 km, after time corrections. The bins are 2 km and 1 km wide for figures a, b and c, d, respectively. The upper labels show the predicted temperature variation using Clapeyron slopes of 4 $MPaK^{-1}$ for the olivine-wadsleyite transition (410) (Katsura et al., 2004) and -1.3 $MPaK^{-1}$ for the post-spinel transition (660) (Katsura et al., 2003)

4.3 Results

In this section, we show the measured relative travel times at each CPP bin as well as representative examples of signal detection (and non-detections) in the relative time-slowness domain. Furthermore, we present estimates for the 410 and 660 depths and the TZT in the Iberian Peninsula and its surroundings including north Morocco.

4.3.1 410 and 660 discontinuities

The relative travel time values with respect to AK135, $(t_{P410s} - t_P)_{Obs} - (t_{P410s} - t_P)_{AK135}$, at each CPP bin and their corresponding standard errors, σ (sigma), are shown in Figs 4.8 (a) and (b), respectively. Similarly, Figs 4.9 (a) and (b) show the $(t_{P660s} - t_P)_{Obs} - (t_{P660s} - t_P)_{AK135}$ and σ values at each CPP bin. The time values in Fig. 4.8 (a) and Fig. 4.9 (a) are represented with bins of 0.25°x0.25° and centred at the central latitude and longitude of the corresponding CPP bin. The 410 map in Fig. 4.8 (a) shows several locations without time value. The origin of these gaps is either due to the lack of $P410s$ detections or due to detections of incoherent low amplitude signals which do not satisfy the employed quality criteria. From the time-slowness stacks (Figs 4.10 a and b) we observe that, for some CPP bins, the $P410s$ is very weak and ambiguous, leading to a non-detection. This lack of detection might be due to structural complexities that cause defocusing or loss of coherence and destructive interference with other coda waves. The gap area coincides with the location of the positive P-velocity anomalies related to the Betic-Alboran slab (e.g., feature B in Fig. 4.20), although the anomaly extends over a larger area.

The interpolated discontinuity depths are presented in Fig. 4.8 (c) for the 410 and in Fig. 4.9 (c) for the 660. We use the nearest-neighbour interpolation algorithm from the GMT plotting tool (Wessel and Smith, 1991) to assign an average value to each node that has one or more points within a radius centred on the node. The average value is computed as a weighted mean of the nearest point from each sector inside the search disk, with radius of 300 km. The yellow triangles in Fig. 4.8 (c) show the locations of the active *anorogenic magmatism* (e.g. fig. 2 in Carminati et al., 2012, (our Fig. 4.23)), of sub-lithospheric origin and occurring after the volcanic episodes associated with the subduction (*orogenic magmatism*) (Lustrino and Wilson, 2007; Lustrino et al., 2011). This activity is mainly Pliocene to recent in age. In this context, active means that these volcanoes erupted recently (from a geological point

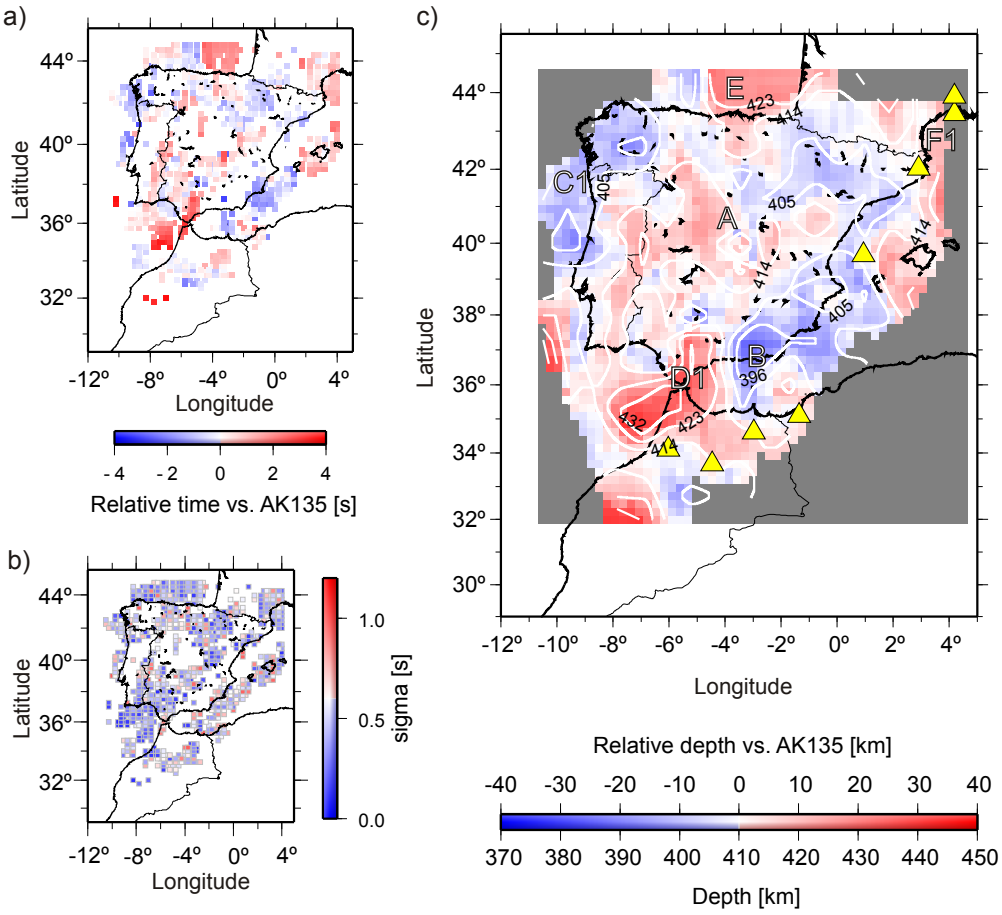

Figure 4.8: **410**. a) $P410s$ relative travel time values with respect to AK135. Each bin is represented with a square of 0.25° width and centered at the central latitude and longitude of the corresponding CPP bin. b) Travel time uncertainty values (sigma) at each location. c) 410 topography constructed using the nearest-neighbour interpolation algorithm over depth values. Areas labeled A-F are features of interest described in the text. The yellow triangles show the locations of the active *anorogenic magmatism* (alkaline magmatism of sub-lithospheric origin) (e.g., Fig. 4.23 (from Carminati et al. (2012))).

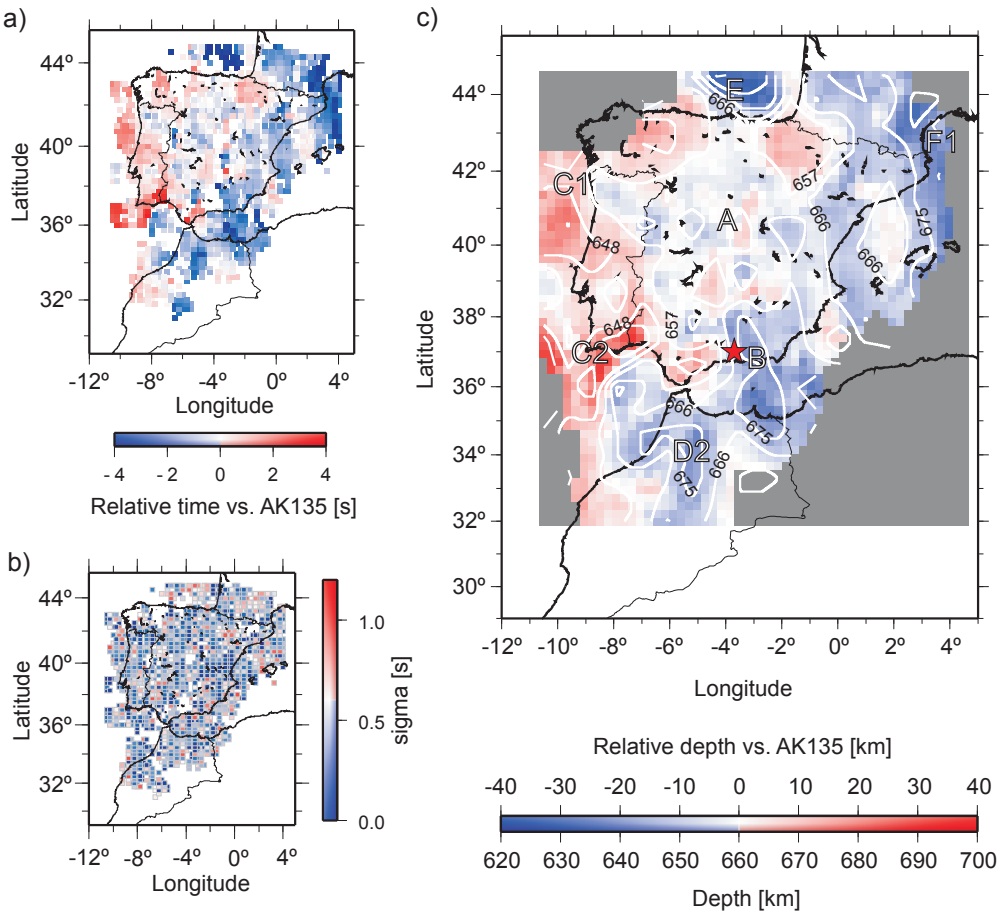

Figure 4.9: **660**. a) $P660s$ relative travel time values with respect to AK135. b) travel time uncertainty values (sigma) at each location. c) 660 topography constructed using the nearest-neighbour interpolation algorithm over depth values. Areas labeled A-F are features of interest described in the text. The red star shows the epicenter of the nest of deep earthquakes beneath Granada (Buforn et al. 2004).

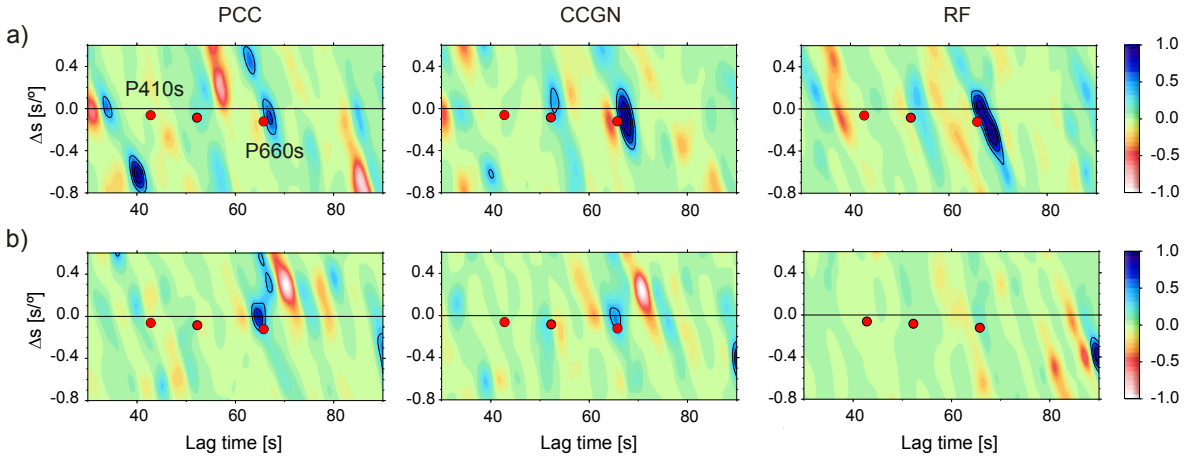

Figure 4.10: Representative examples of **ambiguous or non-detections of the** $P410s$ phase. a) From left to right: stacking of PCCRs, CCGNRs and RFs for a CPP bin located at latitude 40° and longitude 1°. b) Same as (a) but for a CPP bin at latitude 40° and longitude −3°. Red circles mark the theoretical relative travel time and slowness values for $P410s$, $P510s$ and $P660s$.

of view) and could still erupt. Note, that they are all located at the border of areas with a depressed 410. The red star in Fig. 4.9 (c) shows the epicenter of the nest of deep earthquakes beneath Granada (Buforn et al. 2004), which coincides with a transition from depressed to uplifted 660.

The 410 topography shows small depth variations in central Spain of about ±10 km (A in Fig. 4.8 c). In the surrounding areas we observe peak-to-peak variation of about 60 km (excluding the extreme values in Fig. 4.7 a). The 410 is locally uplifted by about 20 km (410 at 390 km) in the Alboran Sea and south Spain (B in Fig. 4.8 c) and in the northwest of Spain is uplifted by about 30 km (C1 in Fig. 4.8 c). In both areas the $P410s$ phase is clearly detected at each CPP bin with at least two of the three techniques, as it is shown in the stacks of Figs 4.11 (a) and (b) for the Alboran Sea and in Fig. 4.12 for the northwest of Spain. The deepest 410 depth values are found in the Gulf of Cadiz, the Strait of Gibraltar and the northwestern part of the sampled Moroccan region (D1 in Fig. 4.8 c). In this area, the 410 is locally depressed by about 30 km. Figs 4.13 (a) and (b), Fig. 4.14 and Figs 4.15 (a) and (b) show representative examples of the detection of $P410s$ in this area. In Fig. 4.16, we show

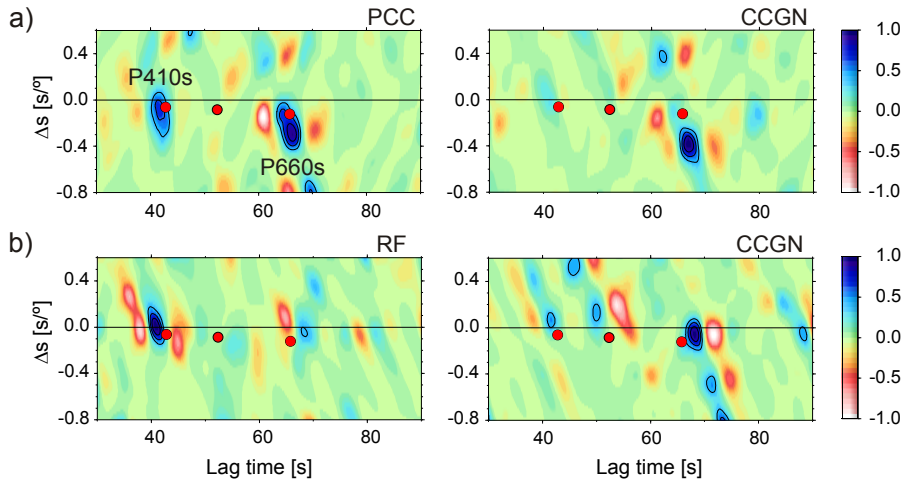

Figure 4.11: Representative examples of stacking results for the **Alboran Sea** (**uplifted 410**). a) From left to right: stacking of PCCRs and CCGNRs for a CPP bin located at latitude 37° and longitude −0.5°. b) Same as (a) but for a CPP bin at latitude 36° and longitude −3°. Red circles mark the theoretical relative travel time and slowness values for $P410s$, $P510s$ and $P660s$.

an example of a CPP stack in the Rif region in Morocco (D1 in Fig. 4.8 c) where the $P410s$ is not detected. We also see a deeper 410 of about 20 km in the north of the Balearic Sea (F1 in Fig. 4.8 c).

In general, the $P660s$ phases are very clear in the stacks of PCCRs, CCGNRs and RFs, as shown in Figs 4.10 to 4.16. The amplitude in these figures are normalized and the visual inspection of maxima is sometimes difficult due to other large amplitude signals which appear in the selected time-slowness window (e.g., in the stacks of CCGN and RF in Fig. 4.10 b at about 88 s and negative slowness). These large amplitude features may cause other signal maxima to appear less pronounced in the amplitude-normalized stacks.

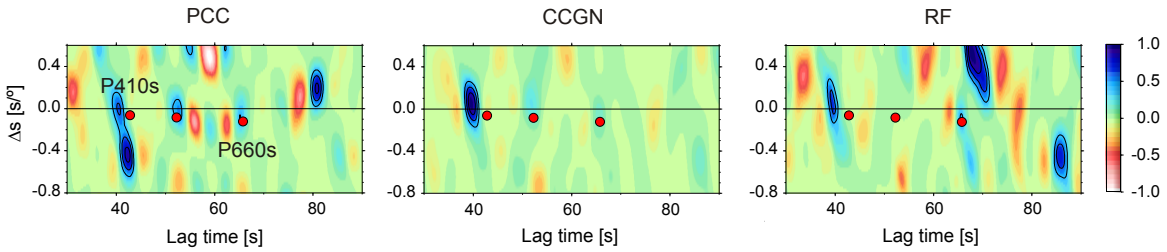

Figure 4.12: Representative examples of stacking results for the **northwest of Spain** (**uplifted 410**). From left to right: stacking of PCCRs, CCGNRs and RFs for a CPP bin located at latitude 43° and longitude −9°. For a reference, theoretical relative travel time and slowness values are marked with red circles for $P410s$, $P510s$ and $P660s$.

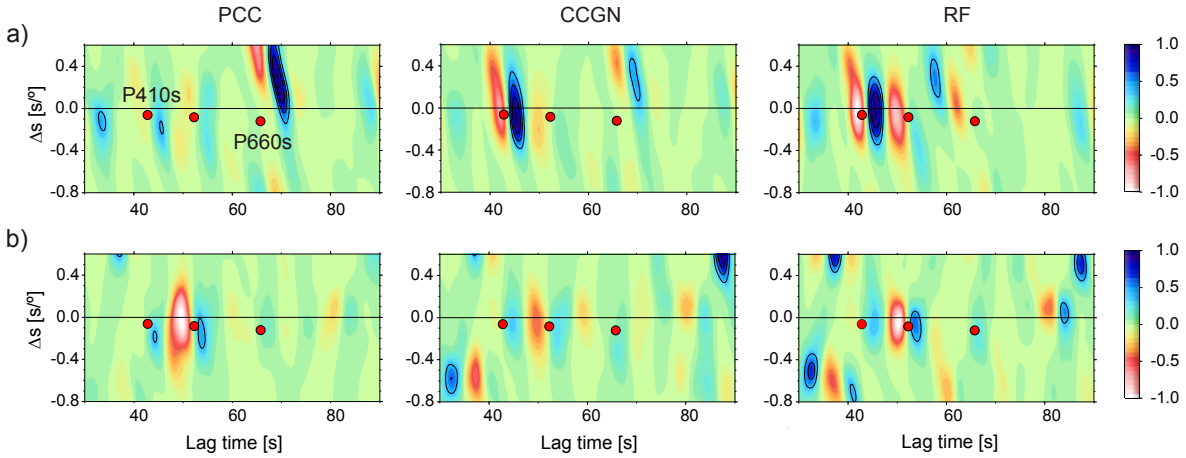

Figure 4.13: Representative examples of stacking results for the **Gulf of Cadiz** (**depressed 410**). a) From left to right: stacking of PCCRs, CCGNRs and RFs for a CPP bin located at latitude 35.5° and longitude −7°. b) Same as (a) but for a CPP bin located at latitude 36° and longitude −7°. For a reference, theoretical relative travel time and slowness values are marked with red circles for $P410s$, $P510s$ and $P660s$.

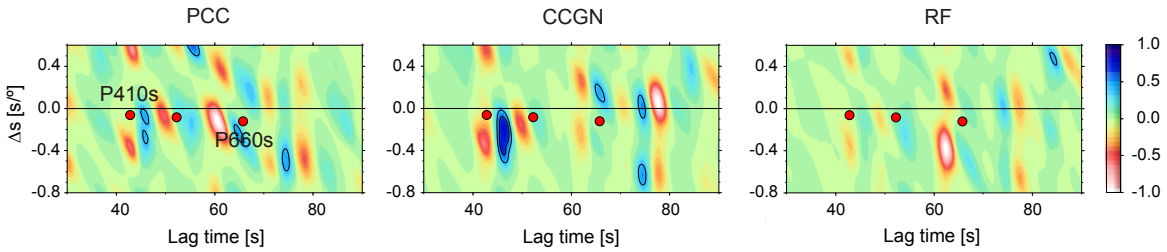

Figure 4.14: Representative examples of stacking results for **western Morocco** (**depressed 410**). From left to right: stacking of PCCRs, CCGNRs and RFs for a CPP bin located at latitude 31.75° and longitude −7.5°. For a reference, theoretical relative travel time and slowness values are marked with red circles for $P410s$, $P510s$ and $P660s$. Detections in the PCC and RF stacks do not pass the automatic control.

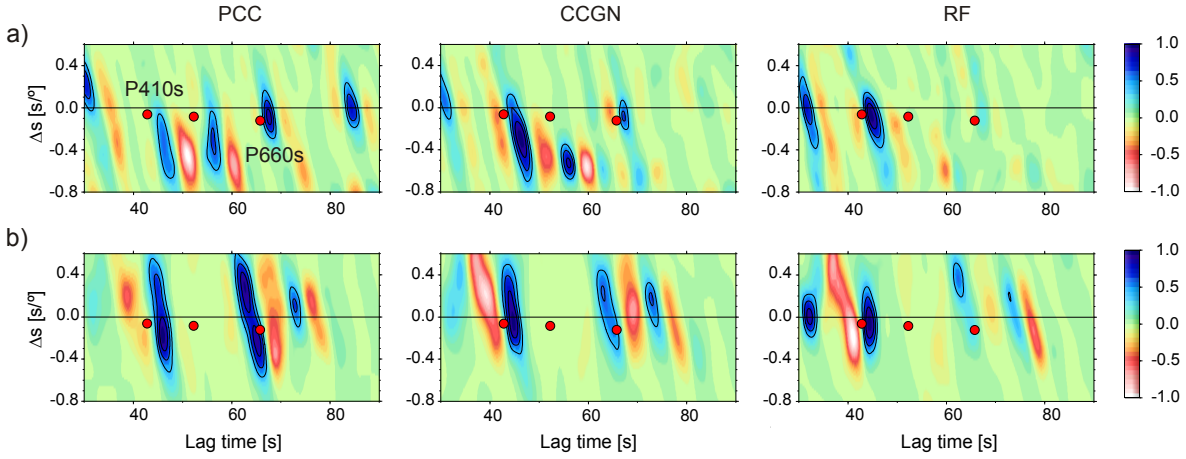

Figure 4.15: Representative examples of stacking results for the **Strait of Gibraltar** (**depressed 410**). From left to right: stacking of PCCRs, CCGNRs and RFs for a CPP bin located at latitude 35.5° and longitude −6°. b) Same as (a) but for a CPP bin located at latitude 36.5° and longitude −5.5°. For a reference, theoretical relative travel time and slowness values are marked with red circles for $P410s$, $P510s$ and $P660s$.

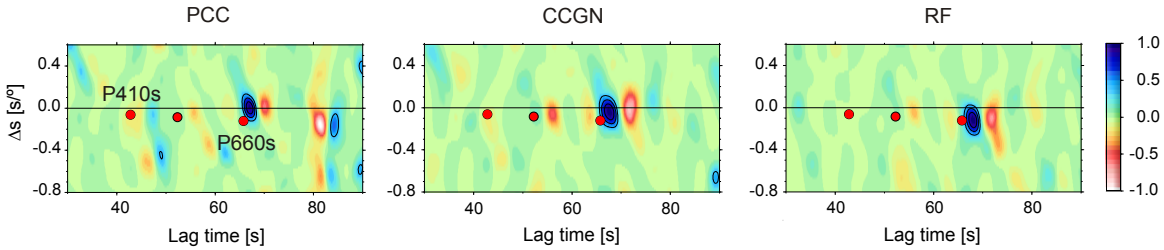

Figure 4.16: Representative examples of stacking results for the **Rif region** (**410 gap**). From left to right: stacking of PCCRs, CCGNRs and RFs for a CPP bin located at latitude 34.75° and longitude −5°. For a reference, theoretical relative travel time and slowness values are marked with red circles for $P410s$, $P510s$ and $P660s$.

The 660 surface has a total peak-to-peak depth range of about 60 km (excluding the extreme values in Fig. 4.7 b). The most prominent feature is a large-scale topographic change from northwest to southeast. Beneath Portugal and the Atlantic Ocean the 660 is elevated by about 20 km (C1 and C2 in Fig. 4.9 c), while it is almost at the reference depth in the central part of Spain with topographic variations of about ± 5 km (A in Fig. 4.9 c). Towards eastern Spain (F1 in Fig. 4.9 c), the Alboran Sea (B in Fig. 4.9 c) and northern Morocco (D2 in Fig. 4.9 c) the 660 is depressed with maximum depth of about 680-690 km. Although features B and D2 are very close, they do not seem to be related; these are considered different features. The 660 depression beneath the Alboran Sea and eastern Spain coincides with the location of two positive P-velocity anomalies, which are related to the Betic-Alboran slab and to the Alpine-Tethys remnant slab (e.g., feature A in Fig. 4.20 and feature A in profiles k to l in fig. A2.2 in Spakman and Wortel (2004)).

4.3.2 Time corrections and the 410 and 660 absolute depths

The 410 and 660 depths can be influenced by the time corrections applied to the measured relative travel time values, $t_{Pds} - t_P$ (d=410, 660), because the upper-mantle anomalies in Villaseñor et al. (2003) that we use to derive the P- and S-wave velocity models are not fully resolved. Indeed, the tomography resolution in Morocco, the Atlantic Ocean and the Bay of Biscay is low due to the poor station coverage in these areas (Villaseñor et al., 2003; Spakman and Wortel, 2004). In central Spain and the southern and eastern coasts of Spain (features A, B, and F1 in Fig. 4.8 and Fig. 4.9), the 410 and 660 depth values are more reliable since the used tomographic model has a better ray coverage in this area and a higher resolution. Nevertheless, the fact that the imaged 410 and 660 depths in Fig. 4.8 (c) and Fig. 4.9 (c) are different from the imaged travel time corrections (Figs 4.5 a and b) strengthens that we are not interpreting structures produced by the corrections. Therefore, although our time corrections bring the discontinuity depth closer to their real depth, improved velocity models would result in more accurate absolute depth values.

4.3.3 TZ thickness

The unknown uncertainties, which depend on the locally variable degree of accuracy of the employed tomography model, are minimized if we consider the TZT rather than the absolute 410 and 660 depth values. Differential travel times $t_{P660s} - t_{P410s}$ are sensitive to variations in discontinuity depths and to 3-D heterogeneities within the mantle TZ, while the influence of the heterogeneities above 410 km depth are removed by the subtraction of travel times. This is true if one assumes that the velocity anomalies equally affect the relative travel times $t_{P410s} - t_P$ and $t_{P660s} - t_P$ or that both ray paths are close enough to be influenced by the same heterogeneities. Consequently, the travel time corrections applied to $t_{Pds} - t_P$ (d=410, 660) do not substantially affect the average value of TZT after time corrections.

The TZT values are computed from the subtraction of the 410 and 660 depths ($TZT = H_{660} - H_{410}$) after interpolation. Fig. 4.17 shows the distribution of TZT before (grey filled bars) and after (red unfilled bars) applying the travel time corrections to the $P410s$ and $P660s$ phases. Before time corrections, the averaged value of the TZT is 252 km, slightly thicker than the AK135 value of 250 km. After time

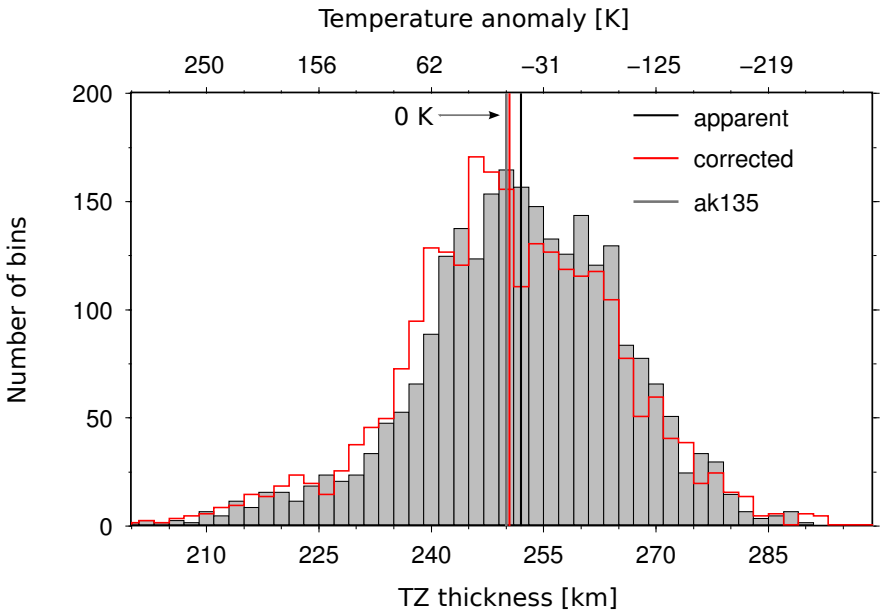

Figure 4.17: Distribution of apparent TZT (grey filled bars) and corrected TZT (red unfilled bars). The black and red lines mark the average apparent TZT of 252 km and the corrected TZT of 250 km, respectively. Histograms were made with 2 km-wide bins. The upper labels show the predicted temperature variation inside the TZ using the corresponding Clapeyron slopes for the 410 and 660.

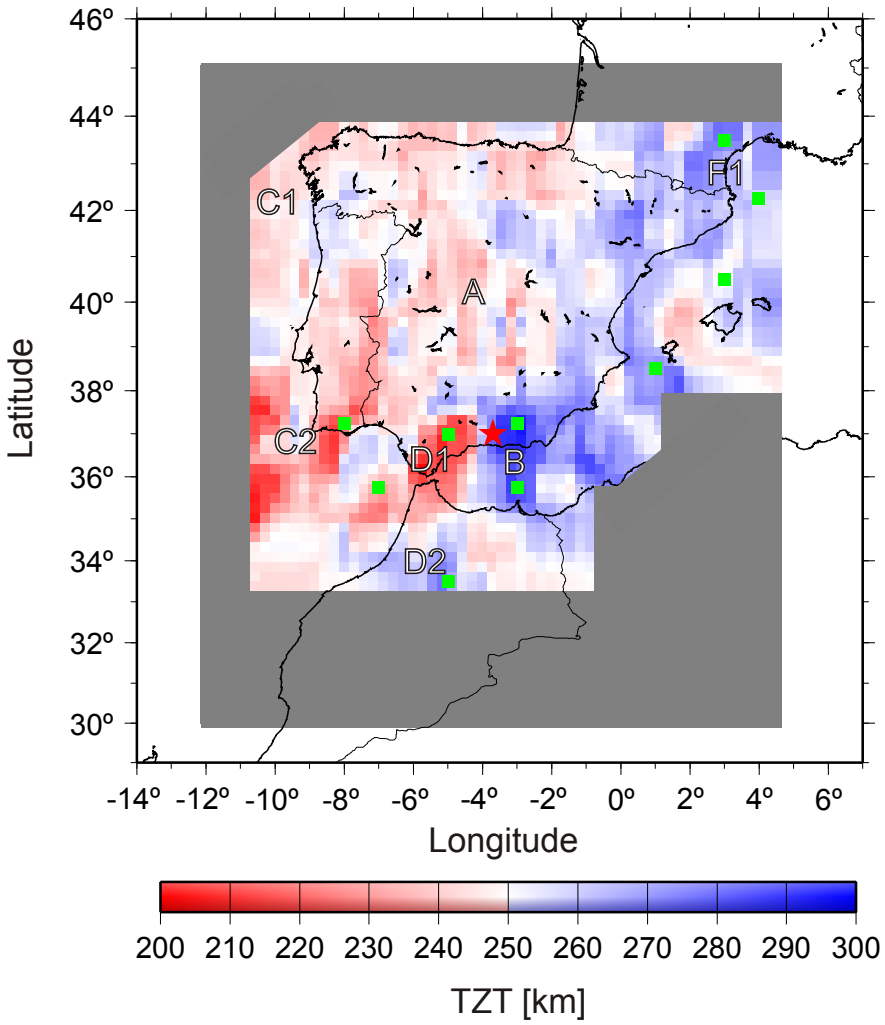

Figure 4.18: **Transition zone thickness** beneath the Iberian Peninsula and north Morocco. Areas labeled A-F are interesting features described in the text. The red star shows the epicenter of the nest of deep earthquakes beneath Granada (Buforn et al. 2004).

corrections the averaged TZT is 250 km. Anyhow, both values are thicker than the global RF average of 242 ± 2 km (Lawrence and Shearer, 2006).

The TZT is shown in Fig. 4.18. The green squares show the location of selected bins with robust 410 and 660 depth values, where the P410s and P660s phases are detected with at least two techniques and with small uncertainty values. These bins are located in areas of special interest, where the TZ shows thickness values larger or smaller than the reference thickness in AK135. The 410 and 660 depths and the TZT for the green squares in Fig. 4.18 are listed in Table 4.1. We observe a large-scale thickness change from southwest to the east. In the central part of Iberia, the TZT shows variations around the mean of about ± 10 km (A in Fig. 4.18). The southwest coast of Iberia (C2 and D1 in Fig. 4.18 and Table 4.1) exhibits a thinner TZ of about 220 km. The southern and eastern coasts of Spain are characterized by a thicker TZ with maximum thickness of about 300 km beneath the Alboran Sea (B in Fig. 4.18 and Table 4.1) and about 280 km beneath the Pyrenees area (F1 in Fig. 4.18 and Table 4.1) and the south part of the Balearic Sea (see Table 4.1). In both areas, the tomographic images (Wortel and Spakman, 2000; Villaseñor et al., 2003; Spakman and Wortel, 2004) show positive P-wave velocity anomalies related to the Betic-Alboran slab and to the Alpine-Tethys remnant slab which lies at the base of the TZ beneath the Pyrenees, southern France, the Alps and the northern Italy/Adriatic region (e.g., feature A in Fig. 4.20 and feature A in profiles k to l in fig. A2.2 in Spakman and Wortel (2004)). Beneath the Alboran Sea, the TZ is thick due to an elevated 410 and a depressed 660 and beneath the south Balearic Sea the TZ is thick mainly due to a depressed 660. On the other hand, beneath the eastern Pyrenees and the northern Balearic Sea both discontinuities are depressed. The broad extension of the thicker TZ beneath the Alboran Sea is controlled by the extended 660 depression, while the 410 is locally elevated in the areas where the TZ reaches the largest thickness value. A thick TZ is also visible beneath the northwest of Morocco (D2 in Fig. 4.18 and Table 4.1), primarily due to an up to 20 km depressed 660 discontinuity. Another interesting result is that the deep earthquakes beneath Granada coincide with a transition from thinner to thicker TZ. In this area, our observations present a large $P410s$ detection gap and a smaller $P660s$ gap. Therefore, the TZ is obtained exclusively from interpolated 410 and 660 values. Thus, although the TZT change is a real feature, the position of the transition from thinner to thicker

Region	$H_{410} \pm \sigma$ [km]	$H_{660} \pm \sigma$ [km]	TZT $\pm \sigma$ [km]	Latitude [°]	Longitude [°]
South Portugal (C2)	420 ± 2	640 ± 6	220 ± 6	37.25	-8
Gulf of Cadiz (D1)	431 ± 3	660 ± 2	229 ± 4	35.75	-7
southwest of Spain (D1)	430 ± 2	644 ± 6	214 ± 6	37	-5
Pyrenees (F1)	409 ± 3	689 ± 3	280 ± 4	43.5	3
north Balearic Sea (F1)	410 ± 8	675 ± 7	265 ± 10	40.25	3
Gulf of Lyon (F1)	424 ± 2	681 ± 6	257 ± 6	42.25	4
south Balearic Sea	403 ± 7	672 ± 8	269 ± 10	38.5	1
Alboran Sea (B)	379 ± 10	679 ± 4	300 ± 11	37.25	-3
Alboran Sea (B)	397 ± 4	683 ± 7	286 ± 8	35.75	-3
Morocco (D2)	410 ± 8	680 ± 5	270 ± 9	33.5	-5

Table 4.1: 410, 660 and TZT values for the selected locations shown with the green squares in Fig. 4.18.

is uncertain, as well as if this is a smooth or abrupt change. Additionally, we find no correlation between the position of the active alkaline magmatism and the TZT.

4.3.4 Additional features in the receiver functions

In this section, we show other observed phases with amplitude comparable to that of $P410s$ and $P660s$ phases. Since the RFs hold the relative amplitude information, we investigate these additional features in the cross-sections of RFs. Fig. 4.19 shows 15 north-south profiles located every 1° in longitude. Each trace in these cross-sections is the stack of RFs with piercing point inside a bin of 1° in latitude and longitude with the centre located at the longitude of the corresponding profile and the indicated latitude in the horizontal axe. Flat zero-amplitude traces correspond to areas without data. From these cross-sections, it is evident that the $P660s$ phase is more robust and laterally coherent than the $P410s$. These cross-sections may not reflect the observed 410 and 660 topographies because the vertical axe corresponds to uncorrected time values and because these sections are computed for only one of the three techniques used to construct the 410 and 660 maps. Therefore, these profiles should not be directly compared with the topography maps of the 410 and 660.

In some regions, the P410s phases are accompanied by an intermittently observed negative amplitude precursory signal, which we attribute to a conversion from a first order decrease in velocity atop the 410 discontinuity (grey-amplitude signals marked with red lines in Fig. 4.19 and denoted as Pws). In some areas, the amplitudes of these particular signals are comparable to that of the $P410s$ phases, such as in the northwest of Spain, beneath the Pyrenees and the north part of the Balearic Sea (aa' and bb' in Fig. 4.19 and region F1 in Fig. 4.8 c) or the northwest area of Iberia (mm' in Fig. 4.19). In other places, the only signal which is clearly seen is the negative one while the $P410s$ amplitudes are significantly diminished, e.g, beneath the western Alboran Sea and its surroundings, where we see a detection gap of converted energy from the 410 (ii' and jj' in Fig. 4.19 and region D1 in Fig. 4.8 c). In other areas, the negative signals show a weaker lateral continuity or they cannot be distinguished from strong side lobes, as indicated with the red arrows in Fig. 4.19. Akin precursors have also been observed by other researchers (e.g., Tauzin et al., 2010; Eagar et al., 2010, and references therein) in other regions and have been interpreted as caused by a melt layer (of low velocity) which is often explained through an increased water content in the TZ (Bercovici and Karato, 2003; Tauzin et al., 2010).

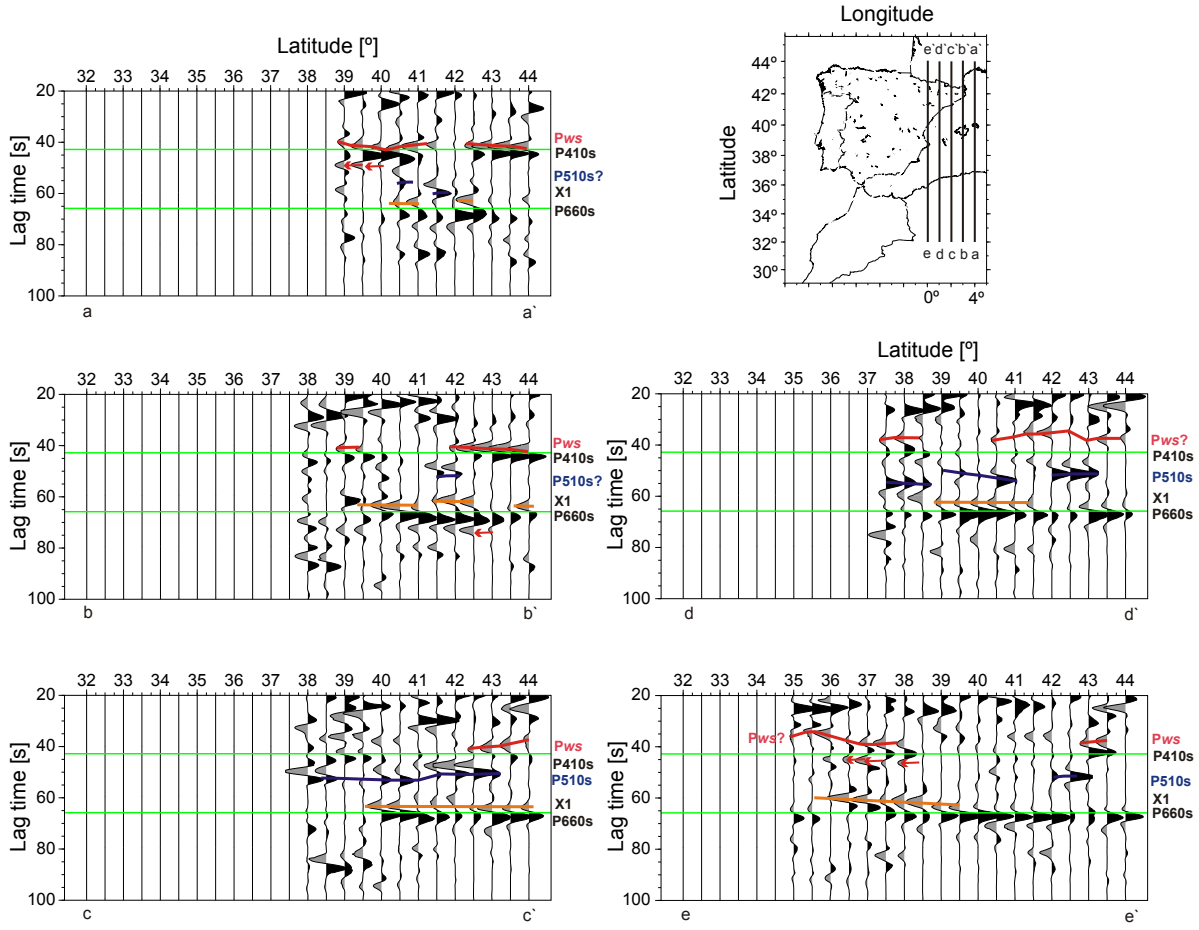

Figure 4.19: Cross-sections of CPP stacked RFs. The records begin 20 s after the P arrival to mask out the time interval dominated by crustal reverberations. Cross-sections are labelled in accordance with the profiles shown in the upper right map. The profiles show the CPP stacks in bins of 1° width in latitude and longitude and centred every 0.5°. The stacks were performed using a fixed relative slowness parameter of $-0.1s/°$ and a reference distance of 80°. Solid green lines mark the reference travel time for the $P410s$ and $P660s$ phases, red lines show the arrival of negative-amplitude signals before the $P410s$ which we denoted Pws, blue lines show the detection of a positive signal that could be the $P510s$ phase and orange lines mark the detection of negative-amplitude arrivals before P660s.

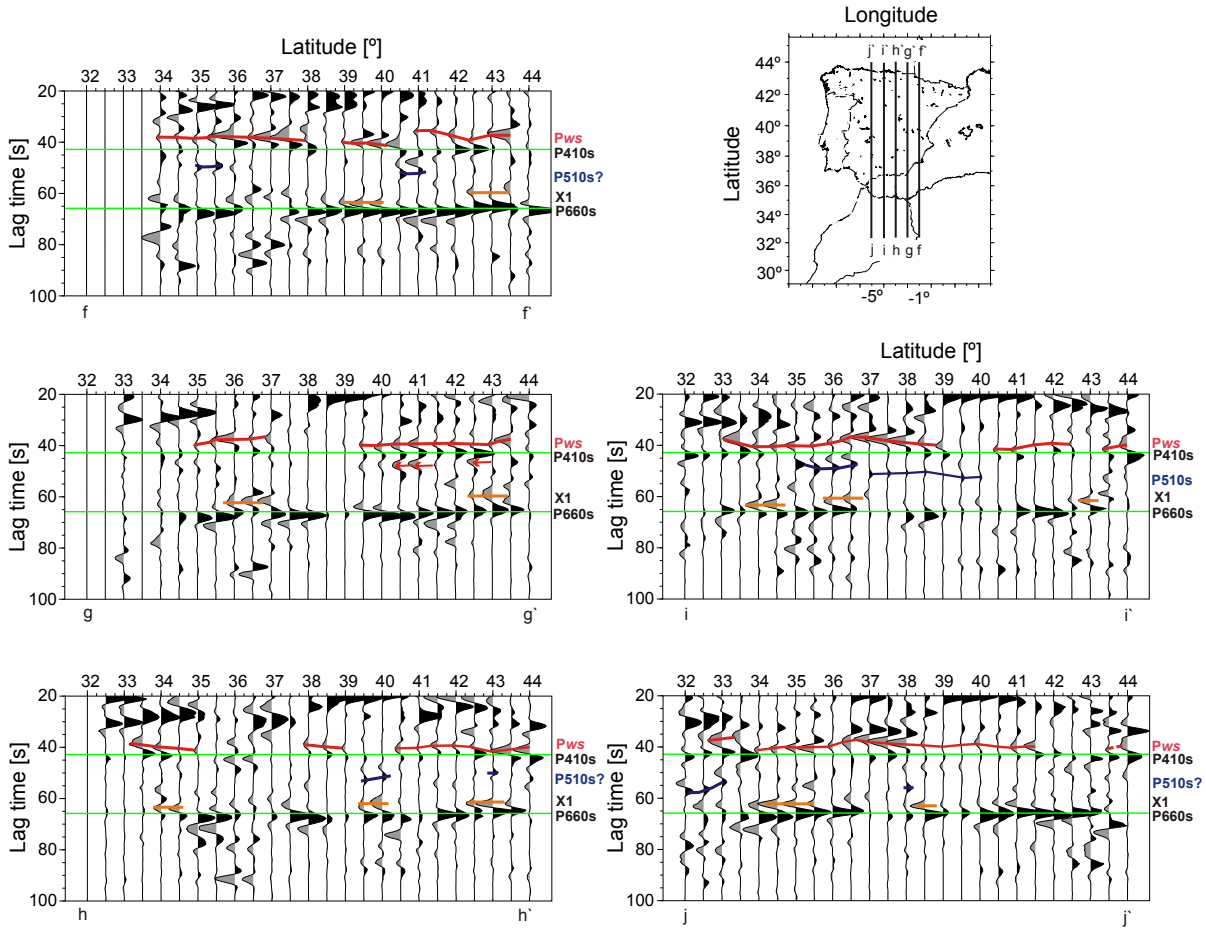

Figure 4.19 continuation

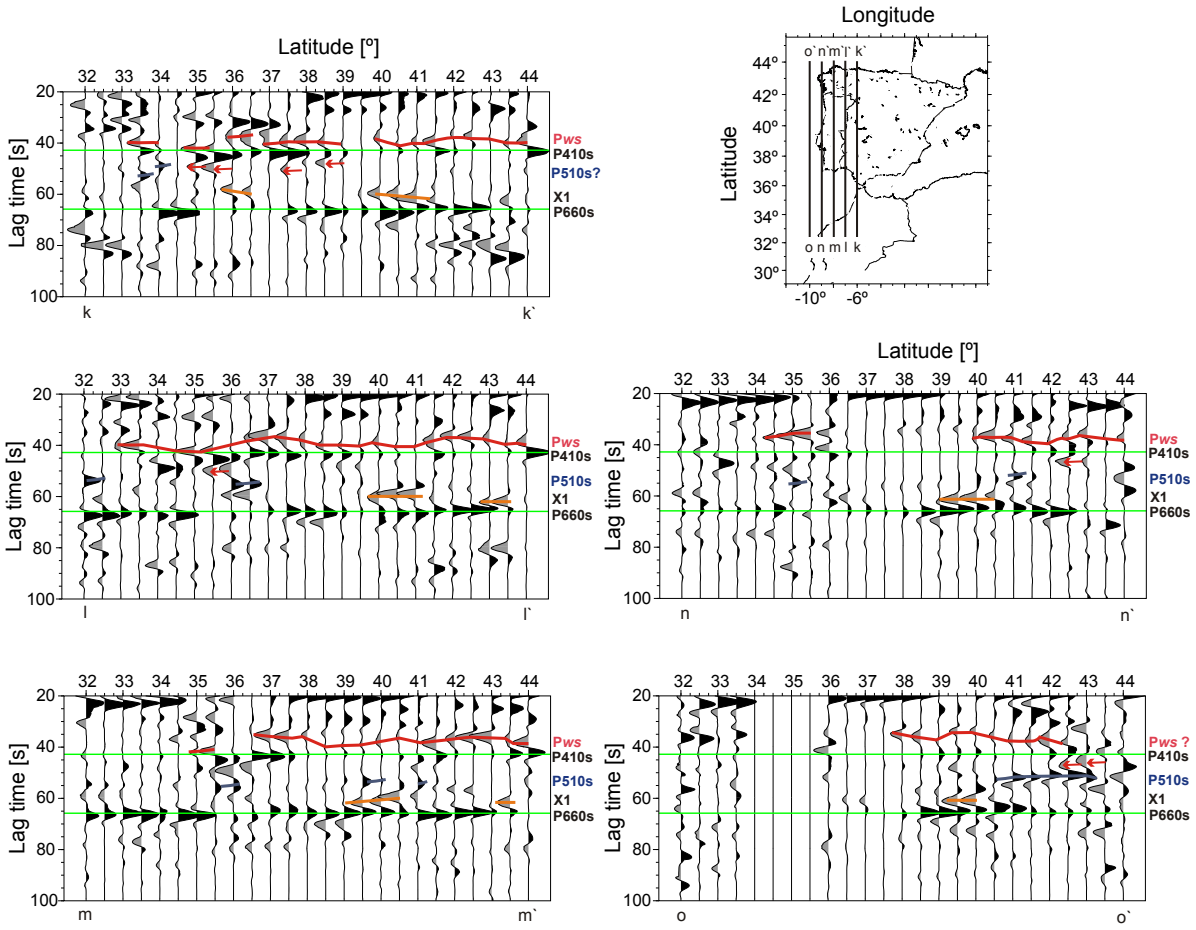

Figure 4.19 continuation

We also observe negative amplitude arrivals before the $P660s$ phases, denoted as X1 and marked with orange lines in Fig. 4.19. In some places, these negative peaks appear to be laterally coherent. In other areas, they appear intermittently. In general, the amplitudes of these signals are comparable to those of the P660s phases. Up to our knowledge, there exists no known mineralogical phase change that would produce the negative signal before $P660s$. Other studies have also observed similar negative impedance features and have interpreted them as accumulated oceanic crust at the base of the TZ (Shen and Blum, 2003; Shen et al., 2008; Eagar et al., 2010), probably coming from crustal decoupling from the slab at TZ pressure and temperature (van Keken et al., 1996; Karato, 1997). In subduction environments, where the slab is stagnant at the base of the TZ and where the cold slab lies atop a warmer mantle, the negative signals are probably associated to a decrease in velocity caused by a positive temperature gradient ($\delta T/\delta z \gg 0$) (Bina and Kawakatsu, 2010). Depending on the stagnation depth, the $rg \rightarrow pv + mw$ phase transition would be located below, above or within this low-velocity layer (e.g., fig. 7 in Bina and Kawakatsu, 2010).

We also note the presence of other intermittent positive amplitude arrivals between $P410s$ and $P660s$. These are the black-amplitude signals marked with blue lines in Fig. 4.19. These signals are less laterally coherent and are likely P-to-s conversions at first order velocity increases within the depth range of 500-550 km and could be signatures from the 510-km discontinuity. This discontinuity has been detected before in global stacks of SS precursors (Shearer, 1990) and has been proposed to be only a regional observable (Revenaugh and Jordan, 1991; Gu and Dziewonski, 1998). Deuss and Woodhouse (2001) confirmed the regional nature of the 510 with SS precursors; they found the 510 in many regions but confirmed its absence in others. In some regions, they found a splitting of the 510. The discontinuity at 510 km depth has been attributed to the wadsleyite-to-ringwoodite transformation in the olivine system by Shearer (1996). However, at approximately the same depth the dissociation of clinopyroxene to calcium-perovskite plus garnet gives origin to an additional discontinuity in fertile regions of the mantle (see Appendix B). Thus, if both phase transformations occur in the same region, two close signals would be detected. The variable arrival time of the positive signals between $P410s$ and $P660s$ may reflect the double origin for the 510.

Besides the TZ-related signals, we also observe laterally coherent positive signals in the time window between 20 and 30 s, after the time interval for the crustal

reverberations. These features can be seen in every profile in Fig. 4.19 and are likely to be P-to-s conversions at first order velocity increases within the depth range of 200-300 km. The Lehmann discontinuity (Lehmann, 1961b, 1964) is defined as a positive seismic discontinuity (velocity increases downward) at about a depth of 220 km. It is thought to reveal the bottom of the asthenosphere. P-to-s conversions at this discontinuity have been reported previously in other regions (e.g., Bostock, 1998; Li et al., 2002), but the analysis of SS precursors has been preferred to study the Lehmann discontinuity (e.g., Shearer, 1990; Vidale and Benz, 1992; Deuss and Woodhouse, 2002, 2004). The positive signal in the time window between 20 and 30 s is probably caused by the Lehmann discontinuity but it is not used in the following analysis and therefore we do not further explore its origin. Studying these discontinuities and the other discontinuities mentioned in this section is beyond the scope of this thesis.

4.4 Discussion

4.4.1 Relation with previous works

We have used a vast volume of data thanks to the IberArray of the TopoIberia project (Díaz et al., 2009), which has permitted us to study in detail and with high resolution a previously under-sampled portion of the TZ discontinuities beneath Iberia and north Morocco. Our results locate the 410 and 660 discontinuities within the expected depth range as obtained by global studies (Shearer, 1991; Revenaugh and Jordan, 1991; Vidale and Benz, 1992; Shearer, 1993; Chevrot et al., 1999; Lawrence and Shearer, 2006; Tauzin et al., 2007), and are further in good agreement with a large scale P-RF study that covered the entire Mediterranean region (van der Meijde et al., 2005). In van der Meijde et al. (2005) two stations are located in central Spain and north Morocco, which show the same TZT variations as observed in our study: small thickness variations beneath central Spain (A in Fig. 4.18) and a thicker TZ beneath Morocco (D2 and feature B in north Morocco in Fig. 4.18). In a previous study, published as Bonatto et al. (2013) and based on fewer stations and larger bin size and bin spacing, we observed the thickening of the TZ towards Africa as a narrow and steep transition between the two continents and we observed a $P410s$ detection gap beneath the Rif. For this second study, more data were available, a fact which has permitted us to increase the spatial resolution. Although we have

increased the amount of data and have improved the resolution, part of the 410 gap remains there. The thickening of the TZ towards Africa seems to be a robust feature; we have estimated a TZT variation from 214 km to 270 km in the Strait of Gibraltar (D1 and D2 in Fig. 4.18). This TZT variation is not seen by Dündar et al. (2011), who studied the 410 and 660 discontinuities beneath the Alboran Sea and close surroundings using P-RFs and the available stations before the IberArray deployment. Their RFs are stacked for two piercing point areas, the Alboran Sea and surrounding areas including south Spain, north Morocco, and Gulf of Cadiz and show a good agreement between the conversions from the different RF groups, within 1 s of the theoretically expected arrivals. Their results do not contradict the presence of topography, which most probably is not seen due to the averaging in the large piercing point area. Our analysis shows systematic variations for independent data from many smaller piercing point areas and for the joint usage of three different techniques.

4.4.2 Interpretation of results

In what follows, we discuss the TZT and the 410 and 660 topography in the study area by proposing different possible scenarios which may explain our results. Interpretation of TZT (and topography of discontinuities) includes temperature and composition of the mantle at these depths.

The tomographic images provide additional information to interpret our results. We use the P-wave tomography of Villaseñor et al. (2003), which, due to the inclusion of regional data for Spain, is a slightly higher resolution version of the original model in Wortel and Spakman (2000). The tomography in the western part of the study area has a lower resolution, therefore, direct comparison of the tomographic images and our TZT (or 410 and 660 depth values) in this area should be taken with care. To estimate the thermal anomalies needed to explain the obtained 410 and 660 topographies, we assume that velocity perturbations in the tomography model are thermally controlled.

To infer TZ temperatures, we consider the detected TZ discontinuities as olivine phase transformations. Under this assumption, the 410 and 660 depth changes are anti-correlated as a response to a thermal anomaly (due to the opposite sign in the Clapeyron slopes of the olivine-to-wadsleyite and ringwoodite-to-perovskite + magnesiowustite phase transformations). While the 410 becomes shallower in colder

regions and deeper in hotter ones, the 660 behavior is opposite. As a consequence, the TZ becomes thicker near subducted slabs and thinner beneath plumes or high temperature regions due to small scale mantle convection (Vidale and Benz, 1992; Helffrich, 2000; Collier et al., 2001; Lawrence and Shearer, 2006). Thus, the similarity between the TZT map (Fig. 4.18) and the tomography image at the same depth (Fig. 4.20) is not unexpected.

4.4.2.1 Relation between TZ discontinuity depths and temperature

The 410 and 660 depths and the TZT have been used before to infer the temperature at the corresponding depths (e.g., Chevrot et al., 1999; Lawrence and Shearer, 2006; Tauzin et al., 2007). The conversions from anomalous TZT (or discontinuity depth) to temperature are based on Clapeyron slopes ($\frac{dP}{dT}$, the slope of the lines in the P-T plot in Fig. 1.5) for the 410 and 660 of 4 $MPaK^{-1}$ and -1.3 $MPaK^{-1}$, respectively (Katsura et al., 2003, 2004; Litasov et al., 2005). These values are based on the assumptions of a dry mantle composition dominated by olivine (pyrolitic mantle composition) and the 410 and 660 discontinuities due to standard olivine-system phase transitions of olivine-to-wadsleyite ($\alpha \rightarrow \beta$) and ringwoodite-to-perovskite+magnesiowustite ($rg \rightarrow pv + mw$), respectively. In order to convert discontinuity depth variations into temperature variations, we use the Clapeyron slope definition, $\frac{dP}{dT}$. If we consider an upper-mantle pressure increase ($\frac{dP}{dz}$) of 100/3 MPa/km, temperature differences ($\delta\mathbf{T}$) can be computed from the following expression:

$$\left(\frac{dP}{dT}\right)_H \approx \frac{dP}{dz}\frac{\delta z_H}{\delta \mathbf{T}}, \tag{4.1}$$

where $\left(\frac{dP}{dT}\right)_{H=410,660}$ is either the 410 or 660 associated Clapeyron slope, and $\delta z_{H=410,660}$ is the difference between the observed depths from the reference. Similarly, under the assumption that discontinuity deflections are due to vertically coherent temperature changes, deviations of TZT from expected values can be translated to temperature variations by means of the following equation (Helffrich, 2000):

$$TZT = TZT_{reference} + \delta\mathbf{T}\frac{dz}{dP}[(\frac{dP}{dT})_{660} - (\frac{dP}{dT})_{410}] \tag{4.2}$$

Equations 4.1 and 4.2 have been used to calculate the predicted temperature differences in Figs 4.7 (a) and (b) and Fig. 4.17. Note that the deeper-than-average (shallower-than-average) 660 discontinuity estimations would correspond to colder-than-average (hotter–than–average) temperature in Fig. 4.7 (b), as opposed to the 410 discontinuity behavior shown in Fig. 4.7 (a). In Fig. 4.17, the thicker-than-average (thinner-than-average) TZT estimations would correspond to colder-than-average (hotter-than-average) temperatures. For a reference, average mantle temperature is about 1350 °C, cold mantle temperature is about 950 °C and hot mantle temperature is about 1750 °C. The reference transition zone thickness of 250 km that we use from AK135 represents a TZ which is about 8 km thicker than the observed global average (Flanagan and Shearer, 1998; Lawrence and Shearer, 2006) and consequently about 60 K colder than average. The computed temperatures should be considered as approximate values, because the Clapeyron slopes used to infer them are laboratory estimates which can contain mistakes difficult to control. A 10 % change of the Clapeyron slopes leads to TZ temperature variation of about 10 K.

4.4.2.2 Compositional considerations

In our interpretation, we also consider changes in mantle composition, which may as well produce topography in the TZ discontinuities. In what follows, we only outline the complexities used in the discussion of results. For further details, see Appendix B and references therein.

The depth of the 410 and 660 are influenced by the presence or abundance of other components in the upper mantle, such as H_2O, Al within garnet or $Fe - Mg$ proportion in olivine:

- The presence of water in the TZ would extend the wadsleyite stability to lower pressures resulting in a shallower 410 discontinuity (Wood, 1995; Smyth and Frost, 2002). Additionally, in cold environments such as the subduction zones, the presence of water in peridotite shifts the post-spinel phase boundary to higher pressures. Thus, the topography of the 410 and 660 associated with slabs (and the TZT) can be attributed not only to cold subduction but also to wet subductions (Litasov et al., 2005).

- In normal to hot upper mantle and in the presence of aluminum within garnet, the garnet-to-perovskite ($gt \rightarrow pv$) transition is expected near the 660 with a

positive Clapeyron slope (Weidner and Wang, 1998; Wang et al., 2004; Akaogi et al., 2002) (see Appendix B). As a consequence, the garnet-related 660 discontinuity deflects downward in a hotter mantle, contrary to the post-spinel transition ($rg \rightarrow pv + mw$), which has a negative Clapeyron slope. In addition, the depth of the garnet-related phase transition is strongly dependent on the aluminum content of the garnet, causing variations in the discontinuity depth by more than 50 km (Weidner and Wang, 1998). Thus, a depressed 660 away from the slab may reflect variations in aluminum content leading to a deeper garnet-to-perovskite transition at normal to warm mantle temperatures (Weidner and Wang, 1998; Wang et al., 2004; Akaogi et al., 2002; Thomas and Billen, 2009).

- The relative proportion of Mg and Fe content in olivine shifts the 410 discontinuity to different pressures (e.g., left panel in Fig. 1.5 in the general introduction). An enrichment of Mg relative to Fe increases the pressure of the $\alpha \rightarrow \beta$ phase loop leading to a deeper 410 (e.g., Fei and Bertka, 1999; Schmerr and Garnero, 2007).

4.4.2.3 Alboran Sea and surrounding areas: thicker TZ

The elevated 410 and depressed 660 in the Alboran Sea lead to a 300 km thick TZ (B in Figs 4.8 c, 4.9 c and 4.18 and in Table 4.1) which is consistent with the position of the positive P-wave velocity anomaly of the Betic-Alboran slab (Wortel and Spakman, 2000; Piromallo and Morelli, 2003; Villaseñor et al., 2003; Bezada et al., 2013) (feature B in Fig. 4.20. Interpreting the 50-km thickened TZ in terms of temperature implies a thermal anomaly of about -315 K for the slab at TZ depths (between 410 km and 660 km). The presence of signal Pws in this area (see profiles ff' to jj' in Fig. 4.19 between latitudes 35° and 38°) indicates the presence of a low velocity layer above the 410, which is often explained as a melting layer induced by dehydration of hydrated wadsleyite. Consequently, if we consider that the Betic-Alboran slab is of oceanic origin (hydrated oceanic lithosphere), then, part of the 410 uplift and 660 depression could be due to a water content increase in wadsleyite and ringwoodite (Litasov et al., 2005). Under this assumption, the temperature anomaly of -315 K could be considered as a higher bound.

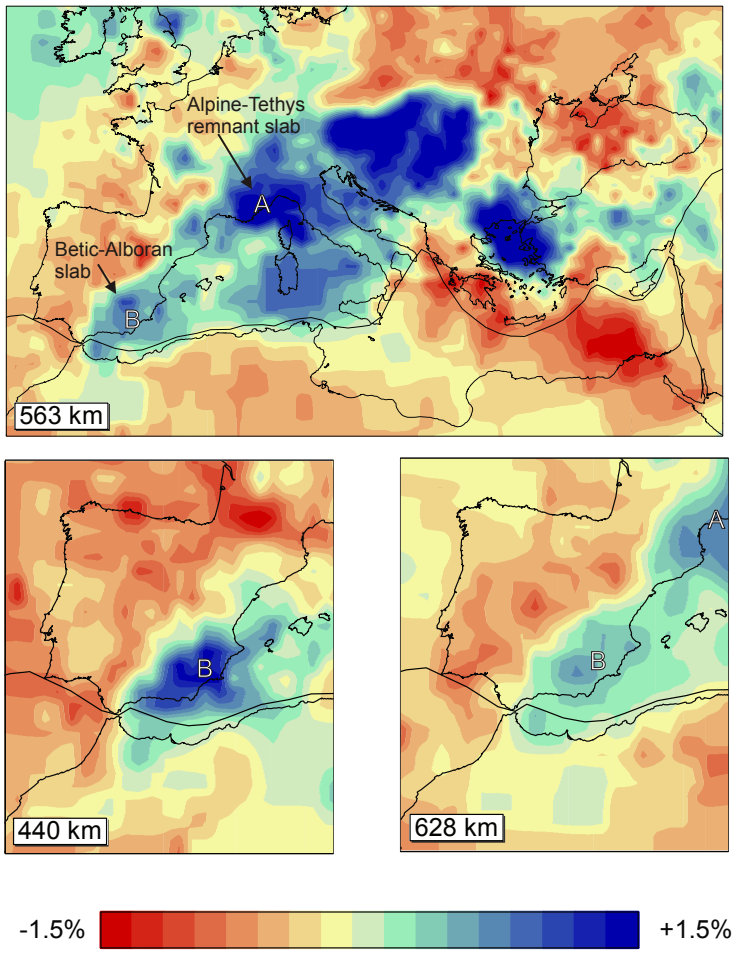

Figure 4.20: Map view of the P-wave tomography in the Mediterranean region from Villaseñor et al. (2003) and for different depths. This model is a slightly higher resolution version of the original model in Wortel and Spakman (2000). Features A and B are the Alpine-Tethys remnant slab and the Betic-Alboran slab, respectively, which are explained in Spakman and Wortel (2004).

In order to visualize the relation between the P-wave anomalies and the TZT (and 410 and 660 topography), we plot our results along 15 north-south profiles and 2 west-east profiles displayed in Fig. E.1 (Appendix E) together with the corresponding cross-sections from the tomography model of Villaseñor et al. (2003). The composed profiles are shown in Fig. E.2 and Fig. E.3 in Appendix E. For each of these profiles, we plot the 410 and 660 depths along three closely separated longitudes (see figure caption) to add robustness to our interpretation. Features A, B, C1-2, D1-2 and F1 are also plotted to easily relate the profiles with the 410 and 660 surfaces in Fig. 4.8 (c) and Fig. 4.9 (c) and the TZT in Fig. 4.18. The profiles that cross the velocity anomaly in south Spain and the Alboran Sea are ee', ff', gg', hh' and ii' in Fig. E.2 and AA' and BB' in Fig. E.3.

- Profiles gg', hh', AA' and BB' demonstrate that the uplifted 410 and depressed 660 beneath the Betics are vertically anti-correlated, as illustrated in **model** I in Fig. 4.21. This implies that the thermal anomaly is likely to extend vertically in depth through the entire TZ, which is consistent with the steep Betic-Alboran slab (Bezada et al., 2013), otherwise we would expect an uncorrelated 410 and 660 topography.

- On the other hand, the 660 depression beneath the Alboran Sea extends over a larger area, which does not coincide with the position of the positive P-velocity anomaly. Profiles ee' and ff', which lie at the east end of the Alboran Sea, show that the 660 is deeper towards Algeria for more than 250 km, away from the position of the positive P-wave anomaly (slab or cold thermal anomaly). The same happens in profiles gg' and hh' but beneath Morocco. We find three different explanations for this long-wavelength depression which are consistent with subduction: (i) relatively cold temperatures surrounding the slab and the presence of water shift the post-spinel phase transformation to higher pressures (depths) (Litasov et al., 2005); (ii) a remnant thermal anomaly from the previous slab location, which is consistent with the kinematic evolution of the slab roll-back proposed by Spakman and Wortel (2004) (see Fig. 4.22 extracted from Spakman and Wortel (2004)); (iii) accumulation of cold material at the bottom of the TZ which cools the 660 and shifts the post–spinel transition to a greater depth. We do not have a preferred explanation because they can all explain our observations equally well.

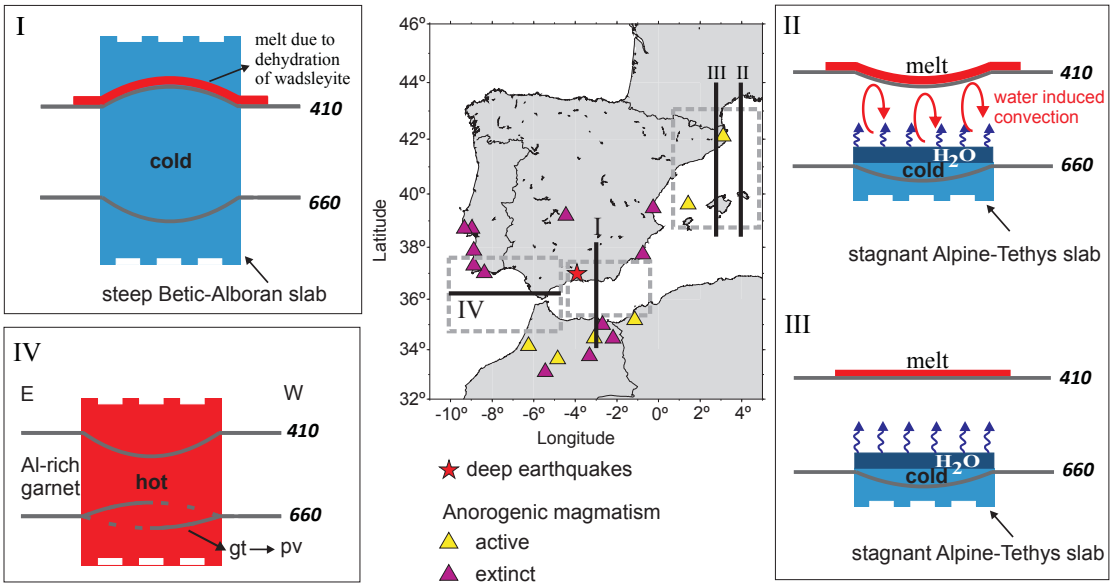

Figure 4.21: Schematic explanation for the proposed models. In these models the topography of the 410 and 660 discontinuities are governed by the temperature inside the TZ. Unless indicated, the discontinuities are due to olivine phase transition.

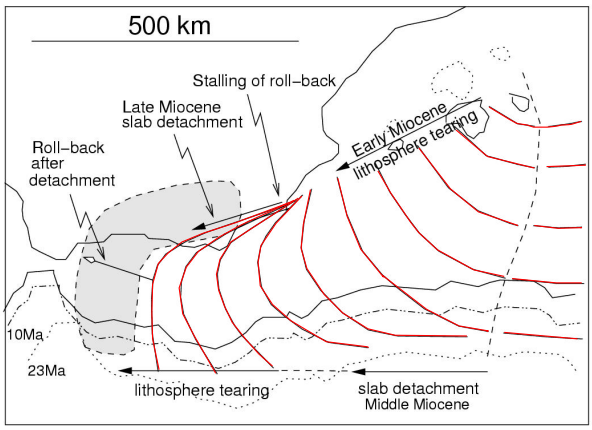

Figure 4.22: Kinematic evolution of slab roll-back in the Betic-Rif-Alboran region from Spakman and Wortel (2004). Grey shaded area gives the present location of the Betic-Alboran slab at a depth of 200 km. Curved red lines denote the location of the subduction trench through time, starting at the Balearic Islands and ending under the Betic.

4.4.2.4 The area of deep earthquakes beneath Granada

Profile ii' in Fig. E.2, which is at the western end of the slab, demonstrates that the depression of the 660 is consistent with the seismic anomaly related with the Betic-Alboran slab. The maximum depression of the 660 ($\sim$ 25 km) includes an area of isolated deep earthquakes beneath Granada (37°N 3.7°E approximately) with similar focal mechanism, magnitudes (M_W) from 4 to 7 and a recurrence time of about 20 years (Buforn et al., 2004, 2011; Bezada and Humphreys, 2012). Furthermore, Fig. 4.18 shows that the location of the nest of deep earthquakes (red star) corresponds to a TZT change from thin to thick, which may be interpreted as a temperature change. In the west-east profile BB' in Fig. E.3 it is evident that the TZT change fairly coincides with the western end of the Betic-Alboran slab. The thinner TZ in this area is due to anti-correlated 410 and 660 depth changes. Using aforementioned assumptions and equation 4.2 with the values in Table 4.1, we estimate a net temperature variation of about 540 K (from about -315 K inside the cold slab to about $+225$ K at the western end of the slab) over a distance of less than 250 km inside the TZ. Thus, the nest of deep earthquakes is located in an area of a high temperature gradient inside the TZ and at the western end of the slab revealed by the tomographic images of Villaseñor et al. (2003).

4.4.2.5 Pyrenees and northeast coast of Spain

Profiles aa', bb' and cc' in Fig. E.2 show that the depressed 660 (in F1) coincides with the location of the positive P-wave anomaly related with the Alpine-Tethys remnant slab (see also Fig. 4.20). Thus, we interpret the 20-30 km downward deflection of the 660 as caused by the cold slab, which shifts the post-spinel transition to greater depths. Using Equation 4.1 and the corresponding Clapeyron slope of the post-spinel transformation, we infer a negative thermal anomaly of about 500-750 K at the 660, which we consider as a higher bound if we assume that part of the 660 depression is caused by the presence of water (Litasov et al., 2005), perhaps from dehydration of the slab. In this area, the 410 is also downward deflected by about 20 km (see F1 in Fig. 4.8 c), however, this deflection is more evident in profile aa' of Fig. E.2, while in bb' the 410 is at its expected depth (see F1 in Fig. E.2). Additionally, in this area we see a strong and clear reversed polarity signal arriving immediately before the

$P410s$ phase (see Pws in profiles aa' and bb' in Fig. 4.19), suggesting water-induced melting atop the 410 (e.g. Tauzin et al., 2010).

We find a thermal explanation to the depressed 410, which is consistent with the presence of the reversed polarity signal before $P410s$ and with the presence of a stagnant slab in the TZ, as proposed for the Alpine-Tethys remnant slab in Spakman and Wortel (2004). Richard and Bercovici (2009) examined the convective stability of the top layer of a stagnant hydrated slab at the TZ by numerical experiments. They found that after a relatively short time after the slab enters the TZ and an initial water content in the slab ($\geq$ 5 wt %) an episode of convection is likely to occur above the slab. The Alpine-Tethys remnant slab is of oceanic origin and probably contains a high proportion of water inside. It is probable that small-scale convections, triggered by slab dehydration, occur above this stagnant slab and provide the needed heat to shift the $\alpha \rightarrow \beta$ phase transition to a higher pressure, i. e., larger depth. Part of the water removed from the stagnant slab can be stored in the β phase (wadsleyite), which is then dehydrated to induce partial melting atop the 410, explaining the reversed-polarity signal before $P410s$. **Model II** in Fig. 4.21 summarizes our preferred model for this region (profile aa' in Fig. E.2), where the red arrows mark the locations of the small-scale convection which is responsible for the downward deflection of the 410. **Model III** illustrates the preferred model for profile bb', where the 410 depression is less clear due to the $P410s$ detection gap. This profile is located at the end of the cold Alpine-Tethys remnant slab and we interpret that the slab only affects the 660's depth.

4.4.2.6 Deeper 660 beneath the western part of the Moroccan region

The maximum observed TZT beneath Morocco (275 km) is about 25-35 km thicker than global averages of 240-250 km, but this is within the expected TZT variations (Flanagan and Shearer, 1998; Chevrot et al., 1999; Lawrence and Shearer, 2006). The thicker TZ beneath the western Moroccan region is mostly due to a deeper 660 discontinuity which shifts downward by as much as 20 km (see D2 in Fig. 4.9 c and in Table 4.1) while the 410 shows less $P410s$ detections (Fig. 4.8 a) and stays on average at its expected nominal depth of 410 km. Under the assumptions of a TZT of 250 km for reference, a pyrolitic mantle composition and using Eq. 4.2, the TZ thickening of 25 km beneath Morocco can be translated into an approximate temperature decrease

of 160 K. However, in the profiles jj', kk' and ll' (in Fig. E.2) we do not find a corresponding positive velocity anomaly in the tomographic image.

In Bonatto et al. (2013), we proposed that a plausible cause for the thickened TZ can be (i) a not considered isothermal low-velocity anomaly (not resolved in the tomographic images) which increases the $P660s$ travel times and which leads to apparent TZT thicker than expected or, alternatively, (ii) an Al-rich garnet-related 660, which in normal to hotter environments is to be expected at greater depth than the post-spinel transition depending on the Al content (Weidner and Wang, 1998; Wang et al., 2004).

A recent tomography study (Bezada et al., 2013), which includes more stations in Morocco, has revealed an irregular but pronounced zone of low velocities beneath the Middle Atlas at 50-125 km followed by a high-velocity body at a depth of about 400-500 km. This pair of anomalies has been interpreted as a drip-like delamination of the Middle Atlas mantle lithosphere. The fast velocity anomaly inside the TZ does not reach the 660 and consequently is discarded to depress the post-spinel transition through its expected colder than average temperature. The high velocity anomaly would therefore only decrease the travel time of the $P660s$ phase, which, without the correct travel time corrections, would lead to apparent discontinuity uplift. However, we observe the opposite, a deeper 660. In this new context our preferred explanation is (ii). In the absence of a hot thermal anomaly, as expected from the tomographic images, the depth variations of the garnet-related 660 beneath Morocco can likely be attributed to variable proportions of Al content within garnet (e.g., Thomas and Billen, 2009), since the Al content also controls the depth of this transition.

4.4.2.7 Thinner TZ beneath Strait of Gibraltar, Gulf of Cadiz and south of Portugal

With the exception of the Spanish side of the Strait of Gibraltar, the thinner TZ in this region is not due to anti-correlated 410 and 660 depths. The 410 is, on average, deeper in the whole area, but the largest depressions are towards the east, beneath the Gulf of Cadiz and the Strait of Gibraltar. On the other hand, the 660 is on average deeper to the east and shallower to the west of the region and it has small length-scale depth changes (see dotted circles in profiles AA' and BB' in Fig E.3). In particular, near the longitude -8° in profile AA' there is a 40-km jump in the 660

depth. Moreover, in the lower panel of this figure, the RF cross-section shows double peaks near $P660s$ at longitude -6° and -5°.

We do not find a clear relation between the tomographic images and the thinned TZ in profiles AA' and BB' (C2 and D1 in Fig. E.3) and profiles kk', ll', mm', nn' and oo' (C2 and D1 in Fig. E.2). In this area, the P-wave anomalies are slightly negative indicating velocities lower than the reference model, which suggests that the mantle is warmer than average. Recently, Monna et al. (2013) published a tomography study which covers the Atlantic domain in the southwest Iberian margin and the Alboran Sea. This study has a higher resolution than previous studies because it includes data from OBS stations in the Gulf of Cadiz and the Atlantic Sea. Below the Atlantic domain, they image a wide area of negative P-velocity anomalies, which is attributed to the presence of a hot upper mantle and which is perhaps related with the late Mesozoic-early Cenozoic alkaline igneous activity of sub-lithospheric origin (e.g., Lustrino and Wilson, 2007; Grange et al., 2010, and references therein), such as observed in south Portugal in Fig. 4.23.

The depth variability of the 660 and the double peaks near $P660s$ suggest the presence of multiple discontinuities near 660 km depth but, due to the used quality criteria, we have detected each time the best quality signal. The only additional discontinuity expected in a warm to hot TZ is the garnet-to-perovskite phase transformation with a positive Clapeyron slope. In warmer to higher mantle temperatures, this discontinuity is shifted to higher pressures (depth), which depend on the Al proportion within garnet (Weidner and Wang, 1998). The presence of multiple discontinuities introduces additional complexities, which make the interpretation in this area difficult. If the TZ temperature in this area is higher than average, then due to the opposite sign in the Clapeyron slopes of the $gt \rightarrow pv$ and the post-spinel phase transitions, we can attribute the deeper 660 to the garnet-related phase transition and the shallower 660 to the post-spinel transition. In this scenario, our preferred model for this region is **model IV** in Fig. 4.21, where a warm thermal anomaly crosses the TZ causing the depression of the 410 and the uplift of the olivine-related 660 discontinuity. This results in the thinning of the TZ while the presence of Al within garnet is responsible for the depressed 660 in such warmer environment.

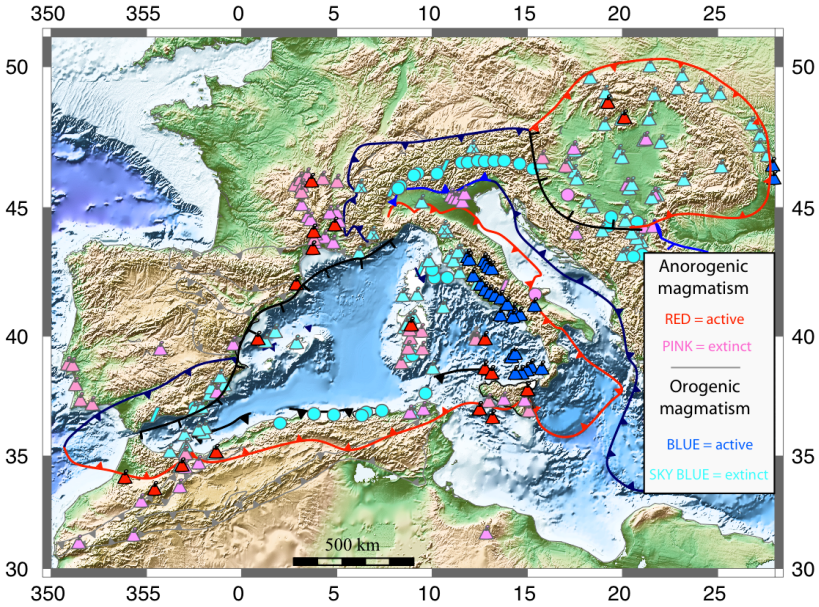

Figure 4.23: Distribution of Tertiary magmatism in the Central-Western Mediterranean region (with permission from Dr. E. Carminati). Red symbols: active anorogenic igneous rocks; Pink symbols: extinct anorogenic igneous rocks. For further explanation and details please refer to the original publication, Carminati et al. (2012), and the references therein.

4.4.2.8 410 depression and anorogenic magmatism

The north of Morocco and the east coast of Spain are characterized by recent igneous activity ($\sim$ 10-0.01 My) of sub-lithospheric origin (yellow triangles in Fig. 4.8), which is also found in all the Mediterranean region as shown in Fig. 4.23. This igneous activity is also known as the Circum-Mediterranean Anorogenic Cenozoic Igneous (CiMACI) Province (Lustrino and Wilson, 2007; Lustrino et al., 2011; Carminati et al., 2012). Several petrological and geodynamic models have been proposed to explain the anorogenic magmatic activity; these are summarized in fig. 18 in Lustrino and Wilson (2007). The models require either (i) active asthenospheric (or deeper) mantle convection (i.e., mantle plumes) or (ii) lithospheric extension (or delamination and detachment) to induce passive adiabatic decompression melting of both asthenospheric and lithospheric upper mantle.

This active anorogenic magmatism, where active means that these volcanoes erupted recently and could still erupt, are located at the border of areas with a depressed 410. We do not see the same spatial correlation with the 660 topography or with the TZT.

Our results can be explained with the mantle-plume model (model i), where the stem of the plume is centered away from the Mediterranean, similar to the model proposed by Duggen et al. (2009) (Fig. 1.6). The plume material would only affect the 410 beneath north Morocco and the eastern coast of Spain. Additionally, this model is consistent with the presence of the reversed polarity signal before $P410s$. The 410 depression can be attributed to a thermal anomaly of about +160 K, while the reversed polarity signal is attributed to the effect of high temperatures on water rich mantle silicate rocks, as has been suggested from S-RF studies in other regions (Vinnik and Farra, 2002, 2007). Although model (i) explains the Pws phase before $P410s$, the detection of this signal is not restricted to a particular tectonic environment, but is rather attributed to a global low-velocity layer of variable thickness within the Earth's upper mantle (Tauzin et al., 2010). Furthermore, this plume-like model is consistent with the thinned TZ beneath the Strait of Gibraltar, Gulf of Cadiz and south of Portugal. In this context, the Alboran slab would be an obstacle for the plume material, which increases the upper-mantle temperature towards the west of the Alboran slab. This temperature increase will result in the shift of the $\alpha \rightarrow \beta$ transformation to higher pressures and to the shift of the post-spinel transition to

lower ones (and the garnet-related phase transition to higher pressures). The plume-like model provides an alternative explanation (to our **model II** in Fig. 4.21 and section 4.4.2.5) for the depressed 410 beneath the northeast coast of Spain, while the explanation for the 660 deflection remains the same.

On the other hand, melt in the overlying mantle, as proposed by model (ii), preferentially extracts Fe, leaving a Mg-enriched residue that should be transported into the mantle transition zone (Schmerr and Garnero, 2007). In a Mg-enriched mantle in the vicinity of the 410, the $\alpha \rightarrow \beta$ phase transition moves to higher pressures (e.g., left panel in Fig. 1.5 in the general introduction), leading to the downward deflection of the 410 discontinuity beneath north Morocco and the northeast coast of Spain. This explanation is consistent with our **model II** for the northeast coast of Spain. The contribution of the Mg-enriched mantle to the depth of the 410 has the same sign as that of a higher temperature due to small scale convection above the Alpine-Tethys remnant slab.

In conclusion, the obtained 410 and 660 topographies in this area can be explained equally well with both models (i and ii). We have no preferred model, and yet there is lack of evidence to suport any of them (Lustrino, 2011).

4.4.2.9 Other features and minor comments

We have recognized several anomalous features in the cross-sections of RFs and large areas of undetected $P410s$ phases. We discuss these particularities in more detail below.

The negative peaks before the $P410s$ phase, suggesting water-induced melting atop the 410 (e.g. Tauzin et al., 2010), are present in the entire region (see Pws in Fig. 4.19). Nevertheless, this signal is more clear, continuous and stronger in the profiles that cross the Alboran Sea (ff', gg', ii' and jj' in Fig. 4.19), the northeast of Spain (aa', bb' and cc' in Fig. 4.19) and the Gulf of Cadiz (AA' and BB' in Fig. E.3). The first two areas coincide with the location of the Betic-Alboran slab and the Alpine-Tethys remnant slab, respectively, which likely contribute to a water concentration increase in the TZ. On the other hand, in the Gulf of Cadiz we have found a thinned TZ which corresponds to a thermal anomaly of +190 K across the TZ and which could be related to plume material that is forced to release water, because the storage capacity of wadsleyite is larger than the overlying olivine (Hirschmann, 2006). In this context, the increased water content could be responsible for a localized higher

amount of melting atop the 410 in the mentioned areas.

The 410 has been less well observed in the Alboran Sea area which leads to observation gaps (Fig. 4.8 a). A detection gap of converted or reflected energy from the 410 in subduction zones has been reported in other studies too, e.g., for near source conversions (Collier and Helffrich, 2001; Tibi and Wiens, 2005), sScS precursors (Tono et al., 2005), and SS precursors (Contenti et al., 2012). Profile AA' and BB' in Fig. E.3 show that the 410 gap coincides with the position of the Betic-Alboran slab. Furthermore, we have noted that the only clear signal in this area is the negative-amplitude signal Pws before $P410s$. We believe that structural complexities cause the 410 observation gap due to defocusing or loss of coherence and destructive interference with other coda waves. Furthermore, the seismic visibility of the 410 is often decreased in subduction areas owing to its thermodynamic properties which may lead to smaller conversions/reflections in colder-than-normal mantle and additional discontinuity broadening in the presence of water (Collier and Helffrich, 2001).

In the north and northwest coast of Iberia the 410 and 660 depths are correlated. Both discontinuities are deeper beneath the Bay of Biscay (feature E in Figs 4.8 and 4.9) and shallower beneath the northwest coast of Iberia (feature C1 in Figs 4.8 and 4.9). In both areas, the TZT is close to the reference value of 250 km. It is probable that the 410 and 660 depth correlation is due to underestimated time corrections on $P410s$ and $P660s$ travel times. This is expected due to the lower resolution of the tomographic images in these areas.

4.5 Summary and conclusions

We have carried out a semiautomatic search for converted phases $P410s$ and $P660s$ beneath the Iberian Peninsula and north Morocco using teleseismic data from 259 stations, most of them belonging to the IberArray of the TopoIberia project. We have used three independent approaches (PCC, CCGN and RF) to estimate the relative travel time of converted phases and a bootstrap algorithm to estimate the time uncertainties. The region has been divided in small areas of common piercing points to perform the stack of correlograms and receiver functions. We have considered only

converted phases with stacked amplitude larger than twice the mean amplitude in the time interval 30-80 s, and with bootstrap time-standard deviation smaller than 1.5 s. Besides, we have performed a thorough visual inspection to avoid spurious detections. Based on a body wave tomography velocity model for the study area, we have applied time corrections to the travel times of the Pds (d=410, 660) phases. These corrected travel times were then converted to depth obtaining the topography maps for the 410 and 660 discontinuities and the TZT map beneath the Iberian Peninsula and its surroundings. The main results are:

- Alboran Sea region: thicker TZ due to vertically anti-correlated 410 and 660 (locally elevated 410 and widely depressed 660).
- South Spain (Granada area): TZT variation of 86 km towards the east (from thin to thick) coinciding with the location of the nest of deep earthquakes.
- Northeast Spain (Pyrenees and Balearic Sea): thicker TZ mainly due to a depressed 660 while the 410 depths are unperturbed or slightly depressed.
- Northwest and central Iberia: normal TZT.
- Morocco: deeper 660 beneath the western part of the Moroccan region, leading to a thicker TZ. The 410 is at normal depth and exhibits a detection gap beneath the Rif area.
- Southwest Iberia and Gulf of Cadiz: thinner TZ due to a depressed 410, while the 660 is shallower to the west and deeper to the east.
- Reversed polarity signal before P410s: observed in the entire region but more clear, continuous and stronger in the Gulf of Cadiz, Alboran Sea and the northeast coast of Spain.
- Spatial correlation between the location of the anorogenic magmatism and the downward deflected 410.

In the discussion we have considered both, thermal and compositional interpretations of our results. Our main conclusions are the following:

- Our results are in good agreement with previous studies in the same area (van der Meijde et al., 2005; Dündar et al., 2011). However, the large data volume provided by the IberArray of the TopoIberia project has permitted us to considerably increase the resolution and to resolve new TZT and topography of discontinuities.

- Alboran Sea:

  - We have found consistency between the thickened TZ beneath the Alboran Sea and the position of a high-velocity anomaly in the tomographic images which have been related to the Betic-Alboran slab. Our results suggest that the slab is still cold enough to induce downward deflection of the post-spinel transformation and uplift of the olivine-to-wadsleyite phase transition.
  - The anti-correlated depth of the 410 and 660 beneath the Alboran Sea have provided indirect and independent (from tomography) evidences confirming the steep nature of the Betic-Alboran slab.
  - The nest of deep earthquakes beneath Granada is in an area of high temperature gradient inside the TZ (of about 540 K over a distance of less than 250 km). This may further help to constrain the origin of the deep earthquakes beneath Granada.

- The depressed 410 beneath the Balearic Sea, the presence of strong Pws phases before $P410s$ and the depressed 660 in the Pyrenees and Balearic Sea are consistent with the presence of the Alpine-Tethys remnant slab. The cold stagnant slab can explain the 660 depression; small-scale convection above the 660, triggered by slab dehydration can explain the depressed 410; and the presence of a water concentration increase in the TZ due to dehydration of the stagnant slab can explain the strong reversed polarity signal before $P410s$. Nevertheless, other models proposed to explain the anorogenic magmatism in the Mediterranean are also consistent with our observations.

- We have proposed a compositional origin for the thickened TZ beneath the western Moroccan region. The post-garnet transition together with an Al-rich mantle can explain the downward deflection of the 660 beneath Morocco and the thicker TZ in this area.

- The decreased visibility of the $P410s$ phase beneath the Rif and beneath the western end of the Alboran Sea is possibly caused by structural complexities and/or the thermodynamic properties of the olivine-to-wadsleyite phase change in colder-than-normal mantle.

- For the Gulf of Cadiz and the southwest coast of Portugal we have proposed a thermally thinned TZ, which is consistent with the tomographic images from Monna et al. (2013). Besides, a warm environment and the presence of Al within garnet would also explain the small length-scale depth changes of the 660. We attribute the deeper 660 to the garnet-related phase transition and the shallower 660 to the postspinel transition.

- The presence of melt atop the 410 may explain reversed polarity arrivals from above this discontinuity. Plume material beneath the Gulf of Cadiz and subducted oceanic-lithosphere beneath the Alboran Sea and northeast Spain could provide the higher water content to explain the stronger reversed polarity signal in these areas.

- We have found that the spatial correlation between the active anorogenic magmatism and the 410 depression beneath Morocco and the northeast coast of Spain can be explained with both groups of models proposed for the origin of this magmatic activity. The estimated 410 depression in this area is consistent with a plume-like model with the steam of the plume away from the Mediterranean and affecting only the upper portion of the TZ or with a Mg-enriched mantle due to decompression melting in the overlaying mantle, which shifts the 410 phase transition to higher pressures.

5

Discontinuity characterization

5.1 Introduction

In this chapter, we study the amplitude of the $P410s$ and $P660s$ phases and the width of the corresponding boundaries, which, together with their topography, provide an important link between mineral physics experiments and seismic observations.

The amplitudes of the seismic phases that interact with the discontinuity (e.g., conversions) provide information about the contrast in velocity (v) and density (ρ) across the boundary. Ideally, the converted phases (Pds) are primarily sensitive to S-wave velocity variations and less sensitive to density contrasts (Ammon, 1991; Juliá, 2007). But in the real Earth a number of factors influence the amplitudes of the converted (and reflected) phases, which may lead to erroneous measurements. Such factors are the dependence of the transmission coefficient of the converted waves on the angle of incidence (or epicentral distance), e.g., with variations of about 10 % every 10° in the AK135 model (Kennett et al., 1995); the interference with other energetic phases; focusing or defocusing effects due to discontinuity or mantle structure; intrinsic attenuation. These complexities may affect the analysis and their influence should be considered to constrain the discontinuities (e.g., Helffrich et al., 2003; Chambers et al., 2005).

The width (or sharpness) of the 410 and 660 is associated to how rapidly the mineral phase reaction responsible for the discontinuity occurs with increasing depth. However, mantle temperature and composition (Fe-Mg partitioning in the olivine-system and the presence of H_2O or garnet) can change the characteristics of the phase transitions, making the interpretation of the corresponding seismic discontinuities more difficult (Katsura and Ito, 1989; Wood, 1995; Stixrude, 1997; Weidner and Wang, 1998; Smyth and Frost, 2002; Wang et al., 2004; Litasov and Ohtani, 2005; Wang and Niu, 2010; Schmandt, 2012). The sharpness of the 410 and 660 provides information about the temperature and composition of the upper mantle and TZ.

Seismically, the 410 and 660 are often approximated as linear velocity gradients, which act as low-pass filters to converted waves, attenuating the high frequency energy. The high corner frequency of these filters is related to the thickness of the velocity jump (Richards, 1972; Paulssen, 1988; Bostock, 1999). Thus, amplitude variations in P-to-s conversions observed with long-period (low-frequency) data can

be interpreted as changes in the velocity contrast, while variations observed using short-period (high-frequency) data can be read as changes in discontinuity thickness. In what follows, we analyse the relative amplitude of the converted phases $P410s$ and $P660s$ and the 410 and 660 thickness for a subset of stations selected from the TopoIberia data set.

5.2 Relative amplitudes

To compare the amplitudes of the converted phases between different measurements a normalization is necessary. Therefore, we use the relative amplitudes of $P410s$ ($P410s/P$) and $P660s$ ($P660s/P$). To investigate them, we have employed the data from the 9 stations presented in Chapter 2 (Section 2.4).

5.2.1 Processing

The amplitude values are measured from the linear stack of RFs (already normalized), which are previously low-pass filtered (0.02-0.12 Hz or 0.03-0.2 Hz) to avoid the attenuating effect of the discontinuity width (Richards, 1972; Bostock, 1999). The epicentral distance interval (from 65° to 95°) used in this analysis minimizes the interference with other phases. The RFs are stacked in the time-slowness domain stabilizing the amplitudes and attenuating the contribution from other phases to the conversions.

5.2.2 Results

Our measured values of relative amplitudes (or the amplitude of the conversion coefficient at low frequencies) are shown in the second ($P410s/P$) and third ($P660s/P$) column of Table 5.1 and plotted in Fig. 5.1 (for the clarity of this figure, the large relative amplitudes of station E125 are excluded, but they have not been excluded from the analysis). The plotted amplitudes are mean values obtained using a bootstrap resampling of 21 repetitions. The $P410s/P$ values vary from $0.038 \pm 0.012(2\sigma)$ to $0.130 \pm 0.022(2\sigma)$ and the $P660s/P$ values from $0.033 \pm 0.010(2\sigma)$ to $0.170 \pm 0.018(2\sigma)$. The largest values are for two close stations in north Spain, EARI and E125. At 95 % confidence level (2σ), the $P660s/P$ values for station ANER, CFON, MTE, EARI and EMIN correspond to the predicted value for AK135 of 0.036 at 80°

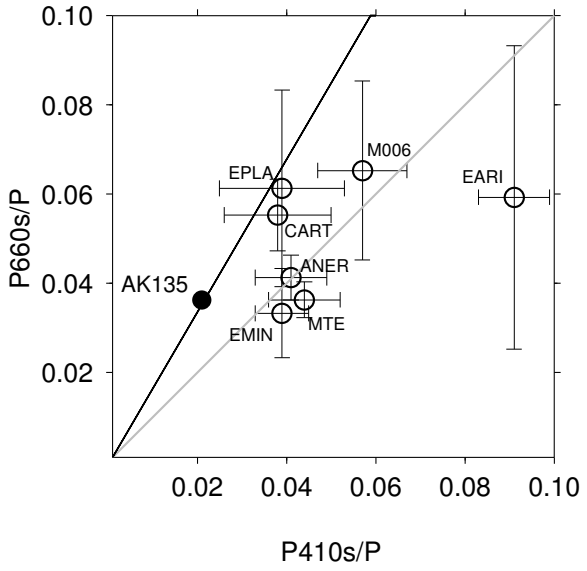

Figure 5.1: Measured $P410s/P$ and $P660s/P$ amplitudes. For the clarity of this figure we excluded E125. Corresponding values are listed in Table 5.1. The gray line is the identity and the slope of the black line (1.7) is the reference $P660s/P410s$ from AK135.

Station	P410s/P ± 2σ	P660s/P ± 2σ	P660s/P410s ± 2σ	Events
ANER	0.041 ± 0.008	0.041 ± 0.005	1.0 ± 0.46	91
CART	0.038 ± 0.012	0.055 ± 0.008	1.45 ± 1.0	78
CFON	-	0.039 ± 0.014	-	56
MTE	0.044 ± 0.008	0.036 ± 0.004	0.8 ± 0.34	76
EPLA	0.039 ± 0.014	0.061 ± 0.022	1.56 ± 1.5	22
EARI	0.091 ± 0.008	0.059 ± 0.034	0.65 ± 0.65	82
E125	0.130 ± 0.022	0.170 ± 0.018	1.31 ± 0.52	16
M006	0.057 ± 0.010	0.065 ± 0.020	1.14 ± 0.8	23
EMIN	0.039 ± 0.006	0.033 ± 0.010	0.85 ± 0.57	82

Table 5.1: Relative amplitude values of the P410s and P660s at individual stations as measured from the linear stack of teleseismic receiver functions (65°-95°).

reference distance. $P660s/P$ is significantly above the predicted value for stations CART, EPLA, E125 and M006. The measurements for stations EPLA, E125 and M006 are based on less than 25 events and have a larger variability as can be seen from their elevated standard deviations. The larger variability can be due to structural complexities and the mean values may not reflect an unperturbed $P660s/P$ measurement. Station CART is in south Spain, over a heterogeneous mantle where the tomographic images show a positive P-wave anomaly and where we have observed large 410 and 660 topography (Chapter 4). Therefore, for this station we cannot discard the presence of a focusing effect due to the discontinuity's topography, which amplifies the converted signals, resulting in larger measured amplitude values. All the stations used in this analysis show $P410s/P$ values above the predicted value for AK135 of 0.021 at 80°. Moreover, it seems that $P410s/P$ is clustered near 0.04.

The obtained mean amplitude values in column 2 and 3 of Table 5.1 represent mean values of the conversion coefficient. The presence of volumetric heterogeneities and/or discontinuity structure can focus (or defocus) waves, resulting in enhanced (or diminshed) amplitudes. This is manifested in the larger scatter that exhibits the measured relative amplitude values for a single station and from individual events. For example, relative amplitude values measured for 16 individual events at station CART vary from 0.04 to 0.2 for $P410s/P$ and from 0.05 to 0.17 for $P660s/P$. Nevertheless, the stacking of RFs from different distances and back azimuths averages the influence of focused or defocused waves stabilizing the amplitude values.

5.2.3 Discussion

The amplitude analysis permits us to qualitatively relate the $P410s/P$ and $P660s/P$ values with velocity contrasts at their corresponding discontinuity depths.

Although stacking stabilizes the estimated amplitude values (in Table 5.1), $P410s/P$ and $P660s/P$ are still influenced by the effect of differential P and S attenuation above the corresponding discontinuity and by the dependence of the conversion coefficients on the incidence angle, i.e., distance range. The amplitude dependence on the distance range is minimized if, instead, we use the ratio $P660s/P410s$ (Helffrich et al., 2003), which is nearly constant at 1.70 (the slope of the black line in Fig. 5.1) for AK135 in the distance range from 65° to 95°. The amplitude ratio also compensates the differential P and S attenuation effect above 410 km depth, which could also be

responsible for amplitude variations (Helffrich et al., 2003). Thus, ideally, we would expect that the estimated $P660s/P410s$ values organize along the black line in Fig. 5.1.

The fourth column of Table 5.1 shows the obtained $P660s/P410s$ values. At stations CART, EPLA, E125 and M006 these values correspond to the predicted value for AK135 at a 95 % confidence level. Therefore, the large $P410s/P$ and $P660s/P$ values measured for EPLA, E125 and M006 are probably caused by non-averaged structure/topography due to the small number of stacked events (less than 25) from a restricted back azimuth range. These large values can also be caused by attenuation effects above 410 km depth. On the other hand, the large values beneath CART (with 78 stacked traces) are probably related to the Alboran Sea heterogeneity (non averaged attenuation effect or focussing of energy due to discontinuity topography). Thus, we may consider that the 410 and 660 velocity contrasts beneath CART, EPLA, E125 and M006 are close to the predicted values in AK135.

Stations ANER, MTE, EARI and EMIN show $P660s/P410s$ estimations clearly below the predicted value of 1.7 for AK135 and they are better organized along the identity function (grey line in Fig. 5.1). These estimations are within the reported values for other regions, which are close to 1 or lower mainly due to a lower $P660s/P$ value (Shearer, 1991; Bostock, 1998; Helffrich et al., 2003; Shen et al., 2008). However, all our anomalous $P660s/P410s$ values correspond to $P410s/P$ ratios which are larger than the expected AK135 value, while the $P660s/P$ ratios are observed with expected amplitudes. Stations ANER, MTE, EARI and EMIN are far from each other and it is difficult to find a common structural explanation (heterogeneity or discontinuity's topography) for the anomalous $P410s/P$ values.

One way to obtain a higher $P410s/P$ value is if there is lower S attenuation above the 410. However, this would also increase the $P660s/P$ value, which is not what we observe. Another possibility is that the S-wave velocity jump at 410 km might be actually larger than in AK135. We need a velocity increment of 0.41 km/s at the 410 to obtain $P660s/P410s = 1$. This corresponds to a velocity increase of 8.4 % at 410 km depth, while this value is 4.3 % in AK135. The large S-velocity jump may be related with the low-velocity layer atop the 410, which is responsible for the amplitude-reversed signal before the P410s arrival (clearly seen in ANER, MTE and EARI in Fig. 2.16). Previous studies for other regions have reported a low-velocity layer atop the 410 with a reduction in velocity of the order of 4-5% (e.g. Song et al.,

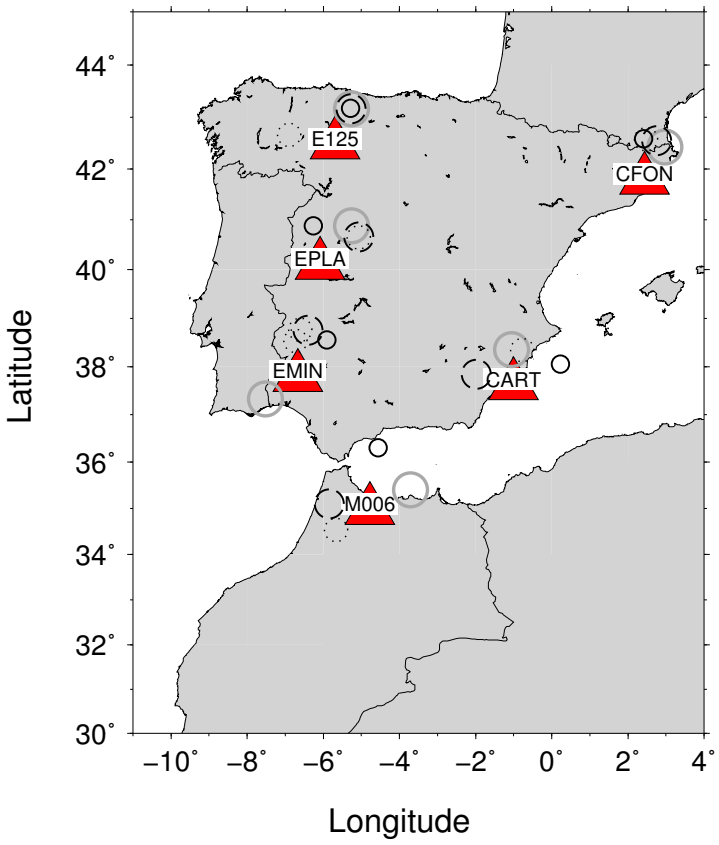

Figure 5.2: Location of the broad-band stations (red triangles) and the piercing point locations (circles) of the P520s phases where we investigated the thickness of the 410-km and 660-km discontinuities.

2004; Vinnik and Farra, 2007; Jasbinsek et al., 2010; Schmandt et al., 2011). A low velocity layer equal in magnitude to the positive velocity jump produced by the α-to-β transition would result in a larger velocity contrast at the 410 leading to larger $P410s/P$ values.

5.3 Width of the 410 and 660 discontinuities

To our knowledge, the 410 and 660 thickness beneath Iberia has been analysed in a previous study only for one single station in central Spain (van der Meijde et al., 2003). The study by van der Meijde et al. (2003) uses RFs and focuses on the entire

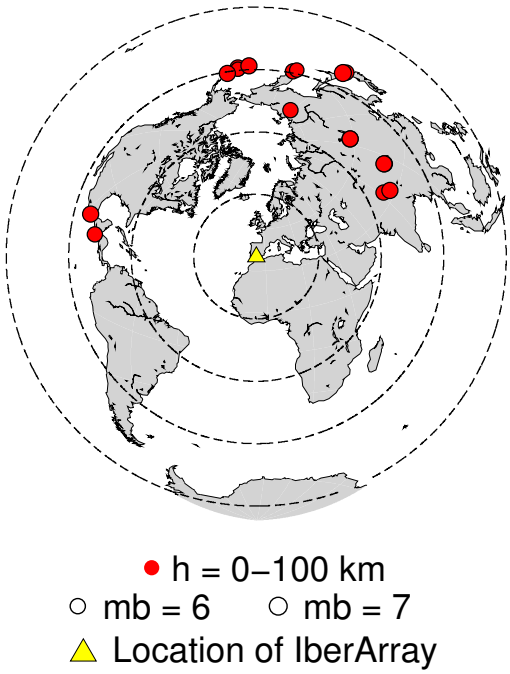

Figure 5.3: Location of the teleseismic events used in the analysis of the 410 and 660 thickness. Dashed circles are plotted every 30°.

Mediterranean region. Their estimated widths of 30-35 km for the 410 and of less than 5 km for the 660 may not represent the thickness beneath our study area and does not provide information on spatial variability and eventual correlation to seismic velocity anomalies.

To investigate the 410 and 660 discontinuity widths and their possible spatial variations we use stations CART, CFON, E125, EMIN, EPLA and M006, which are distant from each other. Fig. 5.2 shows the station locations (red triangles) and the piercing points of P520s phases (circles) for each event-station pair. The teleseismic events are shown in Fig. 5.3 and listed in Table 5.2.

5.3.1 Methodology and processing

Often, the 410 and 660 discontinuities are approximated by linear velocity gradients which extend over a depth range (Δz). Consequently, the corresponding transmission-conversion coefficients (Fig. 5.4) act as low-pass filters to converted waves (Paulssen, 1988; Bostock, 1999). Bostock (1999) demonstrates that significant energy is con-

Station	year.jday.hour.min	Distance [°]	Back azimuth [°]	Depth [km]	mb	Symbol in Figs 5.2, 5.7, 5.8, 5.9
CART	2010.246.11.16	91.22	356.79	23.00	6.5	solid gray
	2008.206.01.43	89.83	13.35	27.00	6.2	dotted
	2010.181.07.22	85.39	287.02	20.00	6.3	dashed
	2007.125.08.51	65.12	64.99	9.00	6.1	solid black
CFON	2008.128.16.02	93.87	32.07	19.00	6.2	solid gray
	2008.207.00.29	87.29	2.17	21.00	5.9	dotted
	2008.217.04.42	85.95	16.56	76.00	5.8	dashed
	2008.220.18.30	86.41	358.82	12.00	5.8	solid black
E125	2011.084.11.36	93.95	24.85	39.00	6.2	solid gray
	2011.097.13.11	77.62	281.96	166.00	6.6	dotted
	2011.173.21.50	92.96	24.14	33.00	6.7	dashed
	2011.211.18.53	95.33	26.25	30	6.3	solid black
EMIN	2007.324.17.55	85.05	236.14	15.00	6.1	solid gray
	2008.141.13.53	91.32	356.58	27.00	6.3	dotted
	2008.174.23.56	72.10	12.29	18.00	6.1	dashed
	2008.240.01.35	72.48	37.67	16.00	6.3	solid black
EPLA	2008.240.01.35	70.39	38.40	16.00	6.3	solid gray
	2008.315.01.22	74.73	53.71	19.00	6.3	dotted (660)
	2008.241.15.22	41.42	197.20	12.00	6.3	dotted (410)
	2009.240.01.52	74.58	53.65	13.00	6.3	dashed
	2010.199.05.56	86.37	350.23	14.00	6.6	solid black
M006	2008.009.08.26	72.32	62.74	10.00	6.4	solid gray
	2009.317.03.05	82.36	240.11	27.00	6.5	dotted
	2008.106.03.03	78.99	278.85	33.00	6.1	dashed
	2008.052.02.46	43.51	7.44	12.00	6.1	solid black

Table 5.2: Teleseismic events used in the analysis of discontinuity thickness.

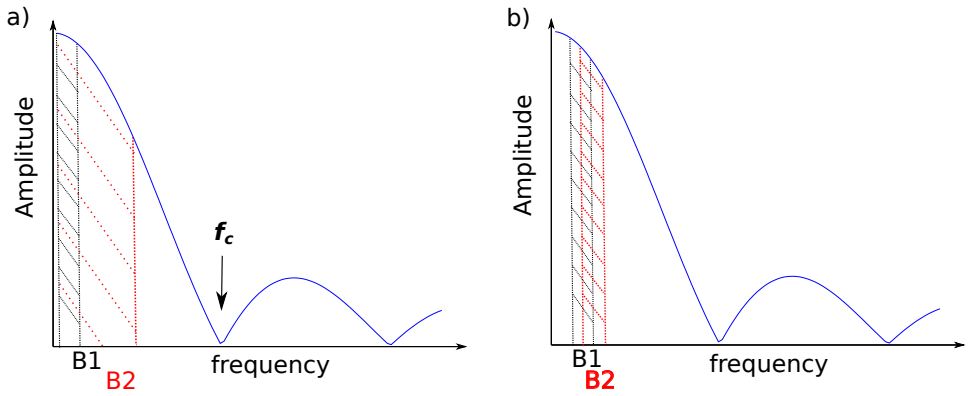

Figure 5.4: Schematic plot to illustrate the frequency dependence of the transmission-conversion coefficient for a linear velocity gradient. a) Methodology 1: the waveform coherence between phases P and Pds (d=410, 660) is investigated filtering Z and R components with different band-pass filters of increasing high corner-frequencies (0.02-0.08 Hz, 0.02-0.16 Hz, 0.02-0.32 Hz Hz, 0.02-0.64 Hz, 0.02-1.28 Hz, 0.02-2.56 Hz). b) Methodology 2: the components are filtered using overlapping band-pass filters (0.02-0.08 Hz, 0.04-0.16 Hz, 0.08-0.32 Hz Hz, 0.16-0.64 Hz, 0.32-1.28 Hz, 0.64-2.56 Hz). The black arrow indicates the high-corner frequency of the transmission-conversion response.

verted from linear velocity gradients with extent:

$$\Delta z < \lambda_P/2, \tag{5.1}$$

where λ_P is the incident P wavelength:

$$\lambda_P = v_P/f_p, \tag{5.2}$$

and v_P is the mean P-wave velocity at the corresponding discontinuity depth. Thus, to constrain the discontinuity thickness, we need to find the highest frequency f_P^{max} for which significant P-wave energy is converted. This approximation assumes that due to the low energy transmission one observes energy only for the frequencies which correspond to the main lobe of the transmission coefficient. If the energy content of the P wave extends to larger frequencies, then, the largest f_P^{max} will approximate the high-frequency corner (f_c) of the transmission-conversion response. Finally, the 410 and 660 discontinuity widths are estimated from Eqs 5.1 and 5.2:

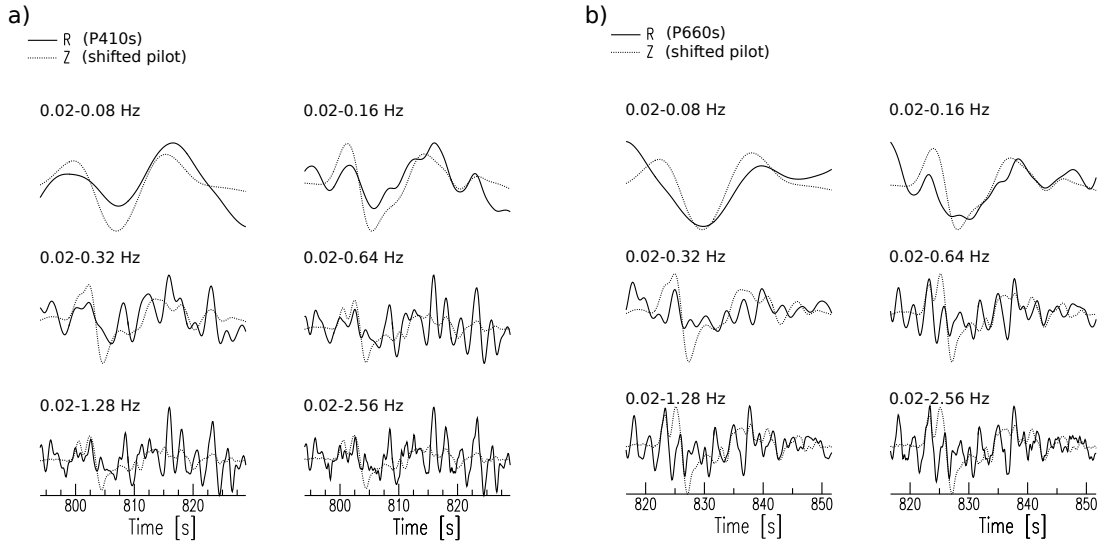

Figure 5.5: Waveform comparison of the direct P-wave in the Z component or the pilot wavelet (dotted line) and (a) the P410s phase in the R component (solid line) and (b) the P660s phase in the R component (solid line). Each panel shows the corresponding P, P410s and P660s waveforms for the event 2010.181.07.22 (as recorded at station CART) after filtering R and Z components with different band-pass filters.

$$\Delta z < v_P/(2f_P^{max}), \tag{5.3}$$

Figs 5.5 (a) and (b) show the waveform comparison between the P phase in the Z component (shifted pilot) and the $P410s$ and $P660s$ phases in the R component after filtering with different band-pass filters. This is a real data example from a teleseismic event (distance=85°) registered at station CART (2010.181.07.22 in Table 5.2). From this figure, it is evident that as the frequency contents of the filter increase, the waveforms of the converted phases (Pds, $d = 410, 660$) and the P phase are less similar. This is because the *low-pass discontinuity* attenuates the high frequency components of the Pds phase.

In order to provide discontinuity thickness estimates, we have designed two approaches which basically find the corner frequencies (f_P^{max} in Eq. 5.3) through measuring the waveform coherence between the conversions Pds (d=410, 660) and the P phase. The waveform coherence is measured using the CCGN (Chapter 2) in different frequency bands. Figs 5.4 (a) and (b) illustrate the two different methodologies to

define the corner frequencies to filter the R and Z components. The blue sinc-like function represents the frequency dependence of the transmission-conversion coefficient. Fig. 5.4 (a) illustrates methodology 1 (M1), where the waveform coherence between P and Pds ($d = 410, 660$) is investigated filtering the Z and R components with different band-pass filters (B1, B2, etc) with increasing high corner-frequency (0.02-0.08 Hz, 0.02-0.16 Hz, 0.02-0.32 Hz Hz, 0.02-0.64 Hz, 0.02-1.28 Hz, 0.02-2.56 Hz). That is, the waveform coherence is determined for a broad frequency band which successively includes higher frequencies to find f_P^{max} (or the approximation of f_c). The estimated f_P^{max} frequency with M1 will be the high corner-frequency of the filter for which the coherence value does not change or present variations smaller than 10 % from the value of the following filter. Fig. 5.4 (b) shows methodology 2 (M2), where the data are filtered using overlapping band-pass filters (0.02-0.08 Hz, 0.04-0.16 Hz, 0.08-0.32 Hz Hz, 0.16-0.64 Hz, 0.32-1.28 Hz, 0.64-2.56 Hz). With M2 the estimated f_P^{max} frequency will be the high corner-frequency of the filter for which the phases show waveform coherence smaller than a defined threshold value (e.g., 0.4).

Figs 5.6 (a) and (b) show the resultant CCGNRs when using both methodologies for the event presented in Fig. 5.5. The frequency bands for method M1 and M2 are written to the right of each cross-correlogram. The coherence values measured with M1 are shown with the dashed circles in Fig. 5.7 (a) for the $P410s$ phase and in Fig. 5.7 (b) for the $P660s$ phase. The corresponding values with methodology M2 are shown in Fig. 5.8 (a) and (b). Both methodologies show similar values for the estimated corner frequencies when using the previously mentioned criteria. For this particular event, we estimated $f_{P,M1}^{max} = 0.64$ Hz and $f_{P,M2}^{max} = 0.32$ Hz for the $P410s$ phase and $f_{P,M1-2}^{max} = 0.16$ Hz for the $P660s$ phase (see black arrows in Figs 5.7 and 5.8). Thus, using Eq. 5.3 with the corresponding averaged value of v_P from AK135 ($v_P^{410} = 9.2$ km/s and $v_P^{660} = 10.5$ km/s), the estimated thickness values are $\Delta z_{410}^{M1} < 7$ km, $\Delta z_{410}^{M2} < 14$ km and $\Delta z_{660}^{M1-2} < 32$ km. The 660 thickness is not well constrained in this example. The discrepancy between $f_{P,M1}^{max}$ and $f_{P,M2}^{max}$ for the P410s phase is probably due to the drop of the amplitude spectrum after 0.3 Hz, which does not favour method M2. Therefore, we used M1 for the remaining stations. The rest of the circles in Figs 5.7 and 5.8 are the measured coherence values for other events registered at station CART (Table 5.2). The figures also show the normalized amplitude spectrum of these events. The frequency content of the pilot in the Z

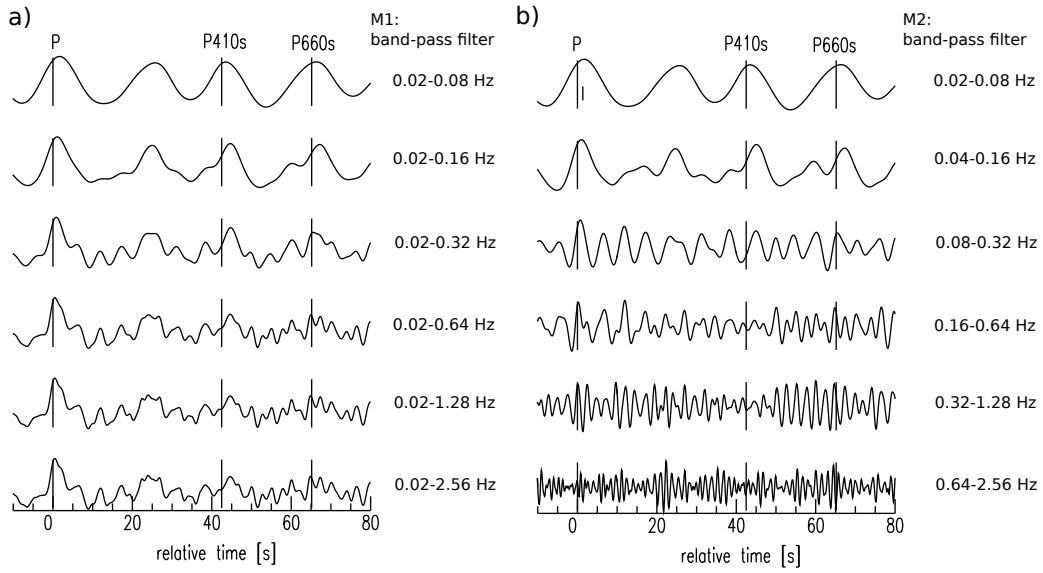

Figure 5.6: CCGNR correlograms of event 2010.181.07.22, as recorded at station CART, after filtering R and Z components for 6 different frequency bands (a) method 1 and (b) method 2.

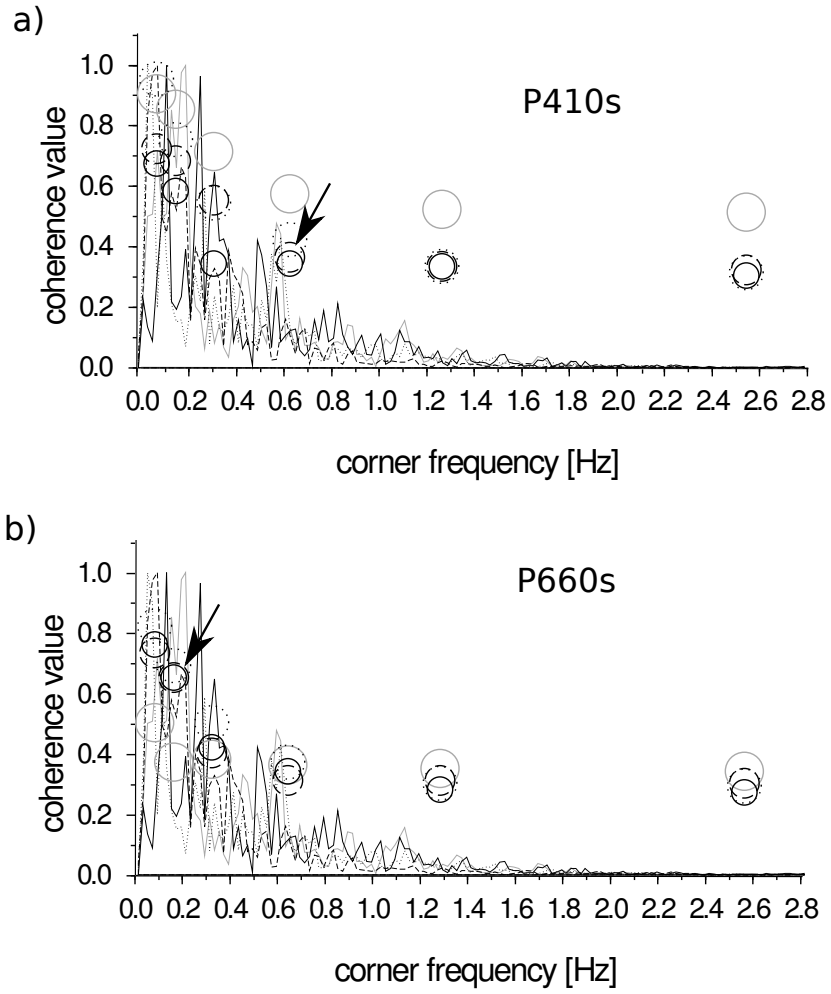

Figure 5.7: CCGN coherence measurements (circles) obtained with methodology 1 (Fig. 5.4 a), for the events registered at station CART. a) P410s phase and b) P660s phase. Black and grey lines show the normalized amplitude spectra for each pilot. The black arrows indicate the coherence value used to define the high-corner frequency of the transmission-conversion response, f_c, for one event (dashed circle).

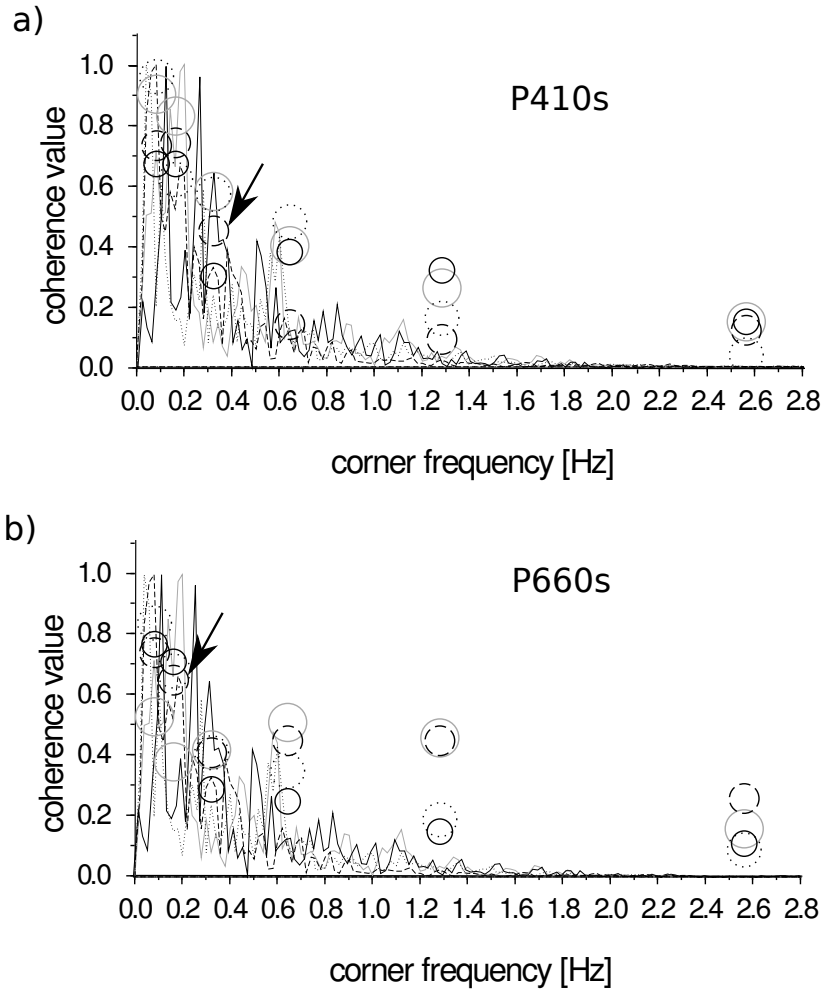

Figure 5.8: CCGN coherence measurements (circles) obtained with methodology 2 (Fig. 5.4 b), for the events registered at station CART. a) P410s phase and b) P660s phase. Black and grey lines show the normalized amplitude spectra for each pilot. The black arrows indicate the coherence value used to define the high-corner frequency of the transmission-conversion response, f_c, for one event (dashed circle).

component for these records is below 0.8 Hz, which is also the frequency content for the events listed in Table 5.2. With these data it is not possible to retrieve an f_P^{max} value larger than 0.8 Hz since as we increase the high-corner frequency of the filters we introduce frequencies that are not present in the P phase. Thus, the spectrum provides information about the smallest thickness that can be resolved with our data, which in our case is about 6 km.

5.3.2 Results

The 410 and 660 thickness values estimated for station CART are shown in Fig. 5.9 with the red bars indicating the estimated values with M2. The thickness values for the rest of the stations were measured using only M1. Some of the stations only have 2 or 3 thickness estimations because we discarded less reliable measurements from other analysed earthquakes (e.g., whenever the $P410s$ or $P660s$ phases show great variability in the travel times for different frequency bands). Our results show large scatter in the discontinuity thickness estimation from different events, even for coinciding piercing points. For example, Δz_{660} at stations CFON, EPLA, EMIN, E125 and Δz_{410} at stations CFON, EMIN, E125 vary by more than about 10 km. These differences are to be expected due to the variable frequency content of the different pilots (P phases) and because each record has a different noise component, which may impair the waveform similarity before we can appreciate the frequency dependent attenuation due to the thickness of the discontinuity. Moreover, waveform alterations can occur as a result of interferences -through multipathing, focusing or defocusing effects, among others- due to the complex wave propagation in the heterogeneous mantle and crust. Therefore, whenever we have more than one measurement for a piercing point cluster, we use the thinnest discontinuity as the upper limit of the discontinuity thickness for that piercing point area. Fig. 5.10 summarizes the results, with each estimated thickness value plotted near the corresponding piercing point or group of piercing points (black numbers for the 410 width and red ones for the 660 width). The red triangles correspond to the stations used in the thickness analysis and the yellow ones show other stations that were also used in Section 5.2. From this analysis, we conclude that the 410 and 660 thickness are on average between 7-16 km with some larger values of about 30 km, which however, could be underestimated in case of unresolved thickness due to noise contamination and/or missing high frequency contents of the P phase.

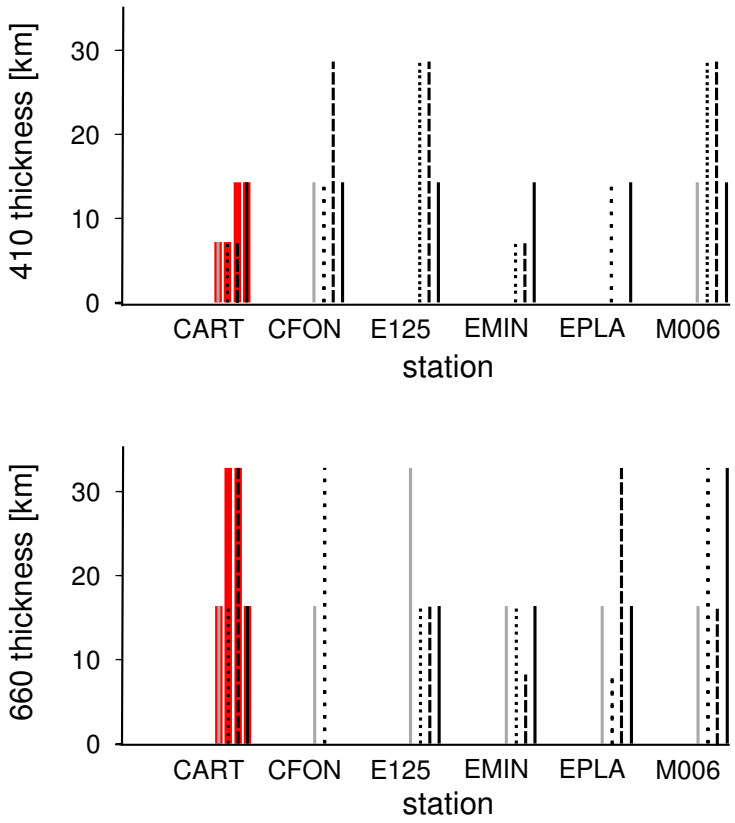

Figure 5.9: Discontinuity thickness estimation of a) the 410-km discontinuity and b) the 660-km discontinuity at 6 different stations (Fig. 5.3).

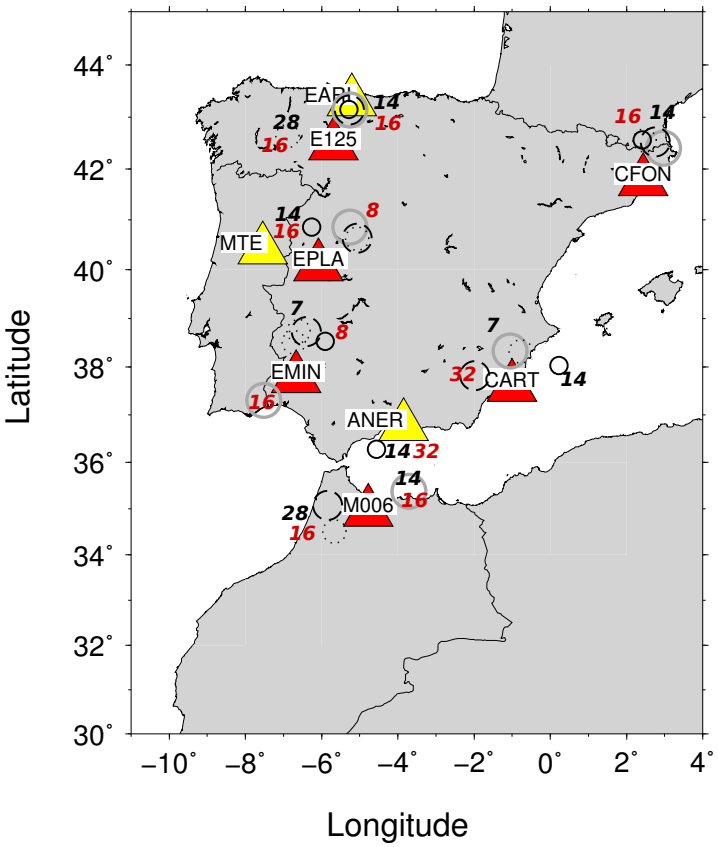

Figure 5.10: Measured values of discontinuity thickness for the 410-km discontinuity (black numbers) and the 660-km discontinuity (red numbers). The values were manually located close to the corresponding P520s piercing points. The red triangles correspond to the stations used in the thickness analysis and the yellow ones show other stations that were also used in Section 5.2.

5.3.3 Discussion

5.3.3.1 Thickness constraints from mineral physics

The published depth interval for the olivine-to-wadsleyite transition (410), in dry $(Mg, Fe)_2SiO_4$-systems and at typical TZ temperatures, ranges between 6 to 18 km (Akaogi et al., 1989; Smyth and Frost, 2002; Frost, 2003). The transition width depends on the Fe content of the olivine-system (wider for higher Fe content) (e.g., Katsura et al., 2004, fig. 3). For a fixed Mg-Fe partitioning, the α-to-β transformation is sharper at higher temperatures but broader at lower temperatures (Katsura and Ito, 1989; Katsura et al., 2004) affecting the visibility of the discontinuity in subduction related environments (Bina and Helffrich, 1994). For example, an increase in T of 100 K will reduce the width of the 410 by 2-3 km (Bina and Helffrich, 1994; Katsura and Ito, 1989). Additionally, H_2O might act to broaden the transformation interval to 22-40 km (Wood, 1995; Smyth and Frost, 2002; Frost, 2003; Litasov et al., 2005; Katsura et al., 2004). For example, a small amount of 100 ppm of water will broaden the transition by about 3 km (Wood, 1995; Frost, 2003). Thus, the expected widths of the 410 range between about 4 to 40 km, depending on the composition (Mg-Fe partitioning and H_2O) and temperature of the upper mantle.

On the other hand, the pressure interval where ringwoodite and perovskite + magnesiowustite (660) coexist is about 0.1-0.5 GPa (5-20 km) (Ito and Takahashi, 1998; Hirose, 2002; Litasov et al., 2005) and it appears to remain narrow over a broad range of temperatures (Ito and Takahashi, 1998). Like the wadsleyite, the ringwoodite has also enhanced water storage capacity over the upper and lower mantle mineral assemblages (Kohlstedt et al., 1996). Although the presence of water can move the post-spinel phase transition to higher pressures in colder environments, it does not have an appreciable effect on the thickness of this transition (Higo et al., 2001; Litasov and Ohtani, 2005). Therefore, the 660 must be a sharp discontinuity with a thickness less than 20 km, if it is solely caused by the post-spinel phase transition. The garnet-to-perovskite phase transition (Appendix B), which is also expected at the base of the TZ, occurs in a wider pressure interval of about 1-1.5 GPa (40-60 km). However, the effective width of these phase transitions could be narrowed by compositional frustration of the full reaction interval in the pure-garnet system (Stixrude, 1997). Therefore, both discontinuities would appear as sharp discontinuities unless they

partially overlap. In this case, it is possible to have a single and broad discontinuity (e.g., Wang and Niu, 2010, in a subduction area in north-east China).

5.3.3.2 Thickness constraints from seismology

Seismically, the 410 and 660 discontinuities have been observed to maximum frequencies of about 1 Hz leading to sharp transitions (< 10 km wide intervals) (e.g. Paulssen, 1988; Vidale et al., 1995; Collier and Helffrich, 1997; Landes et al., 2006). Differences with the mineral physics experiments have been attributed to: presence of non-transforming phases (Stixrude, 1997); focusing effects which might boost the amplitudes of conversions (or reflections) above the corner frequency of the transmission-conversion (or reflection) response (f_c in Fig. 5.4) (Shearer, 2000); non-linear velocity increases, predicted by models of mineral phase changes (e.g., Helffrich and Bina, 1994), where the highest-frequency reflections/conversions are determined more by the sharpness of the steepest part of the profile than by the total layer thickness (Shearer, 2000); gravity-driven diffusion of hydrogen, which may enrich the lower parts of the two-phase region in wadsleyite and the upper part in olivine, thus sharpening the boundary (Smyth and Frost, 2002).

Other studies have reported wider discontinuities. Beneath central Spain, for example, van der Meijde et al. (2003) found a 410 discontinuity of about 30-35 km associated with the presence of water in wadsleyite. In subduction related environments, the 660 has been observed as a wide velocity gradient of about 50-70 km, which has been associated to complex velocity structures due to the post-spinel (olivine phase transition) and ilmenite-to-perovskite (garnet related) phase transitions (Wang and Niu, 2010; Schmandt et al., 2011; Schmandt, 2012).

5.3.3.3 410 and 660 thickness beneath Iberia

We cannot discard a thickness underestimation with our methodology, related to unresolved thickness due to noise contamination and/or missing high frequency contents of the P phase. Therefore, our estimated thickness values of 7 to 30 km, for both discontinuities, can be considered as upper limits on the 410 and 660 velocity gradient thickness beneath Iberia and Morocco.

We have estimated a 660 thickness of 16 km for the entire area with exception of larger thickness values of 32 km beneath south Spain and the Alboran Sea and smaller thickness of 8 km in the central area of Iberia. For the 410 we have estimated

a thickness value of 7-14 km for almost the entire study area, with exception of larger values of 28 km in the north-west corner of Iberia and Morocco. Assuming that our estimated values are well-constrained upper limits, it can be considered that the observed differences in the thickness of the 410 and 660 represent spatial variations of this parameter.

Because the post-spinel transition remains narrow over a broad range of temperatures (and Mg-Fe partitioning), the spatial variation in the 660 thickness might reflect the dual origin of this discontinuity (olivine-related and the garnet-related phase transitions). This complicates the interpretation in normal-to-cold mantle environments, because we cannot be sure to which phase transition one should attribute the 660 width since both discontinuities may appear at similar depth (depending on the Al contents of the garnet), although the post-spinel occurs in a thinner depth interval than the garnet-related phase transition. The broad 660 of about 30 km coincides with the location of the cold Alboran slab. Other studies also reported broad 660 discontinuities in subduction related environments, explained as combined velocity gradients due to post-spinel and ilmenite-to-perovskite phase transitions (Wang and Niu, 2010; Schmandt et al., 2011; Schmandt, 2012). Therefore, if the ilmenite-to-perovskite phase transition is present, the 30 km thickness estimation for the 660 beneath the Alboran Sea might be due to combined velocity gradients.

In Chapter 4, it was shown the presence of a reversed-polarity signal before the P410s (Fig. 4.19), which is attributed to partial melt atop the 410 due to high water concentrations (e.g. Tauzin et al., 2010, and references therein). If the melt interpretation of the $P410s$ precursory signal with reverted polarity is correct, then most of the 410 thickness is likely controlled by the increased water contents. Thus, it seems that the spatial variation of the 410 thickness might reflect variable proportions of water in the TZ minerals (rather than temperature variation or Fe-Mg partitioning). Our estimated values for the width of the 410 (7-14 km) are consistent with 200 to 500 ppm of water in wadsleyite (obtained from fig. 16 in Wood and Corgne, 2007, pp. 81).

Our estimated 660 thickness values are in good agreement with a previous RFs study which covered the entire Mediterranean region (van der Meijde et al., 2003). In their study, van der Meijde et al. (2003) investigate *P-to-s* conversions from the 660 in the Mediterranean region. One of the stations (PAB) in van der Meijde et al. (2003) is in central Spain. For this station, they report a sharp 660 of 5 km width. In good

agreement with van der Meijde et al. (2003) we have estimated a 660 of 8 km width for station EPLA, which is close to station PAB. We have found a 410 thickness of 7-14 km in the same area, which is much thinner than the transition width reported in van der Meijde et al. (2003) of about 30-35 km, consistent with about 700 ppm to 1500 ppm of water in wadsleyite. Although our results are in agreement with lower water contents, the 200 to 500 ppm water concentration in wadsleyite that we estimate is still a considerable amount of water (see fig. 16 in Wood and Corgne, 2007, pp. 81).

5.4 Conclusions

The $P410s$ amplitudes and the 410 widths are consistent with spatial variations in the water concentrations in the TZ beneath Iberia. In particular, the variation of the 410 thickness (7-28 km) agrees with 200-500 ppm of water in wadsleyite. On the other hand, to explain the anomalously high relative amplitude values of the $P410s$ phase ($P410s/P$) we need to assume a negative velocity jump atop the 410, which increases the total velocity jump across the 410 km depth discontinuity. The negative velocity jump immediately above 410 km depth is consistent with the reversed-polarity signal that we observed before $P410s$, which is related with partial melt atop the 410 caused by a water concentration increase in the TZ.

The spatial variation of the 660 thickness might reflect the presence of the garnet-related phase transition (garnet-to-perovskite or ilmenite-to-perovskite) together with the post-spinel. This could lead to complex velocity structures which might be responsible for the broader 660 in the cold Alboran Slab. The estimated relative amplitude values of the $P660s$ phase agree with the velocity jump in AK135 at 660 km depth.

A

Receiver functions

A.1 Transmission path impulse response

The P coda consists of all type of scattered, reflected, diffracted and converted waves. Among these coda waves, are the S waves converted from P waves at the seismic discontinuities below the station. For a teleseismic earthquake, the near-vertically incoming wavefield leads to a separation of the P- and SV-waves energy in the vertical and radial components, respectively. Thus, the P-to-s conversions are detected on the radial component. Consequently, the P coda in the radial component contains information about the structure beneath the station. Deconvolution of the radial component by the vertical component is used to eliminate the source influence and to isolate the P-to-s conversions (Langston, 1979). The resultant time series is called receiver function (RF) and can be viewed as the relative response of the Earth's structure (or transmission path impulse response) near the receiver. Another kind of receiver function is the SV component deconvolved by the P component (Vinnik, 1977), obtained by rotating the radial and vertical components considering the ray incidence angle to maximize SV- and P-wave energy.

In what follows, we explain the RF computation in more detail. The radial component, $r(t)$, of a teleseism can be expressed in terms of the transmission path impulse response, $h(t)$. Using the convolutional model of the trace (eq. 2.6), in the absence of noise, this relation is:

$$r(t) = s(t) * h(t), \tag{A.1}$$

where $s(t)$ is the source wavelet and $*$ denotes convolution. The source wavelet is known as the "*teleseismic source function*", composed of the source function, near source reverberations and the instrument response.

According to the convolution theorem, convolution in the time domain is mapped as multiplication in the frequency domain. The frequency domain form of Eq. A.1 is:

$$R(w) = S(w)\ H(w), \tag{A.2}$$

where the capital letters denote the Fourier transform pairs of the quantities in Eq. A.1 and w is the angular frequency. In what comes next, we omit the frequency argument to clarify the notation.

The objective of the RF technique is to obtain the impulse response H. This objective can be achieved through deconvolution of the radial component R by the source function S. The source function is an unknown parameter which is often approximated with the recorded teleseismic P-wave source function on the vertical component ($S \approx Z$) (e.g., Bostock, 2007). Finally, an estimate of H is obtained, which is denoted as RF.

$$H \approx RF = \frac{R}{Z}. \tag{A.3}$$

There exists a variety of deconvolution techniques to solve Eq. A.2. These techniques are applied either in time or in the frequency domain (e.g. Wiener, 1964; Clayton and Wiggins, 1976; Kikuchi and Kanamori, 1982; Gurrola et al., 1995; Bostock, 1998; Ligorría and Ammon, 1999; Chen et al., 2010). Deconvolution in the frequency domain (Eq. A.3) implies a spectral division. However, the division of small amplitudes (holes in the Z amplitude spectrum) makes the spectral division instable and in practice a regularization of the deconvolution is required. A commonly used strategy in the frequency domain is the water-level method of Clayton and Wiggins (1976). This method fills the spectral holes in Z to prohibit instability resulting from division by very small numbers. The approaches in the time domain are iterative methods, which avoid dividing by the Z spectrum. These iterative methods were first introduced by Kikuchi and Kanamori (1982) to estimate large-earthquake source time functions and then adapted to estimate RFs (Ligorría and Ammon, 1999). The iterative nature of these methods makes them more computation-intensive.

Both, time and frequency domain methods, have been widely used to compute the RFs (e.g. Ammon, 1991; Kind et al., 1995; Dueker and Sheehan, 1997; Vinnik and Farra, 2002; Dündar et al., 2011; Knapmeyer-Endrun et al., 2013) and there is no preferred methodology. Scientists tend to favour a certain method for different reasons and have not explored the full realm of RF deconvolution techniques.

In the following section, we will continue with the water-level deconvolution of Clayton and Wiggins (1976) to compute the RF. We choose this deconvolution method because it is closely related to our approach (see Section 2.2.2).

A.2 Water-level deconvolution receiver functions

In this section, we summarize the water-level deconvolution method from Clayton and Wiggins (1976).

In practice, the spectral division in A.3 is obtained by:

$$RF = \frac{R\ Z^*}{Z\ Z^*}, \tag{A.4}$$

where Z^* is the complex conjugate of Z.

Real seismograms are contaminated with noise ($N = N(w)$). Thus, we consider Eq. A.2 with the noise component ($R = SH + N$) and replace it in Eq. A.4:

$$RF = \frac{S\ Z^*}{|Z|^2}H + \frac{Z^*}{|Z|^2}N, \tag{A.5}$$

where $Z\ Z^*$ was substituted by the power spectrum of the Z component, $|Z|^2$.

When the estimated source amplitude becomes small ($|Z| \sim 0$), the factor multiplying H is $O(1)$ (assuming that Z does not deviate too far from S), however, the factor multiplying N is $O(1/|Z|)$. Therefore, the later can destabilize the deconvolution. In order to prevent the noise term from becoming too large, Clayton and Wiggins (1976) established a minimum amplitude level for the source. The minimum source amplitude is termed the water-level. With this change the RF becomes:

$$RF = \frac{SZ^*\ H + Z^*N}{max\{|Z|^2, k\ |Z|^2_{max}\}}, \tag{A.6}$$

where k is the water-level parameter ($0 \leq k \leq 1$).

Because the teleseismic source function is recorded with less energy at the higher frequencies, the source wavelet and its approximation, Z, naturally act as a low-pass filter. Consequently, $1/Z$ (the operator in the deconvolution) is effectively a high-pass filter and amplifies the unwanted high-frequency noise (Gurrola et al., 1995). The water-level parameter attenuates the high-frequency noise by lowering the amplitude of the high-pass filter to $k|Z|_{max}$. The choice of the water-level parameter is a subjective task. In practice, the water-level deconvolution is performed for a range of $k\ \epsilon\ [0, 1]$ and the stability of the deconvolution is checked by comparing the impulse response for the various water-levels. Typical values of the water-level parameter are 0.0001, 0.001, 0.01, and 0.1.

It is interesting to note that as k approaches unity, the RF is just a scale factor times the cross-correlation of R and Z (Clayton and Wiggins, 1976). This makes our approach in Section 2.2.2 closely related to the water-level deconvolution method if we used the classical cross-correlation in our methodology.

In practice, the seismogram components are bandpass filtered prior deconvolution. The pass-band is commonly defined by the band of significant energy of the seismogram. This filtering is performed to exclude the spurious noise information from the RF, specially at the higher frequencies.

Another common practice is to apply a Gaussian filter (low-pass) during deconvolution, which was introduced by Langston (1979). This prevents from obtaining too much detail which is not warranted by the observations; in other words, it stabilizes the RFs. The same result is obtained if the data is low-pass filtered prior to the water-level deconvolution.

B

The presence of other transforming and non-transforming phases and their geophysical implications

The seismic discontinuities in the TZ at 410, 510 and 660 km depth are related to mineral phase changes in the olivine($(Mg, Fe)_2SiO_4$)-system (Fig. 1.4) (see reviews in Shearer, 2000; Helffrich, 2000). However, there are other reactions taking place in the TZ which involve the mineral garnet. Mineral physics experiments show that, depending on the aluminum (Al) proportion in garnet and the temperature of the mantle, the garnet-related phase transitions are also responsible for a number of discontinuities near the bottom of the TZ (Weidner and Wang, 1998; Hirose, 2002; Wang et al., 2004). Lately, several seismological studies support that garnet phase transformations must be taken into account to interpret the results in high temperature regions of the mantle (Deuss et al., 2006; Deuss, 2007; Cao et al., 2011) or in cold subduction environments (Ai and Zheng, 2003; Schmerr and Garnero, 2007).

B.1 Garnet-related discontinuities near 660 km depth

The reactions which involve the mineral garnet ($X_3Y_2(SiO_4)_3$, where $X = (Ca, Mg, Fe)$ and $Y = (Al, Fe, Cr)$) are gradual and occur over broad depth intervals. In the depth range between 600 and 800 km, the garnet transforms to ilmenite and subsequently to perovskite. These mineral phase transitions depend on temperature and on the Al content of garnet (Weidner and Wang, 1998; Akaogi et al., 2002; Hirose, 2002; Wang et al., 2004). In a pyrolite-like composition, Al proportions larger than 4 % can be considered as high. (Weidner and Wang, 1998; Wang et al., 2006). Therefore, assuming a high Al content:

- At low mantle temperature, the $rw \rightarrow pv + mw$ transition is preceded by the garnet-to-ilmenite phase transition ($gt \rightarrow il$) with a positive Clapeyron slope and by the ilmenite-to-perovskite phase transition ($il \rightarrow pv$) with a negative Clapeyron slope. Because the $il \rightarrow pv$ and the $rw \rightarrow pv + mw$ (Section 1.2.2) may only be separated by 10 km in depth, they may appear as a single seismic discontinuity (e.g. fig. 2 in Weidner and Wang, 1998).

- In normal to hot mantle, the $rw \rightarrow pv + mw$ is followed by the garnet-to-perovskite ($gt \rightarrow pv$) reaction with a positive Clapeyron slope (Weidner and Wang, 1998; Hirose, 2002).

- In hot mantle regions ($\geq 1800°C$), if the Al proportion is very high (e.g., 5 %), the perovskite is not stable and the amount of ringwoodite is diminished by the transition of ringwoodite to garnet (not perovskite) plus magnesiowustite ($rw \rightarrow gt + mw$) (due to chemical interaction between olivine and garnet in a pyrolit-like composition) with a negative Clapeyron slope, and is followed by the $gt \rightarrow pv$ transition (Weidner and Wang, 1998; Hirose, 2002).

In the extreme case of an Al-poor garnet (1 % Al or less), the garnet-related transitions are the $gt \rightarrow il$ and the $il \rightarrow pv$, which will occur at all mantle temperatures (e.g., Wang et al., 2006, table 2). In this case, the perovskite-forming reactions will be the $rw \rightarrow pv + mw$ and the $il \rightarrow pv$ (not $gt \rightarrow pv$).

The orange lines in Fig. 1.6 (Chapter 1) show the response of the garnet-related phase changes to a negative (left) and positive (right) thermal anomaly when the Al proportion in garnet is high. The dashed-green line in the hot-mantle scheme denotes that the $rw \rightarrow pv + mw$ might be completely removed if the Al content in this hot mantle is high (e.g., 4-5 % (Weidner and Wang, 1998)). Indeed, in hot mantle regions with high Al proportion, the garnet-related transitions might be more important than the $rw \rightarrow pv + mw$ and becomes the dominant post-spinel phase transition (Weidner and Wang, 1998; Akaogi et al., 2002; Hirose, 2002; Wang et al., 2004).

B.2 410 and 660 complexities

The presence of other transforming or non-transforming mantle components can change the characteristics of the phase transitions and makes the interpretation of the corresponding seismic discontinuities more difficult. The depth and width of the phase transformations associated with the 410 and 660 are influenced by the presence or abundance of other components in the upper mantle, such as H_2O, Al, or $Fe-Mg$ proportion (Katsura and Ito, 1989; Wood, 1995; Weidner and Wang, 1998; Fei and Bertka, 1999; Akaogi et al., 2002; Smyth and Frost, 2002; Wang et al., 2004; Litasov et al., 2005; Schmerr and Garnero, 2007).

The complexities for the 410 discontinuity are as follows:

- The presence of water in the TZ would extend the wadsleyite stability to lower pressures resulting in a shallower and broader α-to-β transition (Wood, 1995; Smyth and Frost, 2002).

- The width of the 410 is found to increase with decreasing temperature (Katsura and Ito, 1989).

- The relative proportion of Mg and Fe content in olivine shifts the 410 discontinuity to different pressures (see Fig. 1.5). An enrichment of Mg relative to Fe increases the pressure of the phase loops leading to a deeper 410 (e.g., Fei and Bertka, 1999; Schmerr and Garnero, 2007). Besides, phase equilibrium strongly depends on iron content, such that the transition is broadened with iron enrichment.

In conclusion, the detailed form of the 410 may become a very sensitive probe of mantle conditions.

The 660 is more complex because different transformations in olivine and non-olivine components are expected at almost the same depth. These complexities are the following:

- In cold environments, such as the subduction zones, the presence of water in ringwoodite shifts the $rw \rightarrow pv + mw$ phase boundary to higher pressures (Litasov et al., 2005).

- Since two phase transformations occur near 660 km (olivine- and garnet-related) and they depend on mantle temperature and composition (Al content), multiple discontinuities may exist near the bottom of the TZ (e.g., Wang et al., 2006, section 6).

- In the extreme case of a hot mantle and high Al proportions within garnet, the only discontinuity near the bottom of the TZ is the $gt \rightarrow pv$ with a positive Clapeyron slope. The $rw \rightarrow pv + mw$ has a negative Clapeyron slope and does occur in cold mantle regions. The 660-km discontinuity defined by these two transitions has a minimum depth of about 640 km (for a mantle geotherm that reaches 1900 K at 660 km depth) and is deeper in both colder and hotter mantle (Weidner and Wang, 1998, 2000).

- The garnet-related phase transitions depend not only on temperature, such as the $rw \rightarrow pv + mw$ reaction, but on composition as well. The depth of the garnet-related phase transitions is strongly dependent on the Al content of the

garnet, which can cause variations in the discontinuity depth by more than 50 km (e.g., higher Al content leads to deeper $gt \rightarrow pv$ transition at normal to warm mantle temperatures) (Weidner and Wang, 1998; Akaogi et al., 2002; Wang et al., 2004).

B.3 Influence in the TZ thickness

The 410 and 660 complexities should be considered in the interpretation of the TZ thickness:

- In cold environments, the presence of water in wadsleyite and ringwoodite shifts the α-β phase to lower pressures and the $rw \rightarrow pv + mw$ to higher pressures. Thus, a thicker TZ associated with slabs can be attributed not only to cold subduction but also to wet subductions (Litasov et al., 2005).

- In a mantle with sufficient Al content within garnet, the 660 becomes deeper in hotter regions. In combination with a deeper 410 at high temperature, the effect of garnet is to leave the TZT in hot regions almost unaffected (Deuss et al., 2006).

B.4 510-km discontinuity

Around 510 km depth, the olivine goes through another phase transition, the wadsleyite transforms to ringwoodite ($\beta \rightarrow \gamma$-spinel transition) with a positive Clapeyron slope of 6.9 MPa/K (Helffrich, 2000; Suzuki et al., 2000). Although this is a broad discontinuity, the presence of garnet in the mantle will reduce the transformation interval to about 0.7 GPa (20 km) (Frost, 2003). Variations in water concentration inside the TZ or Fe content in olivine does not affect the width of the $\beta \rightarrow \gamma$-spinel transition because H_2O and Fe have similar solubility in both wadsleyite and ringwoodite (Kohlstedt et al., 1996; O'Neill et al., 1993).

The presence of pyroxenes in the upper mantle leads to an additional phase transition near 510 km. Phase equilibrium experiments in pyrolitic compositions indicate that diopside($CaMgSi_2O_6$)-rich clinopyroxene is dissolved into Al-rich garnet to form majorite garnet solid solution (gt s.s.). When the garnet phase becomes saturated in the Ca component at approximately 17 GPa (510 km), it starts to

exsolve (CaSiO3)-perovskite (Ca-pv) with increasing depth in the transition zone (Irifune and Ringwood, 1987; Wood, 2000). This sequence of transitions is expressed as $cpx + gt \rightarrow gts.s. \rightarrow Ca - pv + gts.s.$ In pure diopside-rich systems the 510-km discontinuity would correspond to the dissociation of clinopyroxene ($CaMgSi_2O_6$) to calcium-perovskite plus garnet ($cpx \rightarrow ca - pv + gt$) dissociation (e.g., Akaogi et al., 2004), which is how we referred to this transition in Fig. 1.6. This is a wide transition (40-60 km) but most of the dissociation occurs within the first 10-20 km leading to a seismic discontinuity with an impedance contrast of about 1 or 2 % over 25 km (Saikia et al., 2008).

Because the Clapeyron slope of the $cpx \rightarrow ca - pv + gt$ transition is positive (4 MPa/K) (Saikia et al., 2008) and the Clapeyron slope of the $\beta \rightarrow \gamma$-spinel transition is also positive, both phase transitions will merge at around 540-560 km depth and 1600 K (Thomas and Billen, 2009). For other temperatures double discontinuities are expected. However, the amount of clinopyroxene varies in the mantle. Therefore, the presence or lack of a double discontinuity near a depth of 510 km is an indication of the fertility of that region of the mantle.

C

Supplementary figures for Chapter 2

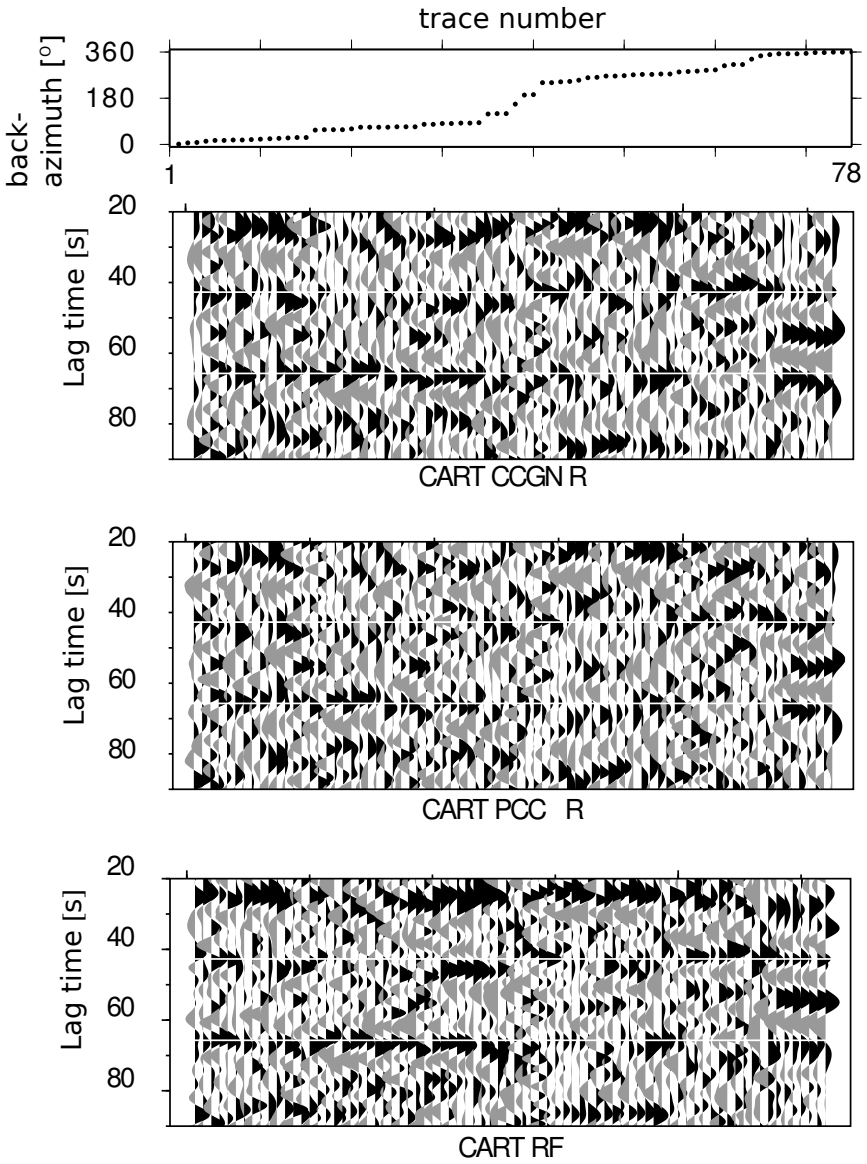

Figure 2.13 continuation.

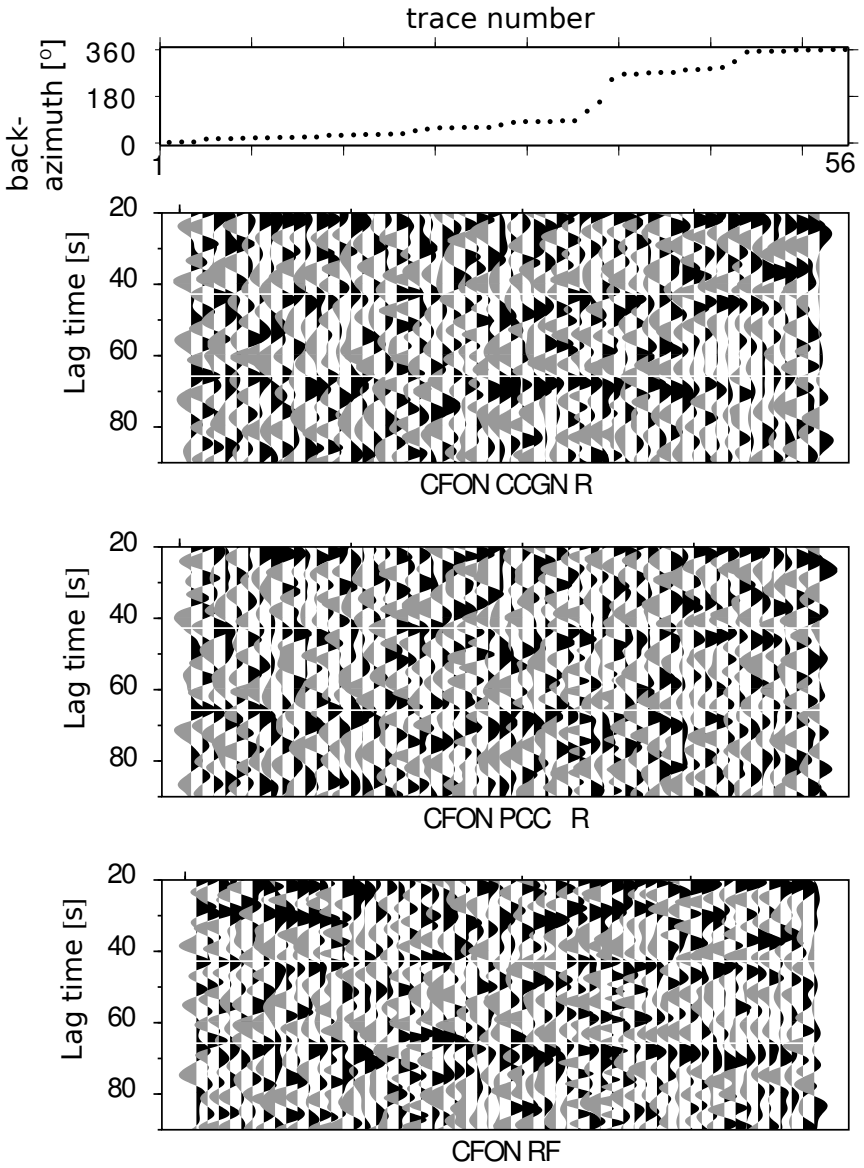

Figure 2.13 continuation.

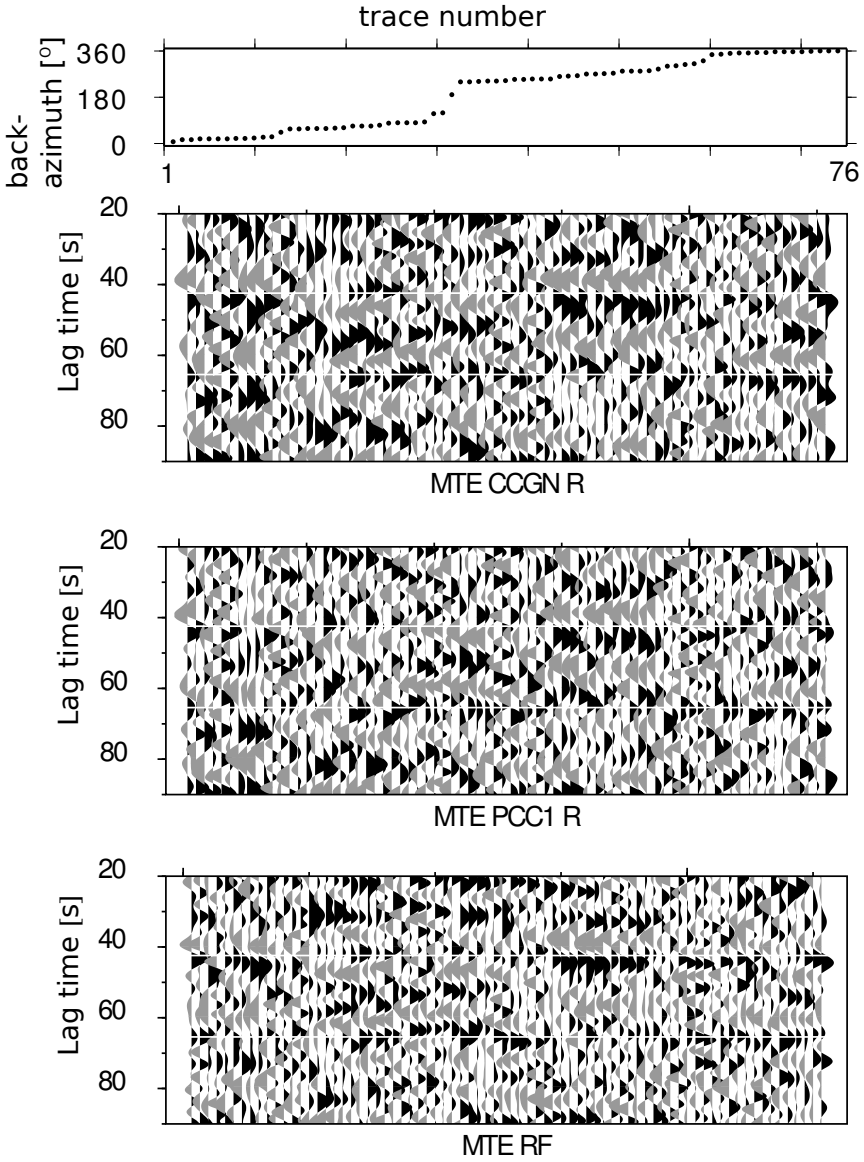

Figure 2.13 continuation.

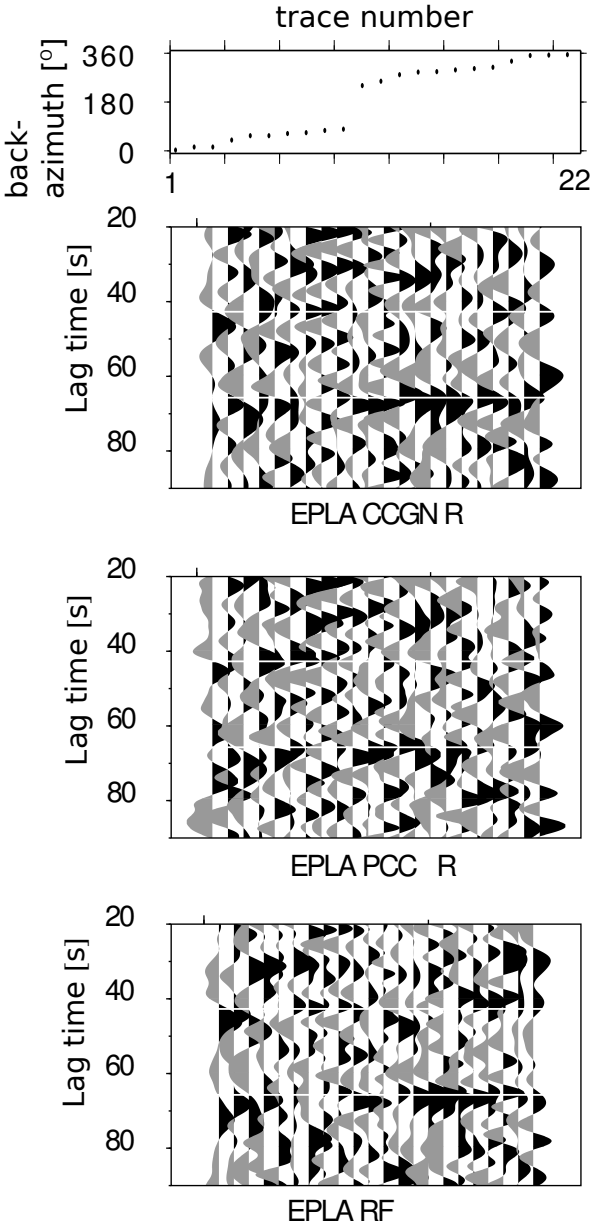

Figure 2.13 continuation.

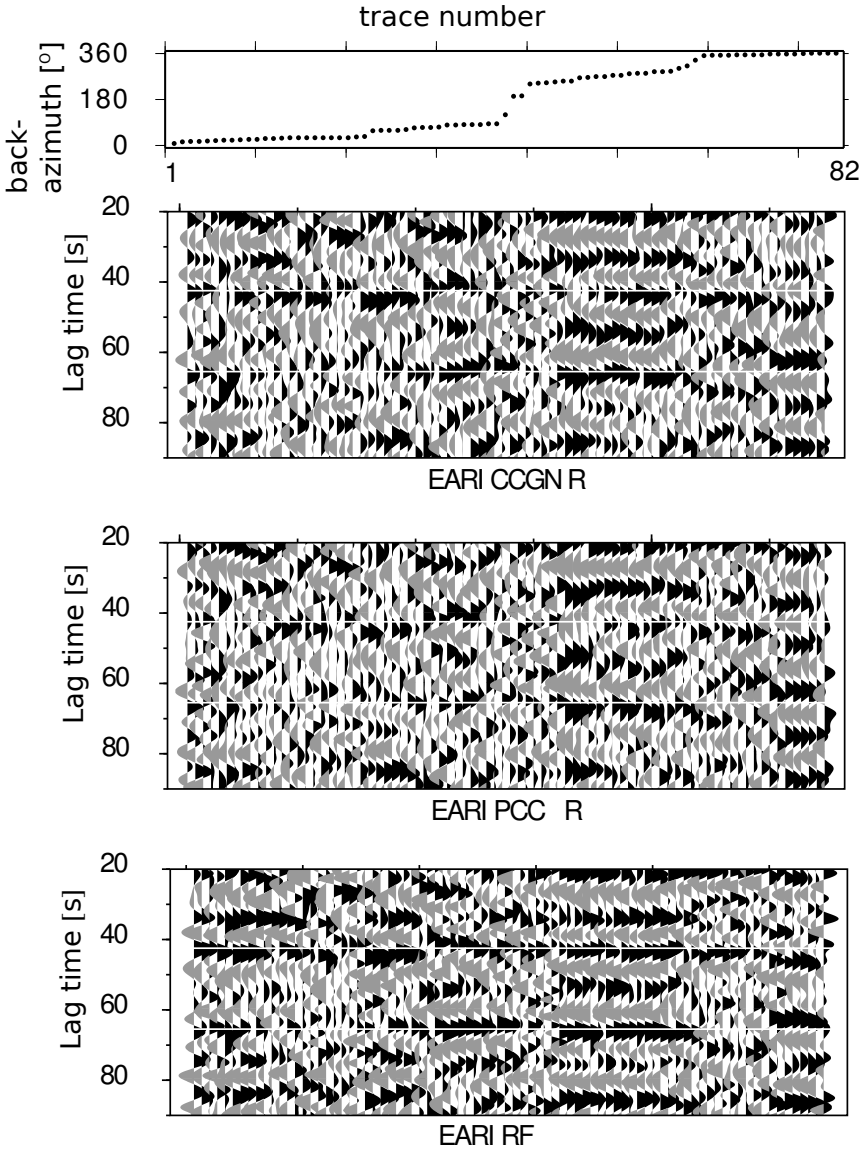

Figure 2.13 continuation.

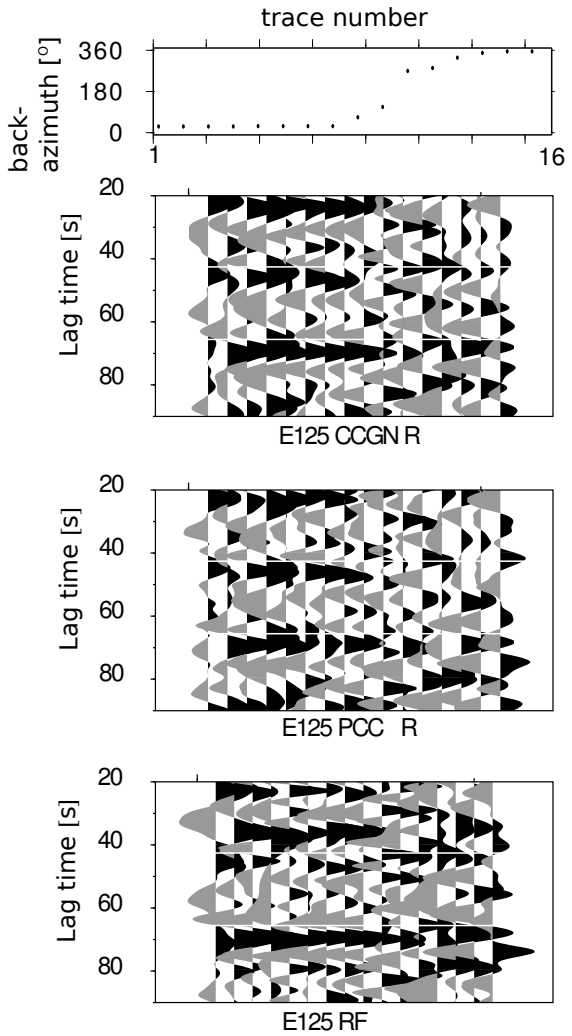

Figure 2.13 continuation.

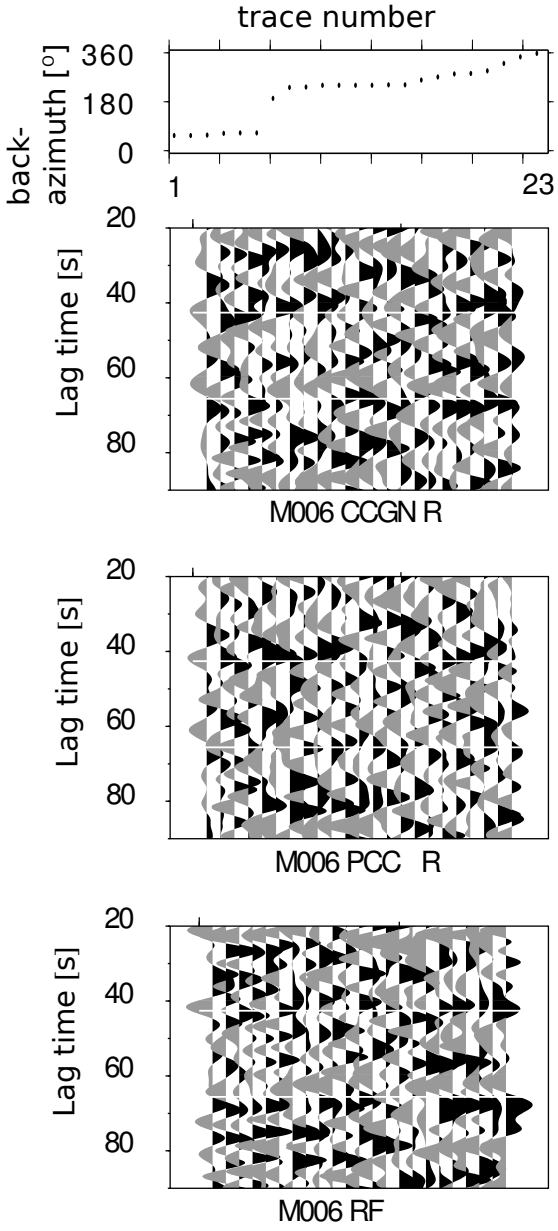

Figure 2.13 continuation.

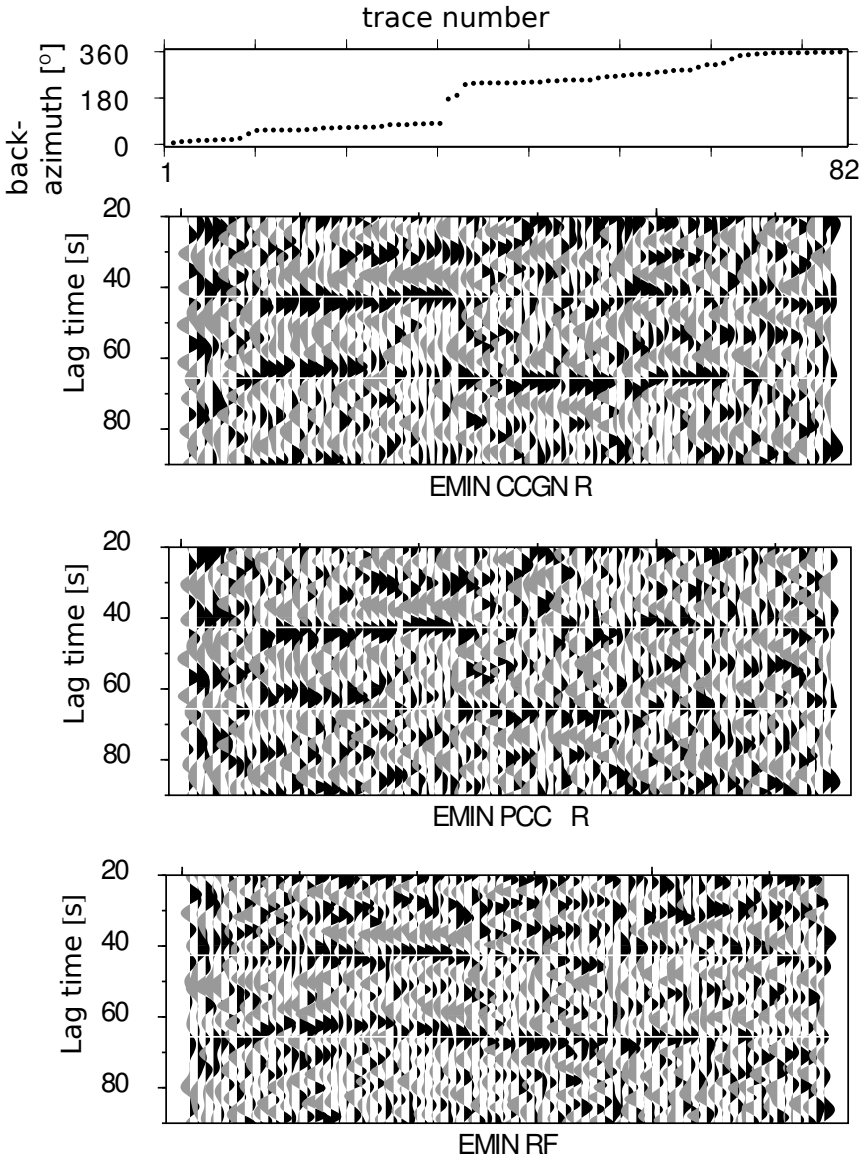

Figure 2.13 continuation.

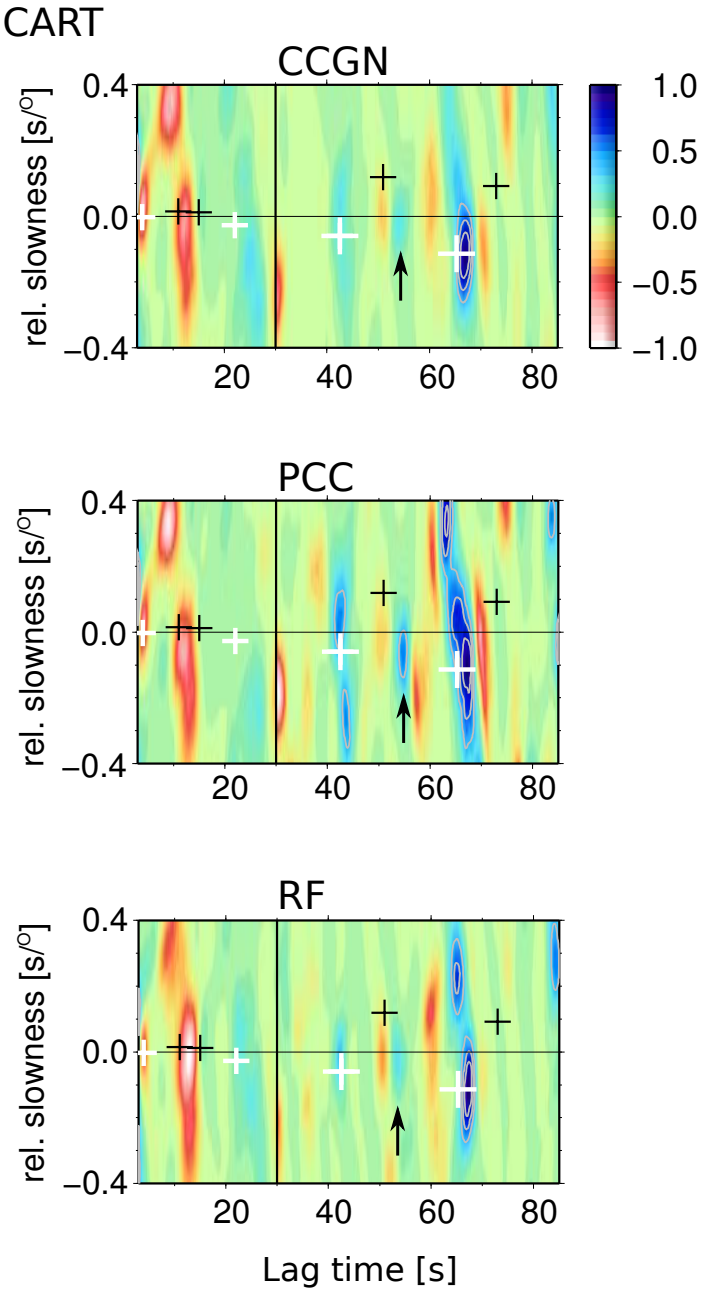

Figure 2.14 continuation.

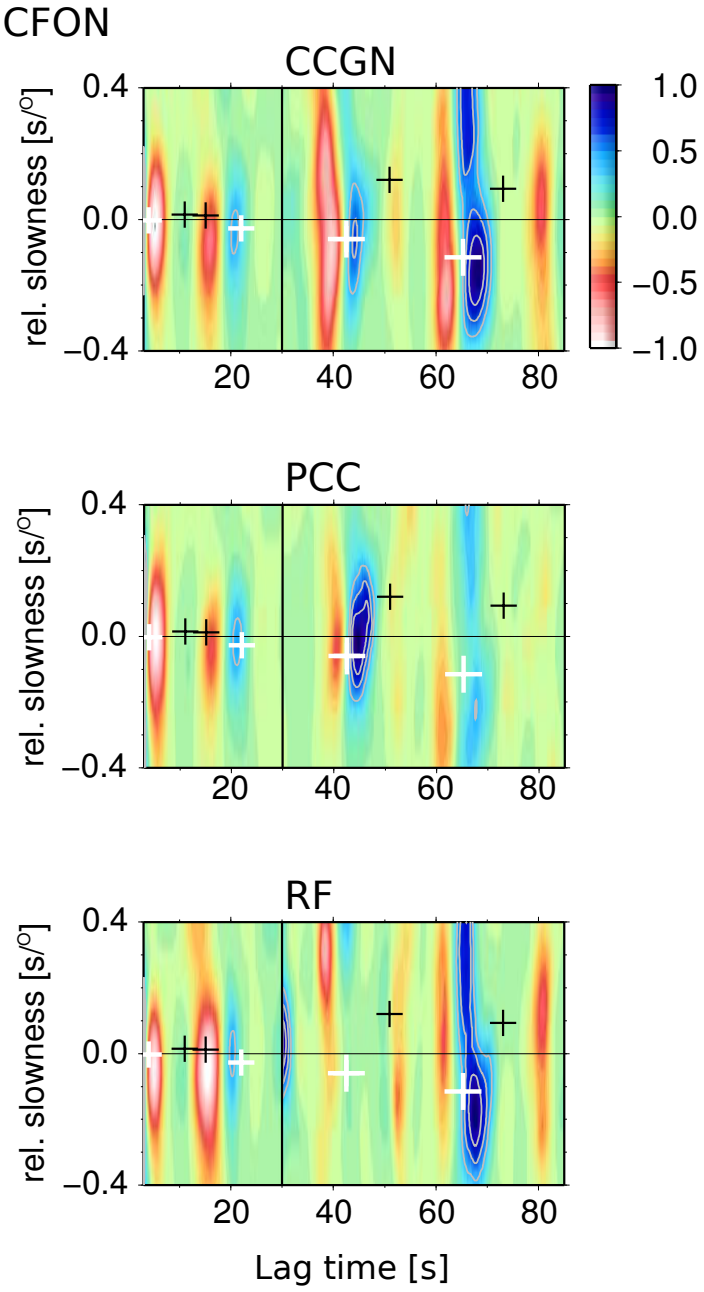

Figure 2.14 continuation.

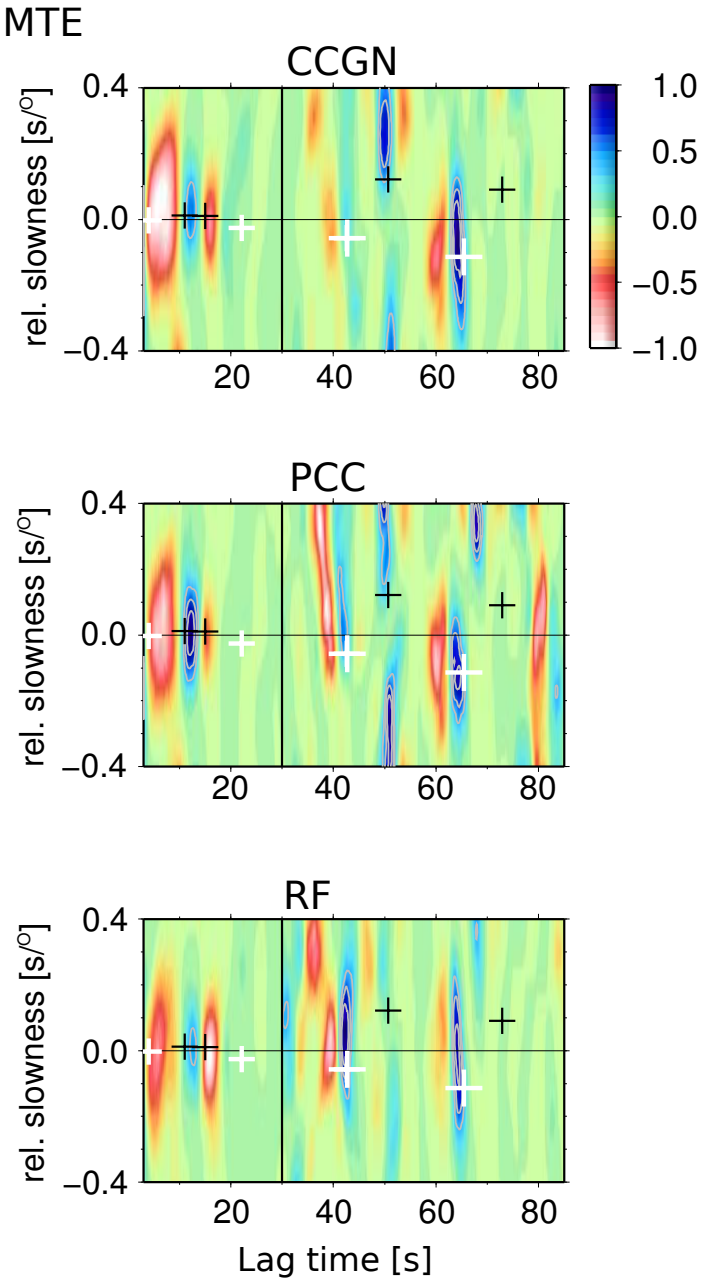

Figure 2.14 continuation.

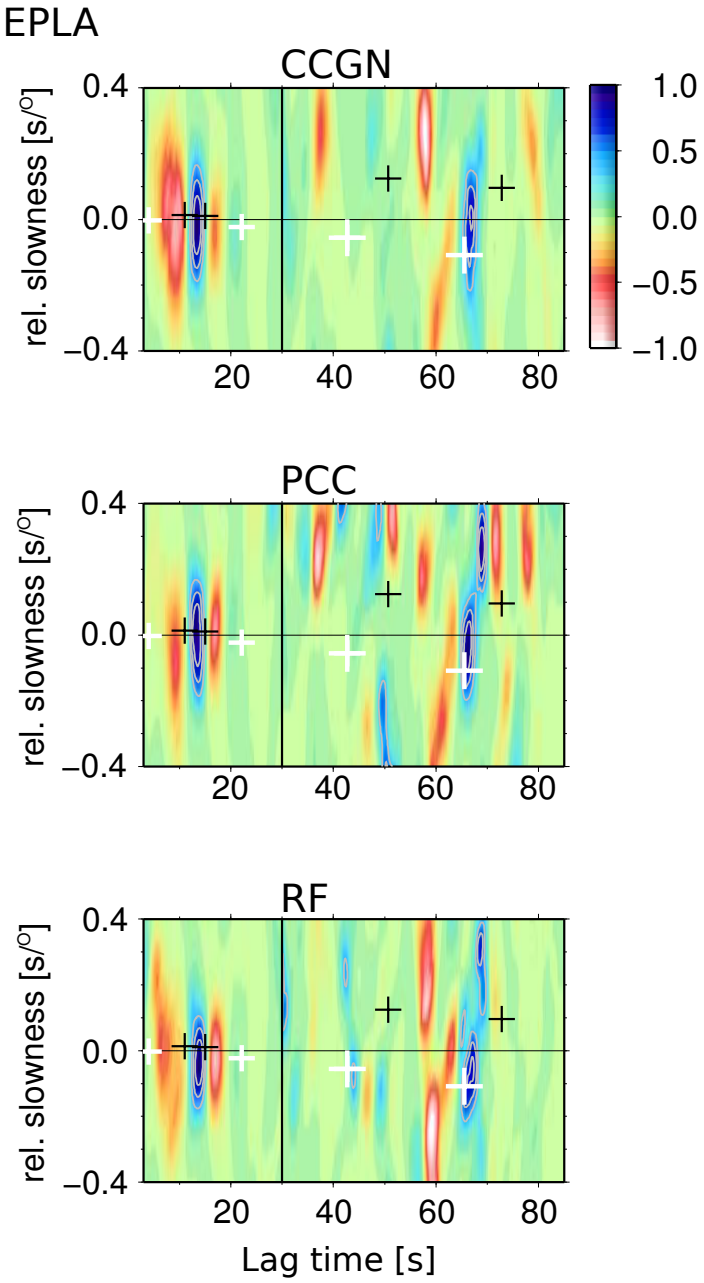

Figure 2.14 continuation.

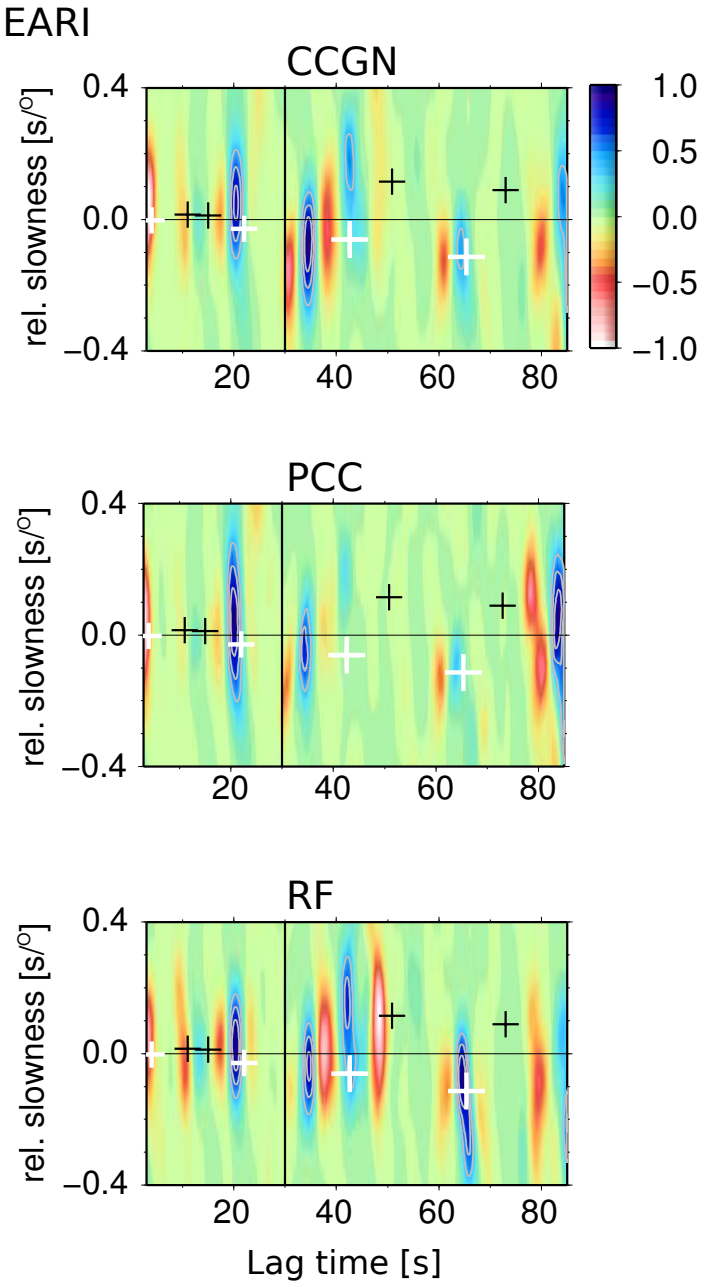

Figure 2.14 continuation.

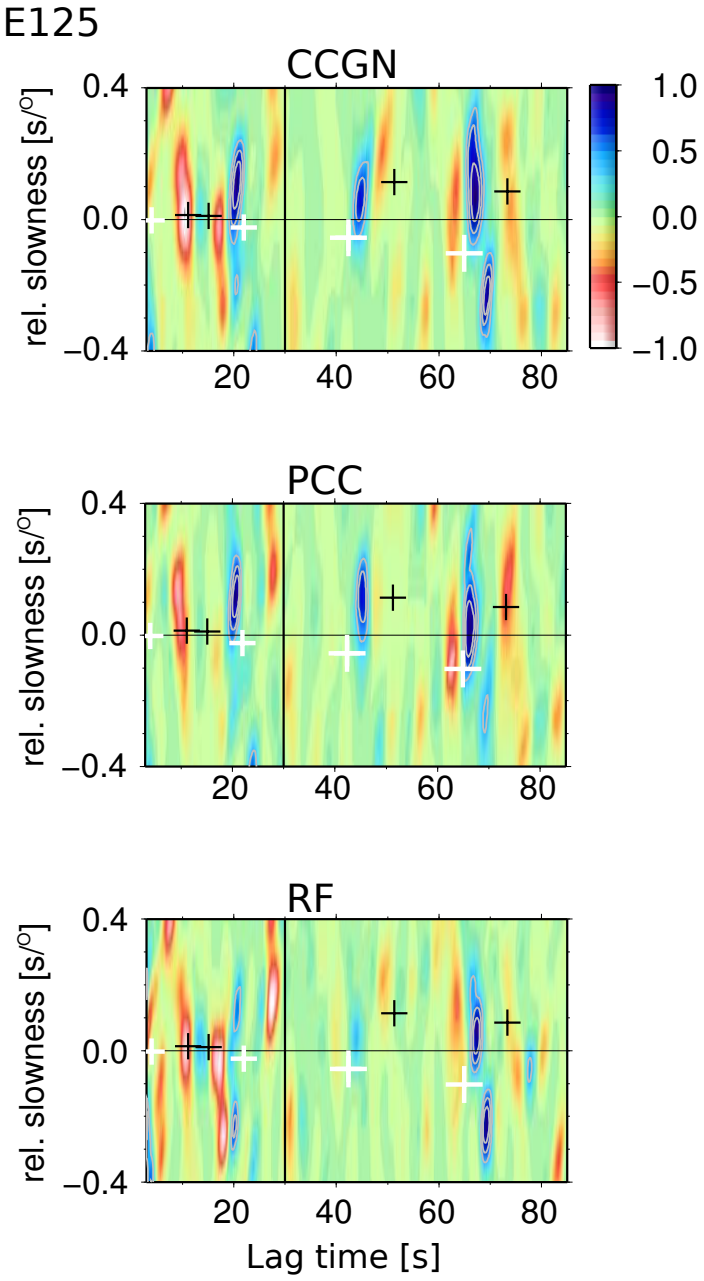

Figure 2.14 continuation.

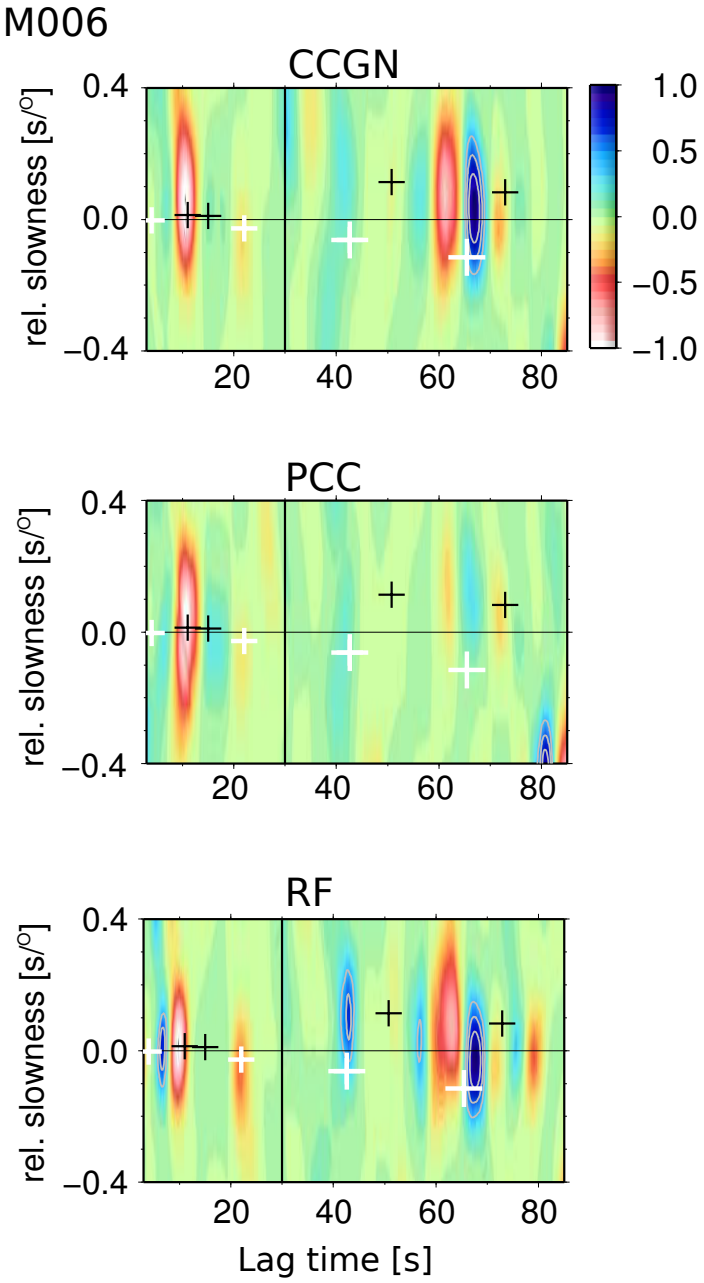

Figure 2.14 continuation.

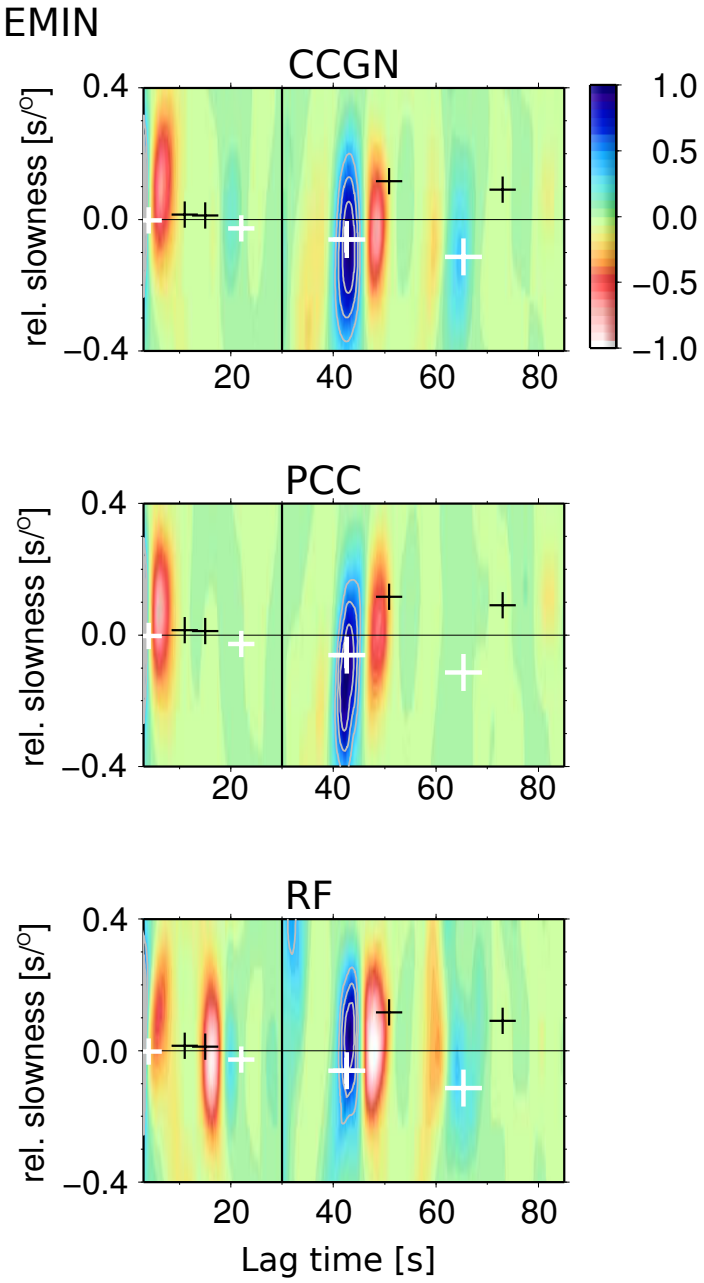

Figure 2.14 continuation.

D

TopoIberia stations

Table D.1: Number of events per station (epicentral distance between 65° and 95°) and the number of PCCRs, CCGNRs and RF which passed the quality control based on SNR. Network codes: IberArray (IB), Catalan Seismic Network (CA), Southern Spain Broad Band Seismic Network (IG), GEOFON (GE), University of Lisbon Seismic Network (LX), Mediterrean Network (MN), Western Mediterranean Seismic Network (WM), Portuguese National Seismograph Network (PM), French Broadband Seismological Network (FR), Ebre Observatory Regional Seismic Network (EB).

Station	Network code	Long [°]	Lat [°]	Events	PCCRs	CCGNRs	RFs
ACBG	IG	-2.1967	36.7674	54	29	26	32
ACLR	IG	-2.5823	37.1897	76	44	41	46
ALHU	IB	-3.8901	35.2133	12	7	6	7
ALJ	IB	-5.6494	36.5299	38	24	25	25
ANER	IG	-3.8453	36.7623	136	90	96	102
ARAC	IG	-6.5647	37.8923	143	93	96	104
ASCB	IG	-2.0057	37.0393	37	19	19	22
ATE	FR	-0.7003	43.0858	21	16	17	17
AVE	WM	-7.4133	33.2981	81	50	52	58
CART	WM	-1.0012	37.5868	135	87	93	88
CAVN	CA	0.7516	41.8826	66	43	42	51
CBEU	CA	2.6769	42.2567	85	60	56	65
CBRU	CA	2.1803	42.2855	78	61	56	60
CCAS	CA	2.9053	41.8840	63	45	42	50
CEST	CA	1.2553	42.6005	74	52	59	55
CEU	WM	-5.3731	35.8987	63	36	43	44
CEUT	IG	-5.3263	35.8830	89	60	59	63
CFON	CA	2.4356	41.7600	76	58	57	62
CGAR	CA	1.9149	41.2944	65	44	43	45
CHAF	IB	-2.4309	35.1835	16	7	6	6
CLLI	CA	1.9742	42.4792	71	51	55	56
CMAS	CA	0.3150	40.7267	69	49	48	57
CORG	CA	1.3176	42.2303	75	47	47	56
CORI	CA	2.0499	41.9735	73	54	55	54

CPAL	CA	3.1636	42.3116	54	35	35	42
CSOR	CA	1.1339	42.3756	71	48	46	52
CTRE	CA	0.7736	42.3242	75	51	53	55
E001	IB	-5.8392	36.1742	63	38	38	33
E002	IB	-5.5137	36.0610	64	43	44	46
E005	IB	-5.2660	36.4294	41	20	21	20
E006	IB	-5.0446	36.9492	22	12	14	14
E007	IB	-3.4292	36.8605	57	40	42	45
E008	IB	-7.1304	37.4969	38	23	25	28
E009	IB	-6.7651	37.4192	50	36	33	38
E010	IB	-6.4431	36.9886	26	13	14	17
E011	IB	-5.9905	37.2103	21	12	14	12
E012	IB	-5.5249	37.3710	22	11	12	9
E013	IB	-4.5339	36.9641	34	21	18	19
E015	IB	-3.1115	37.1743	29	20	22	21
E016	IB	-7.0568	37.9670	29	19	20	23
E017	IB	-6.2289	37.5720	45	29	30	32
E018	IB	-5.9548	37.9803	44	29	31	38
E019	IB	-5.8788	37.7160	19	13	13	12
E020	IB	-4.8445	37.5653	24	13	15	13
E021	IB	-4.9163	38.0057	32	21	16	22
E022	IB	-4.3818	37.9012	28	16	16	16
E024	IB	-3.9241	37.7225	26	18	12	15
E025	IB	-3.4657	37.7016	42	28	28	29
E026	IB	-2.5945	37.4952	30	19	18	19
E028	IB	-6.8073	38.3553	36	23	21	26
E029	IB	-6.1831	38.4397	39	31	31	31
E030	IB	-5.6263	38.4684	52	35	35	39
E031	IB	-4.9967	38.3393	47	22	28	32
E032	IB	-3.4898	38.1135	2	0	1	2
E034	IB	-2.1918	38.2298	9	6	2	8
E035	IB	-0.9356	37.9950	6	3	5	5
E036	IB	-6.4373	38.8498	17	7	7	8
E037	IB	-5.8816	38.8855	31	22	19	21
E038	IB	-5.2358	38.7329	28	18	18	18
E039	IB	-4.6949	38.8226	22	12	15	16
E040	IB	-4.1966	38.6093	45	25	26	27
E041	IB	-3.6572	38.6410	26	16	17	19
E042	IB	-3.0212	38.8149	36	22	21	26
E044	IB	-2.0726	38.8619	22	11	10	9
E045	IB	-0.8590	38.7793	34	19	22	24
E047	IB	-6.1889	39.2847	17	11	10	8

E048	IB	-5.5030	39.3120	11	6	4	5
E049	IB	-4.8329	39.1750	22	13	15	16
E050	IB	-4.1336	39.1026	50	33	26	31
E051	IB	-3.6714	38.9925	39	23	24	25
E052	IB	-3.1002	39.2830	32	21	21	25
E053	IB	-2.5949	39.1870	22	11	13	15
E054	IB	-2.0460	39.3797	7	4	5	7
E055	IB	-1.3775	39.1754	26	20	20	21
E056	IB	-0.6447	39.1320	14	8	11	10
E057	IB	-6.5946	39.7501	37	24	23	28
E058	IB	-5.9240	39.8193	47	27	31	34
E059	IB	-5.1524	39.7364	47	28	29	29
E060	IB	-4.6337	39.7615	24	16	17	16
E061	IB	-3.2685	39.6565	6	3	3	3
E062	IB	-2.5312	39.6399	4	1	1	3
E063	IB	-2.0771	39.9534	9	6	5	7
E064	IB	-1.4590	39.6554	35	24	24	25
E066	IB	-0.4279	39.8718	35	19	21	24
E067	IB	-6.8578	40.2337	33	19	18	20
E068	IB	-6.2108	40.2333	41	22	24	30
E069	IB	-5.4534	40.1428	25	14	12	17
E070	IB	-4.8035	40.2159	42	30	26	27
E071	IB	-4.1883	40.2827	24	19	19	18
E072	IB	-3.5228	40.0747	8	7	5	7
E073	IB	-2.9074	40.1377	12	8	10	9
E074	IB	-2.4199	40.1312	29	20	18	23
E075	IB	-1.5652	40.2348	39	23	25	28
E076	IB	-1.0632	40.1442	22	17	18	17
E077	IB	0.1039	40.2561	40	25	26	34
E078	IB	-6.4826	40.6666	30	16	18	22
E079	IB	-5.8748	40.6505	10	6	7	8
E080	IB	-5.1339	40.6016	30	23	25	25
E081	IB	-4.4157	40.6114	9	4	6	6
E082	IB	-3.8004	40.5317	52	25	23	26
E083	IB	-3.2872	40.5176	13	7	6	9
E084	IB	-2.6451	40.5797	37	22	24	26
E085	IB	-1.9736	40.4993	32	21	18	25
E086	IB	-1.0970	40.5569	53	34	35	34
E087	IB	-0.3186	40.6844	35	22	20	25
E088	IB	-6.1348	41.1293	37	22	23	27
E090	IB	-4.7911	41.0723	9	5	4	4
E091	IB	-4.0895	41.0854	5	2	2	2

E095	IB	-0.8488	41.0381	31	20	21	19
E098	IB	-5.0871	41.5924	16	6	8	10
E099	IB	-4.4576	41.5365	9	6	5	4
E100	IB	-3.7578	41.4956	5	3	3	3
E101	IB	-2.9658	41.4514	11	9	7	9
E103	IB	-1.6995	41.2536	2	1	1	2
E105	IB	-0.3761	41.1875	6	4	4	3
E109	IB	-7.3471	42.1238	37	17	22	22
E113	IB	-4.0885	41.9174	15	8	9	10
E114	IB	-3.3691	41.9179	2	2	2	2
E115	IB	-2.6242	41.8002	6	5	5	5
E117	IB	-1.3961	41.7540	2	1	2	2
E118	IB	-0.9523	42.0055	9	8	6	5
E122	IB	-8.0408	42.3605	32	17	20	21
E124	IB	-6.4946	42.4840	16	12	11	12
E125	IB	-5.6920	42.4543	33	18	18	22
E126	IB	-5.0625	42.4267	32	19	21	24
E129	IB	-2.8457	42.3137	17	13	12	15
E130	IB	-2.2686	42.2638	12	10	8	9
E132	IB	-0.9628	42.3808	25	17	17	17
E134	IB	0.1417	42.2494	20	14	15	18
E138	IB	-7.9689	42.8515	27	16	17	18
E140	IB	-6.8721	42.9504	25	18	19	19
E141	IB	-6.0477	42.8198	25	17	16	20
E142	IB	-5.4193	42.8906	33	27	25	27
E143	IB	-4.6081	42.9062	18	14	13	14
E144	IB	-3.8849	42.8868	22	10	11	14
E147	IB	-2.0077	42.7908	9	4	5	5
E155	IB	-3.9987	43.2448	11	8	8	10
E932	IB	-3.4708	38.1496	3	2	2	3
E961	IB	-3.3326	39.6602	12	10	10	8
EADA	ES	-4.5771	38.1673	110	77	71	85
EALB	ES	-3.0343	35.9399	61	35	34	40
EALK	ES	-1.5071	43.2197	68	48	41	47
EARA	ES	-1.5804	42.7733	113	84	74	85
EARI	ES	-5.2099	43.3012	120	83	89	89
EBAD	ES	-7.0133	38.7556	122	76	72	86
EBEN	ES	-0.2250	38.7038	112	80	72	80
EBER	ES	-2.8896	36.8979	135	89	81	95
EBIE	IB	0.1906	42.6608	94	68	70	69
EBR	EB	0.4933	40.8205	74	55	45	60
ECAB	ES	-5.4186	38.0753	35	18	19	23

ECAL	ES	-6.7371	41.9413	124	76	74	93
ECEU	ES	-5.3768	35.8978	41	28	25	33
ECHE	ES	-0.9690	39.5896	34	22	21	20
EGRO	ES	-7.4831	37.5342	125	75	81	86
EHUE	IB	-2.5940	37.8135	52	30	33	33
EIBI	ES	1.3436	39.0269	133	99	95	108
EJON	ES	2.8886	42.4487	137	95	90	112
ELAN	ES	-3.4340	43.2317	119	94	95	97
ELOB	ES	-8.0611	41.8674	105	72	75	81
ELOJ	IB	-4.1540	37.14642	73	50	58	57
ELUQ	IB	-4.2680	37.5593	44	32	28	35
EMAL	WM	-4.4280	36.7620	156	101	102	115
EMAZ	ES	-8.9765	42.9490	98	72	70	77
EMIJ	ES	-4.7727	36.5645	146	99	108	109
EMIN	ES	-6.6724	37.7675	142	91	96	102
EMIR	ES	1.5258	41.9144	64	44	42	48
EMLI	ES	-2.9500	35.3000	3	1	0	1
EMOS	ES	-0.4721	40.3639	125	79	79	93
EMUR	ES	-1.2405	37.8422	115	75	70	74
ENIJ	ES	-2.2070	36.9715	9	6	7	6
EPLA	ES	-6.0803	40.0642	38	25	26	29
EPOB	ES	1.0786	41.3527	143	93	96	114
EPON	ES	-7.1494	43.3270	75	51	55	63
EQES	ES	-3.0711	37.8028	119	80	67	76
EQTA	ES	-3.4399	37.2050	128	83	90	96
ERTA	ES	0.3335	40.9567	122	82	78	93
ESBB	ES	-3.9630	39.6744	145	88	101	110
ESPR	ES	-5.8562	36.8686	131	80	81	82
ESTP	IG	-4.8661	37.2113	151	97	96	111
ETOB	IB	-1.5478	38.6447	143	81	86	98
ETOS	IB	2.8144	39.7678	123	79	88	96
EVIA	IB	-2.5038	38.6732	17	9	11	12
EVO	WM	-8.0130	38.5320	95	59	55	56
EZAM	IB	-8.6968	42.1482	8	1	1	1
GORA	IG	-3.0398	37.4805	86	57	62	55
GUD	ES	-4.1537	40.6430	34	17	19	18
HORN	IG	-5.2582	37.8466	140	100	101	103
IFR	WM	-5.1272	33.5166	117	72	69	82
JAND	IG	-3.9705	38.2214	147	93	93	106
LIJA	IB	-5.4038	36.9061	49	29	28	28
M001	IB	-6.7560	33.9293	39	19	26	28
M002	IB	-5.9712	35.3704	46	23	27	29

M004	IB	-6.2498	34.7918	26	14	12	11
M005	IB	-5.4031	35.0247	43	22	22	27
M006	IB	-4.7751	34.9384	40	32	31	31
M007	IB	-3.8010	34.7561	62	35	41	42
M008	IB	-2.7973	34.7326	62	38	36	40
M010	IB	-6.3353	34.2061	49	31	32	32
M011	IB	-5.4721	34.0166	63	40	32	31
M012	IB	-5.4343	34.7301	50	36	39	38
M013	IB	-4.4146	34.6103	29	14	6	9
M014	IB	-3.8372	33.9396	57	38	38	41
M015	IB	-3.0350	33.9845	63	39	36	40
M016	IB	-2.1566	34.3786	40	22	23	22
M017	IB	-5.9906	33.6988	69	41	42	44
M018	IB	-4.4485	33.6228	83	45	44	57
M019	IB	-4.4562	31.9377	91	62	60	64
M201	IB	-6.1667	33.2734	28	19	19	21
M203	IB	-5.6310	32.1504	9	7	7	8
M204	IB	-9.0471	30.8646	9	7	7	6
M206	IB	-6.5782	32.8013	22	15	13	17
M207	IB	-8.0624	31.1875	6	4	4	3
M210	IB	-4.0820	32.3543	8	4	5	4
M211	IB	-7.2454	30.9225	25	13	11	18
M212	IB	-6.6679	33.3639	6	5	4	5
M214	IB	-6.6791	31.8222	18	9	12	11
M215	IB	-7.4491	32.0465	18	14	10	13
M216	IB	-3.4073	34.8424	18	11	12	12
MAHO	GE	4.2665	39.8959	122	86	95	102
MELI	WM	-2.9392	35.2899	62	35	36	35
MESJ	LX	-8.2199	37.8397	51	30	35	39
MORF	LX	-8.6508	37.3063	49	37	39	39
MTE	GE	-7.5442	40.3997	113	76	73	84
MVO	PM	-7.0288	41.1645	170	112	111	117
NKM	IB	-5.4104	35.4476	52	31	33	34
PBAR	PM	-7.0609	38.1729	165	105	101	111
PBDV	PM	-7.9312	37.2430	151	87	97	102
PCVE	PM	-8.0390	37.6328	115	74	76	81
PDRG	LX	-7.6383	38.1079	62	42	45	47
PFVI	PM	-8.8268	37.1328	128	83	87	99
PGAV	PM	-8.2698	41.9653	83	50	42	51
PMRV	PM	-7.3896	39.4088	130	79	86	92
PMTG	PM	-8.2253	39.0690	76	42	46	45
PNCL	PM	-8.5290	38.1118	100	62	60	62

POLO	PM	-7.7942	41.3738	91	46	49	57
PVAQ	PM	-7.7173	37.4037	173	117	120	127
PVLZ	WM	-4.3010	35.1730	75	43	35	41
REAL	IB	-5.2078	36.4852	5	2	2	3
ROMA	IG	-0.9181	38.3883	136	84	79	94
RTC	MN	-6.8569	33.9881	72	40	46	49
SELV	IG	-3.7277	37.2383	143	82	83	92
SESP	IG	-2.5445	38.1208	72	46	48	49
SFS	WM	-6.2055	36.4656	91	49	56	41
SJAF	FR	2.8822	42.4845	23	15	17	20
TA01	IB	-2.5174	36.9710	18	12	10	12
TA02	IB	-2.4896	36.9732	10	6	8	9
TA03	IB	-2.5408	37.0028	13	9	8	9
TA04	IB	-2.6005	37.0065	21	14	12	12
TA05	IB	-2.5433	37.0665	18	14	12	15
TA06	IB	-2.5577	36.9314	11	6	5	6
TA07	IB	-2.3825	37.0209	26	17	17	19
TA08	IB	-2.6104	37.0959	11	5	6	8
TA09	IB	-2.5891	36.8785	14	8	6	7
TA10	IB	-2.2858	37.0394	21	12	9	12
TAF	IB	-2.4116	34.8100	70	46	44	51
TIO	WM	-7.2617	30.9267	15	9	4	9
VELZ	IG	-1.9880	37.5838	111	71	71	75
XIII	IG	-1.5952	38.2194	99	46	54	66

E

Supplementary figures for Chapter 4

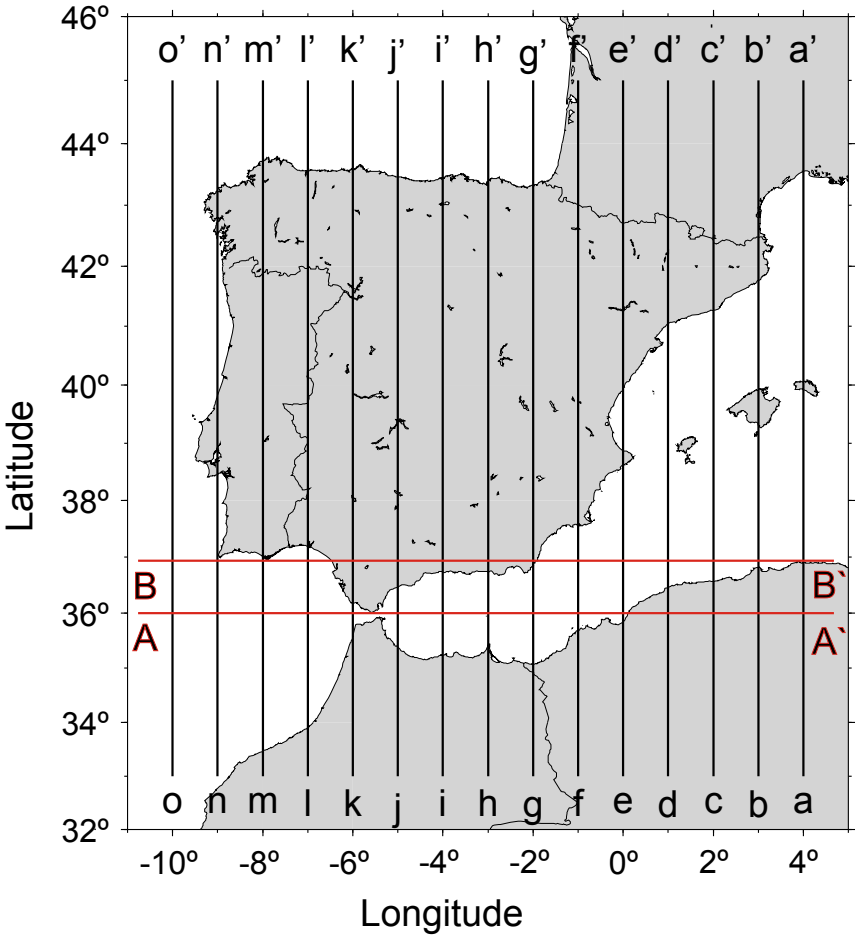

Figure E.1: Map with the profiles shown in Figs E.2 and E.3 . Lines aa' to oo' indicate the central longitude of each profile. Lines AA' and BB' indicate the central latitude.

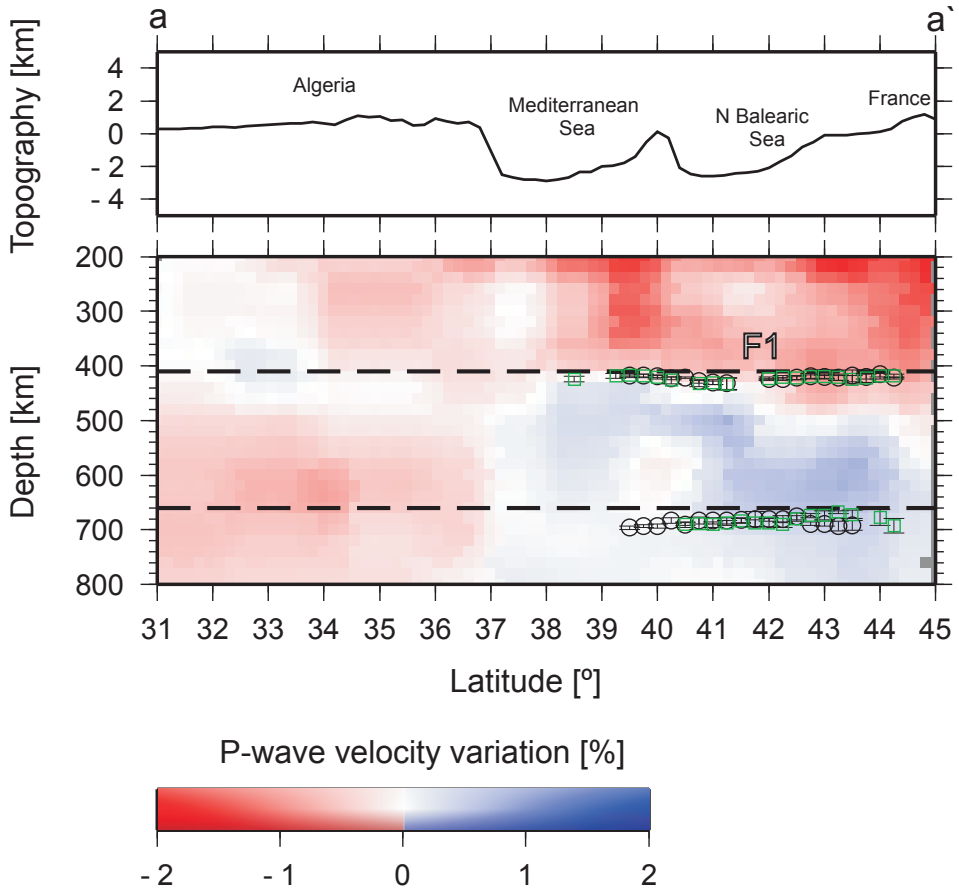

Figure E.2: Cross section of average P-velocity anomalies from the tomographic model of Villaseñor et al. (2003) obtained from corridors of 1.5° width along the north-south profiles shown in Fig. E.1, aa' to oo'. Black circles show the estimated depths of the 410 and 660 discontinuities along the same profiles. Green squares and red triangles show the estimated depths of the 410 and 660 discontinuities 0.25° west and east of the corresponding profiles. Yellow stars in profile ii' show the hypocenters of the deep earthquakes beneath Granada from Buforn et al. (2004). The star size is proportional to the event magnitude, $M_W = 4, 4.8, 7$.

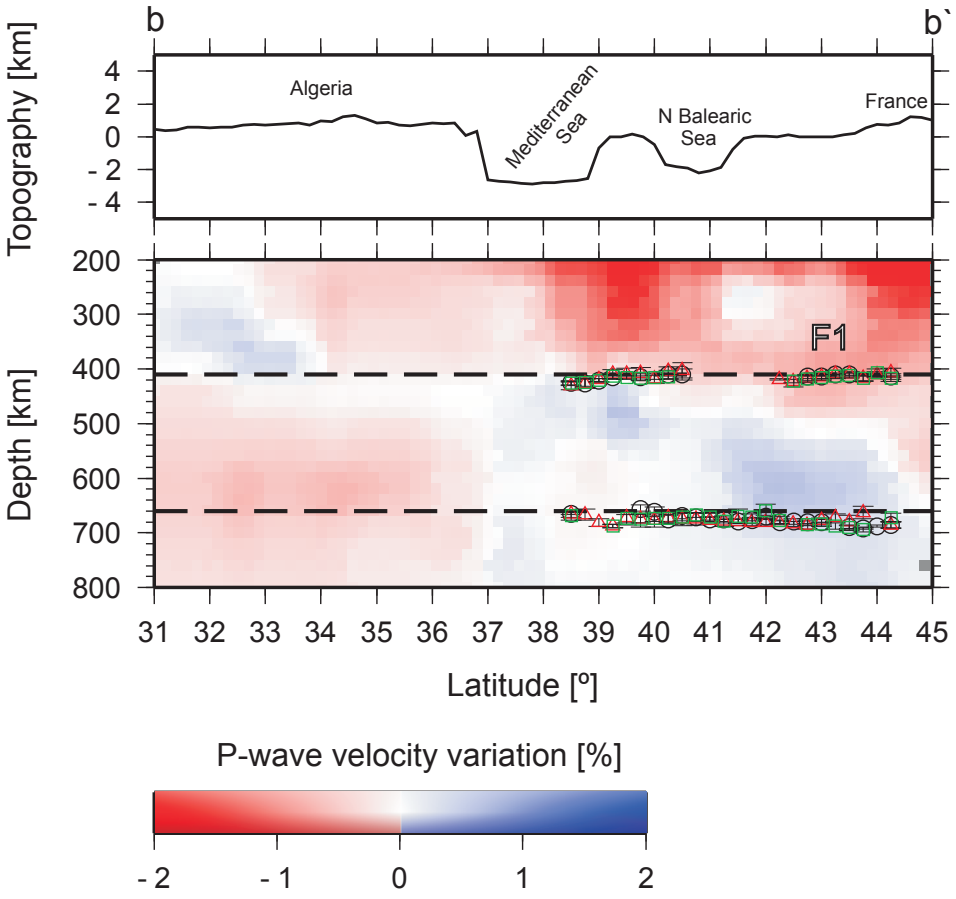

Figure E.2 continuation.

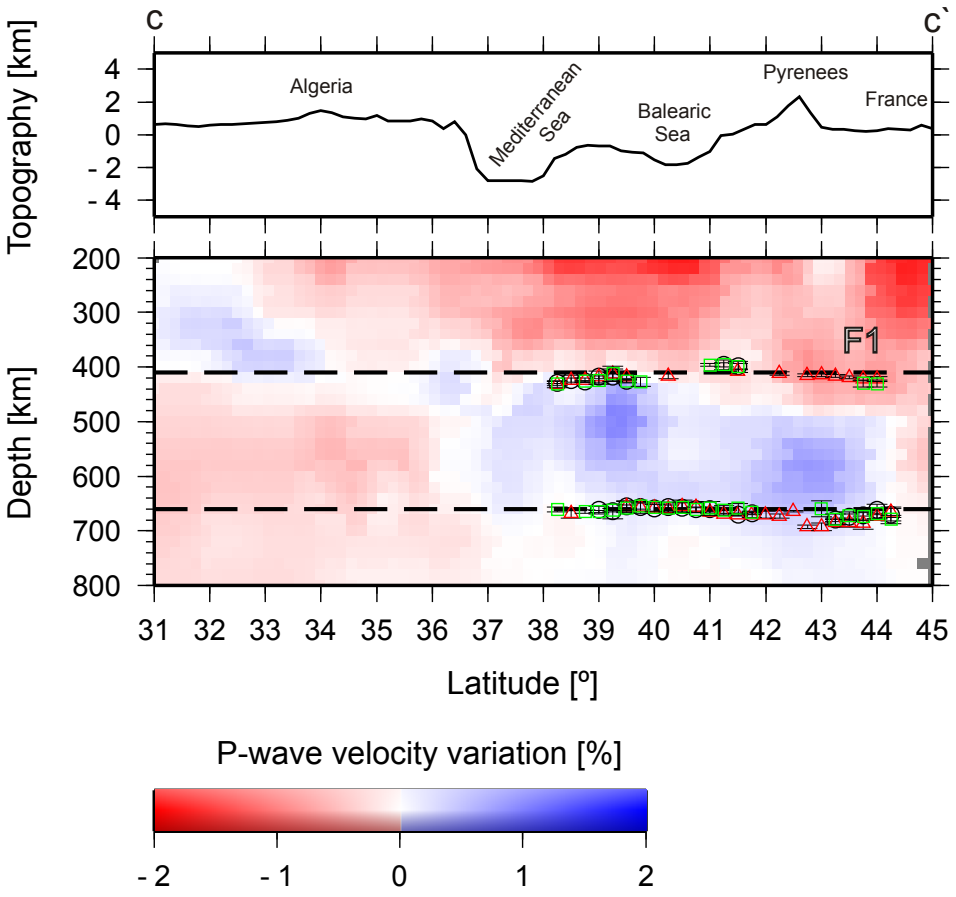

Figure E.2 continuation.

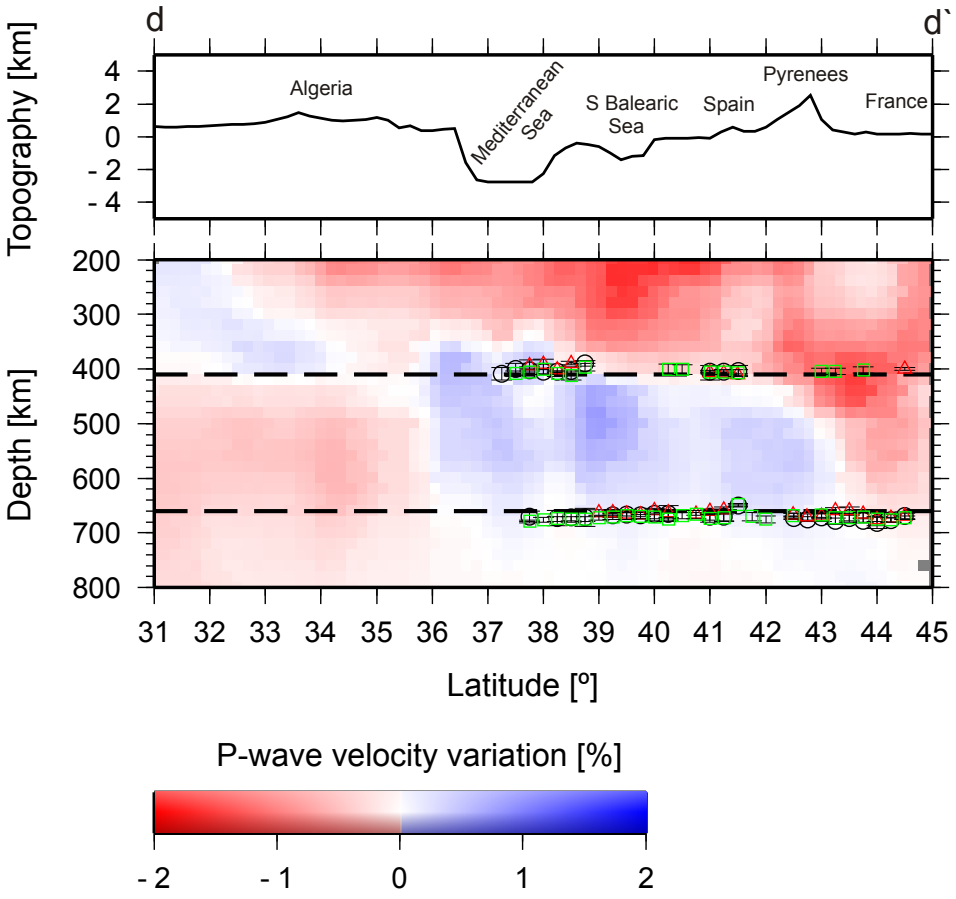

Figure E.2 continuation.

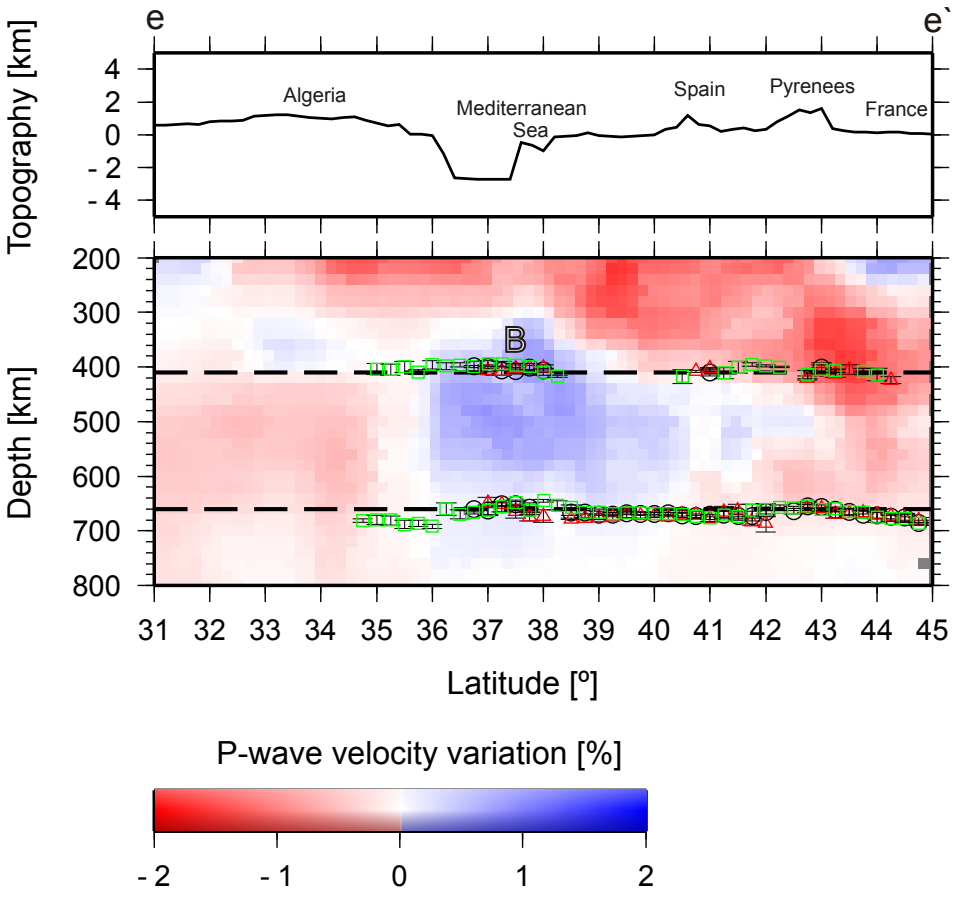

Figure E.2 continuation.

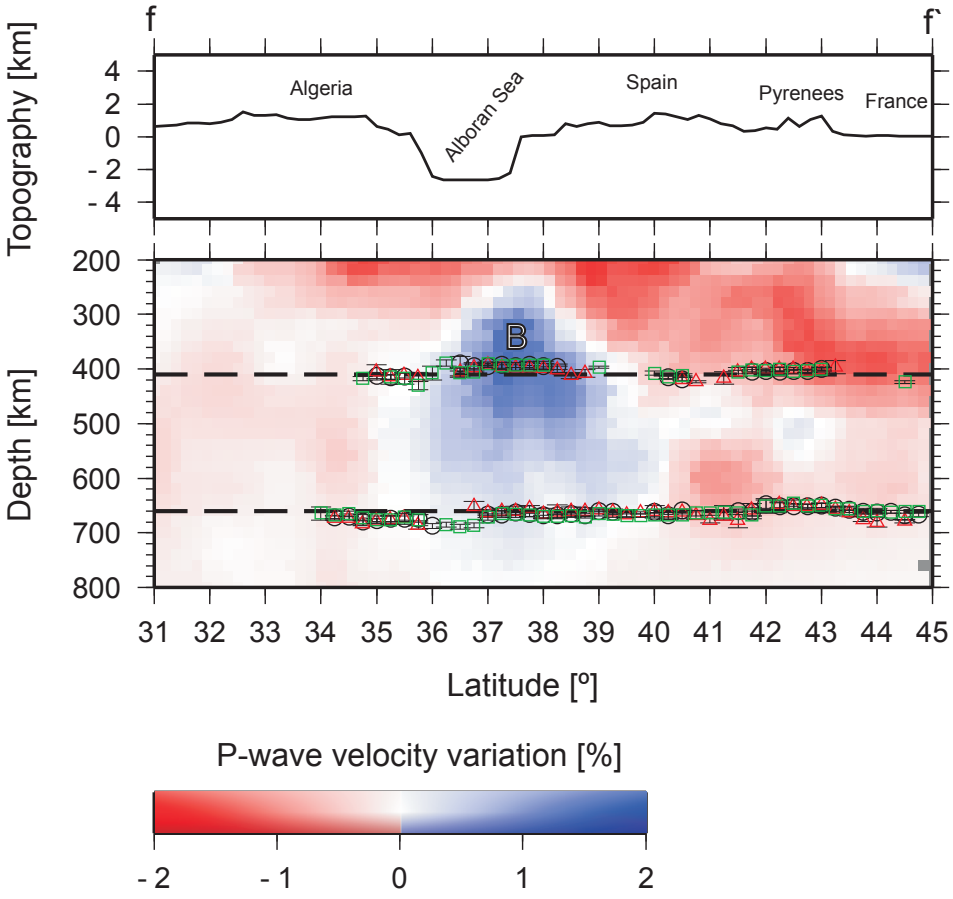

Figure E.2 continuation.

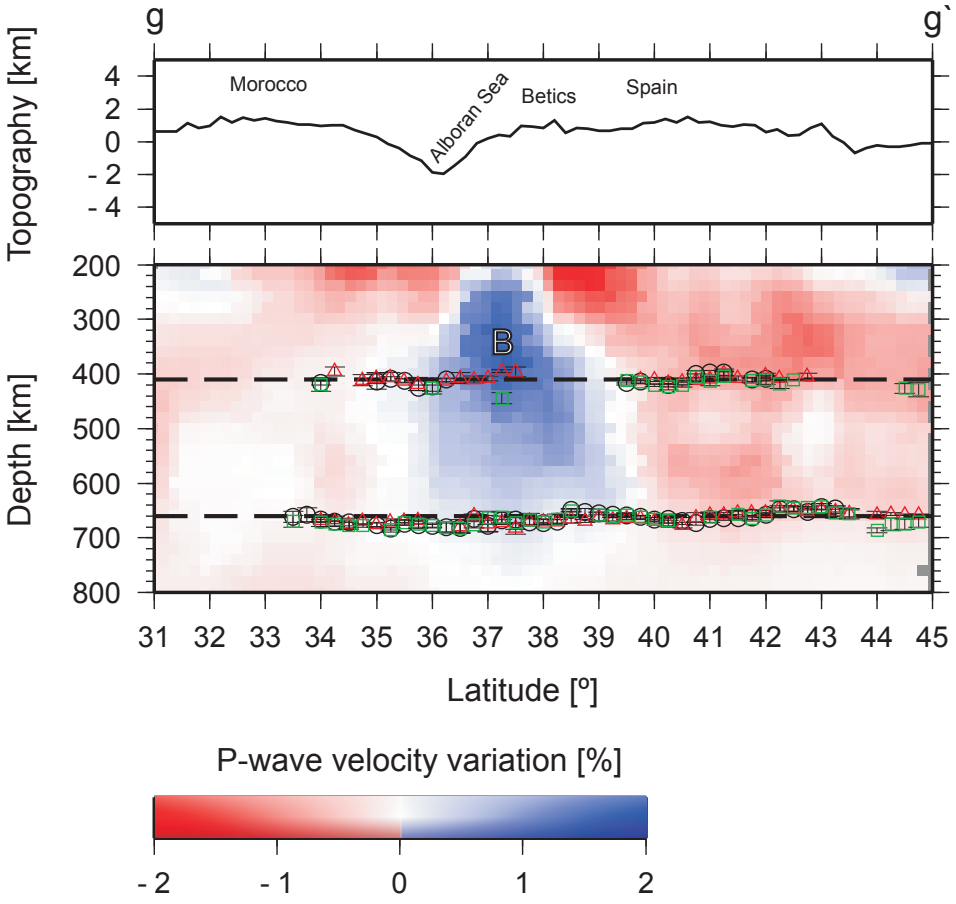

Figure E.2 continuation.

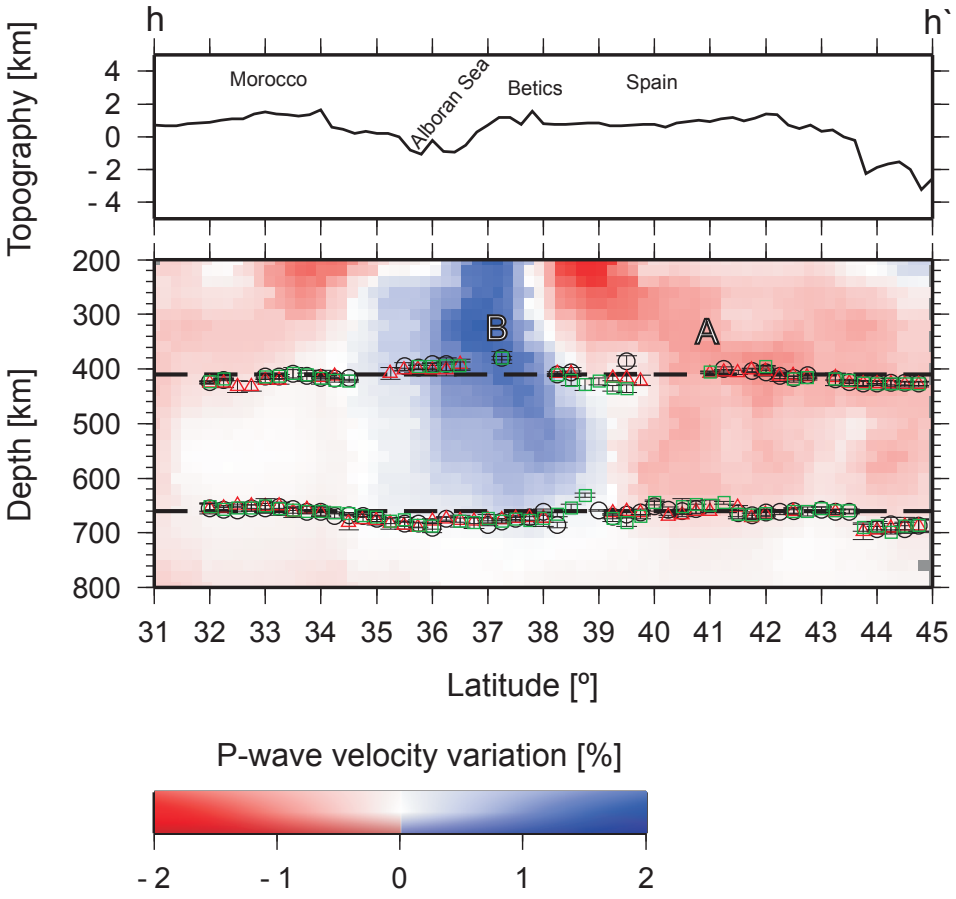

Figure E.2 continuation.

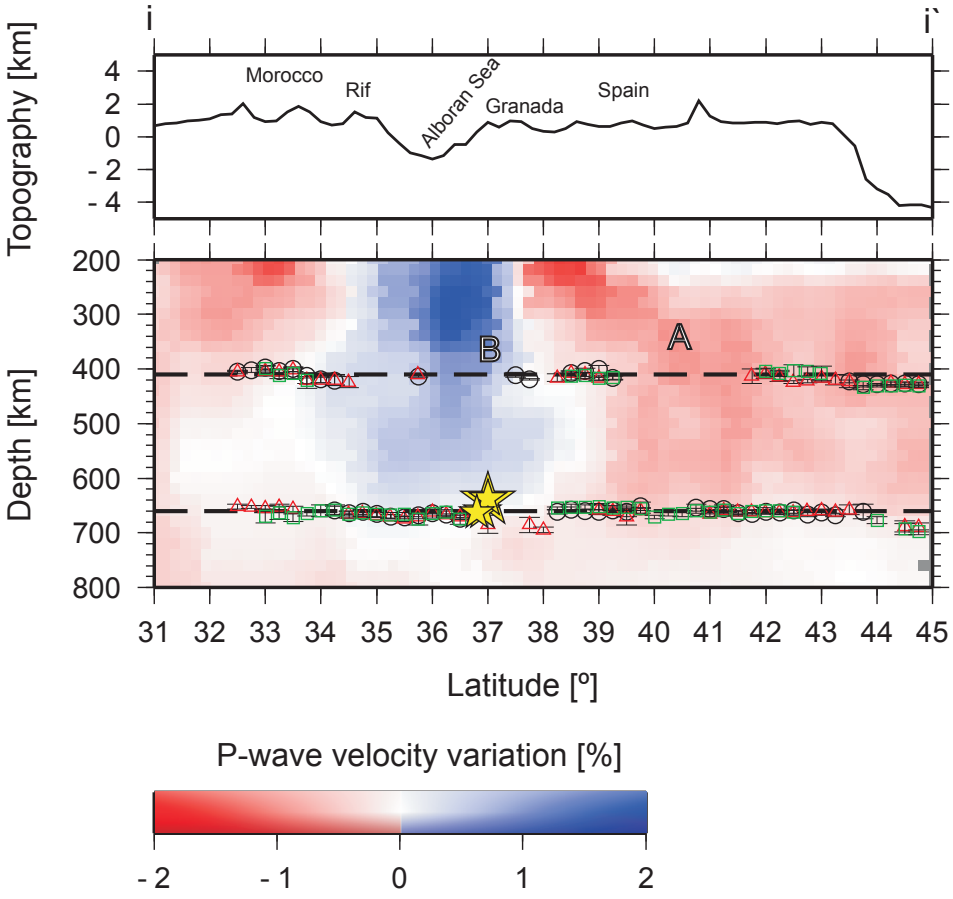

Figure E.2 continuation.

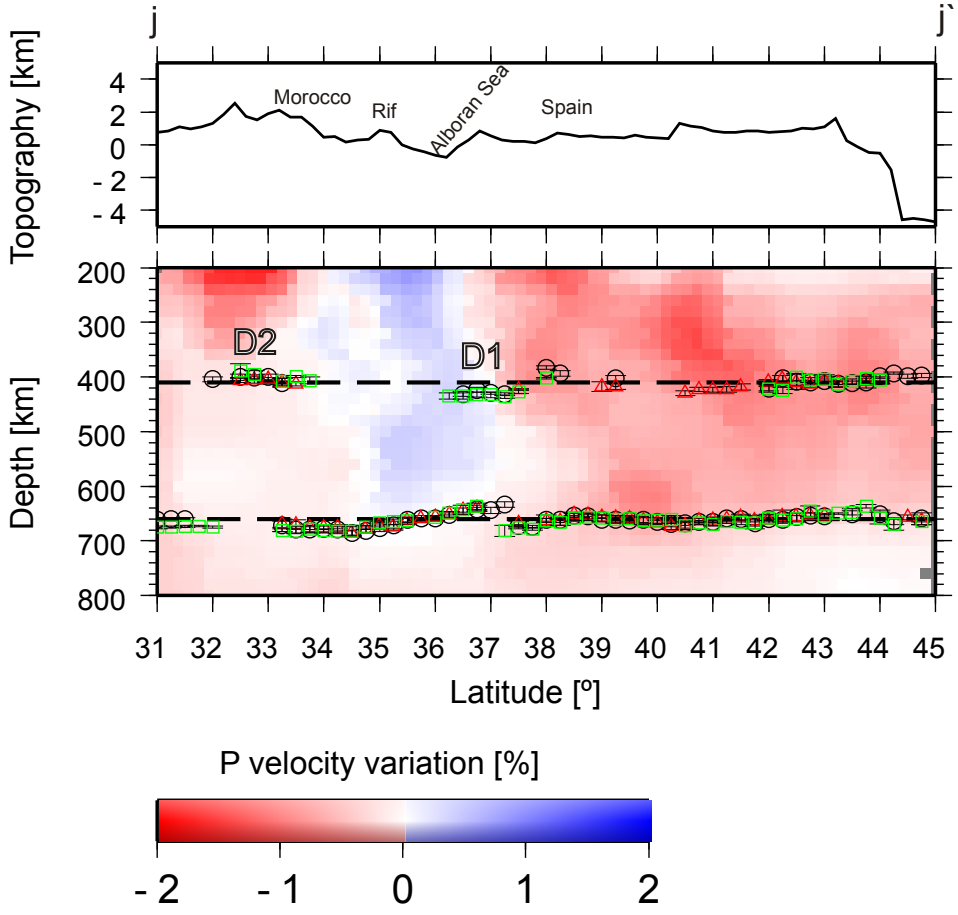

Figure E.2 continuation.

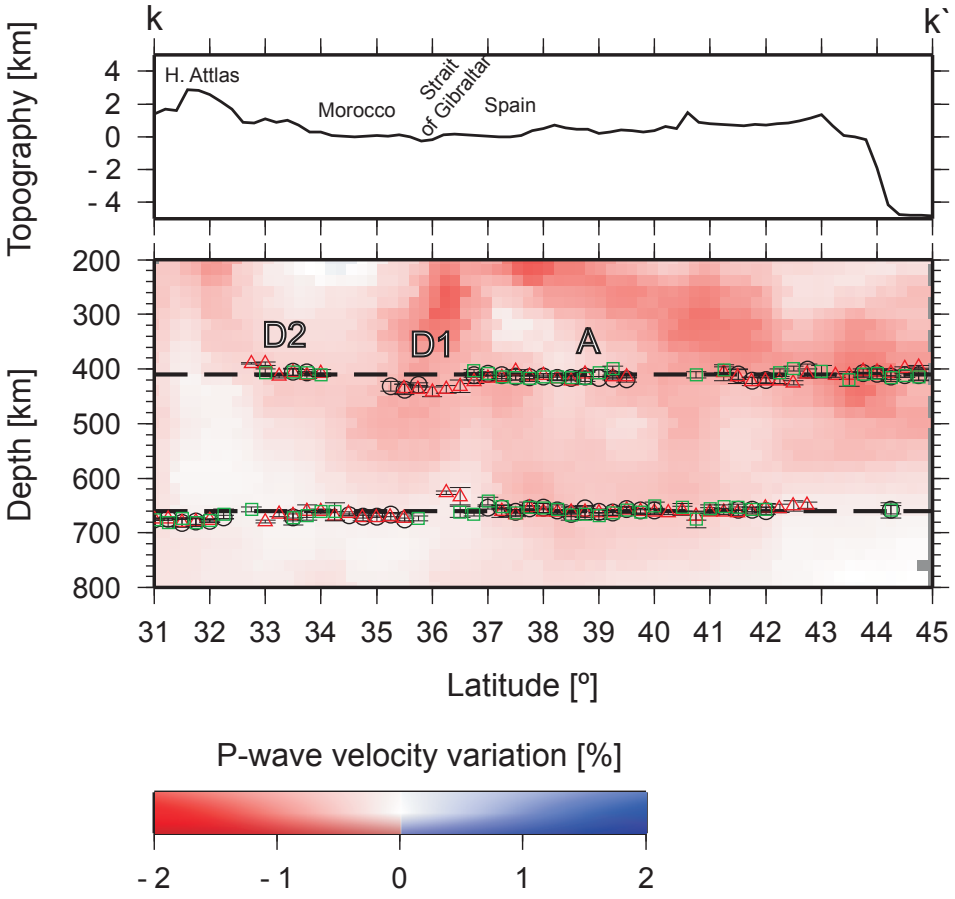

Figure E.2 continuation.

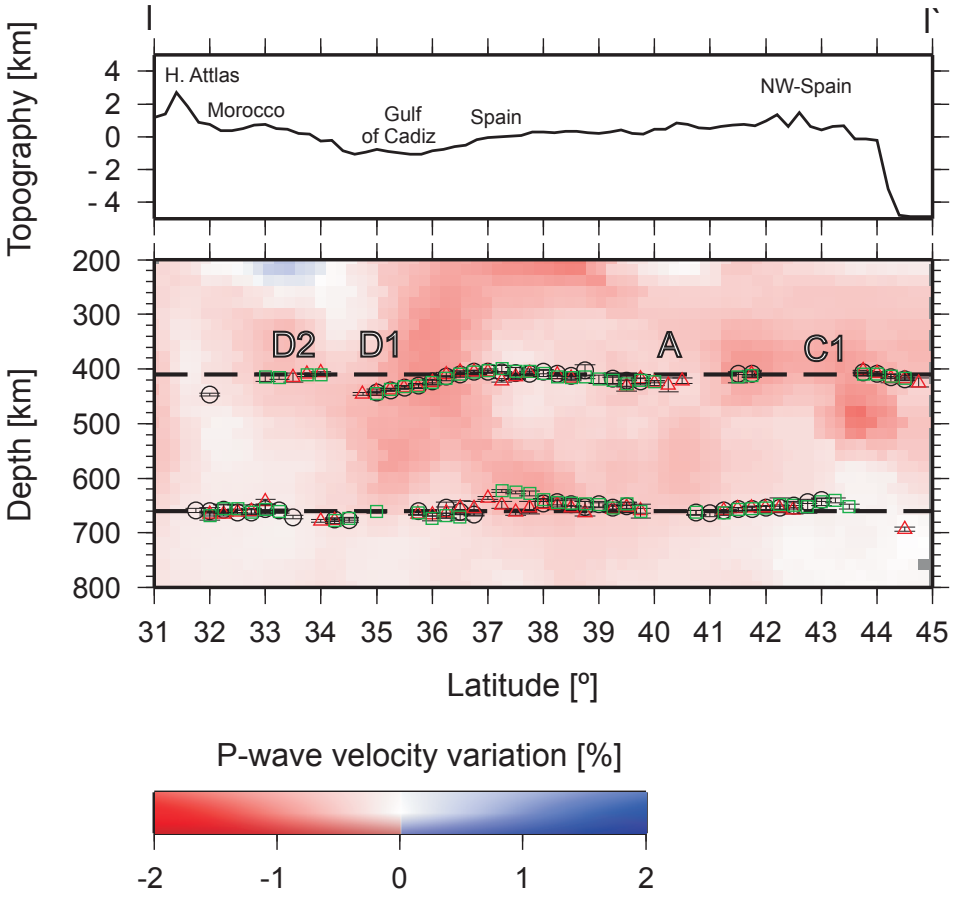

Figure E.2 continuation.

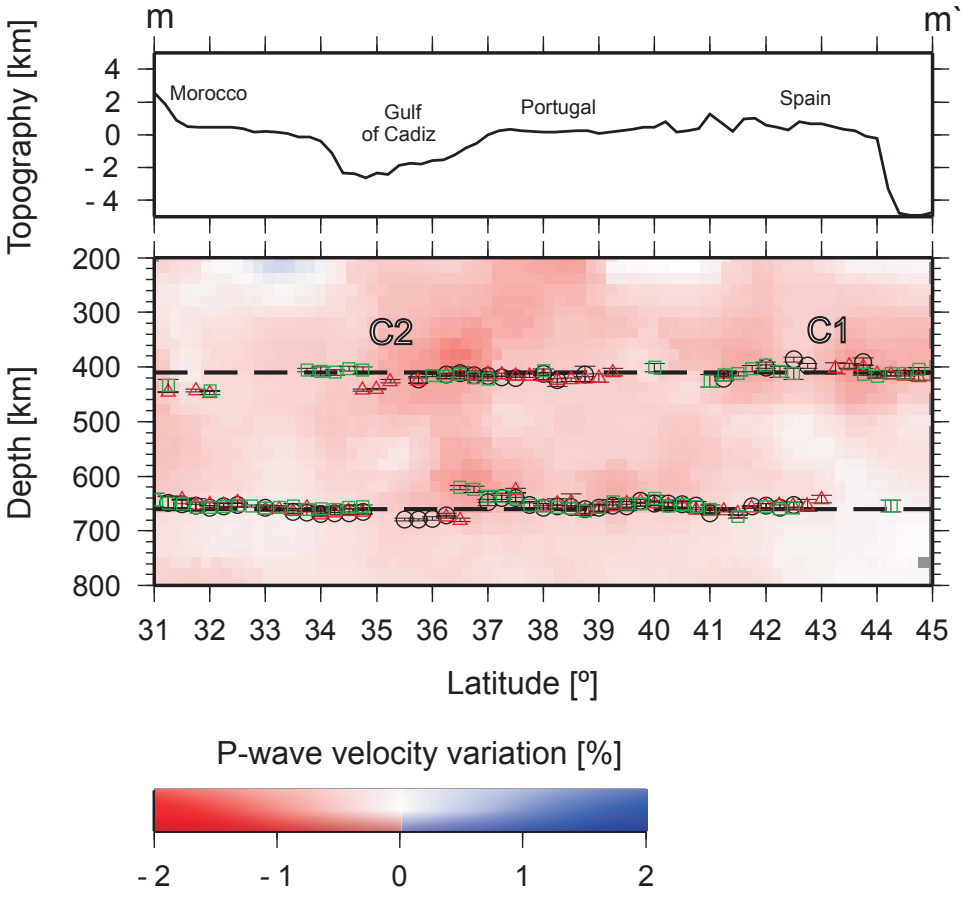

Figure E.2 continuation.

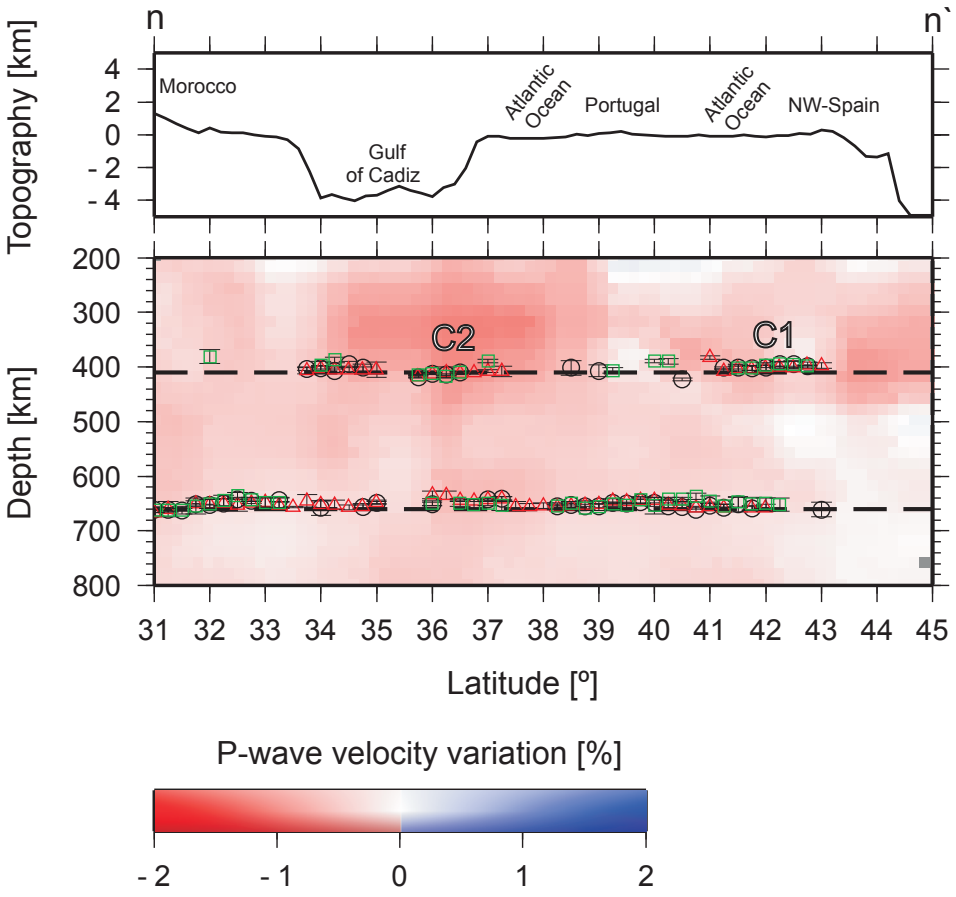

Figure E.2 continuation.

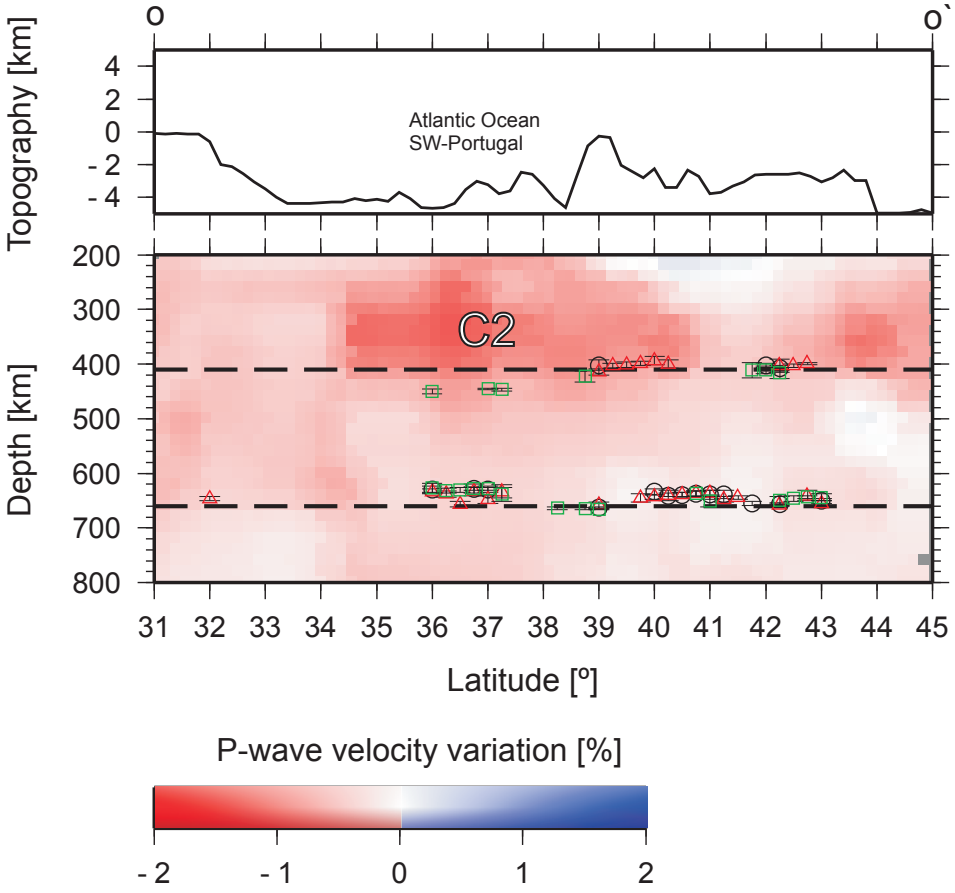

Figure E.2 continuation.

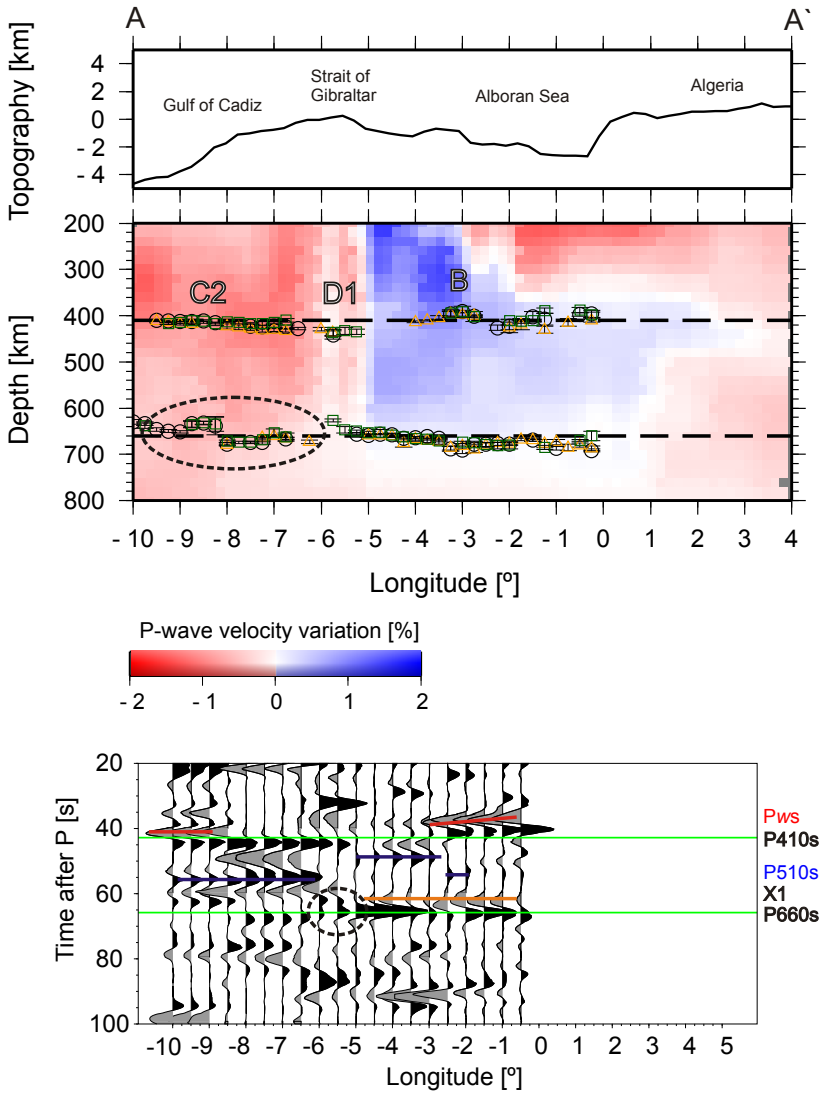

Figure E.3: **Top**: Cross section of average P-velocity anomalies from the tomographic model of Villaseñor et al. (2003) along the profiles AA' and BB' (Fig. E.1). Black circles show the estimated depths of the 410 and 660. Green squares and red triangles show the estimated depth 0.25° north and south of the corresponding profiles. Yellow stars in profile BB' show the hypocenters of the deep earthquakes beneath Granada from Buforn et al. (2004). The star size is proportional to the event magnitude, $M_W = 4, 4.8, 7$. **Bottom**: Corresponding cross-sections of CPP stacked RFs. The profiles show the CPP stacks in bins of 1° width in latitude and longitude and every 0.5°. The stacks were performed using a fixed relative slowness parameter of $-0.1s/°$ and a reference distance of 80°. Solid green lines mark the reference travel time for the $P410s$ and $P660s$ phases, dotted red lines show the arrival of negative-amplitude signals before the $P410s$, Pwd, and dotted blue lines show the possible detection of the $P510s$ phase.

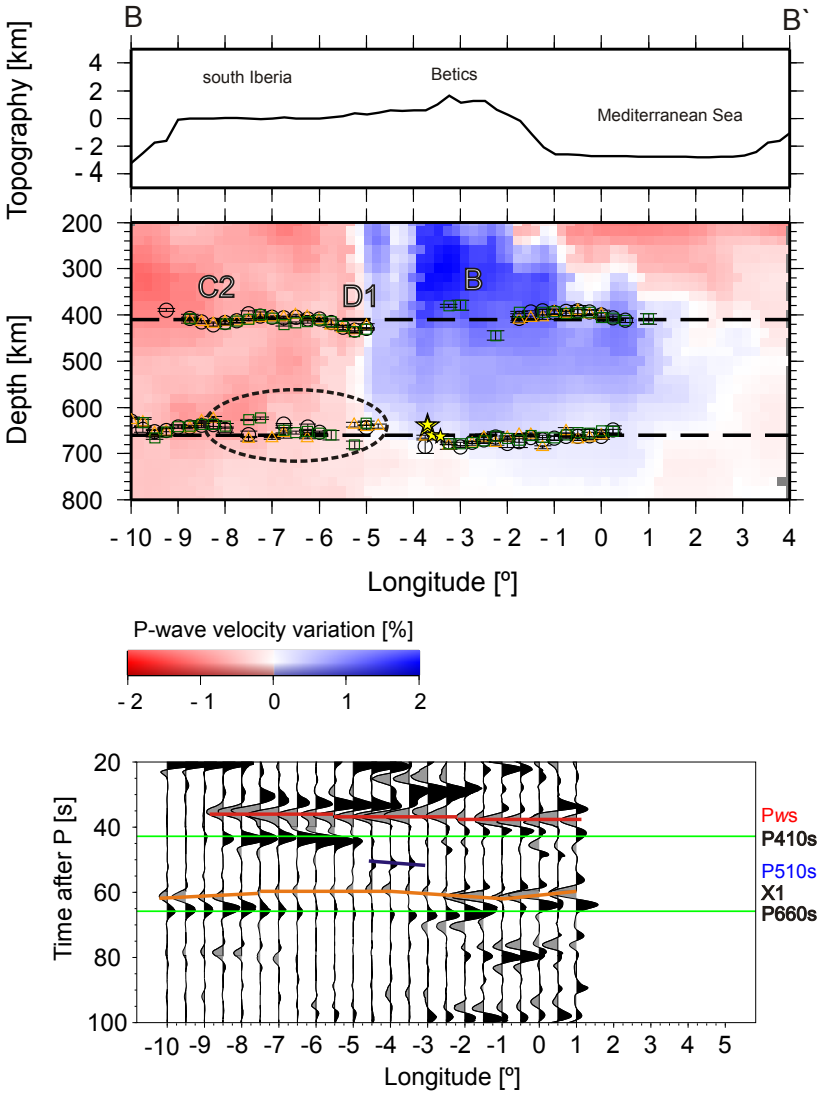

Figure E.3 continuation.

Bibliography

Ai, Y. and Zheng, Z. (2003). The upper mantle discontinuity structure beneath eastern China. Geophys. Res. Lett. *30(21)*, 2089.

Akaogi, M., Ito, E. and Navrotsky, A. (1989). Olivine-modified spinel transitions in the system Mg_2SiO_4 - Fe_2SiO_4: calorimetric measurements, thermochemical calculation, and geophysical application. J. Geophys Res. *94*, 15671–15685.

Akaogi, M., Tanaka, A. and Ito, E. (2002). Garnet−ilmenite−perovskite transitions in the system $Mg_4\ Si_4\ O_{12} - Mg_3Al_2\ Si_3O_{12}$ at high pressures and high temperatures: phase equilibria, calorimetry and implications for mantle structure. Earth Planet. Sci. Lett *132*, 303–324.

Akaogi, M., Yano, M., Tejima, Y., Iijima, M. and Kojitani, H. (2004). High- pressure transitions of diopside and wollanstonite: phase equilibria and thermochemistry of $CaMgSi_2O_6$, $CaSiO_3$ and $CaSi_2O_5$-$CaTiSiO_5$ system. Phys. Earth planet. Inter. *143/144*, 145–156.

Ammon, C. J. (1991). The isolation of receiver effects from teleseismic P waveforms. Bull. Seism. Soc. Am. *81*, 2504–2510.

Anderson, D. (2007). New Theory of the Earth pp. 91–108. Cambridge: Cambridge University Press, second edition.

Argus, D., Gordon, R., Demets, C. and Stein, S. (1989). Plate Motion Circuit and Tectonics of the Gloria Fault. J. Geophys. Res., *94(B5)*, 5585–5602.

Benz, H. M. and Vidale, J. E. (1993). Sharpness of upper-mantle discontinuities determined from high-frequency reflections. Nature , *365(6442)*, 147–150.

Bercovici, D. and Karato, S.-I. (2003). Whole mantle convection and the transition-zone water filter. Nature , *425*, 39–44.

Bezada, M. J. and Humphreys, E. D. (2012). Contrasting rupture processes during the April 11, 2010 deep-focus earthquake beneath Granada, Spain. Earth planet. Sci. Lett., *353-354*, 38–46.

Bezada, M. J., Humphreys, E. D., Toomey, D. R., Harnafi, M. and Dávila, J. M. (2013). Western mediterranean slab rollback revealed by upper mantle tomography. Earth planet. Sci. Lett., *368*, 51–60.

Bina, C. R. and Helffrich, G. (1994). Phase transition Clapeyron slopes and transition zone seismic discontinuity topography. J. Geophys. Res., *99(B8)*, 15853–15860.

Bina, C. R. and Kawakatsu, H. (2010). Buoyancy, bending, and seismic visibility in deep slab stagnation. Phys. Earth Planet. Int., *183*, 330–340.

Bina, C. R. and Wood, B. J. (1987). Olivine-spinel transitions: Experimental and thermodynamic constraints and implications for the nature of the 400-km seismic discontinuity. J. Geophys. Res., *92*, 4853–4866.

Blanco, M. and Spakman, W. (1993). The P–wave velocity structure of the mantle below the Iberian Peninsula: evidence for subducted lithosphere below southern Spain. Tectonophysics , *221*, 13–34.

Bokelmann, G. and Maufroy, E. (2007). Mantle structure under Gibraltar constrained by dispersion of body waves. Geophys. Res. Lett., *34*, L22305.

Bokelmann, G., Maufroy, E., Buontempo, L., Morales, J. and Barruol, G. (2011). Testing oceanic subduction and convective removal models for the Gibraltar arc: Seismological constraints from dispersion and anisotropy. Tectonophysics , *502*, 28–37.

Bonatto, L., Schimmel, M., Gallart, J. and Morales, J. (2013). Studying the 410-km and 660-km discontinuities beneath Spain and Morocco through detection of P-to-s conversions. Geophys. J. Int., *194(2)*, 920–935.

Bostock, M. G. (1998). Mantle stratigraphy and evolution of the Slave province. J. Geophys. Res., *103(B9)*, 21183–21200.

Bostock, M. G. (1999). Seismic waves converted from velocity gradient anomalies in the Earth's upper mantle. Geophys. J. Int., *138*, 747–756.

Bostock, M. G. (2007). 1.07 - Theory and Observations - Teleseismic Body-Wave Scattering and Receiver-Side Structure. In Treatise on Geophysics, (Schubert, G., ed.),, pp. 219–246. Elsevier, Oxford.

Buforn, E., Bezzeghoud, M., Ud´ ias, A. and Pro, C. (2004). Seismic Sources on the Iberia-African Plate Boundary and their Tectonic Implications. Pure appl. geophys., *161*, 623–646.

Buforn, E., Pro, C., Cesca, S., Ud´ ias, A. and del Fresno, C. (2011). The 2010 Granada, Spain deep Earthquake. Bull. Seism. Soc. Am., *101*, 2418–2430.

Buforn, E., Sanz de Galdeano, C. and Ud´ ias, A. (1995). Seismotectonics of the Ibero-Maghrebian region. Tectonophysics , *248*, 247–261.

Buontempo, L., Bokelmann, G. H. R., Barruol, G. and Morales, J. (2008). Seismic anisotropy beneath southern Iberia from SKS splitting. Earth planet. Sci. Lett., *273*, 237–250.

Calvert, A., Sandvol, E., Seber, D., Barazangi, M., Roecker, S., Mourabit, T., Vidal, F., Alguacil, G. and Jabour, N. (2000). Geodynamic evolution of the lithosphere and upper mantle beneath the Alboran region of the western Mediterranean: constraints from travel time tomography. J. Geophys. Res., *105(B5)*, 10871–10898.

Cao, Q., van der Hilst, R. D., de Hoop, M. V. and Shim, S.-H. (2011). Seismic Imaging of Transition Zone Discontinuities Suggests Hot Mantle West of Hawaii. Science , *332*, 1068–1071.

Carminati, E., Lustrino, M. and Doglioni, C. (2012). Geodynamic evolution of the central and western Mediterranean: Tectonics vs. igneous petrology constraints. Tectonophys., *579*, 173–192.

Chambers, K., Deuss, A. and Woodhouse, J. H. (2005). Reflectivity of the 410-km discontinuity from PP and SS precursors. J. Geophys. Res., *110(B02301)*.

Chapman, C., Jen-Yi, C. and Lyness, D. G. (1988). The WKBJ seismogram approximation. In Seismological Algorithms, (Doornbos, D., ed.),, pp. 47–74. Academic Press, London.

Chen, C. W., Miller, D. E., Djikpesse, H. A., U., H. J. B. and Rondenay (2010). Array-conditioned deconvolution of multiple-component teleseismic recordings. Geophys. J. Int., *182*, 967–976.

Chevrot, S., Vinnik, L. and Montagner, J.-P. (1999). Global scale analysis of the mantle Pds phases. J. Geophys. Res., *104(B9)*, 20203–20219.

Clayton, R. W. and Wiggins, R. A. (1976). Source shape estimation and deconvolution of teleseismic body waves. J. R. Astr. Soc., *47(1)*, 151–177.

Collier, J. and Helffrich, G. (1997). Topography of the 410 and 660 km seismic discontinuities in the Izu-Bonin subduction zone. Geophys. Res. Lett., *24*, 15351538.

Collier, J. D. and Helffrich, G. R. (2001). The thermal influence of the subducting slab beneath South America from 410 and 660 km discontinuity observations. Geophys. J. Int., *147*, 319–329.

Collier, J. D., Helffrich, G. R. and Wood, B. J. (2001). Seismic discontinuities and subduction zones. Phys. Earth Planet. Int., *127*, 35–49.

Comas, M. C., Platt, J. P., Soto, J. I. and Watts, A. B. (1999). The origin and tectonic history of the Alboran Basin: insigths from Leg 161 results. In Porc. ODP, Sci. Results, (Zahn, R., Comas, M. C. and Klau, A., eds),, vol. 161,, pp. 555–579. Ocean Drilling Program, College Station, TX.

Contenti, S., Gu, Y. J., Ökeler, A. and Sacchi, M. D. (2012). Shear wave reflectivity imaging of the Nazca–South America subduction zone: Stagnant slab in the mantle transition zone? Geophys. Res. Lett., *39*, L02310.

Demets, C., Gordon, R., Argus, D. and Stein, S. (1990). Current Plate Motions. Geophys. J. Int., *101*, 425–478.

Deuss, A. (2007). Seismic observations of transition zone discontinuities beneath hotspot locations, Vol. Special Paper 430. In Plates, Plumes, and Planetary Processes, (G., F. and J., J., eds),, pp. 121–136. Geological Society of America, Boulder, CO. doi:10.1130/2007.2430(07).

Deuss, A., Redfern, S. A. T., Chambers, K. and Woodhouse, J. H. (2006). The Nature of the 660–km Discontinuity in Earth's Mantle from Global Seismic Observations of PP Precursors. Science , *311(5758)*, 198–201.

Deuss, A. and Woodhouse, J. H. (2001). Seismic Observations of splitting of the mid-transition zone discontinuities in Erath's mantle. Science , *294*, 354–357.

Deuss, A. and Woodhouse, J. H. (2002). A systematic search for mantle discontinuities using SS-precursors. Geophys. Res. Lett., *29(8)*, 90.1–90.4.

Deuss, A. and Woodhouse, J. H. (2004). The nature of the Lehmann discontinuity from its seismological Clapeyron slopes. Earth planet. Sci. Lett., *225*, 295–304.

Díaz, J., Gallart, J., Villaseñor, A., Mancilla, F., Pazos, A., Córdoba, D., Pulgar, J. A., Ibarra, P. and Harnafi, M. (2010). Mantle dynamics beneath the Gibraltar Arc (western Mediterranean) from shear wave splitting measurements on a dense seismic array. Geophys. Res. Lett., *37*, L18304.

Díaz, J., Villaseñor, A., Gallart, J., Morales, J., Pazos, A., Córdoba, D., Pulgar, J. A., Garcia-Lobón, J., Harnafi, M. and Group, T. S. W. (2009). The IBERARRAY broadband seismic network: A new tool to investigate the deep structure beneath Iberia. Orfeus Newsl., *8*, 2.

Duecker, K.G. & A.F. Sheehan, . (1997). Mantle discontinuity structure from midpoint stacks of converted P to S waves across the Yellowstone hotspot track. J. Geophys. Res., *102*, 83130–8327.

Dueker, K. and Sheehan, A. (1997). Mantle discontinuity structure from midpoint stacks of converted P to S waves across the Yellowstone hot spot track. Geophys. J. R. astr. Soc., *47*, 151–177.

Duggen, S., Hoernle, K., van den Bogaard, P., Rüpke, L. and Morgan, J. P. (2003). Deep roots of the Messinian salinity crisis. Nature , *422*, 602–606.

Duggen, S., Hoernle, K. A., Hauff, F., Klügel, A., Bouabdellah, M. and Thirlwall, M. (2009). Flow of Canary mantle plume material through a subcontinental lithospheric corridor beneath Africa to the Mediterranean. Geology , *37(3)*, 283–286.

Dündar, S., Kind, R., Yuan, X., Bulut, F., Sodoudi, F., Heit, B., Kumar, P., Li, X., Hanka, W., Martin, R., Stiller, M., Eken, T., Bianchi, M., Buforn, E. and Davila, J. M. (2011). Receiver function images of the base of the lithosphere in the Alboran Sea region. Geophys. J. Int., *187*, 1019–1026.

Eagar, K. C., Foucha, M. J. and James, D. E. (2010). Receiver function imaging of upper mantle complexity beneath the Pacic Northwest, United States. Earth Planet. Sci. Lett., *297*, 140–152.

Efron, B. and Tibshitani, R. (1986). Bootstrap methods for standard errors, confidence intervals, and other measures of statistical accuracy. Stat. Sci., *1*, 54–77.

Faccenna, C., Piromallo, C., Crespo-Blanc, A., Jolivet, L. and Rossetti, F. (2004). Lateral slab deformation and the origin of the western Mediterranean arcs. Tectonics , *23*, TC1012.

Fadil, A., Vernant, P., McClusky, S., Reilinger, R., Gomez, F., Sari, D. B., Mourabit, T., Feigl, K. and Barazangi, M. (2006). Active tectonics of the western Mediterranean: Geodetic evidence for rollback of a delaminated subcontinental lithospheric slab beneath the Rif Mountains, Morocco. Geology , *34*, 529–532.

Fei, Y. and Bertka, C. M. (1999). Phase transitions in the Earths mantle and mantle mineralogy. In Mantle Petrology: Field Observations and High-Pressure Experimentation: A Tribute to F. R. Boyd, (Fei, Y., Bertka, C. M. and Mysen, B. O., eds),, pp. 189–207. Geochemical Society, Special Publication No 6, Huston.

Flanagan, M. and Shearer, P. (1998). Global mapping of topography on transition zone velocity discontinuities by stacking SS precursors. J. Geophys. Res., *103(B2)*, 2673–2692.

Flanagan, M. and Shearer, P. (1999). A map of topography on the 410-km discontinuity from PP precursors. Geophys. Res. Lett., *26*, 549–552.

Frost, D. (2003). The structure and sharpness of $(Mg, Fe)_2SiO_4$ phase transformations in the transition zone. Earth Planet. Sci. Lett., *216*, 313–328.

Frost, D. J. (2008). The Upper Mantle and Transition Zone. Elements , *4*, 171–176.

Galetti, E. and Curtis, A. (2012). Generalised receiver functions and seismic interferometry. Tectonophysics , *532-535,*, 1–26.

Garcia-Castellanos, D. and Villaseñor, A. (2011). Messinian salinity crisis regulated by competing tectonics and erosion at the Gibraltar Arc. Nature , *480*, 359–363.

Geller, R. J. and Takeuchi, N. (1995). A new method for computing highly accurate DSM synthetic seismograms. Geophys. J. Int., *123*, 449–470.

Grange, M., Schärer, U., Merle, R., Girardeau, J. and Cornen, G. (2010). Plume-Lithosphere Interaction during Migration of Cretaceous Alkaline Magmatism in SW Portugal: Evidence from U-Pb Ages and Pb-Sr-Hf Isotopes. J. Petr., *51(5)*, 1143–1170.

Green, H. and Houston, H. (1995). The mechanics of deep earthquakes. Annu. Rev. Earth Planet. Sci., *23*, 169–213.

Gu, Y. and Dziewonski, A. M. (1998). Global de-correlation of the topography of transition zone discontinuities. Earth and Planetary Science Letters , *157*, 57–67.

Gurrola, H., Baker, G. E. and Minster, J. B. (1995). Simultaneous time-domain deconvolution with application to the computation of receiver functions. Geophys. J. Int., *120*, 537–543.

Gutscher, M., Malod, J., Rehault, J., Contrucci, I., Klingelhoefer, F., Mendes-Victor, L. and Spakman, W. (2002). Evidence for active subduction beneath Gibraltar. Geology , *30*, 1071–1074.

Helffrich, G. (2000). Topography of the transition zone seismic discontinuities. Rev. Geophys., *38(1)*, 141–158.

Helffrich, G., Asencio, E., Knapp, J. and Owens, T. (2003). Transition zone structure in a tectonically inactive area: 410 and 660 km discontinuity properties under the northern North Sea. Geophys. J. Int., *55*, 193–199.

Helffrich, G. and Bina, C. R. (1994). Frequency dependence the visibility depths mantle of and of seismic discontinuitie. Geophys. Res. Lett., *21(24)*, 2613–2616.

Higo, Y., Inoue, T., Irifune, T. and Yurimoto, H. (2001). Effect of water on the spinelpostspinel transformation in Mg_2SiO_4. Geophys. Res. Lett., *28(18)*, 3505–3508.

Hirose, K. (2002). Phase transitions in pyrolitic mantle around 670 km depth: Implications for upwelling of plumes from the lower mantle. J. Geophys. Res., *107(B4)*, 2078.

Hirschmann, M. (2006). Water, melting and the deep Earth H_2O cycle. An. Rev. Earth Planet. Sci., *34*, 629–653.

Hoernle, K., Zhang, Y.-S. and Graham, D. (1995). Seismic and geochemical evidence for large-scale mantle upwelling beneath the eastern Atlantic and western and central Europe. Nature , *374*, 34–39.

Houston, H. (2007). 4.11 - Deep Earthquakes. In Treatise on Geophysics, (Schubert, G., ed.),, pp. 321–350. Elsevier, Oxford.

Irifune, T. and Ringwood, A. E. (1987). Phase transformations in primitive MORB and pyrolite compositions to 25 GPa and some geophysical implications. In High-Pressure Research in Mineral Physics: A Volume in Honor of Syun-iti Akimoto, Geophys. Monogr. Ser., (Manghnani, M. and Syono, Y., eds),, vol. 39,, pp. 221–242. AGU, Washington, D. C. doi:10.1029/GM039p0231.

Ito, E. and Takahashi, E. (1998). Postspinel transformations in the system Mg_2SiO_4–Fe_2SiO_4 and some geophysical implications. J. Geophys. Res., *94(B8)*, 10637–10646.

Jasbinsek, J. J., Dueker, K. G. and Hansen, S. M. (2010). Characterizing the 410 km discontinuity lowvelocity layer beneath the LA RISTRA array in the North American Southwest. Geochem. Geophys. Geosyst., *11*, Q03008.

Juliá, J. (2007). Constraining velocity and density contrasts across the crustmantle boundary with receiver function amplitudes. Geophys. J. Int., *171(1)*, 286–301.

Karato, S. (1997). On the separation of crustal component from subducted oceanic lithosphere near the 660 km discontinuity. Phys. Earth Planet. Inter., *99*, 103–111.

Katsura, T. and Ito, E. (1989). The system $Mg_2SiO_4 - Fe_2SiO_4$ at high pressure and temperature: precise determination of stabilities of olivine, modifed spinel and spinel. J. Geophys. Res., *94*, 15663–15670.

Katsura, T., Yamada, H., Nishikawa, O., Song, M., Kubo, A., Shinmei, T., Yokoshi, S., Aizawa, Y., Yoshino, T., Walter, M. J. and Ito, E. (2004). Olivine-wadsleyite transition in the system $(Mg, Fe)_2SiO_4$. J. Geophys. Res., *109*, B02209.

Katsura, T., Yamada, H., Shinmei, T., Kubo, A., Ono, S., Kanzaki, M., Yoneda, A., Walter, M. J., Ito, E., Urakawa, S., Funakoshi, K. and Utsumi, W. (2003). Post-spinel transition in $Mg_2\ SiO_4$ determined by high P-T in situ X-ray diffractometry. Earth Planet. Sci. Lett., *136*, 11–24.

Kawai, K., Takeuchi, N. and Geller, R. J. (2006). Complete synthetic seismograms up to 2 Hz for transversely-isotropic spherically symmetric media. Geophys. J. Int., *164*, 411–424.

Kennett, B. L. N., Engdahl, E. R. and R., B. (1995). Constraints on seismic velocities in the Earth from traveltimes. Geophys. J. Int., *122*, 108–124.

Kennett, B. L. N. & Engdahl, E. R. (1991). Traveltimes for Global Earthquake Location and Phase Identification. Geophys. J. Int., *105*, 429–465.

Kikuchi, M. and Kanamori, H. (1982). Inversion of complex body waves. Bull. Seism. Soc. Am., *72(2)*, 491–506.

Kind, R., Kosarev, G. and Petersen, N. (1995). Receiver functions at the stations of the German Regional Seismic Network (GRSN). Geophys. J. Int., *121*, 191–202.

Kind, R. and Li, X. (2007). 1.17 - Deep Earth Structure - Transition Zone and Mantle Discontinuities. In Treatise on Geophysics, (Schubert, G., ed.),, pp. 592–611. Elsevier, Oxford.

Knapmeyer-Endrun, B., Krüger, F., Legendre, C., Geissler, W. and PASSEQ, W. G. (2013). Tracing the influence of the Trans-European Suture Zone into the mantle transition zone. Earth Planet. Sci. Lett., *363*, 73–87.

Kohlstedt, D. L., Keppler, H. and Rubie, D. C. (1996). Solubility of water in the α, β, and γ phases of $(Mg, Fe)_2SiO_4$. Contrib. Mineral. Petrol., *123*, 345–357.

Landes, M., Ritter, J. R. R., OReilly, B. M., Readman, P. W. and Do, V. C. (2006). A N-S receiver function profile across the Variscides and Caledonides in SW Ireland. Geophys. J. Int., *166*, 814–824.

Langston, C. A. (1979). Structure under Mount Rainier, Washington, inferred from teleseismic body waves. J. Geophys. Res., *84*, 4749–4762.

Langston, C. A. & Hammer, J. K. (2001). The vertical component P–wave receiver function. Bull. seism. Soc. Am., *91(6)*, 1805–1819.

Lawrence, J. F. and Shearer, P. M. (2006). A global study of transition zone thickness using receiver functions. J. Geophys. Res., *111*, B06307.

Lehmann, I. (1959). Velocities of longitudinal waves in the upper part of the Earth's mantle. Ann. Geophys., *15*, 93–113.

Lehmann, I. (1961a). S and the structure of the upper mantle. Geophys. J. R. astr. Soc., *4*, 124–138.

Lehmann, I. (1961b). S and the structure of the upper mantle. Geophysical Journal of the Royal Astronomical Society , *4*, 124–138.

Lehmann, I. (1964). On the velocity of P in the upper mantle. Bulletin Seismological Society of America , *54*, 1097–1103.

Li, A., Fischer, K. M., van der Lee, S. and Wysession, M. E. (2002). Crust and upper mantle discontinuity structure beneath North America. J. Geophys. Res., *107*, B5.

Li, X. and Yuan, X. (2003). Receiver functions in northeast China – implications for slab penetration into the lower mantle in northwest Pacific subduction zone. Earth Planet. Sci. Lett., *216*, 679–691.

Ligorría, J. P. and Ammon, C. J. (1999). Iterative Deconvolution and Receiver-Function Estimation. Bull. seism. Soc. Am., *89(5)*, 1395–1400.

Litasov, K. D. and Ohtani, E. (2005). Phase relations in hydrous MORB at 18-28 GPa: Implications for heterogeneity of the lower mantle. Phys. Earth Planet. Inter., *150*, 239–263.

Litasov, K. D., Ohtani, E., Sano, A., Suzuki, A. and Funakoshi, K. (2005). Wet subduction versus cold subduction. Geophys. Res. Lett., *32*, L13312.

Lonergan, L. and White, N. (1997). Origin of the Betic-Rif mountain belt. Tectonics , *16*, 504–522.

Lustrino, M. (2011). What 'anorogenic' igneous rocks can tell us about the chemical composition of the upper mantle: case studies from the circum-Mediterranean area. Geol. Mag., *148(2)*, 304–316.

Lustrino, M., Duggen, S. and Rosenberg, C. L. (2011). The Central-Western Mediterranean: Anomalous igneous activity in an anomalous collisional tectonic setting. Earth-Sciences Reviews , *104*, 1–40.

Lustrino, M. and Wilson, M. (2007). The circum-Mediterranean anorogenic Cenozoic igneous province. Earth-Science Reviews , *81*, 1–65.

Macera, P., Gasperini, D., Piromallo, C., Blichert-Toft, J., Bosch, D., del Moro, A. and Martin, S. (2003). Geodynamic implications of deep mantle upwelling in the source of Tertiary volcanics from the Veneto region (south-eastern Alps). J. Geodyn., *36*, 563–590.

Mancilla, F., Stich, D., Morales, J., Juliá, J., Diaz, J., Pazos, A., Córdoba, D., Pulgar, J. A., Ibarra, P., Harnafi, M. and Gonzalez-Lodeiro, F. (2012). Crustal thickness variations in northern Morocco. J. Geophys. Res., *117*, B02312.

Mezcua, J. and Martínez-Solares, M. (1983). Sismicidad del área Ibero-Mogrebí. Instituto geográfico Nacional, Madrid.

Monna, S., Cimini, G. B., Montuori, C., Matias, L. M. M., Geissler, W. H. and Favali, P. (2013). New insights from seismic tomography on the complex geodynamic evolution of two adjacent domains: Gulf of Cadiz and Alboran Sea. J. Geophys. Res. *in press*.

Morales, J., Serrano, I., Javajoy, A., Galindo-Zaldívar, J., Zaho, D., Torcal, F., Vidal, F. and González Lodeiro, F. (1999). Active continental subduction beneath the Betic Cordillera and the Alboran Sea. Geology *27*, 735–738.

Murakami, M., Hirose, K., Kawamura, K., Sata, N. and Ohishi, Y. (2004). Post-Perovskite phase transition in $MgSiO_3$. Science *304*, 855–858.

Murakami, M., Sinogeikiin, S., Hellwig, H., Bass, J. and Li, J. (2007). Sound velocity of $MgSiO_3$ perovskite to Mbar pressure. Earth planet. Sci. Lett. *256*, 47–54.

Nagaya, M., Oda, H., Akazawa, H. and Ishise, M. (2008). Receiver Functions of Seismic Waves in Layered Anisotropic Media: Application to the Estimate of Seismic Anisotropy. Bull. Seism. Soc. Am. *98(6)*, 2990–3600.

Neele, F., De Regt, H. and VanDecar, J. (1997). Gross errors in uppermantle discontinuity topography from underside reflection data. Geophys. J. Int. *129*, 194–204.

Negredo, A. M., Bird, P., Sanz de Galdeano, C. and Buforn, E. (2002). Neotectonic modelling of the Ibero-Maghrebian region. J. Geophys. Res. *107(B11)*, 2292.

O'Neill, H. S. C., McCammon, C. A., Canil, D., Rubie, D. C., Ross, C. R. and Seifert, F. (1993). Mössbauer spectroscopy of mantle transition zone phases and determination of minimum Fe^{3+} content. Am. Mineral *78*, 456–460.

Oyarzun, R., Doblas, M., LpezRuiz, J. and Cebri, J. (1997). Opening of the central Atlantic and asymmetric mantle upwelling phenomena: Implications for long-lived magmatism in western North Africa and Europe. Geology *25*, 727–730.

Paulssen, H. (1985). Upper Mantle Converted Waves Beneath The NARS Array. Geophys. Res. Lett. *12(10)*, 709–712.

Paulssen, H. (1988). Evidence for a Sharp 670-km Discontinuity as Inferred From P-to-s Converted Waves. J. Geophys. Res. *93(B9)*, 10489–10500.

Phinney, R. (1964). Structure of the Earth's Crust from Spectral Behavior of Long–Period Body Waves. J. Geophys. Res. *69(14)*, 2997–3017.

Piromallo, C. and Morelli, A. (2003). P wave tomography of the mantle under the Alpine-Mediterranean area. J. Geophys. Res. *108(B2)*, 2065.

Platt, J. and Vissers, R. (1989). Extensional collapse of thickened continental lithosphere: a working hypothesis for the Alboran Sea and Gibraltar Arc. Geology *17*, 540–543.

Revenaugh, J. and Jordan, T. H. (1991). Mantle layering from ScS reverberations, 2, The transition zone. J. Geophys. Res. *96(B12)*, 19763–19780.

Revenaugh, J. and Sipkin, S. (1994). Seismic evidence for silicate melt atop the 410 km discontinuity. Nature *369*, 474–476.

Richard, G. C. and Bercovici, D. (2009). Water-induced convection in the Earth's mantle transition zone. J. Geophys. Res. *114*, B01205.

Richards, P. (1972). Seismic waves reflected from velocity gradient anomalies within the Earth's upper mantle. J. Geophys. Res. *38*, 517–527.

Ringwood, A. E. (1975). Composition and Petrology of the Earths Mantle. McGraw-Hill, New York.

Ritsema, J. and Van Heijst, H. J. (2002). Constraints on the correlation of P- and S-wave velocity heterogeneity in the mantle from P, PP, PPP and PKPab travel times. Geophys. J. Int. *149*, 482–489.

Rosenbaum, G., Lister, G. and Duboz, C. (2002). Relative motions of Africa, Iberia and Europe during Alpine orogeny. Tectonophysics *359*, 117–129.

Royden, L. (1993). Evolution of retreating subduction boundaries formed during continental collision. Tectonics *12(3)*, 629–638.

Saikia, A., Frost, D. and Rubie, D. (2008). Splitting of the 520-kilometer seismic discontinuity and chemical heterogeneity in the mantle. Science *319*, 1515–1518.

Schimmel, M. (1999). Phase cross-correlations: design, comparisons and applications. Bull. Seismol. Soc. Am. *89(5)*, 1366–1378.

Schimmel, M. and Paulssen, H. (1997). Noise reduction and detection of weak, coherent signals through phase-weighted stacks. Geophys. J. Int. *130*, 497–505.

Schimmel, M., Stutzmann, E. and Gallart, J. (2011). Using instantaneous phase coherence for signal extraction from ambient noise data at a local to a global scale. Geophys. J. Int. *184*, 494–506.

Schmandt, B. (2012). Mantle transition zone shear velocity gradients beneath US-Array. Earth Planet. Sci. Lett. *355-356*, 119–130.

Schmandt, B., Dueker, K. G., Hansen, S. M., Jasbinsek, J. J. and Zhang, Z. (2011). A Sporadic Low-Velocity Layer Atop the Western Us Mantle Transition Zone and Short-Wavelength Variations in Transition Zone Discontinuities. Geochem. Geophys. Geosyst. *12*, Q08014.

Schmerr, N. C. and Garnero, E. J. (2007). Upper Mantle Discontinuity Topography from Thermal and Chemical Heterogeneity. Science *318*, 623–626.

Seber, D., Barazangi, M., Ibenbrahim, A. and Demnati, A. (1996). Geophysical evidence for lithospheric delamination beneath the Alboran Sea and Rif-Betics mountains. Nature *379*, 785–790.

Shearer, P. (1990). Seismic imaging of upper-mantle structure with new evidence for a 520-km discontinuity. Nature *344*, 121–126.

Shearer, P. M. (1991). Constraints on Upper Mantle Discontinuities From Observations of Long-Period Reflected and Converted Phases. J. Geophys. Res. *96(B11)*, 18147–18182.

Shearer, P. M. (1993). Global mapping of upper mantle reflectors from long-period SS precursors. Geophys. J. Int. *115*, 878–904.

Shearer, P. M. (1996). Transition zone velocity gradients and the 520 km discontinuity. J. Geophys. Res. *101*, 3053–3066.

Shearer, P. M. (2000). Upper mantle seismic discontinuities. In Earth's Deep Interior: Mineral Physics and Tomography from the Atomic to the Global Scale, Geophysical Monographs, (Karato, S.-I., Forte, A., Liebermann, R., Masters, G. and Stixrude, L., eds), vol. 117, pp. 115–131. AGU Washington, D. C.

Shearer, P. M. (2009). Introduction to Seismology. Second edition, Cambridge University Press, Cambridge.

Shen, X. and Blum, J. (2003). Seismic evidence for accumulated oceanic crust above the 660-km discontinuity beneath southern Africa. Geophys. Res. Lett. *30(18)*, 1925.

Shen, X., Zhou, H. and Kawakatsu, H. (2008). Mapping the upper mantle discontinuities beneath China with teleseismic receiver functions. Earth Planets Space *60*, 713–719.

Sheriff, R. (1996). Understanding the Fresnel zone. Geophysical Corner , 1–2.

Smyth, J. R. and Frost, D. (2002). The Effect of Water on the 410-km Discontinuity: An Experimental Study. Geophys. Res. Lett. *29*.

Song, T. A., Helmberger, D. V. and Grand, S. P. (2004). Low velocity zone atop the 410 seismic discontinuity in the northwestern United States. Nature *427*, 530–533.

Spakman, W. (1990). Images of the upper mantle of central Europe and the Mediterranean. Terra Nova *2*, 542–533.

Spakman, W. and Wortel, M. J. R. (2004). A tomographic view on western Mediterranean geodynamics. In The TRANSMED Atlas–The Mediterranean Region From Crust to Mantle, (Ziegler, P., ed.), pp. 31–52. Springer Berlin.

Stich, D., Serpelloni, E., Mancilla, F. and Morales, J. (2006). Kinematics of the Iberia-Maghreb plate contact from seismic moment tensors and GPS observations. Tectonophysics *426*, 295–317.

Stixrude, L. (1997). Structure and sharpness of phase transitions and mantle discontinuities. J. Geophys. Res. *102*, 14835–14852.

Suetsugu, D., Saita, T., Takenaka, H. and Niu, F. (2004). Thickness of the mantle transition zone beneath the South Pacific as inferred from analyses of ScS reverberated and Ps converted waves. Phys. Earth Planet. Int. *146*, 35–46.

Suzuki, A., Ohtani, E., Morishima, H., Kubo, T., Kanbe, Y., Kondo, T., Okada, T., Terasaki, H., Kato, T. and Kikegawa, T. (2000). In situ determination of the phase boundary between wadsleyite and ringwoodite in Mg_2SiO_2. Geophys. Res. Lett. *27*, 803–806.

Tauzin, B., Debayle, E. and Wittlinger, G. (2007). The mantle transition zone as seen by global Pds phases: No clear evidence for a thin transition zone beneath hotspots. J. Geophys. Res. *113*, B08309.

Tauzin, B., Debayle, E. and Wittlinger, G. (2010). Seismic evidence for a global low-velocity layer within the Earth's upper mantle. Nature Geoscience *3*, 718–721.

Thomas, C. and Billen, M. I. (2009). Mantle transition zone structure along a profile in the SW Pacific: thermal and compositional variations. Geophys. J. Int. *176*, 113–125.

Tibi, R. and Wiens, D. A. (2005). Detailed structure and sharpness of upper mantle discontinuities in the Tonga subduction zone from regional broadband arrays. J. Geophys. Res. *110*, B06313.

Tono, Y., Kunugi, T., Fukao, Y., Tsuboi, S., Kanjo, K. and Kasahara, K. (2005). Mapping of the 410– and 660–km discontinuities beneath the Japanese islands. J. Geophys. Res. *110*, B03307.

van der Lee, S., Paulssen, H. and Nolet, G. (1994). Variability of P660s phases as a consequence of topography of the 660 km discontinuity. J. Phys. Earth Planet. Inter. *86*, 147–164.

van der Meijde, M., Marone, F., Giardini, D. and van der Lee, S. (2003). Seismic Evidence for Water Deep in Earth's Upper Mantle. Science *300(5625)*, 1556–1558.

van der Meijde, M., van der Lee, S. and Giardini, D. (2005). Seismic discontinuities in the Mediterranean mantle. J. Phys. Earth Planet. Inter. *148*, 233–250.

van Keken, P. E., Karato, S. and Yuen, D. A. (1996). Rheological contol of oceanic crust separation in the transition zone. Geophys. Res. Lett. *23*, 1821–1824.

Verges, J. and Fernandez, M. (2012). Tethys-Atlantic interaction along the IberiaAfrica plate boundary: The BeticRif orogenic system. Tectonophysics *579*, 144–172.

Vernant, P., Fadil, A., Mourabit, T., Ouazar, D., Koulali, A., Davila, J. M., Garate, J., McClusky, S. and Reilinger, R. (2010). Geodetic constraints on active tectonics

of the Western Mediterranean: Implications for the kinematics and dynamics of the Nubia-Eurasia plate boundary zone. J. Geodyn. *49*, 123–129.

Vidale, J. E. and Benz, H. M. (1992). Upper-mantle seismic discontinuities and the thermal structure of subduction zones. Nature *356(6371)*, 678–683.

Vidale, J. E., Ding, X.-Y. and Grand, S. P. (1995). The 410-km-depth discontinuity: A sharpness estimate from near-critical reflections. Geophys. Res. Lett. *22*, 2557–2560.

Villaseñor, A., Spakman, W. and Engdahl, E. R. (2003). Influence of regional travel times in global tomographic models. Geophys. Res. Abstr. *5*.

Vinnik, L. (1977). Detection of waves converted from P to SV in the mantle. J. Phys. Earth Planet. Inter. *15*, 39–45.

Vinnik, L. P. and Farra, V. (2002). Subcratonic low velocity layer and flood basalts. Geophys. Res. Lett. *29(4)*, 1049.

Vinnik, L. P. and Farra, V. (2007). Low S velocity atop the 410-km discontinuity and mantle plums. Earth Planet. Sci. Lett. *262(3-4)*, 398–412.

Wang, B. and Niu, F. (2010). A broad 660 km discontinuity beneath northeast China revealed by dense regional seismic networks in China. J. Geophys. Res. *115*, B06308.

Wang, Y., Uchida, T., Zhang, J., Rivers, M. L. and Sutton, S. R. (2004). Thermal equation of state of akimotoite MgSiO3 and effects of akimotoite–garnet transformation on seismic structure near the 660 km discontinuity. J. Phys. Earth Planet. Inter. *143/144*, 57–80.

Wang, Y., Wen, L., Weidner, D. and He, Y. (2006). SH velocity and compositional models near the 660-km discontinuity beneath South America and northeast Asia. J. Geophys. Res. *111*, B07305.

Weidner, D. and Wang, Y. (1998). Chemical- and Clapeyron-induced buoyancy at the 660 km discontinuity. J. geophys. Res. *103(B4)*, 7431–7441.

Weidner, D. and Wang, Y. (2000). Phase transformations: implications for mantle structure. In Earth's Deep Interior: Mineral Physics and Tomography from the Atomic to the Global Scale, Geophys. Monogr. Ser., (Karato, S.-I., Forte, A., Liebermann, R., Masters, G. and Stixrude, L., eds), vol. 117, pp. 215–235. AGU Washington, D. C.

Wessel, P. and Smith, W. H. F. (1991). Free software helps map and display data. EOS Trans., AGU *72*, 441.

Wiener, N. (1964). Extrapolation, interpolation, and smoothing of stationary time series: with engineering applications. The MIT Press, Cambridge, MA.

Withers, M., Aster, R., Young, C., Beiriger, J., Harris, M., Moore, S. and Trujillo, J. (1998). A Comparison of Select Trigger Algorithms for Automated Global Seismic Phase and Event Detection. Bull. Seism. Soc. Am. *88(1)*, 95–106.

Wood, B. (1995). The effect of H2O on the 410-kilometer seismic discontinuity. Science *268*, 74–76.

Wood, B. (2000). Phase transformations and partitioning relations in peridotite under lower mantle conditions. Earth Planet Sci. Lett. *174*, 341–354.

Wood, B. and Corgne, A. (2007). 2.04 - Mineralogy of the Earth - Trace Elements and Hydrogen in the Earth's Transition Zone and Lower Mantle. In Treatise on Geophysics, (Schubert, G., ed.), pp. 63–89. Elsevier Oxford.

Wortel, M. J. R. and Spakman, W. (2000). Subduction and Slab Detachment in the Mediterranean-Carpathian Region. Science *290*, 1910.